Master's thesis

NTNU
Norwegian University of Science and Technology
Faculty of Natural Sciences

Brynjar Morka Mæhlum

Finding performance parameters and implementing bulk corrections for SEM EDS data in open-source software

Master's thesis in Nanotechnology
Supervisor: Antonius T. J. van Helvoort
June 2023

NTNU
Norwegian University of
Science and Technology

Brynjar Morka Mæhlum

Finding performance parameters and implementing bulk corrections for SEM EDS data in open-source software

Master's thesis in Nanotechnology
Supervisor: Antonius T. J. van Helvoort
June 2023

Norwegian University of Science and Technology
Faculty of Natural Sciences

NTNU
Norwegian University of
Science and Technology

Abstract

This work is aimed at improving SEM EDS analysis through (1) measurement of performance parameters and (2) bulk corrections for qualitative analysis in open-source software. The developed routines were tested on EDS spectra of GaAs and GaSb wafers, acquired using a FEI Apreo SEM with an Oxford Instruments X-Max^N 80mm^2 EDS detector.

The performance parameters are calculated in a Jupyter notebook to test the EDS setup and the selected acquisition settings, with the goal of revealing potential errors and finding the optimal settings. The parameters investigated are energy resolution, Fiori peak-to-background ratio (P/B), Duane-Hunt limit, peak ratios, scale, offset, and peak deviations. The results from the equipment used in this work show that the system specifications are met. The energy resolution was measured to be on average 127 eV, with some variations between specimen, reference peak, and acquisition settings. The highest Fiori P/B ratio was 770 for Ga Kα in GaAs, and 410 for Sb Lα in GaSb. The scale was 10 eV/channel, confirming that the energy axis was well calibrated. Low levels of coincidence counts were observed when the input count rate was below 50k cps. Settings and factors affecting the performance parameters are identified, for example how the Fiori P/B is observed to be highly specimen dependent. It is discussed how different calculation methods of energy resolution and Fiori P/B affects the results, making the metrics less suited to compare different EDS hardware. In future work, the performance test routine should include metrics like the detectors' linearity, stability, and efficiency, which all require an expanded notebook and extended acquisition routine.

To improve quantification routines in SEM EDS analysis, implementation of bulk corrections in open-source Python software is explored. Bulk corrections from the model made by Pouchou and Pichoir in 1991 are implemented, more specifically the XPP version. The results are compared to the commercial software AZtec, to the quantification routine in the open-source Python package HyperSpy, and to a simple implementation ZAF corrections. The quantification routine in HyperSpy use the thin film approximation, and this study show that SEM bulk specimen should not be treated as thin films. AZtec is most accurate, but it is a black box software where the user-end documentation is limited. Black box software is not flexible and not transparent; thus the results cannot be verified, and the analysis cannot be widened. The implemented XPP model seems more promising than the ZAF model, but this first implementation needs to be further refined, for example through updated input factors like the mass absorption coefficient. The code in this work is published under the MIT license, and the work is a step towards better EDS analysis.

Sammendrag

Målet med dette arbeidet er å forbedre analysen av data fra energidispersiv røntgenspektroskopi i skanneelektronmikroskop (SEM EDS) gjennom (1) måling av ytelsesparametere og (2) bulkkorrigeringer for kvalitativ analyse i åpen kildekodeprogramvare i Python. De utviklede rutinene ble testet på EDS-spektre av GaAs- og GaSb-wafere, hvor dataen ble innhentet fra en FEI Apreo SEM med en Oxford Instruments X-Max^N 80mm^2 EDS-detektor.

Ytelsesparameterne blir beregnet i en Jupyter notebook for å teste EDS-oppsettet og de valgte innhentingsinnstillingene. De undersøkte parameterne er energioppløsning, Fiori topp-til-bakgrunn forholdet (P/B), Duane-Hunt-grensen, toppforholdstall, energiskala, forskyvning og toppavvik. Resultatene viser at systemspesifikasjonene til det brukte utstyret er oppfylt. Energioppløsningen ble målt til 127 eV, med noe variasjon mellom prøvene, referansetoppene og innhentingsinnstillingene. Den høyeste Fiori P/B var 770 for Ga Kα i GaAs og 410 for Sb Lα i GaSb. Skalaen var 10 eV/kanal, som viser at energiaksen var godt kalibrert. Det ble observert lave nivåer av sammenfallende tellinger når telleraten var under 50k tellinger per sekund. Innstillinger og faktorer som påvirker ytelsesparameterne er identifisert, for eksempel hvordan Fiori P/B-forholdet er avhengig av prøven. Det blir diskutert hvordan ulike beregningsmetoder for energioppløsning og Fiori P/B påvirker resultatene, noe som begrenser sammenlikningsgrunnlaget mellom ulike systemer. I fremtidig arbeid bør rutinen for ytelsestesting bli utvidet for blant annet å bestemme detektorenes linearitet, stabilitet og effektivitet, noe som krever en utvidet Jupyter notebook og mer omfattende innhentingsrutiner.

For å forbedre kvantifiseringsrutinene i SEM EDS-analyse, er implementeringen av bulkkorrigeringer i Python utforsket. Den mest lovende modellen er basert på arbeidet til Pouchou og Pichoir i 1991, spesifikt XPP-versjonen. Resultatene er sammenlignet med den kommersielle programvaren AZtec, en kvantifiseringsrutine i HyperSpy, og en enkel implementering av ZAF-korrigeringer. Kvantifiseringsrutinen i HyperSpy bruker tynnfilmtilnærmingen, og denne studien viser at SEM-bulkprøver ikke bør bli behandlet som tynnfilmer i kvantifisering. AZtec er mest nøyaktig, men det er en svart-boks programvare der dokumentasjonen for brukeren er begrenset, hvilket betyr at brukeren ikke kan verifisere resultatene og ikke utvide analysen etter egne behov. Den implementerte XPP-modellen ser mer lovende ut enn ZAF-modellen, men denne første implementeringen trenger videre utvikling, for eksempel ved oppdatering av inputvariabler som masseabsorpsjonskoeffisienten. Koden i dette arbeidet er publisert under MIT-lisensen, og arbeidet representerer et skritt mot bedre EDS-analyse.

Preface

This master's thesis is the final part of my master's degree in nanotechnology at the Norwegian University of Science and Technology (NTNU). The work explores the realm of SEM EDS analysis and focuses on enhancing its quantitative capabilities through open-source software. The thesis builds upon my previous work on similar topics conducted in autumn 2022 and represents a focused and dedicated effort from January to June.

I am grateful to my supervisor Professor Antonius T. J. van Helvoort for his guidance and enthusiasm throughout the project. The Research Council of Norway is acknowledged for the support to the Norwegian Micro- and Nano-Fabrication Facility, NorFab, project number 295864.

May this thesis contribute to the field of SEM EDS analysis.

Brynjar Morka Mæhlum

Trondheim, June 6, 2023

Abbreviations

AZ	AZtec
AEM	Analytical Electron Microscope / Microscopy
BSE	Backscattered Electrons
CL	Cliff-Lorimer
cps	Counts Per Second
DT	Dead time
EDS	Electron Dispersive X-ray Spectroscopy
EDSX	Electron Dispersive X-ray Spectroscopy
EDX	Electron Dispersive X-ray Spectroscopy
EM	Electron Microscope / Microscopy
HS	HyperSpy
ICR	Input count rate
OCR	Output count rate
PT	Process time
SE	Secondary Electrons
SEM	Scanning Electron Microscope / Microscopy
STEM	Scanning Transmission Electron Microscope / Microscopy
TEM	Transmission Electron Microscope / Microscopy

Contents

Chapter 1

Introduction

Properties of materials are strongly related to their nanoscale composition and structure [1]. The main tool for studying nanoscale structures is electron microscopy (EM), which are divided into scanning electron microscopy (SEM) and transmission electron microscopy (TEM) [2, 3]. The composition at the nanoscale can be studied by analyzing the X-ray spectrum created from the interactions between the material and the electron probe in the EM, thus getting both structural and compositional information [4]. The composition is revealed in the X-ray spectrum, where the characteristic X-ray lines have energy dependent on the atom of origin, which is a well understood quantum mechanical process [2, 5]. The most common technique for analyzing the X-ray spectrum is energy dispersive X-ray spectroscopy (EDS). In EDS the electron beam of the microscope excites the material that generates the characteristic X-rays, which are detected and sorted by energy in an accumulating digital histogram. Even though EDS have limited energy resolution and is affected by several artifacts, it is the most common technique for analyzing the X-ray spectrum in EM.

There are three main techniques in EM for analyzing characteristic X-rays: X-ray fluorescence (XRF), wavelength dispersive spectrometers (WDS), and energy dispersive X-ray spectroscopy [4]. In XRF the material is excited by a beam of high-energy X-rays or gamma rays. The spatial resolution of XRF is limited both by the fact that the beam cannot be focused as thin as the electron beam and that the beam X-rays can penetrate deeper into the material [6]. XRF have some advantages over EDS, such as a very low detection limit and the possibility of being handheld, but the limit in spatial resolution makes it less suitable for EM, thus XRF is therefore not used in this work. In WDS the material is excited by electrons as in EDS, where the detector has a mechanical spectrometer which is tuned to only one wavelength at a time, that gives a high energy resolution around 10 eV and a high quality spectrum, i.e. a high peak-to-back-ground ratio and limited number of artifacts. The main issue with WDS is that the setup is much larger than a normal SEM and that the WDS technique is much slower than EDS, usually without the spatial resolution of a SEM [2]. Despite the limitations of EDS, the technique is easy to use in EM and gives a high spatial resolution, which makes it the most used analytical technique in research and industry for electron microscopy.

In order to improve the performance of SEM EDS, it is necessary to examine the entire process from signal creation

to interpretation, including the data treatment. By doing so, it becomes possible to identify and address factors that may be responsible for reduced performance. The EDS signal can be influenced by a range of factors between its creation and detection. As such, it is important to have a comprehensive understanding of (i) the experimental setup characteristics, (ii) the acquisition settings, and (iii) the possible post-acquisition data treatment in order to improve the EDS analysis. This is schematically illustrated in Figure 1.1. In this work, performance parameters of the setup (i) and the acquisition settings (ii) are investigated, as these have overlapping metrics. The parameters investigated are the Fiori peak-to-background ratio (P/B) [7], energy resolution, Duane-Hunt limit [8], peak ratios, scale, offset, and peak deviations. The acquisition setting which affect the parameters and the spectrum quality are beam energy, probe current, process time, and acquisition time [2], in addition to the EDS detector, the specimen analyzed and the calculations methods used. Understanding and having a thorough knowledge of one's experimental setup is of utmost importance for users, as it allows for higher quality results through the optimization of the setup and the acquisition, and faster troubleshooting when problems arise. Finally, post-acquisition data treatment (iii) can have a significant impact on the compositional results. Post-acquisition data treatment are for example model fitting, noise treatment, quantification methods, and bulk corrections for SEM EDS data [2,3,5,9]. Characterization of key parameters is necessary to ensure that a spectrum is acquired correctly, and the detector is operating properly, potentially revealing the need for correction.

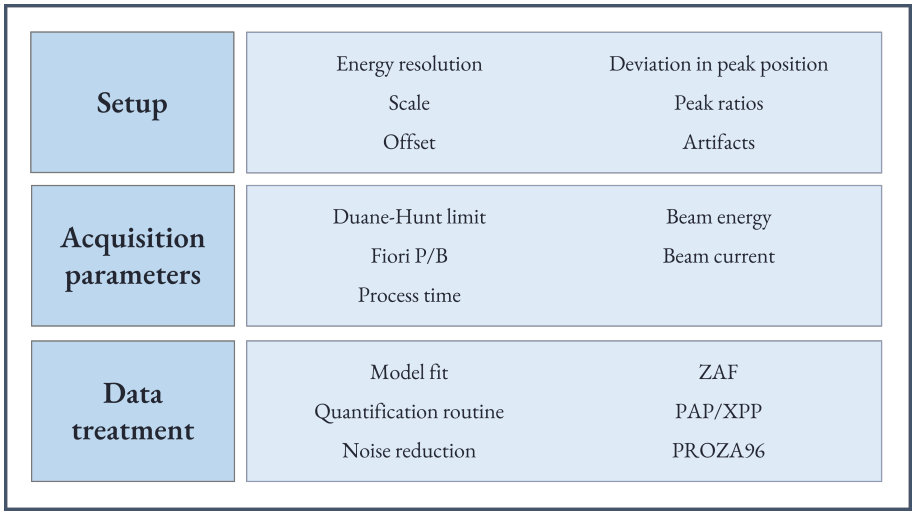

Figure 1.1: Schematic illustration of parameters that can affect SEM EDS analysis, divided into three groups. This work focuses on some parameters, with the aim of improving the performance of SEM EDS.

An additional challenge to improving EDS is that the data treatment in commercial software systems is often not transparent and lacks sufficient open documentation. This can limit the ability to improve compositional analysis for a given setup and data set. Typically, only default quantification methods, such as Cliff-Lorimer [10], are included, while alternative methods, such as optimized correction methods that address weaknesses of default quantification routines and factorless quantification [11], are not be available. In recent years, there has been a growing movement towards open science [12]. Community-driven freeware and open-source software have gained importance in the EDS community, for example through the development of open file formats such as .msa and .emsa [13]

and open source software for data analysis. For SEM EDS analysis, the main non-commercial software is probably DTSA-II [14], which is developed at NIST by Nicholas W. M. Ritchie, inspired by the original DTSA microanalysis software developed by Chuck Fiori, Carol Swyt-Thomas, and Bob Myklebust. For TEM EDS analysis, the Python library HyperSpy [15] is likely the most used open-source software. HyperSpy does have quantification routines implemented, but they are not adapted to SEM EDS signals. However, HyperSpy has the advantage of being Python-based, which has become a primary programming language for scientific and collaborative work. Being Python based enables the analyst to benefit from the integration of algorithms from other fields, such as statistics or machine learning, available in Python libraries such as SciPy [16]. Therefore, HyperSpy is a flexible and dynamic platform available for advancing EDS data analysis.

Earlier work has attempted to improve TEM EDS analysis by making routines for characterizing performance parameters, where a common approach involves analyzing a spectrum of a NiO thin film [17, 18]. Nylund [19] and Skomedal [20] have developed Jupyter notebooks to extract characteristics, such as offset and energy resolution, but even though the reports are available through NTNU Open, the notebooks are not publically available to the electron microscopy community. Moreover, the notebooks are less suited for lower voltages and bulk samples commonly used in SEM, as Nylund and Skomedal worked with TEM-specimen. Skomedal worked partly with STEM, showing that the notebook is relevant for lower voltages, but the effect of bulk samples is not addressed, which will be addressed in this work. Another focus in this work, is to find reference values valid for the modern silicon drift detectors (SDDs). Reference values for characteristics like the Fiori P/B [7] are available in the literature, but these values are specified for older Si(Li) type of EDS detectors and may not apply to the SDDs [21]. To fill this gap, a Python notebook for characterization of performance parameters in a SEM EDS setup will be developed and published, including transparent documentation. The main focus will be SEM EDS, but the notebook should also be applicable to TEM EDS. Following the notebook will be a proposition for a SEM EDS tailored test specimen. This work will contribute to improving the EDS setup and acquisition of EDS data, which will aid quantitative analysis of EDS data, as this is the most used method for compositional analysis with nm spatial resolution today [2].

The overall aim of the project is to improve SEM EDS data analysis in open-source software. The first goal is to systematically go through parameters that characterize the performance of a SEM EDS setup and selected acquisition settings, such as the energy resolution and the Fiori P/B. The main focus is to describe possible metrics and implement them in open-source code, which allows for transparent and reproducible characterization of the performance. The second goal is to develop open-source software for bulk quantification of EDS data, possibly as an addition to the HyperSpy package. The default approach for bulk is a ratio approach with a sensitivity factor [2]. HyperSpy have an implementation of the Cliff-Lorimer quantification method for thin specimen, which is similar to the ratio approach, but bulk specimen needs an iterative and model-based correction routine for atomic number (Z), absorption (A) and fluorescence (F) [2]. Alternatively, calculation of the depth distribution $\phi(\rho z)$ can be used to correct for bulk effects [2, 9]. The $\phi(\rho z)$ corrections explored in this work are the XPP model, which is a version of the PAP model [9], and is supposedly the bulk corrections used in the commercial software AZtec [22, 23]. Neither the ZAF nor $\phi(\rho z)$ corrections are implemented in the published version HyperSpy, and thus this work can serve as a starting point for implementing these corrections in HyperSpy or similar open-source software packages.

This report is structures as follows. The theory chapter covers first the basics of characteristic X-ray generation, the SEM setup, and the EDS system. Then the theory of the performance parameters and the bulk corrections are covered. The method chapter covers the experimental setup, and the data treatment. The following chapter presents the results from the characterization of the performance parameters, and the quantification with and without bulk corrections. The discussion chapter connects the theory and the results, and the conclusion chapter summarizes the findings. Lastly, suggestions for future work are given, followed by the references and the appendices. All the developed code is available on GitHub, and an accompanying notebook is provided in Appendix A.

Chapter 2

Theory

Energy dispersive X-ray spectroscopy (EDS) is a technique for analyzing the elemental composition of a sample with a high spatial resolution, widely used in scanning electron microscopy (SEM) and transmission electron microscopy (TEM) [2, 3]. The technique is based on excitation of core shell electrons, which are bound to the atom with different strengths in different elements, and the following electron relaxation which results in an emitted photon with very specific energy. EDS can be used to determine both the qualitative and quantitative composition of a sample. This theory chapter will cover the generation of X-rays, the SEM system, the EDS detector, data processing of spectra, performance metrics for EDS, and quantification routines without and with correction models.

2.1 Generation of X-rays

To improve the performance of EDS, it is crucial to have a solid understanding of the generation of characteristic X-rays, which forms the basis for the EDS detector and data processing of spectra. The quantum mechanical process of X-ray formation is well understood, and the details can be found in Goldstein [2, Ch. 4.2], Jenkins [4], and Hollas [5, Ch. 8.2]. This section will provide an overview of the fundamental elements in the process, drawing from these sources unless otherwise noted. This section covers the formation of characteristic X-rays, their naming convention, energy and intensity, and background X-rays. The central elements of the section is summarized in Table 2.3.

2.1.1 Characteristic X-rays

The formation of characteristic X-rays from an incident electron beam, or a high (> 0.5 kV) energy photon, is an inelastic quantum mechanical scattering process. The formation can be viewed as a two-step process, where the first step is the ionization of an inner shell in the atom, and the second step is the relaxation of an electron from a higher orbital to the hole left by the ejected electron. The energy difference in the relaxation is the energy of the characteristic X-ray. Figure 2.1 shows in a schematic way the formation of characteristic X-rays with the atom as in

the Bohr model, where ionization and relaxation is divided into two steps. The figure shows three possible radiative relaxations, which produce three characteristic X-rays with different energies.

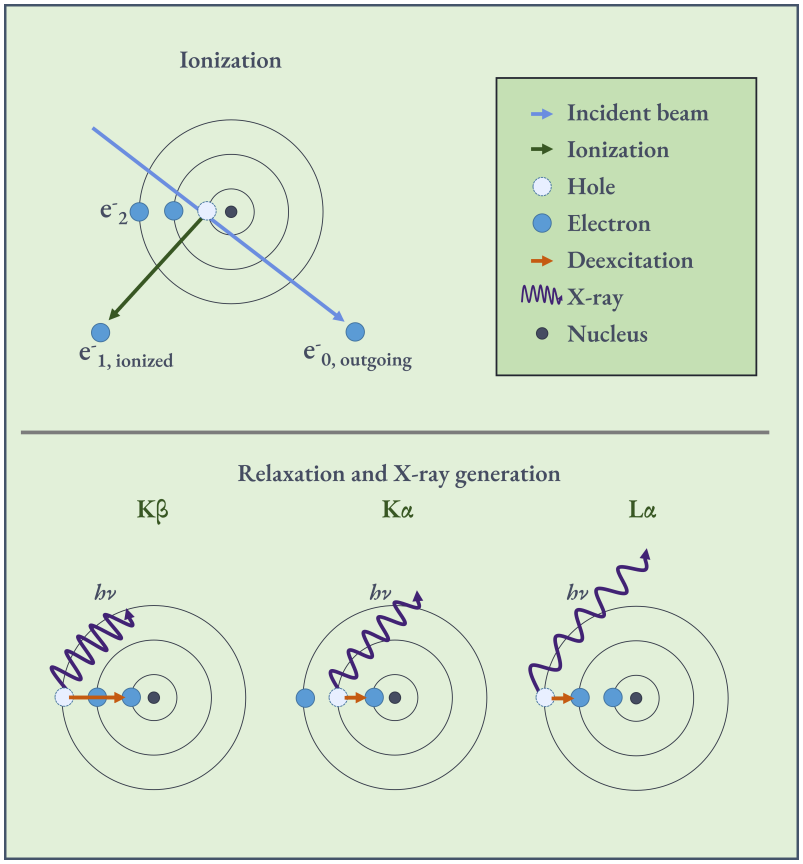

Figure 2.1: The formation of characteristic X-rays with the atom as in the Bohr model, where ionization and relaxation is divided into two steps. The three relaxations shown produce three characteristic X-rays with different energies. Increased energy is illustrated as X-rays with shorter wavelengths.

The incident electron, marked with the blue arrow and annotated as e_0^-, interacts with the atom A and ionizes an inner shell electron, marked with the green arrow and annotated as e_1^-. The ionization leaves a hole in the core orbital. The electron from the beam have a kinetic energy of E_0, and loose energy to both breaking the binding energy of the core orbital and to the kinetic energy of the ionized electron. The binding energy of the core orbital is E_C, **the critical ionization energy**. E_C is dependent on the atomic number of the atom, as higher Z binds the core electron tighter to the nucleus. For an ionization to happen, E_0 must be higher than E_C. The ionization is given in Equation (2.1), and the energy balance is given in Equation (2.2). An X-ray photon with energy higher than the binding energy of the core orbital can also do the ionization. If a characteristic X-ray photon is doing the ionization, the process is named the fluorescence effect and the resulting photon is called a secondary X-ray.

$$e^-_{0,\,\text{incident}} + A \rightarrow e^-_{0,\,\text{outgoing}} + A^+ + e^-_{1,\,\text{ionized}} \tag{2.1}$$

$$E_{0,\text{ incident}} = E_{0,\text{ outgoing}} + E_C + E_{1,\text{ kinetic}} \tag{2.2}$$

The second step is the relaxation, illustrated in the bottom part of Figure 2.1 and expressed in Equation (2.3). An outer shell electron, annotated as e_2^-, relaxes to the hole in the inner shell, and the difference in energy between the orbital is emitted as a photon. This photon is the characteristic X-ray, and the energy of the photon can be expressed as $h\nu$ [5, Eq. (8.12)]. The energy of the characteristic X-ray is the difference in energy between the ionized orbital and the orbital filling the hole, shown in Equation (2.4). The energy of the characteristic X-ray is usually measured directly in keV [2, Eq. (4.2b)].

$$e^-_{2,\text{ outer shell}} + \text{"inner shell hole"} \longrightarrow e^-_{2,\text{ inner shell}} + h\nu_{\text{X-ray}} \tag{2.3}$$

$$h\nu_{\text{X-ray}} = E_C - E_{2,\text{ binding of outer shell}} \tag{2.4}$$

As seen in Equation (2.4), the critical ionization energy E_C is slightly higher than the energy of the characteristic X-ray ($h\nu_{\text{X-ray}}$). If the incident energy on an atom is exactly the critical ionization energy, the atom might be able to absorb this energy and emit a characteristic X-ray, but the probability of this happening is very low [2, 5]. When the incident energy is slightly higher than the energy of the X-ray line, the probability of absorption increase abruptly. The abrupt increase of the absorption slightly above a characteristic X-ray line is called an **absorption edge** [2]. The probability of absorption is given by the **mass absorption coefficient**, noted as μ_ρ in this work, which is dependent on the energy of the X-ray. μ_ρ for a material can be plotted as a function of the energy of the X-ray, and the absorption edges are clearly visible as nearly vertical increase of μ_ρ in the plot. Figure 2.2 shows μ_ρ for GaAs and GaSb, with the energy of relevant characteristic X-ray lines as dotted vertical lines. The mass absorption coefficient, or mass attenuation coefficient, is defined as the attenuation coefficient of the material is normalized by the density of the material [2]. The normalization by the density makes the mass absorption coefficient a material property which tells how likely a mass of the material is to absorb X-rays. It is common to write the mass absorption coefficient as μ/ρ, but it is written μ_ρ in this work to clearly show that it is referring to one specific value for the material, which have the unit cm^2/g. The mass absorption coefficient of a mixture of elements, e.g. GaAs, is a combination of the mass absorption coefficients of the elements in the mixture, and can be calculated with HyperSpy [15][1]. HyperSpy contains the mass absorption coefficients of the elements as a function of energy, with data from a NIST database [24]. Figure 2.7 combines an EDS spectrum with the mass absorption coefficient of Si, and shows how the absorption increases at the absorption edge. As μ_ρ for an element is relatively low at the energy of the elements own characteristic X-ray lines, the probability of absorption is low. For example, a Fe Kα X-ray in Fe has a low probability of ionizing the same transition in another Fe atom. This makes an element relatively transparent to its own characteristic X-rays [2, Ch. 4.4]. After the sharp increase at the absorption edge, the probability of absorption decreases. This makes the probability of ionization greatest when the energy is just above the

[1] http://hyperspy.org/hyperspy-doc/current/api/hyperspy.misc.material.html

critical ionization energy. If the energy is significantly higher than the critical ionization energy, the probability of ionization is lowered [25, p. 78]. This implies that using a higher energy for ionization is not necessarily better, which is discussed more in Section 2.3.2.

When the outer shell electron is relaxed, a new hole is generated in the outer shell. This leads to a cascade of relaxation events, but the energies of these transitions are too low to emit characteristic X-rays. These and other non-radiative relaxations will not be discussed further.

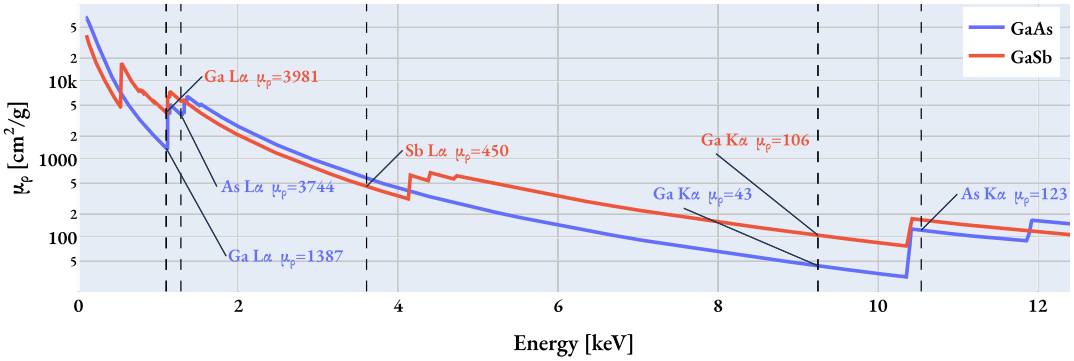

Figure 2.2: The mass absorption coefficients (μ_ρ) of GaAs (blue) and GaSb (red), with characteristic X-ray energies marked with vertical lines. The μ_ρ of each specimen at the characteristic X-ray lines are annotated in the corresponding color, in units of cm^2/g. Note how much μ_ρ increases at the absorption edge, which is slightly higher than the energy of the characteristic X-ray. The absorption edge in GaSb around 0.5 keV is the M-lines of Sb, and the additional steps after Sb Lα is the Lβ lines.

In the second step of the X-ray formation process described in Equation (2.3), there is also a probability that the energy from the relaxation is not used to emit a photon, but used to eject another electron from a higher energy orbital, giving it kinetic energy. This results in the ejection of two electrons, one from the core orbital and another from the higher energy orbital, known as an Auger electron. Auger electrons are useful for surface studies since they can only penetrate approximately 2 nm of solid material, thereby not escaping from inside the sample. The emitted X-rays, on the other hand, are isotropically emitted from a large volume and can penetrate up to 4000 nm, as the absorption of X-ray photon is far less likely than that of a charged electron. The ratio of characteristic X-ray photons to Auger electrons is known as the **fluorescence (quantum) yield**, ω.

$$\omega = \frac{\text{X-ray photons}}{\text{Auger electrons}} \tag{2.5}$$

The fluorescence yield is dependent on the ionized atom, with in general higher fluorescence yields for heavier atoms. ω is also dependent on the shell that is ionized, with the typical trend being $\omega_K > \omega_L > > \omega_M$ [2, p. 267]. The dependence on Z and the shell is shown in Figure 2.3, a figure adapted from Goldstein [2, Fig. 4.3 (d)].

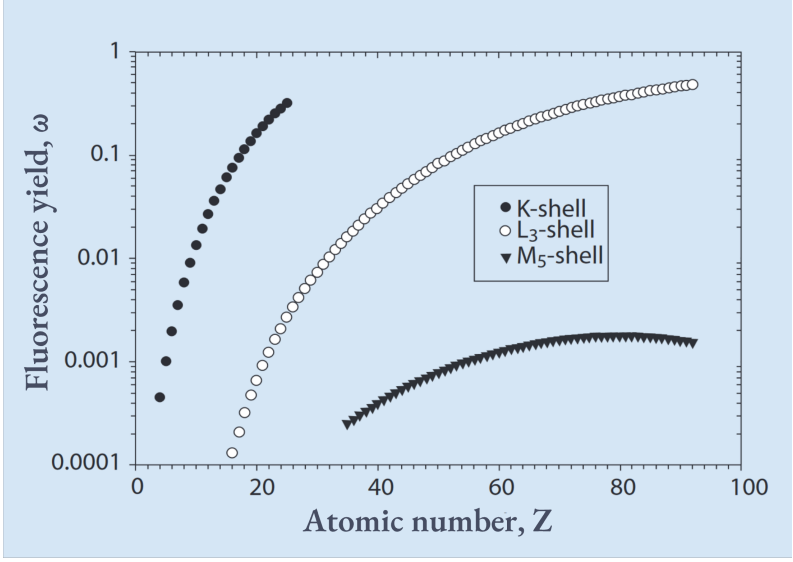

Figure 2.3: ω for K-, L- and M-shell, as a function of atomic number Z. Adapted from [2, Fig. 4.3 (d)].

2.1.2 The naming convention of characteristic X-rays

This subsection explains the Siegbahn naming convention for characteristic X-rays, which is used in this thesis. The Siegbahn notation is based on the Bohr model of the atom and intensities of the X-ray lines in a spectrum. As the Bohr model is a simplification of the actual atom, the Siegbahn notation is somewhat confusing when looking at the actual orbital transitions, as they are illustrated in Figure 2.4. It should be noted that The International Union of Pure and Applied Chemistry (IUPAC) made a new and systematic naming convention for X-ray lines [26]. However, the Siegbahn notation is still the most used convention [2, Ch. 4.2.4], and is for example used in HyperSpy, and is therefore used in this thesis. Additionally, the IUPAC notation is not connected to the intensity of the X-ray lines, which is a useful property when discussing the X-ray lines in a spectrum. A table showing the correspondence between the two naming conventions is shown in Table 2.1. The IUPAC naming convention notes both the orbital in the inner and outer shell, thus Table 2.1 shows what the possible observable transitions in EDS between 0.1 and 25 keV are. Figure 2.5 shows the actual L-lines from Sb in an EDS spectrum.

The transition lines are grouped and named based on the orbital the vacancy is in, and the orbital the electron is relaxed from. The naming convention is semi-systematic because it is the original empirical system published in Nature by the Swedish physicist Kai Siegbahn in 1916 [27], without the modern theoretical knowledge on orbitals. A family of X-ray lines is named by the shell of the generated hole, i.e. the principal quantum number n of the vacancy orbital. Relaxations to the innermost shell $n = 1$ is named K-transitions, relaxations to $n = 2$ is L-transitions, relaxations to $n = 3$ is M-transitions. The lines in the families are further grouped with Greek letters or other symbols, where the order is related to their relative intensity: $\alpha > \beta > \gamma > \nu > \zeta$. Additionally, the minor L-shell transitions in split into families notated with Latin letter subscripts: l, s, t, u, and v [2, Ch. 4.2.4]. Lines which are closely related are given a subscript number, where 1 is the most intense line. As the energy resolution of EDS is limited, a single peak in a spectrum can consist of multiple transitions which are closely related, e.g. $K\alpha_1$

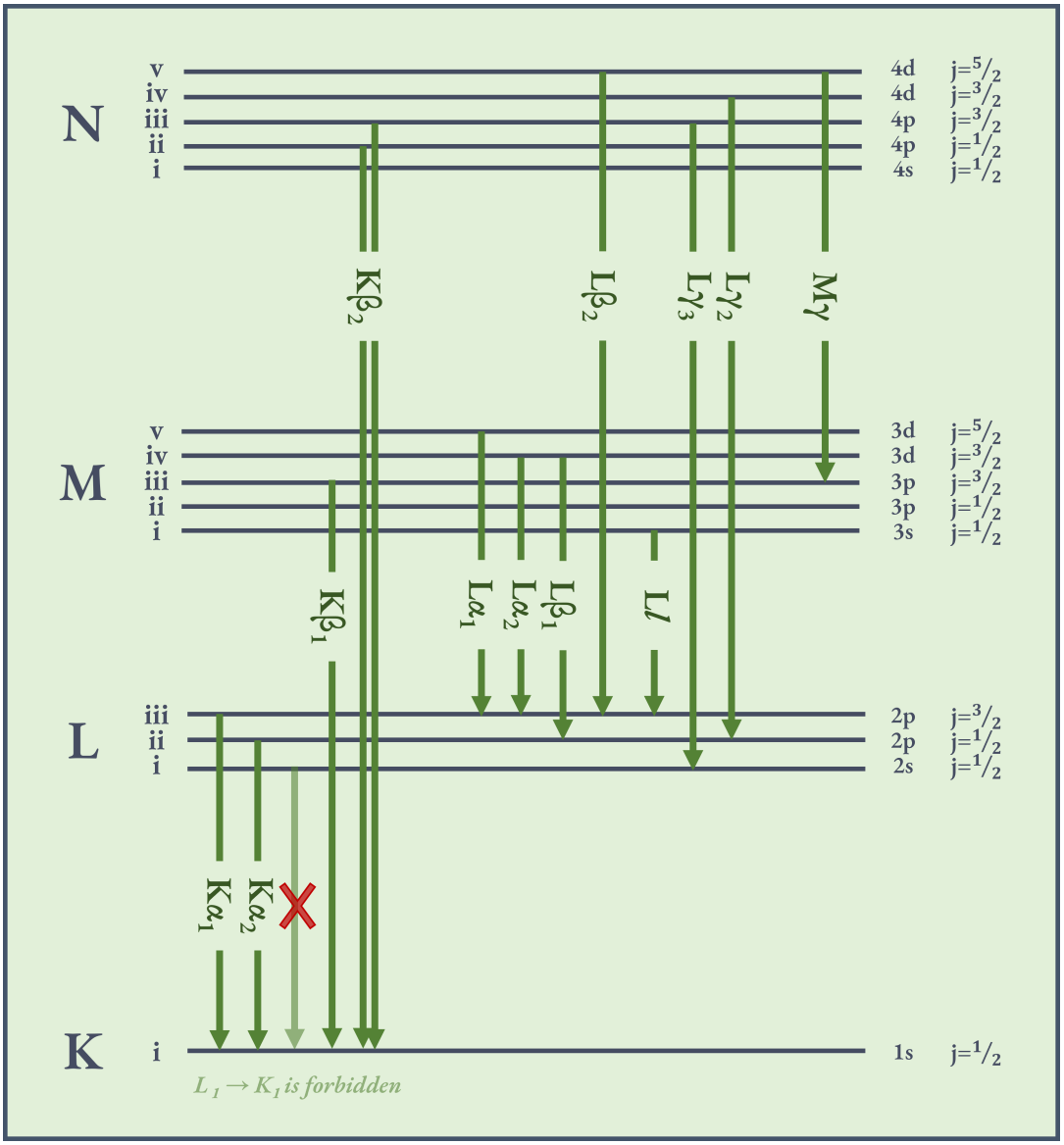

Figure 2.4: Schematic of the electron relaxations with their naming convention. The horizontal lines are the orbitals in the different shells, and the arrows are the relaxations. The distance between the orbitals is not to scale. The shell name and orbital number are shown on the left, and quantum number n, l, and j are shown on the right. The orbital names (s, p, and d) are the azimuthal quantum number l. The figure also show one forbidden line, where l does not change. Table 2.1 include more transitions. Figure 2.5 shows the Sb L-lines in a spectrum.

Table 2.1: The naming of characteristic X-ray lines. The table includes lines observed in EDS from 0.1 to 25 keV. The IUPAC notation is first the inner orbital, then the outer orbital. The Siegbahn notation is the inner shell and the lines relative intensity. Figure 2.4 visualize some lines in the table. As seen for the M transitions, the Siegbahn notation does not cover all possibilities. Remake of Table 4.1 in Goldstein [2].

Siegbahn	IUPAC	Siegbahn	IUPAC	Siegbahn	IUPAC
$K\alpha_1$	K-L_3	$L\alpha_1$	L_3-M_5	$M\alpha_1$	M_5-N_7
$K\alpha_2$	K-L_2	$L\alpha_2$	L_3-M_4	$M\alpha_2$	M_5-N_6
$K\beta_1$	K-M_3	$L\beta_1$	L_2-M_4	$M\beta$	M_4-N_6
$K\beta_2$	K-$N_{2,3}$	$L\beta_2$	L_3-N_5	$M\gamma$	M_3-N_5
		$L\beta_3$	L_1-M_3	$M\zeta$	$M_{4,5}$-$N_{2,3}$
		$L\beta_4$	L_1-M_2		M_3-N_1
		$L\gamma_1$	L_2-N_4		M_2-N_1
		$L\gamma_2$	L_1-N_2		M_3-$N_{4,5}$
		$L\gamma_3$	L_1-N_3		M_3-O_1
		$L\gamma_4$	L_1-O_4		M_3-$O_{4,5}$
		$L\eta$	L_2-M_1		M_2-N_4
		Ll	L_3-M_1		

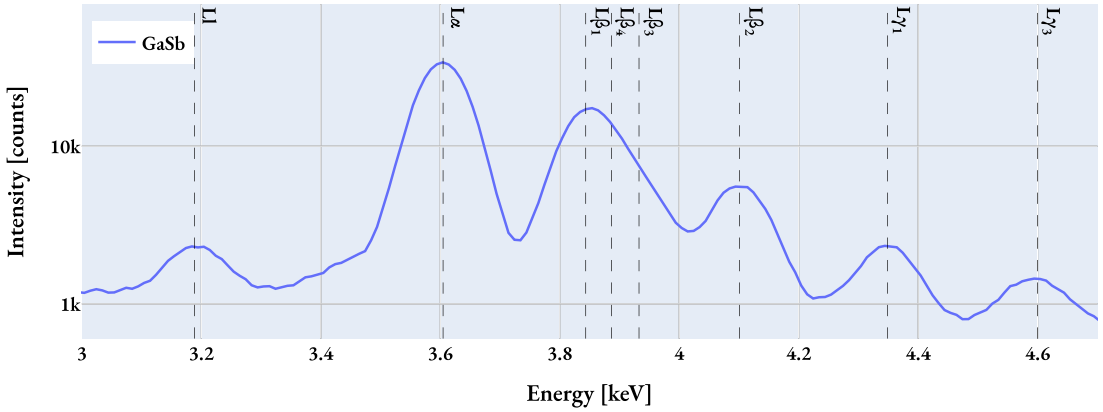

Figure 2.5: Example spectrum of the Sb L-peaks in a GaSb wafer. Taken at 30 kV, 50 pA, process time 6, live time 120 s, ICR at 17000 cps, and 43% DT. For further experimental details, see Chapter 3.

and $K\alpha_2$ making the $K\alpha$ line. Resolving $K\alpha_1$ and $K\alpha_2$ in EDS is usually first possible for elements heavier than tin with $Z = 50$ [5, Ch. 8.2.2.3]. Heavier element have both more possible lines and more resolved lines, as the orbitals have higher energy differences.

Putting these three naming conventions together, we name the transition $L_3 \rightarrow K_1$ as $K\alpha_1$, and $L_2 \rightarrow K_1$ as $K\alpha_2$, with more examples in Figure 2.4. The transition $L_1 \rightarrow K_1$ has $\Delta l = 0$ and is thus forbidden by the selection rules, see Equation (2.6). In gallium the $K\alpha_1 = 9252$ eV and $K\alpha_2 = 9223$ eV [28] have an energy difference of $\Delta E = 27$ eV, which is too low to be resolved in EDS.

2.1.3 Energy and width of characteristic X-ray lines

The energy of the X-rays is the energy difference between the orbitals, and the spread in energy from a single line is typically between 1-10 eV. The energy difference between the orbitals increase with atomic number Z, as the inner electrons are bound tighter to the nucleus. A table with the energies of the relevant characteristic X-rays in this thesis is given in Table 2.2. The table also includes the relative weight of the lines, which is the intensity of the line relative to the strongest line in the group. The most central parts of the energy of the X-rays have been mentioned earlier, but the width of the lines is also important. This section also includes where the energy of X-rays can be found.

The natural width of Mn $K\alpha$ is around 1.5 eV, while the measured width in EDS is typically between 120-140 eV [2, Ch. 16.1.1]. This peak broadening is due to counting statistics and instrument electronics, which is discussed in Section 2.3.1. The broadness of the peaks in EDS increase with energy, and the peak broadening effect is the most limiting factor for the energy resolution of EDS. The change from lines to broadened peaks is illustrated in Figure 2.8. Data tools have been developed for EDS to identify and separate peaks which overlap in energy, like peak deconvolution and peak fitting. Higher resolution can be achieved by analyzing the wavelength rather than the energy of the X-rays. This is called wavelength dispersive X-ray spectroscopy (WDS), and has an energy resolution of ca. 10 eV [2, 3], but is less practical than EDS and will not be discussed further.

The energy of characteristic X-rays has been measured and calculated, and published in tables and databases. One source is the X-ray Data Booklet [28], another is one of the NIST X-ray databases, like the "X-Ray Transition Energies Database" [29]. The Python package HyperSpy includes an elemental database with the energy of characteristic X-rays [15], which is based on NIST database 66, "X-Ray Form Factor, Attenuation, and Scattering Tables" [24]. The different sources are focused on certain areas, like how NIST database 128 [29] includes experimental data, while the HyperSpy database is less comprehensive but faster to use. An analyst should be aware of the limitations of the used source, like how the HyperSpy database does not include the M-lines for Sb. The limited energy resolution of EDS combined with overlapping peaks can lead to mislabeling in the qualitative analysis, which is discussed in Section 5.2.4. The reason for the missing M-lines in the HyperSpy database is probably a down prioritization due to the low intensity of these M-lines, which is discussed in the next section.

2.1.4 Intensity of characteristic X-rays

Just as the energy of the X-ray lines increase with atomic number, the number of possible lines increase too. As the energy difference between orbitals increase, close lines like Kα_1 and Kα_2 are, as explained earlier, resolved. The number of possible lines increase with Z because there are more orbitals giving more possible transitions. However, not all transitions are allowed, and their intensity varies. The selection rules, given in Equation (2.6), govern which transitions are allowed. The selection rule applies to the electron which is being relaxed, and it is [5, Sec. 8.2.2.2]:

$$\Delta n \geq 1; \qquad \Delta l = \pm 1; \qquad \Delta j = 0, \pm 1 \tag{2.6}$$

Where Δn is the change in principal quantum number, Δl is the change in orbital angular momentum, and Δj is the change in total angular momentum. The orbital angular momentum is also called the azimuthal quantum number. The three quantum numbers are included in Figure 2.4, for K to N_5. Lines which are forbidden by the selection rules, like the transition from K to L_1, have an intensity of zero. Some lines are allowed, but have too low intensity to be detected in EDS.

The ionization cross-section is the probability of an ionization for a given line, originally described by Bethe [30] as:

$$Q_T = \frac{\pi e^4 b_s n_s}{E_0 E_C} \log\left(\frac{c_s E_0}{E_C}\right) \tag{2.7}$$

Where Q_T is the total scattering cross-section, e is the elementary charge, n_s is the number of electrons in the ionized shell, b_s and c_s are constants for the shell of ionization, E_0 is the incident electron energy, and E_C is the critical ionization energy. The ionization cross-section is strongly dependent on the atomic number of the element of interest, and higher Z have higher E_C.

The generated intensity of the allowed lines is proportional to the electron dose from the probe, the number of atoms and the atomic weight of the given element, the fluorescence yield, and the ionization cross-section. The electron dose is a function of the probe current and the acquisition time. The dependency of the number of atoms of the given element is crucial, as this is the basis for the quantitative analysis in EDS. The factors mentioned above are discussed further in the section on quantitative analysis in EDS Section 2.5. Calculating the intensity of characteristic X-ray lines from bulk specimen is not trivial, but in Goldstein there is an experimentally based equation for this: [2, Eq. 4.8]:

$$I \approx i_p (U - 1)^n \tag{2.8}$$

Where I is the relative intensity of X-rays from different atomic numbers and shells, i_p is the probe current, U is the overvoltage (covered in Section 2.3.2), and n is a constant which depends on Z and the excited orbital. It is stated in Goldstein that n is typically between 1.5 and 2.0, and the equation is based on the work presented and published by Lifshin et al. 1980 [31].

Additionally, the intensity of detected X-rays is not the same as the intensity of the X-rays which are generated. The probability of absorption is a function of density and increase with the travel distance. Photons with lower energy are absorbed more easily than photons with higher energy, i.e. the escape depth of the X-rays increase in general with energy. Expressed in terms of the absorption coefficient μ and the path length l, the intensity is reduced by:

$$I_{\text{escaped}} = I_{\text{generated}} \cdot e^{-\mu l} \tag{2.9}$$

Where μ is dependent on the material (Z) and the energy of the X-rays. When a thin specimen ($<$ 30 nm) is analyzed [32], the absorption effect can be ignored. This is the so-called thin film approximation, used for example in the Cliff-Lorimer quantification routine, see Section 2.5. When thicker samples are analyzed, the absorption and fluorescence effect must be taken into account for the quantitative analysis [2]. Escape probability and depth is also dependent on the absorption edges present. When an X-ray photon is absorbed within the specimen, it can ionize an atom and generate a new X-ray with a lower energy, which is the previously mentioned fluorescence effect. When thin samples are analyzed, the fluorescence effect can be ignored, but when thicker samples are analyzed, the fluorescence effect can be significant. For secondary fluorescence to happen, a characteristic X-ray must be absorbed, and it must have higher energy than the critical ionization energy of other lines in the material. If the absorbed X-ray have an energy higher than the $E_C + 5$ keV of the other lines, the fluorescence effect is negligible [2, p. 306]. The fluorescence effect is also dependent on the path length of the X-rays in the specimen. Compensation for the fluorescence effect is discussed in Section 2.5.1.

2.1.5 Background X-rays

The detected spectrum contains more than peaks from characteristic X-ray lines as discussed so far. In addition to the characteristic X-rays generated, the electron beam generates background X-rays. The background radiation is also called the bremsstrahlung, breaking radiation, and the continuum radiation. These X-rays are formed by the deacceleration of the incident beam electrons in the Coulomb fields of the atoms in the specimen, where the electron loose kinetic energy. This effect includes both velocity and directional changes, and the changes in the incident electrons paths are visualized in a Monte Carlo simulation in Figure 2.12. Acceleration and deacceleration of charged particles emits photons [33]. The background X-rays are white noise, giving no information about the sample. However, the background radiation can be used to calculate at least one parameter describing the detector performance, namely the Duane-Hunt limit covered in Section 2.4.2. Through pre-modelling of the background based on the sample geometry and composition, the background signal can also be used to check for incorrect tilt or shadowing [34]. To do accurate qualitative analysis, the background radiation must be subtracted from the total spectrum. This can be done in multiple ways, like pre-modelling, linear interpolation, background filtering, and background modelling [35]. In this thesis, the background is modelled as a polynomial function of the energy and fitted to the data with the least squares method [15].

The energy lost by an electron in a single scattering event can be any value from almost zero to the incident electron energy, E_0. In other words, the background X-rays can have any energy from around 100 eV to the incident electron

energy [2, Ch. 4.3]. The probability of a background X-ray with energy E can be described by the Kramer's cross-section and empirically estimated as:

$$N(E) = \frac{KZ(E_0 - E)}{E} \tag{2.10}$$

Where $N(E)$ is the number of background X-rays with energy E, K is Kramer's constant, Z is the atomic number of the specimen, and E_0 is the incident electron energy. As seen in Equation (2.10), the formation of background radiation is inversely proportional to the energy of the X-rays, i.e. $N(E) \propto 1/E$. However, the low energy X-rays formed inside the specimen are absorbed by the specimen, resulting in a difference between the detected and the generated background X-rays. The difference between the generated and detected background X-rays is visualized in Figure 2.6. The detected background X-rays have a maximum in the low keV region, depending on the specimen and acceleration voltage. The peak is typically around 2 keV. When the energy approach zero, the detected background decrease rapidly. In addition, the absorption edges of the materials in the specimen influence the intensity of the background radiation, as described in Section 2.1.1. As the specimen absorbs more above an absorption edge, the intensity of the background can be observed to decrease abrupt just above a strong absorption edge [2, p. 59]. This effect was observed in the authors project thesis, with a suggestion of splitting the background modelling into two parts, one for the low energy background and one for the high energy background [36]. The effect of the absorption edge was observed to variate, being strongest for the highest peak in the lower keV region. An example of the effect of the absorption edge is shown in Figure 2.7. Modelling the background as two connected polynomials could be a potential improvement of the model fitting [11, 15], and thus making the qualitative analysis more accurate, especially for low keV analysis.

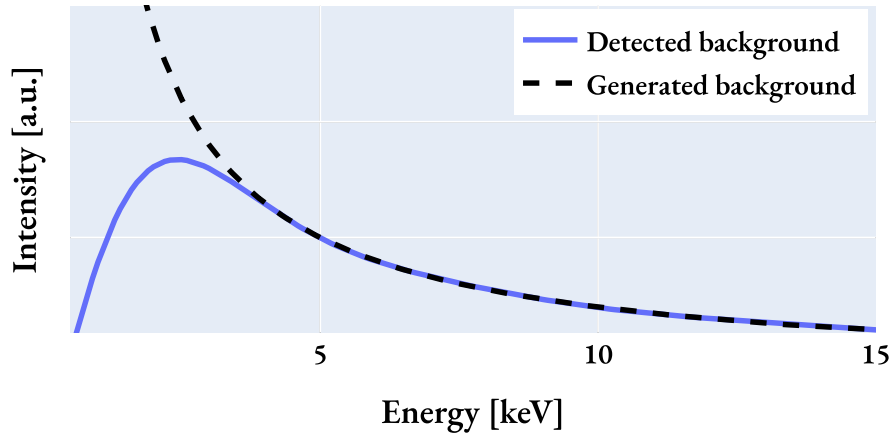

Figure 2.6: The difference between the generated and detected background X-rays. The detected background is shown in blue, and the generated background is shown in the dashed black line.

The formation of background radiation is anisotropic, with higher intensity for the forward scattered signal. In thin samples, where the electron beam trajectories are almost aligned, this anisotropy can cause a variation in the continuum intensity along the beam, with the forward direction differing from the backward direction. However,

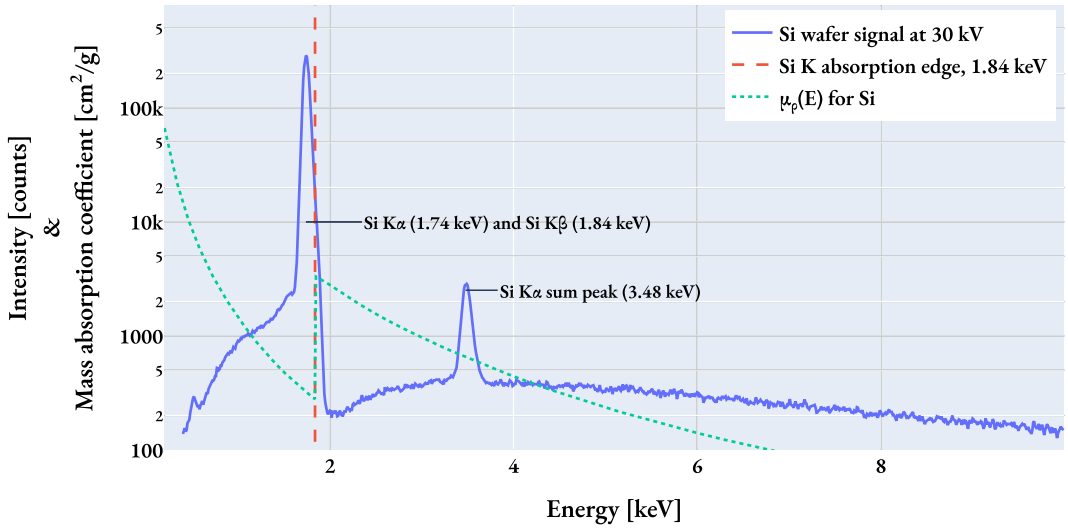

Figure 2.7: The effect of the absorption edge on the background radiation. The spectrum in blue is from a Si wafer and the red dashed line is the Si K absorption edge at 1839 eV [15, 37]. The background is abruptly reduced just above the absorption edge. The green dotted line is the mass absorption coefficient (μ_ρ) of Si as a function of energy, which increase with a factor of 10 at the absorption edge. The spectrum shows the overlapping Si Kα and Kβ peaks, the Si sum peak and a small O Kα signal. Sum peaks are discussed in Section 2.3.3. The spectrum data was acquired in the authors' project report work [36].

in thick samples, elastic scattering randomizes the beam electron trajectory segments, effectively eliminating this anisotropy and resulting in an isotropic X-ray continuum. This is visualized in the schematic of the interaction volume in Figure 2.11, and the previous mentioned Monte Carlo simulation in Figure 2.12.

2.1.6 From theory to an observed spectrum

This last part of the section combines the different parts of the theory to the observed spectrum. Figure 2.8 shows a schematic of the steps from a theoretical spectrum to an observed spectrum of GaAs. Panel (a) shows a theoretical spectrum with only the characteristic lines. Panel (b) shows the lines broadened to Gaussian peaks due to the limited energy resolution (see Section 2.1.3) on a background, where the detected background is modelled as a polynomial function of the energy. The generated background is described by Kramer's cross-section in Equation (2.10), while a modelled background is typically just the best fitting sixth order polynomial when the peaks are removed [15]. Notice how the peaks broaden more with higher energy. Peak broadening with energy is discussed more in Section 2.4.3 and described with Equation (2.13). Panel (c) shows an observed spectrum, where the unevenness of the recorded counts is visible. The observed spectrum is recorded in a SEM with an EDS detector. The experimental setup is discussed in Section 2.2 and Section 2.3. The observed spectrum also shows peaks which are artifacts, like a noise peak and a small Si Kα peak at 1.74 keV, which is the internal fluorescence peak. The artifacts in the EDS spectrum are discussed in Section 2.3.3.

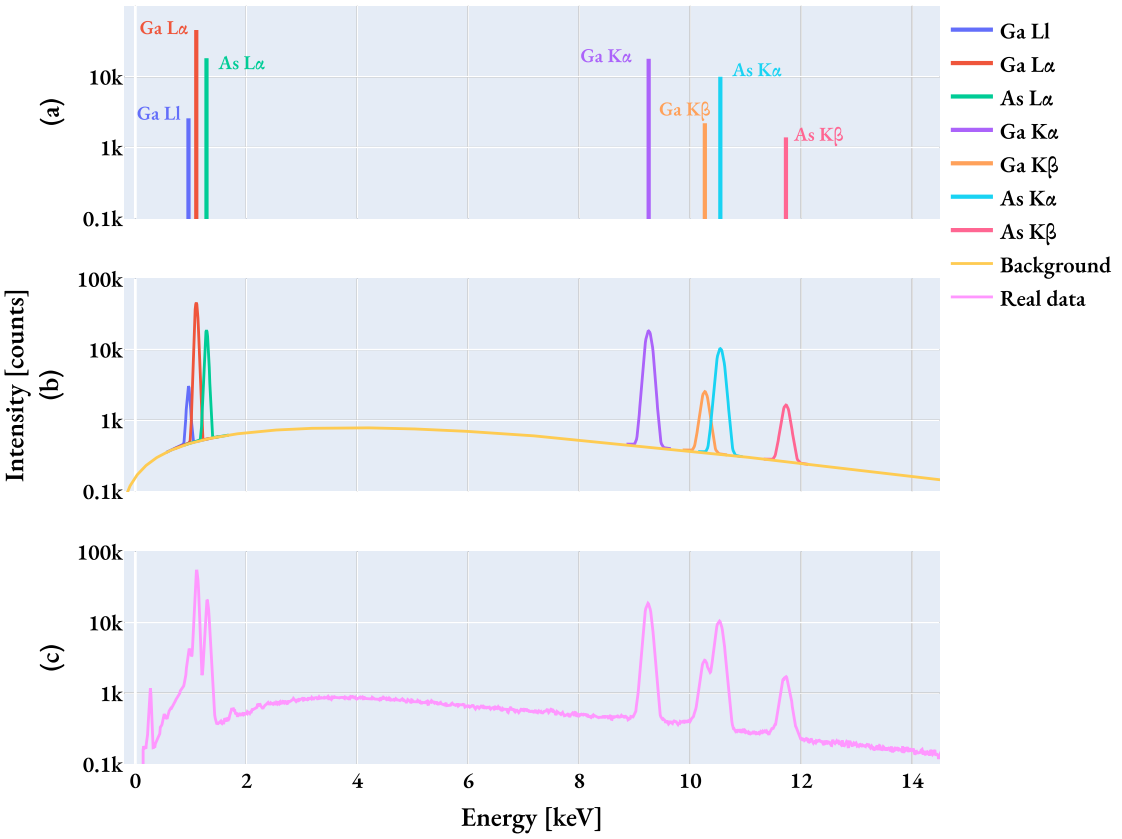

Figure 2.8: From theory to an observed spectrum. (a) a theoretical spectrum with only the characteristic lines, (b) lines broadened to peaks on a background, and (c) an observed spectrum. The spectrum is of GaAs, and the peak names are annotated in (a). The background in (b) is modelled as a polynomial function of the energy. (c) show the noise peak and a small internal fluorescence peak at 1.74 keV (Si Kα), before and after the L-lines, respectively.

Table 2.2: The line energies of the most relevant lines in this thesis. The energies and weights are from HyperSpy [15]. The relative weights are the intensity relative to the strongest line in the group, i.e. Lα or Kα.

Energy *[keV]*	Element	Line	Relative weight
0.277	C	Kα	1.00
0.525	O	Kα	1.00
0.957	Ga	Ll	0.05
1.098	Ga	Lα	1.00
1.120	As	Ll	0.05
1.125	Ga	Lβ_1	0.17
1.195	Ga	Lβ_3	0.05
1.282	As	Lα	1.00
1.317	As	Lβ_1	0.17
1.386	As	Lβ_3	0.05
1.740	Si	Kα	1.00
1.839	Si	Kβ	0.03
3.189	Sb	Ll	0.04
3.605	Sb	Lα	1.00
3.844	Sb	Lβ_1	0.43
3.886	Sb	Lβ_4	0.09
3.933	Sb	Lβ_3	0.15
4.101	Sb	Lβ_2	0.16
4.349	Sb	Lγ_1	0.06
4.600	Sb	Lγ_3	0.03
9.252	Ga	Kα	1.00
10.264	Ga	Kβ	0.13
10.544	As	Kα	1.00
11.726	As	Kβ	0.15
26.359	Sb	Kα	1.00
29.726	Sb	Kβ	0.15

Table 2.3: Definitions for various terms related to the generation of X-rays, Section 2.1.

Name	Definition
Characteristic X-ray	An X-ray photon originating from a certain orbital transition, with a very specific energy.
Incident (electron) beam	The incident electron beam from the EM, which ionize the atoms and produce the signals detected. See Figure 2.1.
Inner shell electron	The electron in the orbital closest to the atomic core. This is the electron that is ionized. See Figure 2.1.
Outer shell electron	The electron from the outer orbital which is relaxed into the hole left by the ionized electron. See Figure 2.1.
Atomic number, Z	The atomic number of the element.
Critical ionization energy, E_C	The energy required to ionize the element of interest. Dependent on Z and the orbital to excite.
Secondary fluorescence	When an X-ray photon loose energy to ionize another atom, thus creating a new characteristic X-ray.
Absorption edge	The energy where μ_ρ abruptly increase, because the energy is slightly above the E_C, and incoming electrons can thus ionize the respective line. See Figure 2.7.
Fluorescence yield, ω	The ratio of characteristic X-rays to Auger electrons, which change for the ionized shell ($\omega_K > \omega_L >> \omega_M$) and tend to increase with Z. See Figure 2.3.
Ionization cross-section, σ_T	The probability of the ionization at a certain energy for a given line. See Equation (2.7)
Selection rules	Quantum mechanical rules which specifies the allowed orbital transitions for the relaxing electron. See Equation (2.6).
Background X-rays	X-rays generated by deacceleration of the electrons in the Coulomb fields of the atoms, which is noise in the analysis. See Figure 2.6.
Relative weight	The relative intensity of a line compared to the strongest line in the group.
Line vs. peak	In this work, line generally refers to the characteristic X-ray, while peak refers to the broadened signal in the spectrum.

2.2 Scanning electron microscopy (SEM)

This study involves the use of a controllable nanometer-scale electron beam to generate an X-ray spectrum for analyzing the composition of small volumes, primarily a SEM equipped with an EDS detector. In SEM the electron beam has energies in the range $1 - 30$ kV and bulk specimens are usually analyzed. In TEM the electron beam has energies in the range $100 - 300$ kV and thin specimens (< 100 nm) are usually analyzed. The differences between SEM and TEM EDS analysis will be addressed at the end. Electron microscopes are often equipped with an EDS detector to provide analytical capabilities that complement imaging and diffraction analyzes. This section provides a brief overview of how the electron beam is created and controlled in the electron microscope, as well as information on electron-matter interaction, imaging detection and image contrast in SEM. If not stated otherwise, this section on SEM is based on Goldstein [2]. A summary of terms in the section is provided in Table 2.4.

2.2.1 Electron beam generation and control

A schematic of a SEM is shown in Figure 2.9. The **electron gun** is the source of the electron beam, where electrons are emitted with high kinetic energy by a high voltage. Currently, field emission guns are standard because they produce a brilliant beam compared to thermoinonic filament, and thereby high signal and good spatial resolution with the possibility of sum nm spot size. The emittance of the electron gun is controlled by the user with the beam current and the accelerating voltage. The acceleration voltage, or the beam energy E_0, is typically in the range of $1 - 30$ keV. The beam current is typically in the range of $0.01 - 10$ nA.

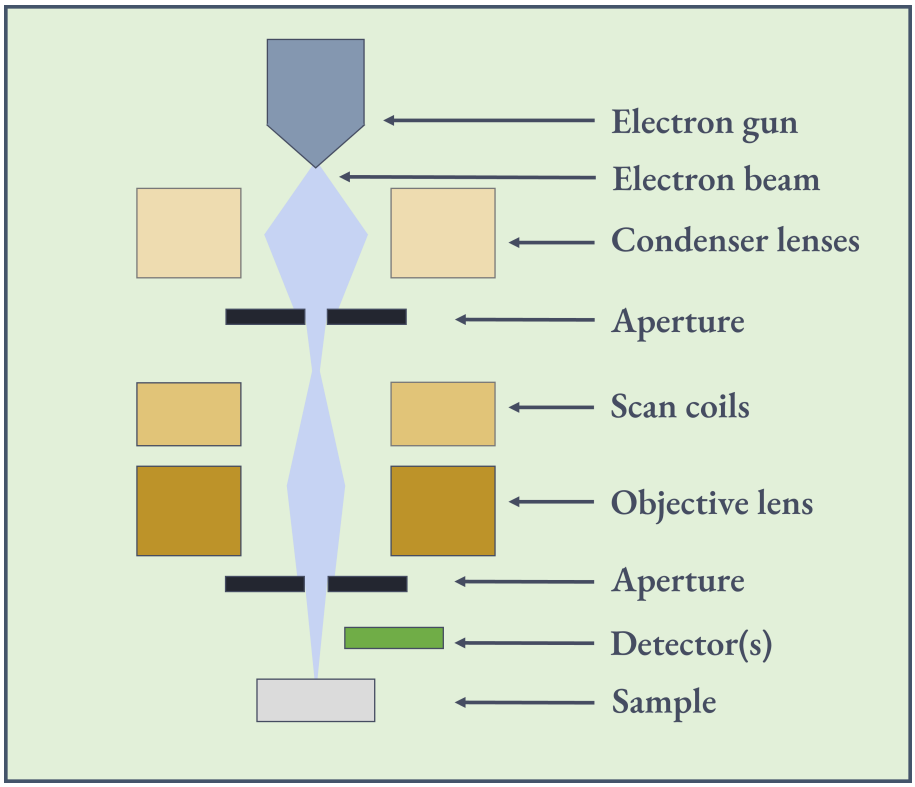

Figure 2.9: Illustration of the main parts in an SEM.

The electron beam is shaped and controlled by **electromagnetic lenses and apertures**. A narrower beam allows higher resolution, as both the probe size is smaller and the electrons closer to the center of the beam axis have fewer aberrations [38]. The apertures are a physical barrier that limits the beam size. A smaller probe with fewer aberrations is better for high resolution details, but the signal is also reduced as there are fewer electrons in the probe. The condenser lenses are used to control the spot size and the shape of the beam. The final lens, the objective lens, fine-tunes the beam's focus on the sample surface. If the specimen is magnetic, the beam can be affected by the magnetic field of the sample. Stigmator are used to prevent the beam from being elliptical. The user of the microscope adjusts the focus with the objective lens and roundness of the probe with the stigmator. The probe size can also be adjusted by changing the working distance, which is the distance between the objective lens exit and the sample surface. Short working distances can produce the smallest probes, but they limit the depth in imaging and possibly the amount of signal that reaches the EDS detector.

The position of the probe on the surface is controlled by the **scanning coils** located between the condenser and objective lenses. These scanning coils are used to create a raster scan, where the probe is moved in a grid pattern across the sample surface. In each position the detector(s) register a signal, which is put together to form an 2D image, where each probe position corresponds to a pixel in the image. The raster scan is visualized in Figure 2.10. The figure shows a probe that is moved in a grid pattern across the sample surface, resulting in a 2D image with different intensities. The EDS signal is chosen for the visualization in the figure, but the same principle with the image being an intensity map applies to other signals like secondary electrons. Scanning the probe over a smaller area, with equally many pixels, results in a zoomed in image. The scan is controlled by the dwell time, which is the time spent recording a signal in each position. Higher dwell times giving higher signal intensity which usually results in a clearer image, but long dwell time can result in beam damage issues, e.g. carbon deposition on the sample surface.

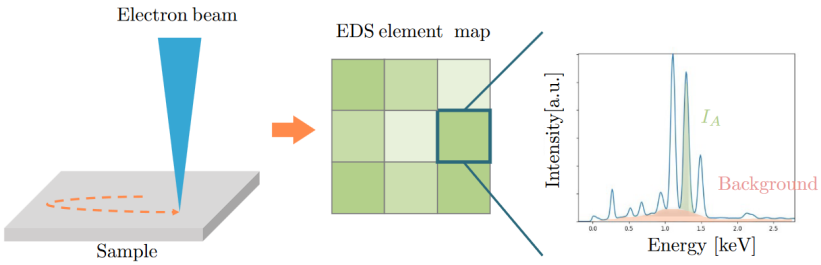

Figure 2.10: Illustration of a raster scan in an SEM. The probe is moved in a grid pattern across the specimen surface, and the detector(s) register a signal for each position. The signal intensity recorded in each position corresponds to the color of the pixel in the resulting 2D image. This figure is adapted from Skomedal [20, Fig. 2.14].

2.2.2 Signals and image formation

The interaction between the electron beam and the specimen results in a range of signals, illustrated in Figure 2.11. The signals are briefly described in the following paragraphs, and they are: Auger electrons, secondary electrons, backscattered electrons, characteristic X-rays and background X-rays. The detected signals are determined by what

type of detector is used.

The different signals created when the electron beam hits the specimen originate from different depths, illustrated by the **interaction volume** in Figure 2.11. The interaction volume has a droplet shape showing where the different signals are formed and emitted from. The depth of formation is dependent on the beam energy, as higher E_0 makes the electron beam penetrate deeper into the specimen. When a signal is formed inside the specimen, the signal can be absorbed or scattered within the specimen before it is detected. The probability of the escape of a signal is dependent on the energy of the signal, the depth of generation, and the properties of the elements in the specimen. Higher energy signals penetrate longer, and can thus escape from deeper inside the specimen. Both the density of the specimen and the atomic number of the elements in the specimen affect the probability of escape. Additionally, the geometry of the specimen can affect the probability of escape. Figure 2.11 is annotated with schematically estimates for the depth of origin of the different signals detected [2,5]. Hence, the specimen geometry can be important. A more accurate escape depth and interaction volume can be achieved by using a Monte Carlo simulation of the interaction of the beam with the sample [2, Ch. 4.3.4]. Figure 2.12 shows examples of Monte Carlo simulations in different bulk specimen. Note that SE yield and interaction volume depends on Z and E_0.

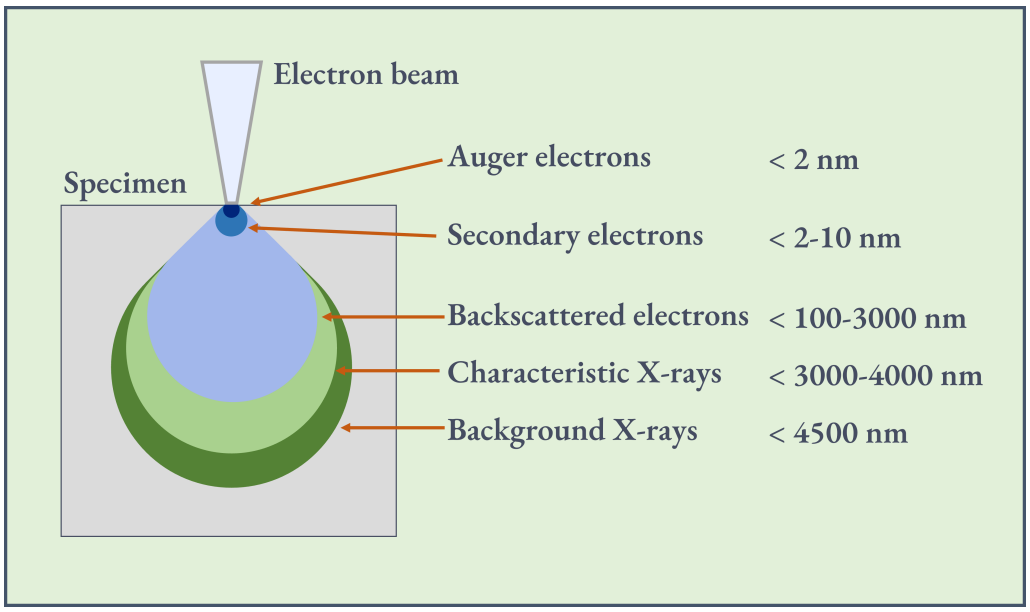

Figure 2.11: Illustration of the interaction volume in a bulk sample, which is the regions from where the generated signals can escape the sample. The blue signals are electrons and the green signals are X-rays. The given depths are very rough estimates [2, 5], as the depth strongly depends on the beam energy and the elements in the sample, as well as the geometry of the sample.

Auger electrons are emitted in the following way: an incident electron ionizes an inner shell electron of an atom, which makes an outer shell electron relax to the hole in the inner shell, and the energy difference is used to emit another electron, which is an Auger electron. Auger electrons have very low specific energy and are only detectable from the surface of the specimen, having an escape depth around 2 nm [5].

Secondary electrons (SE) are formed by inelastic scattering between incident beam electrons and valence electrons

of the atoms in the specimen. The weakly bound valence electron is knocked out of the atom, but with low kinetic energy from 0 to 50 eV. A plot of the distribution of the kinetic energy of the SE is shown in Figure 2.13, which is from a Cu sample with a 1 keV beam. Since the SE have low energy, they cannot travel far inside the sample before they are absorbed or scattered, and the SE signal is thus used to get topological information. If the beam is hitting the surface near an edge, the SE can escape at the edge, giving topological contrast.

Backscattered electrons (BSE) are from elastic scattering between incident beam electrons and atoms, where the scattering results in a reversed trajectory and thus making the incident electrons escape up through the sample surface. The scattering process is interactions with the orbitals and the nuclei of the atoms, and since the BSE are the incident electrons, their kinetic energy is in the keV range. Monte Carlo simulations shown in Goldstein [2, Fig. 2.16 b] show that more than half of the backscattered electrons in carbon retain more than 50% of the initial energy of the incident beam electrons. Atoms with higher atomic number have more protons and more electrons, giving them a higher probability of the scattering process, and thus making the BSE signal proportional to the atomic number, Z, of the atoms. Thereby BSE images can give a fast and rough qualitative overview of the composition distribution. As the BSE signal originates from deeper inside the sample, the topological information is limited. Figure 2.12 show Monte Carlo simulations with a 20 keV beam energy on C, Si, Cu, and Au. The figure show that a higher Z gives more BSE, marked as red lines. Additionally, the figure show that the size of the interaction volume is dependent on Z too, as all the scatterings are more concentrated in (d) with Au. The blue lines are electrons which have had all their energy absorbed within the specimen. In addition to the three types of electron signals, the beam interaction can also create X-ray photons. Figure 2.14 show the difference between a SE and a BSE image.

Formation of **characteristic X-rays** are covered in detail in Section 2.1.1. In short, formation of characteristic follow the same principle as Auger electrons, but the energy difference between the outer and inner orbital is used to emit X-rays instead of electrons. Typical escape depths for X-ray signals are around 4000 nm [5], but the variations are large. The escape depth depends on the energy of the photon and the density of the sample. Lastly, the **background X-rays** are formed by the deacceleration of the incident beam electrons because of the Coulomb fields of the atoms in the specimen, and this deacceleration of charged particles emits photons [33]. The background X-rays are white noise, giving no information about the sample, and is generated in the whole interaction volume.

The signals generated in the interaction volume can be **absorbed or scattered within the specimen**. For example, secondary electrons can be generated near the surface by BSE, and are then called SE_2. The SE with topological contrast (from the targeted area) are called SE_1. The SE_2 signal carries the same information as the BSE signal, since the amount of SE_2 is proportional to the amount of BSE. An SE signal generated from a BSE hitting something in the chamber is called a SE_3 signal, and SE signal from pre-specimen sources like the final aperture is called SE_4. The final SE image can be a combination of all the SE classes. The SE detector can be optimized, for example with in-lens configuration, to only detect SE_1 and thereby give a better spatial resolution. Other examples of signal absorption is the generated X-ray strays due to fluorescence, which is covered in Section 2.3.3.

While a range of signals are formed by the interaction of the beam with the specimen, **the observed signals** depend on the detector used. One type of SE detectors are the Everhart-Thornley detector [39], which combines the SE

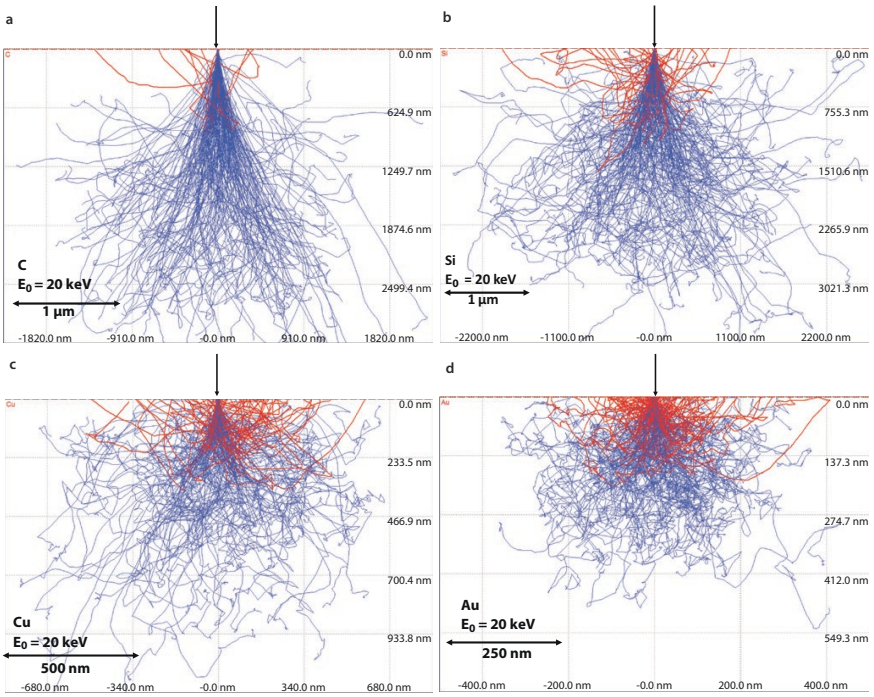

Figure 2.12: Monte Carlo simulation of the interaction volume in C, Si, Cu, and Au with 20 keV beam energy. The red lines mark the incident electrons with reversed trajectory, which are the BSE. The figure is adapted from Goldstein [2, Fig. 2.2].

signal with the BSE signal to get both topological and compositional contrast in the same image. BSE detectors can be annular solid state detectors or in-lens detectors. BSE imaging or combination of BSE and SE can be used to get initial compositional information before detailed quantitative EDS analysis. EDS detectors are covered in detail in Section 2.3. The signal from all types of detectors can be viewed as a spectrum, where the intensity of the signal is proportional to the number of electrons or X-rays detected. A SE image is the 2D representation of a set of spectra, where each pixel is a 1D spectrum with the number of SE electrons detected as a function of energy. In a 2D image, the intensity of a pixel is proportional to the sum of the number of electrons detected on that probe position. Figure 2.13 show what the spectrum from a single pixel in a SE image would look like. The same is true for BSE images, only with a higher energy range. Both SE and BSE detectors are counting the number of electrons detected, and the energy of the electrons is not used. An electron microscope can be fitted with an electron spectrometer to measure the energy of the electrons, but this is not common as it requires a more complex detector design than counting detectors. However, the signal in EDS detectors is recorded in each pixel as a digital histogram of the energy of the detected X-rays, making a spectrum map. This allows for the creation of a 2D map of the elemental composition of the sample, as specific elements can be given colors in the image. This is a very powerful tool for the analysis of samples, and is covered in detail in Section 2.3. EDS spectra can also be recorded as a 1D spectrum from a point on the sample.

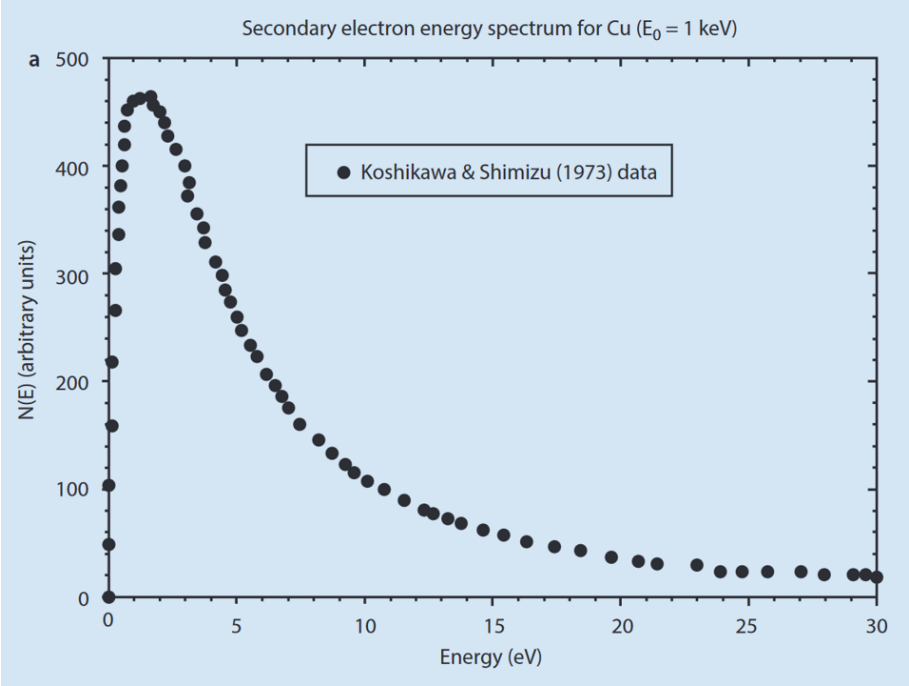

Figure 2.13: The figure shows the spectrum from a single pixel in a SE image. The specimen is Cu, and the incident beam energy is 1 keV. Similar spectrum would be recorded in a BSE image, but with peaks at different energies for the different elements. Normal SE and BSE images only record the sum of the registered electrons, and not the energy of the electrons. The figure is adapted from Goldstein [2, Fig. 3.1 a], which use data from [40].

2.2.3 Note on transmission electron microscopy

There are several similarities between the SEM setup described above and TEM in scanning mode. Both setups use lenses to form a fine probe that is rastered over the sample using scanning coils. However, in the present work, the focus is mostly on SEM EDS, and the TEM setup is only briefly introduced, with a focus on the relevant differences to SEM EDS. Firstly, the beam energy in TEM is higher ($100 - 300$ kV vs $1 - 30$ in SEM), which can affect the likelihood of X-ray line creation. Secondly, to transmit electrons, the specimen in TEM is thin (< 100 nm), resulting in higher spatial resolution due to a smaller interaction volume. The interaction volume in a bulk SEM specimen is illustrated in Figure 2.11, but as the thickness of TEM specimen are in the nanometer range, the interaction volume is severely reduced. This reduced interaction volume also decreases the likelihood of absorption and fluorescence, simplifying calculations and avoiding corrections. However, a thinner specimen produces less signal and can result in a poorer signal-to-noise ratio. These two aspects are the key differences, and TEM image formation is not discussed further in this work.

Table 2.4: Definitions for various terms related to scanning electron microscope, Section 2.2.

Name	Definition
Electron gun	The source of the electron beam.
Beam energy, E_0	The voltage applied that accelerates the electrons in the beam.
Beam current, i_b	The current of electrons emitted from the electron gun. This is not the current hitting the specimen (probe current), as the probe current is limited by the apertures and loss in the column and chamber.
Probe size	The cross-section of the electron beam when it hits the sample.
Electromagnetic lenses	The lenses which shape and control the electron beam in the column. Condenser lenses, scanning coils, and objective lens.
Aperture	A physical barrier with a hole in the middle which allows only part of the signal to pass through.
Interaction volume	The volume in the sample where the different signals originate from.
Auger electrons	A signal of electrons emitted from the surface of the sample.
Secondary electrons	A surface sensitive signal of electrons used to produce topological images.
Backscattered electrons	Beam electrons which have had their trajectory reversed through the scattering processes. The BSE signal has Z contrast.

(a)

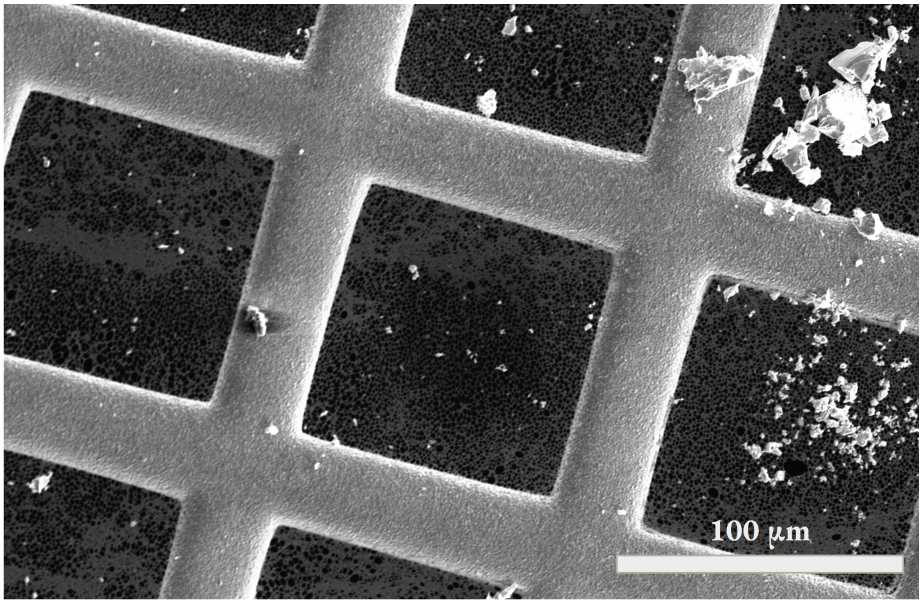

(b)

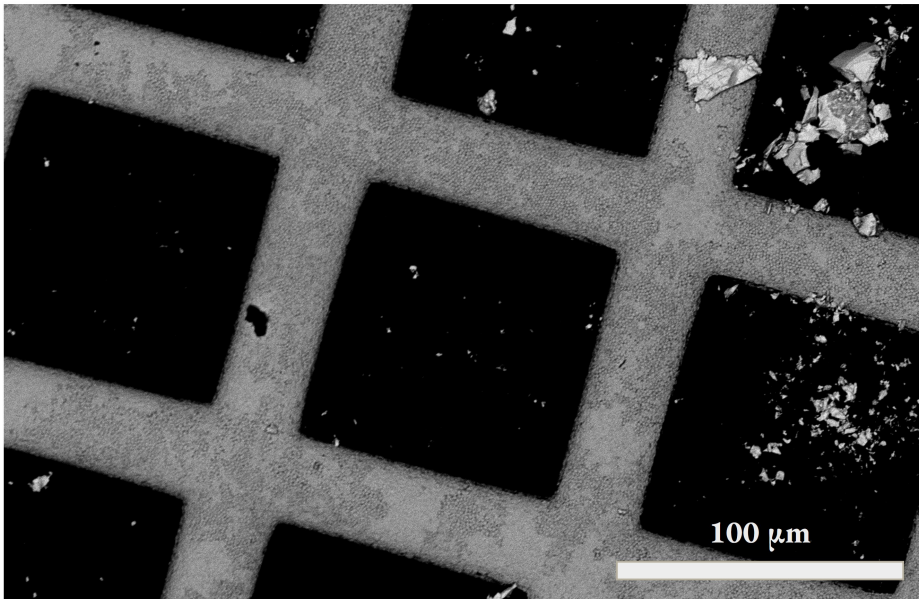

Figure 2.14: Example of the difference between SE and BSE images. The image is a Cu grid with a C-film, and the material on top is GaAs. The SE image in panel (a) shows more spatial details, and the topological information of the grid. The BSE image in panel (B) is flatter, i.e. show little topological information, but the Z-contrast of the different materials give an initial compositional overview. For example, the contamination in the middle left is probably carbon, as the C-film, as both are black. The different Z of the grid and the deposited material is also visible. The images were acquired in [36].

2.3 Energy dispersive X-ray spectroscopy (EDS)

The EDS system is made up of the detector capturing incoming X-rays, the electronics converting the analogue signal to a digital signal, and the software on the computer to analyze the signal through plotting and quantification. The output of an EDS analysis is either a spectrum or a spectrum map, where the spectrum is a histogram with the number of X-rays detected as a function of energy. Even though the resulting spectrum appears to be acquired simultaneously at all energies, the spectrum is actually acquired one count at a time. This section covers first the hardware and the principles of EDS detectors, then the information in a spectrum, and finally user controlled parameters in the EDS analysis. Section 2.4 covers parameters used to quantify the performance of the EDS system. This section is based on Goldstein [2] and Jenkins [4], if not stated otherwise.

2.3.1 EDS detectors hardware

Detecting X-rays is a three-step process illustrated in Figure 2.15, nowadays done with a silicon drift detector (SDD). The older Si(Li) detectors have similar working principles, but are generally performing worse than SDD. The worse performance comes from the fact that the Si(Li) detectors have lower count rates and smaller solid angle, as well as being less practical due to the need of liquid nitrogen cooling. However, parts of the literature is old and based on the Si(Li) detector, and thus both detector types is described below. Both detectors are Si based diode-structures, where incoming X-rays ionize Si atoms, creating electron-hole pairs. The number of electron-hole pairs proportional to the energy of the incoming X-ray, and hence the X-ray signal can be plotted as function of its energy. The electron-hole pairs is driven by an electric field towards the contact points, where they are converted into a voltage signal and amplified by FET transistors. Finally, the electronics assigns the voltage signal to a specific energy range, called a channel. While the electronics is converting the voltage signal, the detector is shut down by the controlling software, i.e. not recording incoming X-rays. The time the detector is shut down is called dead time, and is discussed in Section 2.3.2. Each voltage signal registered corresponds to one count in the given channel. The width of a channel is usually set to 10 eV, thus the scale of most spectra is 10 eV per channel. The number of channels in a spectrum is typically 1024 or 2048. The number of counts stored in a channel is the signal intensity. Details about the signal is covered in Section 2.3.3. Table 2.5 summarize this section.

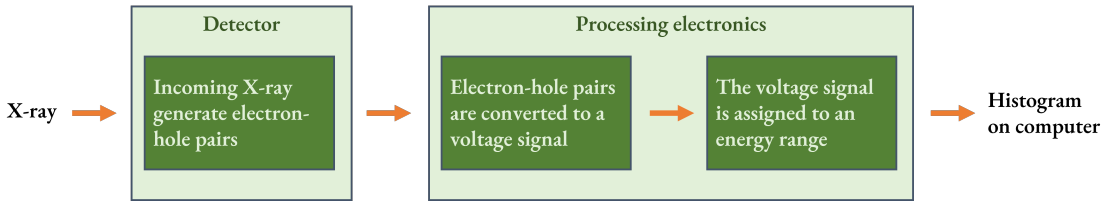

Figure 2.15: The figure shows the three-step process of detecting X-rays in EDS detectors.

The Si(Li) detectors are silicon crystals drifted with lithium, with a p-i-n diode structure. The generation of detectable electron-hole pairs happens in the thick intrinsic region. The thinner n- and p-type regions are referred to as dead layers, because the electron-hole pairs generated there are not collected. The layer where detectable electron-hole pairs are generated is called the active layer. The thickness of the detector is typically $2-5$ μm, which allows for

a high detection efficiency at higher energies, since few X-rays are able to pass through the intrinsic layer without generating electron-hole pairs. The number of electron-hole pairs created is proportional to the energy of the X-ray, since one pair requires 3.8 eV of energy. A reverse bias over the detector makes the charge carriers drift towards the detector contact, where they are measured by the electronics after being amplified. Since electron-hole pairs can be thermally excited, the detector is cooled to liquid nitrogen temperature to prevent this. The liquid nitrogen cooling also prevents the lithium from diffusing under the field within the detector and reduce the electronic noise from the amplifiers in the electronics.

The SDDs are also silicon crystals, but with a much thinner active layer and generally a different design. A schematic of an SDD is shown in Figure 2.16. Incoming electrons pass through the collimator, which is an aperture that limits the angle which the X-rays can enter the detector. The collimator limits detection of X-rays from other parts of the sample and the chamber. The detector window is a barrier that maintains vacuum in the detector, usually made of beryllium or being polymer based. Beryllium windows strongly absorb low energy X-rays, allowing only X-rays above Na to pass through, while polymer windows are transparent down to 100 eV, but are less robust. Some detectors, especially in TEM, are windowless. The sensor in SDDs is a thin layer of doped Si, with ring electrodes on the anode side. The X-rays enter through the cathode side, ionize Si atoms, and create electron-hole pairs, which are drifted by the ring electrodes towards the center. In the center of the backside is a small anode, where the electron-hole pairs are collected. The anode is connected to a FET transistor which amplifies the voltage signal. The signal is then sent to the electronics, where the pulse processor is converting the analogue signals to digital signals. The digital signals are sent to the multichannel analyzer, which makes a digital spectrum sent to the computer.

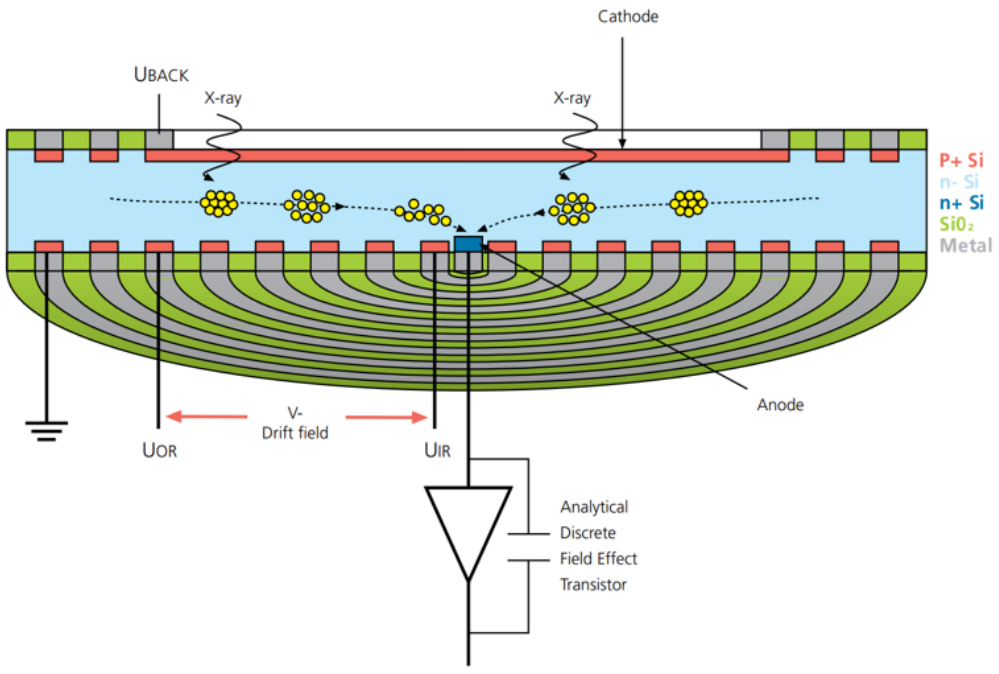

Figure 2.16: A schematic of the side view of a silicon drift detector (SDD). The collimator and window would be placed in front of the cathode. The figure is adapted from Oxford Instruments [41].

There are some key differences between the Si(Li) and SDD detectors. The cooling needed in the more modern silicon drift detectors (SDD) is not as strong as for the Si(Li) detectors. The SDDs need no more than a Peltier cooling (ca. −20 to −30°C), which is easy to operate and maintain. The anode in the SDDs is just a small centerpiece, while in the Si(Li) detectors the anode covers the whole detector. As the anode is smaller, the capacitance is lower and the voltage noise is reduced. In SDDs the area of the active layer can be made bigger with a constant anode size, which keeps the capacitance constant. [33]. An increase in capacitance is not good, as it is limiting both resolution and throughput [2, Ch. 16.3.9]. A bigger active area allows more counts per second, as it is increasing the solid angle, explained further down. The lower voltage noise in SDDs allow both a cleaner signal and a shorter process time, because the pulse processor does not need to do signal averaging. The shorter process time allow significantly higher count rates and high speed mapping. High speed mapping is a key feature in SEM EDS, which is not available or less accurate in other X-ray analysis methods. One of the drawbacks of the SDDs compared to the Si(Li) detectors, is the detector efficiency (ε), illustrated in Figure 2.17. The lower efficiency of the SDDs is due to the thinner active layer, which allows high energy X-rays to pass through without generating electron-hole pairs.

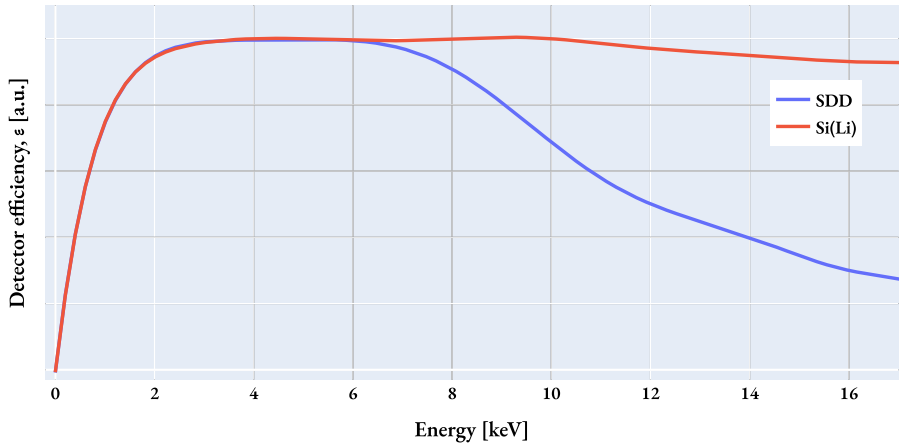

Figure 2.17: Illustration of the detector efficiency (ε) of a Si(Li) and an SDD, as a function of the X-ray energy. The efficiency of the SDDs decrease at higher energies because the active layer is thin, and thus high energy X-ray photons have a higher probability of passing through without creating an electron-hole pair. Figure adapted from [35].

The position of the detector affects the analysis, and the geometry around the detector is illustrated in Figure 2.18. The number of X-rays hitting the active area of the detector is dependent on the solid angle (Ω) and take-off angle (TOA), which covers both tilt of the specimen and the detector. Ω, is an expression of the fraction of the sphere with radius from the center of the detector to the sample that the detector is covering. In Figure 2.18 Ω is marked as a yellow triangle, but in 3D it has a cone shape, measured in steradians. The whole hemisphere above the surface of the sample equals 2π steradians, and Ω of the detector is the fraction of this hemisphere that is covered by the detector. A bigger detector covers a bigger fraction of the hemisphere, and thus collects more X-rays. Ω is the active area (A) of the detector divided by the square of r, the distance from the detector to the incident point of the probe on the specimen. Moving the detector closer to the sample increases Ω, and thus the number of counts.

When the sample is in horizontal position, the TOA is equal to the elevation angle of the detector, which is typically between 35 and 40 degrees [14]. Changing the tilt of the sample changes the TOA, and can increase intensity of the signal and reduce the path length in the specimen, and thereby reduce the absorption of the X-rays. The azimuthal angle is marked as *az* in the figure, and is the position of the detector in the xy-plane, measured from the x-axis. The azimuthal angle is important in the link between a SEM image and the corresponding EDS spectrum, as the azimuthal angle tells where the apparently X-ray illumination is coming from. The working distance (WD) is the distance from the end of the SEM column to the sample, and is marked as WD in the figure. The optimal WD is the height where the straight line of sight from the detector to the sample and the incident point of the probe on the sample coincide. Both a too low and too high WD will limit the number of counts, and most EDS operating software specify an optimal WD for the detector.

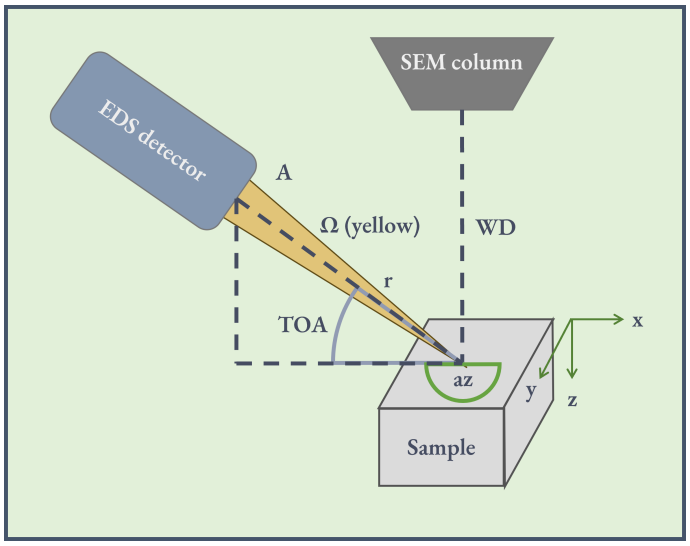

Figure 2.18: A schematic of the geometry of the sample and detector in EDS. The solid angle (Ω) is a function of *A* and *r*, giving the fraction of the hemisphere above the sample that is covered by the detector. X-rays with trajectory outside the yellow triangle will not hit the detector. The *TOA* is take-off angle, *WD* is working distance, *az* is the azimuthal angle, *A* is the active area of the detector, and *r* is the distance from the sample to the detector.

One of the main drawbacks of the EDS is the poor energy resolution. The natural line widths of the X-ray lines treated in this work is around 10 eV, but the peak widths in EDS spectra are around ten times larger, as stated in Section 2.1.3. The shape of the natural lines are Lorentzians, but the inaccuracy of the energy resolution of the electronics combined with counting statistics broadens the peaks to Gaussians. The Gaussian broadening is mainly due to the electronics, which handles X-ray pulses corresponding to energies between 0.1 and 40 keV. The energy resolution of an EDS detector is usually reported as the FWHM of the Mn Kα line, which is in SDDs is typically between 120 and 140 eV. A higher FWHM means a lower energy resolution, because the peaks still have the same amount of counts, but are spread out over a larger energy range. When peaks are spread more, it is harder to distinguish between them, and thus FWHM is a measure of the energy resolution. This effect is illustrated in Figure 2.19, which is a plot of the Mn Kα line with the same total counts and different FWHMs. The plot shows both a linear and logarithmic y-axis, to illustrate the difference between the two. The FWHMs are

marked as dashed lines. The acquisition parameters can to some degree affect the energy resolution, mainly via the process time, discussed more in Section 2.3.2. The process time is a trade-off between the energy resolution and the throughput. Energy resolution is also discussed more in Section 2.4.3.

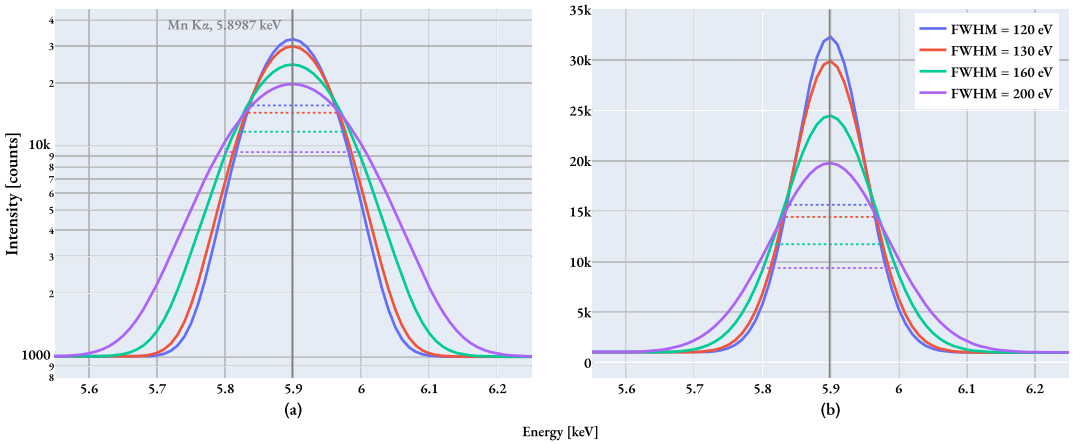

Figure 2.19: Illustration of different energy resolutions of EDS detectors. The natural line width of the Mn Kα line is around 10 eV, but the peak width is more than ten times larger. The energy resolution depends on the detector, but also the acquisition parameters. The total counts in the peaks are the same. The dashed lines are the FWHM of the peaks. Panel (a) is a logarithmic y-axis, and panel (b) is a linear y-axis.

As the electronics broadens the peaks to Gaussian curves, the model fitting of the peaks are done by the equation $f(x) = \frac{A}{\sqrt{2\pi}\sigma} \exp\left[-\frac{(x-x_0)^2}{2\sigma^2}\right]$. Where A is the amplitude, x_0 is the mean, σ is the standard deviation, and x is the energy. The model fitting in this thesis is done using the HyperSpy package [15]. With the sigma of a Gaussian curve, the full width at half maximum (FWHM) can be calculated as FWHM $= 2\sqrt{2\ln(2)}\sigma$. Different detectors and detector settings can give different peak widths, and thus the FWHM are used as a measurement of the resolution of the detector and the acquisition parameters. The relation between peak width and peak energy is described in Section 2.4.3.

Table 2.5: Definitions for various terms related to EDS detectors, Section 2.3.1. In the order they appear in the text.

Name	Definition
SDD	Silicon drift detector, the most common detector. High count rates, fast processing, and low capacitance. See Figure 2.16.
Si(Li) detector	The older type of detectors. Much of the literature published is based on these detectors.
Channel	A discrete energy interval in the measured histogram. Usually 10 eV.
Scale	Energy per channel.
Signal intensity	The number of counts stored in a channel. Signal intensity can also be expressed as counts per second, but counts is used in this work.
Active layer	The part of the detector where the detectable electron-hole pairs are generated.
Dead layer	The Si layer in the detector where generated electron-hole pair are not drifted to the anode and thus not detected.
Collimator	An aperture for the EDS detector, blocking the X-rays with a too high angle, i.e. coming from areas outside the probed spot.
Detector window	A barrier to keep vacuum in the EDS detector.
Detector efficiency, ε	The ratio of the detected X-rays to the number of X-rays incident on the active detector. Some X-rays pass straight through the thin SDD detectors without being detected. See Figure 2.17
Solid angle, Ω	The area of the detector that is exposed to the sample. Bigger solid angle gives more counts. $\Omega = \frac{A}{r^2}$, where A is the area of the active layer and r is the distance from the sample to the detector. See Figure 2.18.
Take-off angle	The angle between the sample surface and the detector. TOA increase or decrease with specimen tilt, see Figure 2.18.
Azimuthal angle	The angle around the beam (seen from above) between the detector and a reference line, e.g. the chamber door. See Figure 2.18.
Working distance	The distance between the SEM column and the sample surface. See Figure 2.18.
Peak broadening	The broadening due to the counting electronics.

2.3.2 The user controlled parameters

The acquisition of EDS spectra is controlled by a set of parameters, which the user can adjust to optimize the analysis. This section will discuss the most important parameters, and how they affect the analysis. At the end of the section the parameters are summarized in Table 2.6.

The **beam energy** (E_0) is the kinetic energy of the electrons which are exciting the X-rays, and this energy is set by the acceleration voltage of the electron beam. The beam energy must be higher than the **critical ionization energy** (E_C) of the element of interest, which is the minimum energy needed to remove an electron from an atom. The ratio of the beam energy to the critical ionization energy is the **overvoltage** (U):

$$U = \frac{E_0}{E_C} \tag{2.11}$$

The overvoltage is different for all the lines in the spectrum, as it is dependent on the critical ionization energy of each line. When the overvoltage for a specimen is discussed, it is referring to the overvoltage for the line of interest with the highest critical ionization energy.

To produce a satisfactory amount of X-rays, it is not enough to just have the overvoltage slightly above 1, as the **ionization cross-section**, Q, plays a critical role. The ionization cross-section can be viewed as the probability of an ionization, as described in Section 2.1.4 and Equation (2.7). The relation between the overvoltage and the ionization cross-section is shown in Figure 2.20. As seen in the figure, the probability of ionization increase sharply until U is around 4, and then it decreases. An equation for the relation between the ionization cross-section and the overvoltage is given in the PAP model for quantitative EDS analysis, which is discussed in Section 2.5.3 with Equation (2.35), and illustrated in Figure 2.30. Having an overvoltage below 1 results in no X-rays generated for the line of interest, which is shown by the line starting at 1. With SEM EDS the overvoltage is typically in the area where the ionization cross-section is changing the most, thus the overvoltage is an important parameter. In addition to the effect of the ionization cross-section, the overvoltage is important for how deep the electron can penetrate and still ionize the higher energy lines. In each scattering process, illustrated in Figure 2.12, the electron loose energy. If the overvoltage for a line is 1, an electron which already have scattered and lost some energy will not have enough energy to ionize the line of interest. This results in fewer generations of X-rays from that line, i.e. low intensity of the line. As the overvoltage increase from 1, there is an increase in both the ionization cross-section and the amount of electrons with enough energy to scatter multiple times and still ionize the line of interest. When the overvoltage is higher, the electrons can scatter multiple times within the specimen before they ionize the highest excitation, which makes the probability of that ionization higher. ISO 22309 about quantitative analysis in SEM advise an overvoltage of 1.8 [13], and ASTM E1508 on the same topic advise an overvoltage of at least 1.5 [42]. In Goldstein the advice is to keep the overvoltage above 1.5 [2, Ch. 20.2.2]. A higher overvoltage will produce more X-rays, but also decrease the spatial resolution of the analysis as the interaction volume is increased with E_0.

The **beam current** (i_b) is the current applied in the electron gun to eject the beam electrons, and it is measured in nA or pA. A higher current will produce more X-rays. Multiple papers and textbooks like Goldstein advise

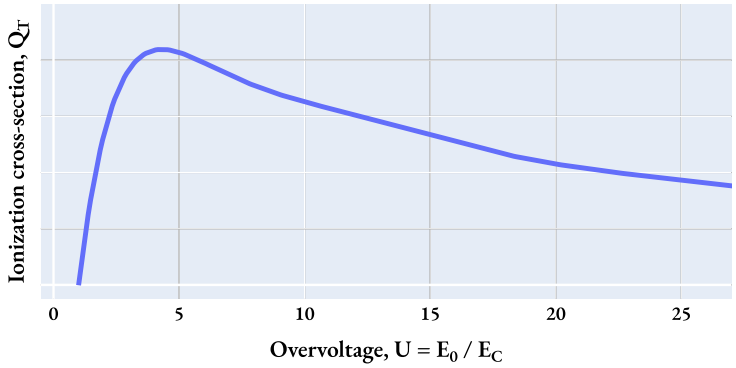

Figure 2.20: The ionization cross-section as a function of overvoltage. Adapted from [3, Fig. 4.4].

the measurement of the current hitting the specimen. This would allow more possibilities for specimen analysis and setup characterization, for example computing absolute concentrations and calculating the solid angle of the detector. The beam current is set by software, but the current hitting the specimen needs to be measured and this requires addition equipment in the form of a Faraday cup and a good ammeter. These extra equipment were not available in the present study, but could be a good addition to future work. The beam current in this work is thus the current set on the SEM and not the current hitting the specimen. When the current hitting the specimen is discussed, it is referred to as the **probe current**. Increasing the beam current do increase the probe current, but some electrons are lost in the SEM column, and the probe current is thus lower than the beam current. The user can control the beam current directly, but not the probe current. Some samples are sensitive to beam damage, and on such specimen the probe current should be low. Controlling the beam current is done to achieve suitable counts per second, depending on what the specimen can cope with without damage and the targeted accuracy of the EDS analysis.

The **count rate** is the number of counts per second (cps), and is affected by multiple factors like the beam energy (probability of X-ray creation), beam current (proportional to creations), the solid angle (detector geometry) and the processing capabilities of the electronics. A good spectrum needs many counts in total, especially if minor elements in specimens are to be detected, and even more when minor elements are to be quantified. The number of X-rays per second which produce electron-hole pairs in the active layer of the detector is called the **input count rate** (ICR). The number of counts being outputted from the electronics to the memory of the computer is called the **output count rate** (OCR). The OCR is limited by the processing capabilities of the electronics, as the electronics needs a certain amount of time to convert the voltage signal into a count. When a voltage signal is converted into a count, the input of the electronics is shut down for a short time, and this time is called the **dead time**. Thus, the OCR is lower than the ICR. The OCR also include the coincidence peaks, which is when two X-rays are counted as one. Coincidence peaks are discussed in Section 2.3.3. The OCR is the **throughput** of the detector. Throughput is a general term for of how much information a system can process per units of time, and in EDS the information is the X-ray counts.

As mentioned above and in Section 2.3.1, the detector needs to shut down the input of the electronics while con-

verting a voltage signal into a count. This time is called the **dead time** (DT), and is according to the ISO standard 15632 measured in seconds [43]. The dead time is often reported as a percentage of the **real time**, which is the total time it takes to acquire a spectrum. The time when the detector is actively detecting X-rays is called the **live time**, and is the real time minus the dead time. The dead time can be described by the real time and live time, or by the ICR and OCR.

$$DT\% = \frac{\text{Real time} - \text{Live time}}{\text{Real time}} = 1 - \frac{\text{OCR}}{\text{ICR}} \tag{2.12}$$

A high dead time reduce the OCR relative to the ICR. A higher count rate increase the dead time, as there will be more events to process. More events per unit of time also increase the probability of coincidence peaks. Different sources advise slightly different thresholds for the dead time to prevent coincidence peak events. According to the ASTM 1508 the highest throughput is achieved with a dead time around 40% [42]. However, the standard also state that coincidence peak events are beginning to become a problem at dead times above 40%, and advise dead times between 20% and 30% to get good spectra. Another source, a paper from 2015 by D. Newbury and N. Ritchie on high accuracy quantification with SDDs, advises a dead time below 15%, preferably below 10% [44]. In Goldstein, it is stated that the Si(Li) detectors were usually operated at low count rates and thus handled coincidence events (see Section 2.3.3) better than SDDs, and that for Si(Li) detectors 30% dead time was "close to optimal for all vendors and most samples" [2, p. 466]. Further it is stated in Goldstein that SDDs should not be operated according to specific dead times, but rather according to an acceptable low coincidence rate. With different advice on maximum DT, the best procedure is probably to follow the last advice mentioned from Goldstein. This requires the user to make a pre-analysis of the coincidence rate.

The DT is influenced by the **process time** (PT), which is the time the electronics have to process the signal from the detector. A longer PT makes the energy resolution better, as the electronics have more time to assess the photon energy. However, a longer PT also reduce the count rate, as the detector is shut down for a longer time. Thus, the PT is a trade-off between throughput and energy resolution.

When mapping a specimen, the **dwell time** is the time the electron beam is on each position (pixel) the specimen. Higher dwell time tends to give higher signal intensities and better spatial resolution, but factors like charging, specimen drift, beam damage, and contamination can limit the effect of increased dwell time. Charging is when the specimen is charged by the electron beam, and can cause the incoming electrons to be deflected. Charging can be identified by a significant lower effective beam energy than the set beam energy, which is explained in Section 2.4.2. If the specimen is drifting (moving) slightly during the mapping, the spatial resolution will be reduced harshly. Faster mapping will reduce the effect of specimen drift. Beam damage on the specimen can change in the chemistry of the specimen or do milling of the specimen surface. Contamination introduced by the electron beam is typically in the form of carbon. If carbon is present in the camber, it can be deposited on the specimen surface by the beam.

Table 2.6: Definitions for various terms related to the user settings in EDS, Section 2.3.2.

Name	Definition
Beam energy, E_0	The energy of the electrons from the beam when they enter the specimen.
Critical ionization energy, E_C	The energy required to ionize the element of interest. Dependent on Z and the orbital to excite.
Overvoltage, U	$U = E_0/E_C$, which is required to be high enough to achieve enough ionizations.
Beam current, i_b	The current used to emit the electrons from the electron gun.
Probe current	The current that hits the specimen.
Count rate	The number of X-ray counts per second (cps).
Input count rate, ICR	The number X-rays per second creating electron-hole pairs in the active layer in the detector.
Output count rate, OCR	The actual number of counts registered and outputted to the memory. The OCR is lower than the ICR because of the dead time, and because the OCR includes coincidence events.
Throughput	How much information a system can process per units of time. In EDS the throughput is the OCR.
Real time	The time in seconds in takes to acquire a spectrum. Real time = dead time + live time.
Dead time, DT	The amount of time when the input to the electronics is shut off, because an analogue voltage signals is being converted to a digital count. Dead time is both expressed in seconds and as a percentage of the real time.
Live time	The time in seconds when the detector is actively registering counts.
Process time, PT	A system setting for how much time the electronics have to convert the voltage signal. Longer times give more accurate assessment of the energy. The process time is a trade-off between throughput and energy resolution.
Dwell time	The time the electron beam is on each pixel in the 2D image. Higher times increase signal intensities and spatial resolution, but can introduce issues.

2.3.3 Spectral artifacts

A real EDS spectrum contains the peaks from the characteristic X-rays, the background radiation, and other artifacts. As the characteristic X-rays and the background have been covered above, this section is an overview of the other artifacts. These include coincidence peaks, the noise peak, strays/spurious X-rays, the Si escape peak, and internal Si fluorescence peak. The artifacts can be used to characterize the performance of the detector and the selected settings for the acquisition. In general, the artifacts are unwanted, as they reduce the signal in the actual peaks and clutter the analysis. Thus, awareness of the possible artifacts is important for a thorough analysis of the spectrum. The artifacts are illustrated in Figure 2.21, and summarized in Table 2.7.

Acquiring a good spectrum requires a certain amount of counts, but having a high count rate increase the probability of **coincidence peaks**. Coincidence peaks are also called sum peaks. Coincidence peaks are when two X-rays are counted as one, where the assigned energy is the sum of the two X-rays. If the detector is open and two X-rays hit the active area in the same time window, both X-rays produce electron-hole pairs and the resulting voltage pulse is equal to the sum of the energies. This effect is called pulse pile-up. The probability of pulse pile-up is proportional to the count rate. Different detectors can achieve different count rates, and their electronics are designed to handle their possible count rates. This is reflected in the detectors process time settings, which have to be different for a detector that can reach $1E4$ cps compared to a detector that can reach $1E6$ cps. Additionally, the SDD detectors have lower capacitance than the Si(Li) detectors, which makes pulse pile-up problems lower in the SDDs as the electronics can process the pulses faster [42]. The count rate is related to the dead time through the ICR and OCR, as described in Equation (2.12). As such, it has been common to suggest a certain dead time to avoid coincidence peaks, which is discussed in Section 2.3.2. A coincidence peak from Si is shown in Figure 2.7, and coincidence counts from the background is shown in Figure 2.26. Limiting the coincidence peaks is important for accurate quantification, as the coincidence peaks are counts belonging to other peaks, and a coincidence peak can lead to misidentification of elements not present.

Another artifact which give similar issues as coincidence peaks is **stray radiation**, or spurious X-rays. Strays are X-ray signals which originate from outside the targeted area, and are thus not part of the spectrum of interest. The strays can be generated from either a deflected electron or from an X-ray through fluorescence. Deflected electrons are from the beam, or BSE electrons, which both have a high energy. The fluorescence X-ray are generated by characteristic X-rays or background X-rays, which typically have lower energy than the deflected electrons. This difference in energy can be used to determine the origin of the strays, which is discussed in Section 2.4.6, based on the work by Egerton and Cheng [17]. The spatial regions where a stray X-ray can originate is: (a) inside the specimen, but outside the targeted area, (b) from the chamber, (c) from an eventual specimen holder, and (d) from the detector. To limit the strays, the collimator in front of the detector is a physical barrier which only allows X-rays from a certain angle to reach the detector. This requires the detector to be aligned correctly, which could be tested with a tilt series, where the stray signal should be independent of the tilt angle. The stray signal is made by a combination of the detector and the specimen, thus it is not possible to measure the stray signal in a blank specimen (of vacuum) and subtract that signal from a measurement. Stray signals need to be handled from case to

case, as different specimen give different stray signals on the same detector.

Strays originating from the (d) the detector results in both the **internal fluorescence** peak and **silicon escape peaks**. The incoming X-ray can ionize Si atoms in the detector. If the ionized Si is in the dead layer of the detector, the ionized Si will emit a characteristic X-ray which can be detected in the active area of the detector. This is the internal fluorescence peak, and is located at 1.74 keV, i.e. the Si Kα peak. As SDDs have much thinner dead layers than the Si(Li) detectors, the internal fluorescence peak is much smaller for the SDDs. The incoming X-ray which ionizes a Si atom loose some energy, which results in the count being recorded at 1.74 keV lower than where the incoming X-ray was supposed to be. The counts at 1.74 keV lower than the incoming X-ray make the escape peak. Both escape peaks and sum peaks are most probable to occur from the strongest line, as there are more events where these artifacts can occur [42].

Most spectrums have a **noise peak** around 0 keV, which is present due to electronic noise in the detector [23]. The noise peak is also called the zero peak. All detectors have this type of noise, but some vendor software remove the noise peak automatically. The AZtec software does not remove the noise peak, and it is therefore important to be aware of the noise peak. For example, during model fitting, the noise peak should be removed to avoid a bad background fit in the lower energy region. The simple solution is to inspect where the noise peak ends, and cut of the spectrum at that energy. As the noise peak is located sufficiently close to zero, no information is lost by cutting off the spectrum at the noise peak.

The artifacts mentioned above are in varying degrees present when acquiring a spectrum, but some vendor software have built-in methods to remove or reduce the artifacts. In Goldstein at page 274, it is shown that an escape peak was present using software from 2011, but the artifact was automatically and digitally removed in the 2014 version of the same software [2, Fig. 18.7]. The AZtec software have a built-in method to remove coincidence peaks, called "Pulse Pile Up Correction" [23]. The AZtec user manual state that this method works best for single pixels or areas with the same composition, and that it might produce bad results when scanning over a larger heterogeneous area [23, p. 99]. Aside from this brief description, a user does not get any information on how the method works. This illustrates one of the challenges with digital solutions implemented by the vendors, as the software is a black box which can enhance the spectrum, but also produce bad results due to incorrect handling of artifacts.

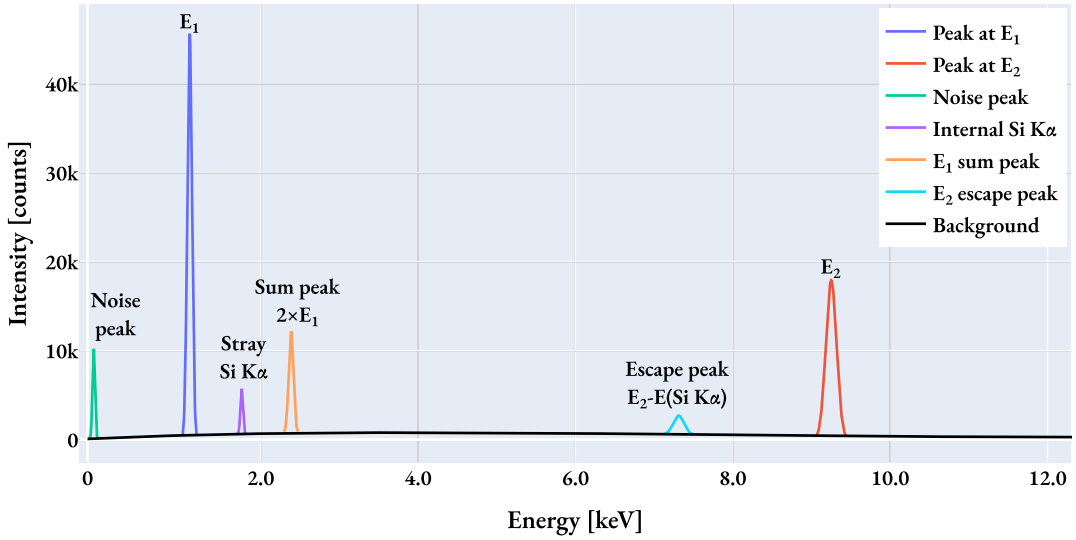

Figure 2.21: Some possible artifacts in EDS spectra.

Table 2.7: The spectrum artifacts in EDS, Section 2.3.3. See Figure 2.21 for an illustration of the artifacts.

Artifact name	Definition
Background X-rays	The white noise generated as $1/E_0$. The detected background is reduced at low energies due to absorption, see Figure 2.6.
Coincidence peaks	When two X-rays are counted as one, resulting a count at the sum of the energies. Increase with count rate, but advices to limit the artifact is usually given in terms of dead time. See Figure 2.7.
Stray radiation	X-ray signals which originate from outside the targeted area. Generated from deflected electrons or X-ray photons. Can originate from the specimen, the chamber, an eventual holder, or the detector.
Internal fluorescence peak	A stray from the detector at 1.74 keV, due to ionization of Si in the detector, which emits a Si Kα X-ray that afterwards is registered by the detector.
Escape peak	A signal from a characteristic line which have lost 1.74 keV due to its ionization of an Si atom in the detector.
Noise peak	The peak around 0 keV, which is present in all detectors due to electronic noise.

2.4 EDS performance parameters

The aim of this work is to improve EDS bulk quantification, and one way to do that is to improve the performance of the EDS setup and acquisition parameters, which is two first rows in Figure 1.1. Identifying potential issues with the EDS setup can be done through certain performance parameters. A performance check can reveal errors in the setup and acquisition parameters, and it can make the input parameters for the quantification more accurate. Vendors of EDS detectors like Oxford Instruments provide a guide for how to calibrate their detectors, but these guides are limited to calibration of energy resolution and scale [23]. As both Thompson in [45] and Goldstein in [2] writes, the state of an EDS setup is characterized by more than its energy resolution and scale. In 1986 Williams criticized the lack of standardized performance criteria for EDS in analytical electron microscopes (AEM), and suggested three standardized metrics [46], but these metrics were not widely adopted. Routines for a performance check seems to vary significantly between different laboratories. The industry and standard authorities have not yet agreed on a standard set of metrics, aside from the energy resolution, measured by the FWHM the Mn Kα line.

An ISO standard for selected SEM EDS performance was introduced in 2002 (revised in 2012 and 2021), which includes details on calibration metrics [43]. Some literature is available on performance parameters for TEM EDS setups, e.g. the work of Egerton and Cheng [17], updated and easily accessible in the info-sheet by Ted Pella [18], which also sells NiO thin film test standards. Literature on performance parameters for SEM EDS setups are less common, but some papers [14, 47, 48] are available and the software DTSA-II [47] includes a quality control program, described in the textbook by Goldstein [2]. Goldstein also include details on a range of parameters, such as linearity and stability of the detector, along with possible SEM EDS issues, such as beam-sensitive specimen and specimen with irregular topography [2]. The similarities between EDS in SEM and TEM allow much overlap in the performance parameters, but there are also some differences. One of the challenges in this work is to find the most relevant test characteristics for SEM, and especially what ranges of values should be acceptable for a well performing detector. Out of range values could indicate a suboptimal setup or affect calculating composition. Identification of setup parameters with optimization and correction should lead to better EDS analysis. The value range challenge is affected by both the change from TEM to SEM and the change from the older Si(Li) detectors to the now more commonly used SDDs. In this section, each of the test characteristics is described with what it is, how it is measured, and what values that should be acceptable. Before the test characteristics are described, an overview is given and a summary table is given at the end of the section in Table 2.8.

2.4.1 Overview

The parameters measured, or the metrics, are the energy resolution, the scale and offset, peak ratios, deviations in peak positions, the Duane-Hunt limit, and the Fiori peak-to-background ratio.

The goal of the performance check is to identify potential issues with the detector and acquisition setup. Is the detector performing as expected and stated in the specifications? Is the spectrum reflecting the acquisition parameters set by the user? Are stray radiation present? How well are the peaks defined? Are the peaks in the correct positions? Do the peaks have enough counts? Could the acquisition be done faster with equally good results? The

performance parameters described in this section can be used to answer these questions. At the end of the section, Table 2.8 contains a summary of each parameter, and what it can reveal.

Figures 2.22 to 2.25 are schematic illustrations of the performance parameters. Figure 2.22 shows the Duane-Hunt limit, which is the minimum beam energy required to produce a signal. Figure 2.23 shows the different signal-to-noise ratios, which is quantified by the Fiori peak-to-background ratio. Figure 2.24 shows the deviations in peak positions, which is an affected by the energy scale and offset, and which part of the spectrum is used for calibration. Figure 2.25 shows the effect of stray radiation, which is can be quantified by calculating peak ratios between a stray and a non-stray peak. Energy resolution is illustrated above, in Figure 2.19.

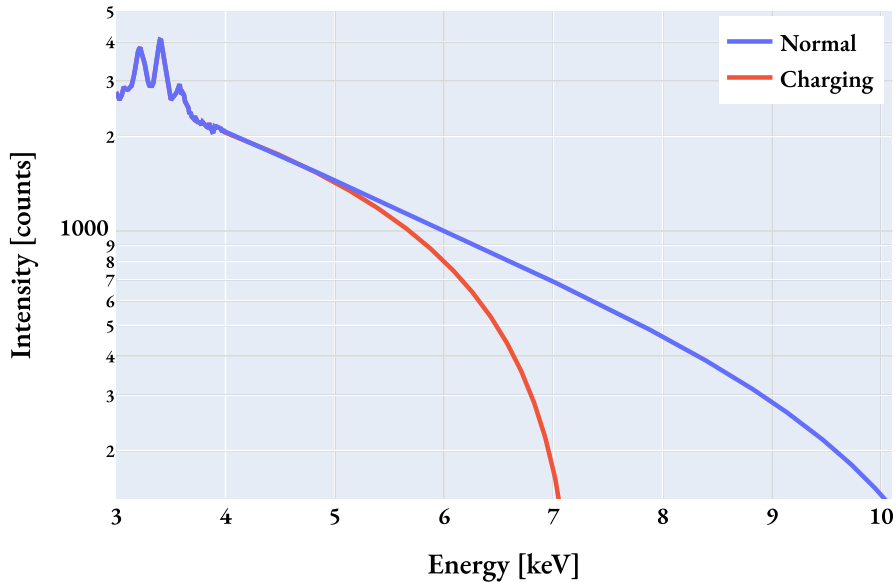

Figure 2.22: Illustration of a spectrum where the Duane-Hunt limit is different due to charging. The charging sample (red) has a lower effective beam energy than expected (10 keV). The sample with good conductivity (blue) has the expected beam energy (10 keV).

Recording the necessary metrics for the performance parameters requires a sample with some specific properties. The test sample should be homogeneous with a known composition, and the elements present should have lines at both low and high energies. The lines should not be high enough to cause overvoltage issues, as was noted with Mo Kα in [36]. Even at 30 kV, the Mo Kα line at 17.47 keV had very low intensity, making the analysis done with this peak less reliable. The peaks in the spectrum from the test specimen should overlap less than the expected energy resolution and preferably be well separated, as severe overlaps will make the fitting of the peaks less accurate. For repeatability, the sample should not be reactive. Additionally, the sample should preferably both be easy to acquire and not expensive. When vendors, like Ted Pella who provides the NiO test sample for TEM, are used, the sample might not be available immediately, and the delivery time can be long, as experienced during this work and in the project report [36].

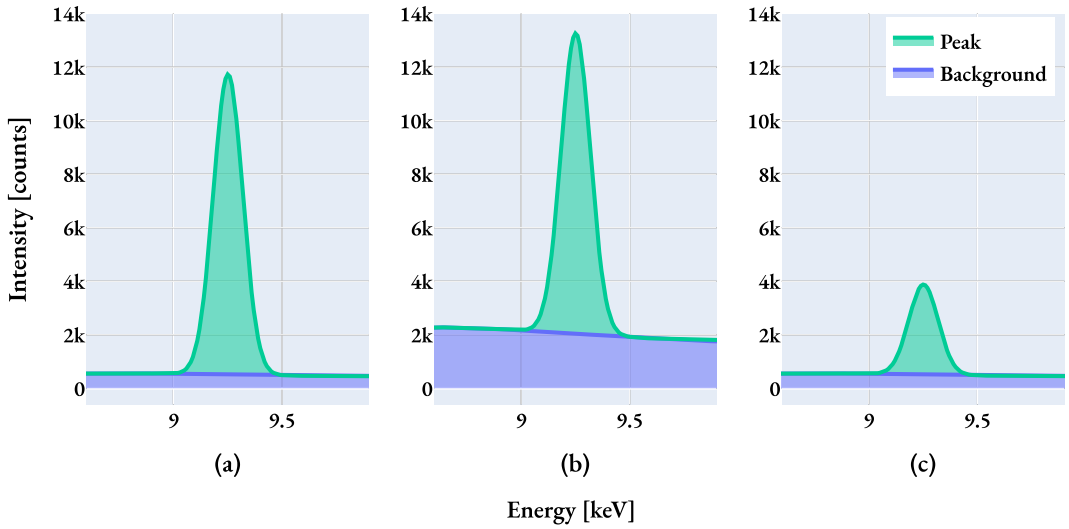

Figure 2.23: Illustration of different spectra with signal-to-noise ratios. The peak intensity is the green area, and the background is the blue. Panel (a) has a high SNR. Panel (b) has a lower SNR due to a higher background intensity. Panel (c) has a lower low SNR due to a lower peak intensity. Even though the illustrated background here is linear, that is not always the case.

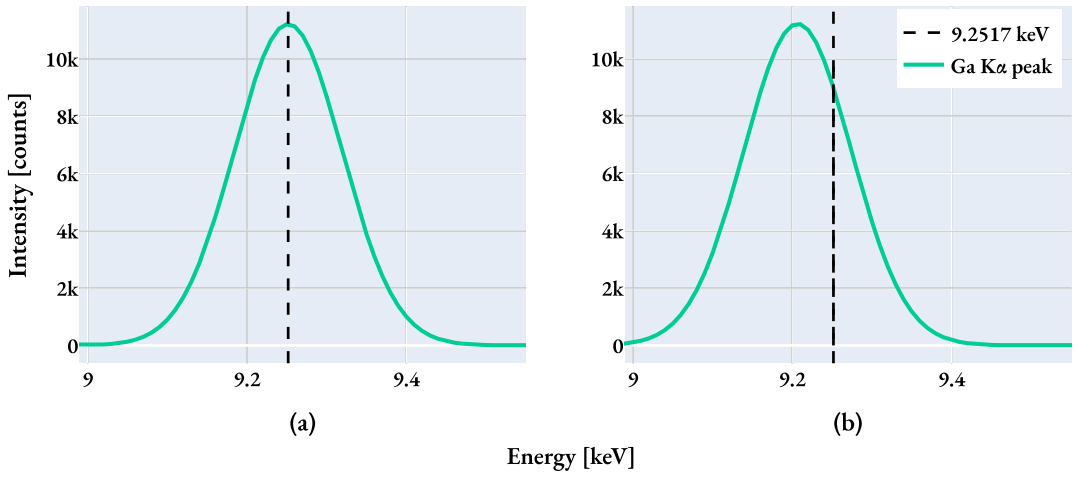

Figure 2.24: Illustration of peak deviations. Panel (a) is well calibrated for the medium high energy Ga Kα peak. Panel (b) is calibrated only for low energy peaks, where the Ga Kα peak is shifted.

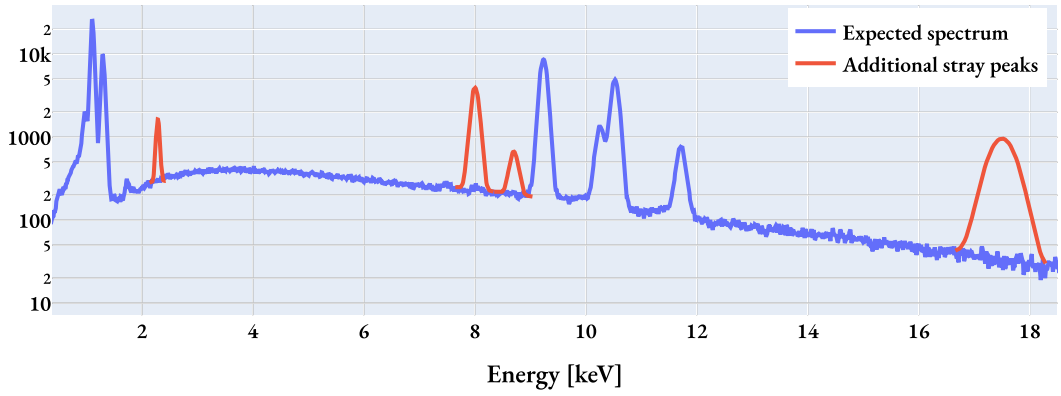

Figure 2.25: Illustration of strays. The expected spectrum (blue) has additional peaks (green) due to stray radiation. The example is a GaAs sample with strays of Mo Lα, Cu Kα, Cu Kβ, and Mo Kα.

2.4.2 Duane-Hunt limit

The Duane-Hunt limit is the maximum energy of the X-ray background radiation, which originates from a paper from Duane and Hunt in 1915 [8]. The acceleration voltage selected by the user is the nominal beam energy, while the effective beam energy is the Duane-Hunt limit, and these two values can deviate significantly. The effective beam energy is the incident beam energy, E_0, that excites X-rays in the specimen. As seen in Figure 2.26, the detected X-rays decline rapidly and linearly towards the nominal beam energy, but the counts does not go to zero. It is not possible to excite X-rays above the effective beam energy, thus the spectrum should be cut off at the beam energy to allow better model fitting. The counts above the Duane-Hunt limit are due to coincidence events, where two X-rays are detected as one, as explained in Section 2.3.3.

Finding the effective beam energy is done by fitting a linear function to background, where the intersection of the linear fit and the x-axis is the effective beam energy [47] [2, Ch. 9.1.3]. This solves the ambiguity of the exact beam energy, which is present because of the coincidence counts that gives the spectrum a tail past the effective beam energy.

There will be some deviation between the nominal beam energy and the effective beam energy, typically up to 0.2 keV. Different specimen will have different deviation, due to varying conductivity. Specimen with low conductivity will get problems with charging, which will lowers the effective beam energy. Thus, a deviation between the nominal and effective beam energy of several kilo-electronvolts is a sign of charging [48]. Charging of specimen are covered in detail in a paper by Postek and Vladár [49]. Another explanation of a large deviation is that the voltage indicated by the SEM is imprecise, and E_0 is a central metadata factor in data treatment routines, such as fitting and quantification. If either the metadata is wrong or the specimen is charging, a quantitative analysis will yield poor results [50]. Thus, the Duane-Hunt limit is an important metric to verify.

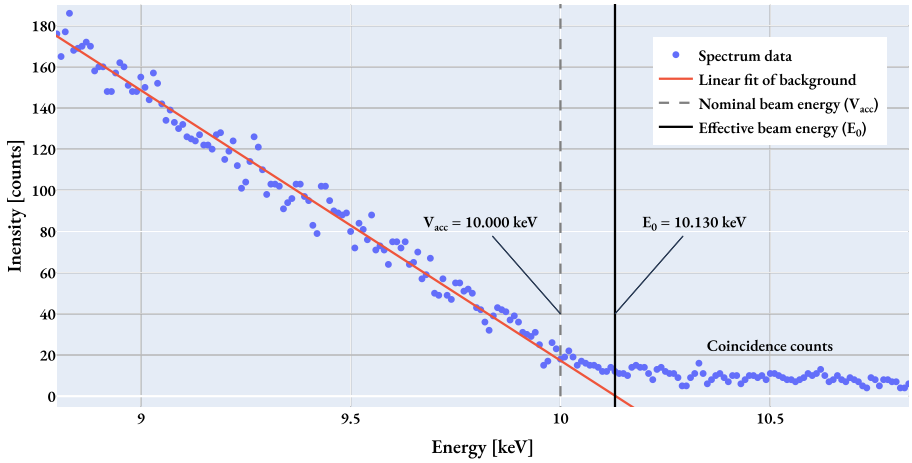

Figure 2.26: Illustration of the Duane-Hunt limit. The blue dots are the X-ray counts, and the red line is a linear fit of the background. The gray dashed line is the nominal beam energy, and the black line is the effective beam energy.

2.4.3 Energy resolution

The energy resolution of an EDS system is the ability to distinguish two lines at different energies, and is measured by the FWHM of the Mn Kα peak. Two partly overlapping peaks have high contrast if the peak maximums and the valley between the peaks are well separated. The contrast increase with better energy resolution, as the peaks are more separated. The convention of using the Mn Kα peak as the reference for the energy resolution is because of its position at 5.8987 keV, which gives an indication for both the lower and higher energies used in EDS. All EDS detectors have a stated energy resolution in its specifications, however the actual resolution of a given spectrum varies some with the acquisition settings for the same detector. Thompson shows that with the dead time kept constant, a higher input count rate gives worse resolution, with the example of 121 eV resolution with $<$ 5k cps, and 140 – 150 eV resolution with $>$ 100k cps [45]. Thompson claims that EDS specifications are based on acquisition designs with low input counts. The process time setting is also affecting the energy resolution. A longer process time gives the electronics more time to process and assign the energy of the incoming count, and thus gives better resolution. However, a long process time gives lower count rates and longer acquisition times.

Even though the Mn Kα peak is the most common reference for the energy resolution, other peaks can be used to get additional information. Detectors which shall perform at low energies ($>$ 1 keV), should also report the FWHM of F, and possibly of C. This is the advice given in the ISO 15532 standard [43]. As this low energy range is not the main focus of this thesis, such low energy peaks have not been included in the specimen used for the tests. The remainder of this section will focus on the Mn Kα peak.

Three different approaches to measure the energy resolution are described below. The first is to directly measure the Mn Kα peak in a specimen with Mn. The second is using the Ni Kα peak and multiply it by a factor of 0.926, which is suggested by Ted Pella, Inc. [18]. The third is to use any peak in the spectrum, and calculate what the energy resolution would be if there was a Mn Kα peak in the spectrum, using Equation (2.13). The second approach is a

special case of the third, where the Ni Kα peak is used as the reference peak, but with a much simplified equation which is only valid in certain FWHM ranges. The third approach is the one which is used in the code developed in this work.

The industry standard for the energy resolution is to measure the FWHM of the Mn Kα peak generated by an ^{55}Fe source, when the detector is off the microscope. This is the advised method in the ISO 15632 on EDS performance parameters [43]. The argument for doing this is that the energy resolution is not a function of the microscope, thus measuring the energy resolution off the microscope negates all possible influences from the microscope. The ISO standard recognize that this is not easily done by users, and thus suggesting polished Mn as a substitute. Measuring the FWHM of Mn directly would be the most straight forward approach for a user, but it requires a suitable Mn specimen. The FWHM measurement should be from a numerical fitting of a Gaussian to the peak, because it limits the effect of the background, and it uses all the information in the peak instead of just three points (the peak maximum, the left and right half maximum).

Another approach, which can be used when a sample with Ni is available, is to measure the FWHM of Ni Kα and multiply the value with 0.926 [51]. This approach is based on a round-robin study in 1995 [51] where five TEM laboratories were given a standard NiO test specimen with a series of EDS test measurements to be done, where one of the tests were focused on the energy resolution. The test used the Ni Kα and O Kα peaks, where the FWHM of these two lines were measured, and a linear correlation between photon energy and the square of the energy resolution was assumed. Then the FWHM of Mn Kα was determined by interpolation, and the factor 0.926 was reported as a sufficiently good conversion from Ni Kα to Mn Kα for the five TEM laboratories. This approach is the recommended method provided by Ted Pella Inc., who manufactures standardized NiO test specimens for TEM [17, 18].

A third and more general approach, is to use the energy calibration method in HyperSpy, which estimates the FWHM of Mn Kα. The method, `calibrate_energy_axis()`, is available for SEM and TEM EDS spectrum. The method has `calibrate='resolution'` and `xray_lines='all_alpha'` as default arguments. The estimation of the FWHM of Mn Kα is done in two steps. The first step is to fit the width of all the lines in the spectrum, which is needed to get a correct reference peak width, i.e. an account for the peak broadening of the detector. The second step utilizes an equation by Fiori and Newbury from a conference paper in 1978, and while this original paper is hard to get hold of (neither the NTNU library nor paper depositories could provide it), the equation is included in Goldstein [2, Ch. 16.1.1] with a reference to the original paper[2]. The equation use one known line in the spectrum to estimate what the FWHM would be at an arbitrary energy:

$$\mathrm{FWHM}(E) = \sqrt{2.5 \cdot (E - E_{\mathrm{ref}}) + \mathrm{FWHM}_{\mathrm{ref}}^2} \tag{2.13}$$

Where E is the energy of the wanted FWHM, i.e. Mn Kα for estimating the energy resolution. E_{ref} is the energy of a reference line in the spectrum, and $\mathrm{FWHM}_{\mathrm{ref}}$ is the FWHM of that line. Both the energies and FWHMs are in eV.

[2] One of the two authors of the original 1978 publication is D. Newbury, who is also the second author of the Goldstein textbook [2].

When using the HyperSpy method `calibrate_energy_axis`, the user should be aware of the argument `xray_lines`, which can either be a list of strings with line names or `'all_alpha'`, the latter being the default value for the argument. As of HyperSpy v1.7.3, the reference line in Equation (2.13) is the first line in `xray_lines`, which becomes the alphabetically first line when using `'all_alpha'`. The fact that the reference line is only the first line in the list, is not documented clearly in the HyperSpy documentation, and can yield unexpected results when the first line is affected by much noise or severe peak overlap. Setting the energy resolution of a spectrum could be done as the average of several distinct peaks, it could be the lowest estimate, the average of the three lowest, or another selection. For comparative purposes, the same selection should be used, and it should be clear which selection was used. This is a focus in this work.

As the energy resolution is a function of the count rate and the process time, it is probable that EDS vendors report the energy resolution with a low count rate and a long process time. To clarify such possibilities, the ISO standard state that the ICR should be < 1000 cps when the best energy resolution is reported [43]. Further, the standard states that detectors with possibilities for high count rates should also specify the energy resolution at a high count rate, e.g. $1E6$ cps. This can be seen in the specifications of Oxford Instruments EDS detector called X-max^N, while the slightly older version called "X-max" only specified a single energy resolution without additional information.

The energy resolution of an acquired spectrum should be close to what the specifications of the EDS. Deviations below the specification should raise suspicion, as energy resolution is one of the main selling points that EDS detector vendors use. Deviations above the specification could be related to the acquisition settings set by the user. If the user cannot achieve the energy resolution in the specification with optimal settings, the user should probably contact the EDS detector vendor for support. In Goldstein, it is stated that most specimen would benefit of a small loss in energy resolution to get higher throughput [2, 16.3.2]. The trade-off between energy resolution and throughput allows a small loss in resolution for a high gain in throughput. However, the user must be aware of the elements in the specimen, as overlapping peaks become more difficult to resolve with a lower energy resolution. Thus, the user should adjust the trade-off according to the specimen used and the aim of the analysis.

2.4.4 Scale, offset, and peak position deviation

The scale and offset are the parameters used to set the energy axis, and the deviation of peak position is a measure of the accuracy of the energy axis. The scale is the energy width of one channel, and the offset is the energy of the first channel in the spectrum. Another name for the scale is the gain or the dispersion. The peak position is calculated as the deviation from the peak center to the theoretical line energy. Calibration of the energy axis is done by: (1) fitting the background and Gaussian curves to the peaks in the spectrum, (2) calculate the theoretical energy difference between two or more peaks, and (3) use the difference between the theoretical and the measured energy difference to calibrate the energy axis. The calibration can be done by hand, or by using the HyperSpy function `calibrate_energy_axis`. The HyperSpy function needs the argument `calibrate` to be either `'scale'` or `'offset'`, which specifies if the scale or the offset should be calibrated. The function also takes the argument `xray_lines`, which is used to specify the peaks that should be used for the calibration. In the project report, the author made a function from scratch to calibrate the energy axis, which was used for a lab exercise in the course

TFY4255 [36].

Calculating the scale and offset is done to verify that the system is operating correctly. The scale and offset should be close to the values that are set by the user for the acquisition. The peak position deviation is calculated to verify that the energy axis is calibrated correctly. If there is a noticeable deviation, the user should probably contact the SEM EDS responsible for technical support.

2.4.5 Fiori peak-to-background ratio

One of the metrics describing the quality of a spectrum is the relation between the signal in peaks and in the background, which is most commonly described by the Fiori peak-to-background ratio (P/B), at least for TEM EDS [3]. The Fiori P/B ratio is the sum of counts in a peak divided by the background in a 10 eV wide window at the center of the peak, which is illustrated in Figure 2.27. This is a signal-to-noise ratio (SNR) metric, where the signal is the peak intensity and the noise is the background intensity. The ISO 15632 standard use an SNR metric which is purely directed towards manufactures [43]. That approach is not further discussed in this thesis, as it is not relevant for the user. Some modern detectors can acquire extremely high counts per second, partly because of the larger sensor sizes, like the newest Oxford Instruments detector Ultim Max EDS with up to 170 mm^2, which supposedly can acquire up to $1.5E6$ counts per second [52]. However, having a high count rate does not necessarily mean that the spectrum yielded will have high quality, because the energy resolution can be poor, the signal in the peaks can be very low compared to the background, and the relative amount of artifacts can increase [43].

As a counterweight to the possible unwanted effects of a high count rate, the ISO 15632 standard state that all specifications should be marked with the used count rate [43]. Having a metric for the ratio between the signal in peaks and in the background is important both for establishing what makes a good detector, and also if an acquired spectrum have high quality. The peak-to-background ratio in a certain detector will vary with the specimen studied and the detector settings, and can thus be used as a parameter to assess the quality of a spectrum. The Fiori P/B was originally made for TEM and STEM, i.e. thin specimen with low background, but arguments for why and how it is relevant for SEM are presented below. The original definition of the Fiori P/B is from a publication by Fiori, Swyt, and Ellis in 1982 [7] in *Microbeam Analysis 1982*, where the definition is set as:

$$\text{Fiori P/B} = \frac{\text{Total counts in the peak above the background}}{\text{Background counts in a 10 eV window at the peak center}} = \frac{P}{B} \tag{2.14}$$

The Fiori P/B is illustrated in Figure 2.27. A paper from Zemyan and Williams in 1994 [53] includes the definition and a brief discussion of why the Fiori P/B metric is superior to other P/B metrics. A more detailed discussion on the different P/B metrics are published by Williams in *Microbeam Analysis* in 1986 [46]. The main advantages are the simplicity, robustness, and relevance to the generated characteristic X-rays in general. The metric can be used to assess artifacts in an acquired spectrum by either comparing the metric to a reference spectrum from the same detector, or by comparing to theoretical predictions. The robustness of the Fiori P/B comes from how the metric can be used on different detectors to compare the quality of the spectra they yield. The metric is unaffected by different energy resolutions, as all the counts in the peak are included in the numerator, thus different peak

broadening does not affect the metric. This is also true for change in peak broadening due to different detector settings, like increasing the count rate. The relevance to the generated characteristic X-ray comes from having the denominator as a fixed 10 eV window, or approximated only one channel, which puts the metric in the same order of magnitude as the natural width of the line. All these arguments were made for TEM, but they are equally true for SEM, and thus the metric is relevant for SEM EDS.

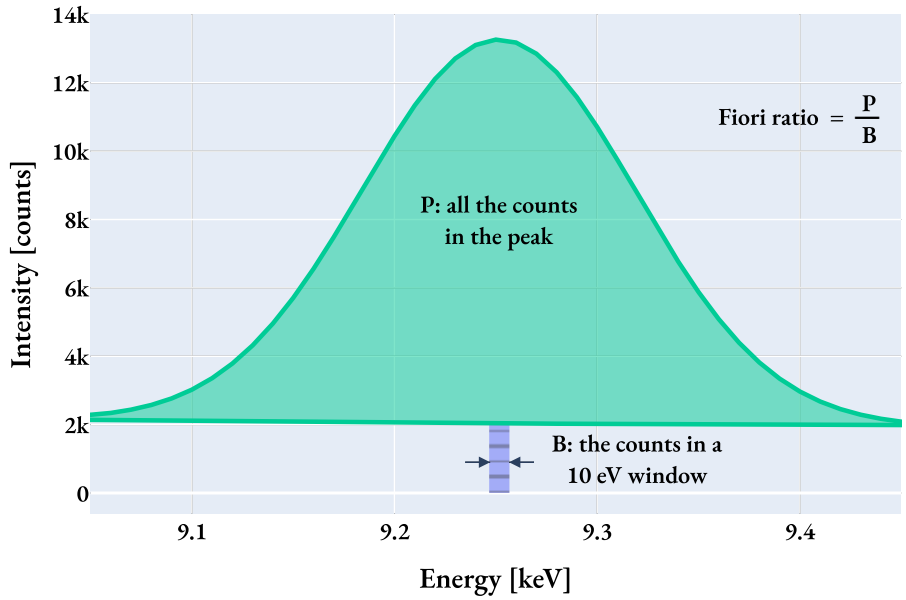

Figure 2.27: Illustration of the Fiori peak-to-background ratio. P is all the counts in the actual peak, not including the background. B is the counts in a 10 eV window at the peak center. Figure adapted from [53].

Even though the definition of the Fiori P/B is simple, the actual calculation of the metric is confusingly described slightly different in different sources. Calculating the metric the same way is critical for comparing the results on different setups. When the metric was developed, model fitting of the spectrum was not as trivial as it is today, and thus integration windows were used to estimate the peak and the background. In the 1986 paper by Williams, the background B can be estimated by peak subtraction after using library standard, or B can be calculated with the specimen used as its own standard. Using the specimen as its own standard seems to be the common way of calculating the B. This is the way Zemyan and Williams define B in their 1994 paper [53], illustrated in Figure 2.28, adapted from their paper. The figure illustrates one of the ways to calculate the P and B: the background is estimated as the average counts in two integration windows before and after the peak divided by the number of channels, and the peak is estimated as the integrated counts minus the averaged background.

Since the use of integration windows have to be done manually, the robustness of the metric is lowered. The user must set the integration windows so that they do not include any other minor peaks, the background windows must be close enough to the peak so that the averaged background represents the background under the peak well enough, and the integration window of the peak must include the counts in the peak, but not include counts from other peaks. Where the peak starts and ends is a subjective choice, and will vary between users. Giving hard thresholds in energy is not an ideal solution, as the broadening with different settings can make an unwanted peak

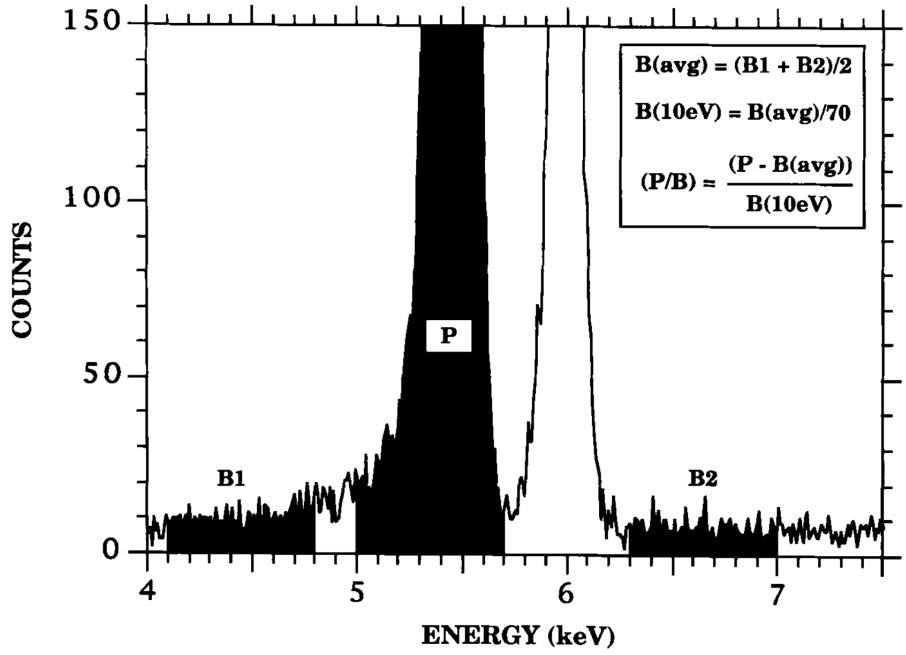

Figure 2.28: Illustration of how the Fiori P/B is calculated in practice, with integration windows. The background is the average of B1 and B2. The peak intensity are the counts in the middle intergration window, minus the average background. Figure adapted from [53].

to "bleed" into an integration window. The different integration windows specified are probably due to different materials used for the test. The integration windows have to be adapted to the material, as suggested test materials can have other peaks close to the main peak, e.g. the peak between "P" and "B2" in Figure 2.28. The topic of choosing a test material is part of the discussion in Chapter 5.

The problem with subjective choice of integration window, because of the lack of an agreed test standard [46], is exemplified in the EDAX Insight newsletter from September 2018 [54]. The newsletter contains an illustration of the Fiori P/B where the background windows are $>$ 2 keV away from the peak. This choice is not in agreement with their reference. The widths of the integration windows are also varying in different papers, which probably does not affect the results too much as the background is converted to an estimate for a 10 eV window, but it is not ideal. In EDAX Insight a 300 eV window is used for each background area far from the peak, but the paper that they refer to uses two 500 eV window directly before and after the peak [17]. For calculation of P, the Zemyan and Williams paper from 1994 use a 700 eV window [53], and the Ted Pella info-sheet on their NiO standard sample uses a 600 eV window [18]. This is probably a result of different materials, i.e. Cr and Ni, having different peak widths, but it is not ideal for comparison. The inconsistency of the actual calculation of the Fiori P/B is a problem for the metric. This problem could be solved by fitting the spectrum to a model, and using the fitted curves to calculate the P and the B, to easily compare reported or claimed values from different setups. The metric might be more comparable on different setups if the calculations are done truer to the original definition, which also would make the metric more robust as the users subjective opinions does not affect the calculation. Calculating the Fiori

P/B through model fitting is explored in this work.

There are some papers [17, 17, 18] suggesting acceptable thresholds for the Fiori P/B, but they are for TEM EDS spectra. It is stated in Williams and Carter [3, p. 614] that in a well constructed AEM the Fiori P/B ratio should increase with increasing beam energy. This should probably be true for SEM EDS setups too, and it is explored in this work. TEM EDS signals can have lower relative background intensity compared to SEM EDS signals, because the specimen is thin for TEM as explained in Section 2.2.3. This implies that a threshold should be lowered for SEM EDS signals. Egerton and Chengs paper from 1994 [17] suggests that a good TEM setup with a good signal have a Fiori P/B above 3000, while a number under 1000 indicates a bad signal. Such high numbers might be too high for SEM EDS signals, but it is not clear what the threshold should be. Additionally, the as the P scales with the composition and element, the threshold should be related to the composition and material. As the Fiori P/B is dividing the total area of a peak, which typically spans $20 - 60$ channels with 10 eV/channel, while the background is only from one channel, the metric should be a high number. It might be that the threshold should be related to the specific detector, as detectors have a different background intensity. Another potential use of the metric is to optimize the acquisition settings for specific specimen. Higher numbers indicate a better signal-to-noise ratio, which should allow for better quantification of the specimen. This is explored and focused on in this work, rather than trying to find a specific SEM threshold for the Fiori P/B.

2.4.6 Peak ratios - carbon contamination and stray radiation

A peak ratio, i.e. the counts in one peak divided by the counts in another peak, can be used to discover different issues with a detector. Table 2.2 show the theoretical ratios inside families, i.e. between α and β lines, but not the ratio between K and L. Theoretical ratios between K and L can be found in the X-ray Data Booklet [28]. Egerton and Cheng [17] show that a change in the ratio of the Ni Kα to the Ni Lα peak can be used to discover hydrocarbon contamination and icing of the detector. The latter is not an issue with the newer SDDs, as they are not cooled down with liquid nitrogen. The Ni Kα line is at 7.48 keV, while the Ni Lα line is at 0.85 keV, which is closer to the C K absorption edge, resulting in a higher sensitivity to hydrocarbon contamination. Other peaks could also be used for this purpose, as long as one is close and above the C Kα line and the other is far above. The Ted Pella Info sheet [18] contains a formula for calculating the thickness of the contamination layer, but the assumptions used are not valid for SEM EDS signals. A good reference numbers have not been identified for this metric for SEM EDS, and will depend on the chosen test specimen. However, detecting the contamination can be done by comparing a K/L peak ratio over time, where a decrease is an indication of carbon contamination.

Another use of peak ratios is to give information about the stray radiation. This requires a specimen with a certain geometry, more specifically a specimen where the beam can be directed at one point with certain elements, and electrons deflected from the beam and secondary fluorescence happens at another area with different elements. An example of such a specimen is a thin film on a substrate with a TEM grid pattern suspending the film, for example the NiO thin film on a Mo TEM grid from Ted Pella. The beam is directed at the thin film, and the strays are recorded from the grid. Two different metrics can be determined from such a specimen: (i) the intensity of the strays, and (ii) the predominant source of the strays. (i) The intensity of the strays is given by the ratio of Ni Kα peak

to Mo Kα peak. An ideal setup have zero intensity in the Mo Kα peak. The stray radiations are unwanted signals, which can be a problem for quantification. (ii) The predominant source of the strays is given by the ratio of Mo Kα peak to Mo Lα peak. This is based on the assumption that the high energy Mo Kα at 17.48 keV are generated by deflected electrons with a high energy, while the lower energy Mo Lα at 2.29 keV are primarily generated by secondary fluorescence. Both X-ray photons from background radiation and other elements can excite the Mo Lα line, but the Mo Kα line is almost only excited by electrons with a high energy, as the background is low at higher energies.

Table 2.8: Summary of the performance parameters covered in this thesis.

Parameter	Definition	Characterizes
Duane-Hunt limit	The effective incident beam energy, i.e. the maximum energy generating X-rays. Found by linear regression [2, 8, 47]. See Figure 2.26.	Charging issues and verifies the selected E_0.
Energy resolution	Measured as the FWHM(Mn Kα). Can be measured directly or calculated with Equation (2.13) [2, Ch. 16.1.1]. $\mathrm{FWHM}(E) = \sqrt{2.5 * (E - E_{\mathrm{ref}}) + \mathrm{FWHM}_{\mathrm{ref}}^2}$	The detector specifications and the settings used for acquisition.
Scale and offset	The width of each channel and the zero-offset of the spectrum.	The settings selected by the user.
Deviations in peak positions	How many eV the center of the fitted Gaussian deviate from the theoretical peak center.	The accuracy of the calibration.
Fiori P/B ratio	A signal-to-noise ratio. The sum of all the counts in a peak divided by the background counts in a 10 eV window under the peak center [3, 7]. See Equation (2.14) and Figure 2.27.	The detector quality and quality of the acquired spectrum.
Peak ratios	Counts in one peak divided by the counts in another peak. With specific specimen geometry, this can be used to characterize strays. [17, 18].	Information about stray radiation, and carbon contamination.

2.5 Quantitative EDS analysis

This work aims to improve the analysis for SEM EDS data, and this section will focus on the quantitative analysis, a part of the third area of improvement, illustrated in Figure 1.1. The hypothesis is that for bulk specimens matrix corrections have to be incorporated in the quantifications routines. The focus within the quantitative analysis has thus been to implement matrix corrections in a Jupyter notebook which could be developed further, for example as an addition to the HyperSpy package. It is stated in the ASTM 1508 standard [42] that there are multiple approaches for matrix corrections with some differences, but the accuracy of the EDS analysis is probably not limited by the accuracy of the matrix correction [42]. The two matrix correction methods explored and tested in this work are (1) absorption correction through ZAF corrections, and (2) the XPP version of the PAP model [9]. This section will start with an introduction to the principle of quantitative EDS analysis, before the two correction methods are presented in detail.

2.5.1 Principle

The principle of quantitative EDS analysis was introduced by Castaing in 1951 [55], where he showed that quantitative data could be obtained by comparing the X-ray intensity from element A in an unknown sample to the same intensity in a sample with a known concentration of element A. The known sample is referred to as the standard, and was frequently selected to be pure elements for convenience. Using the same instrumental conditions on the known and the unknown, Castaing showed that the *generated intensity* ratio can be related through the *mass concentration* ratio of the two samples, as shown in:

$$\frac{C_{\text{unknown}}}{C_{\text{standard}}} = \frac{I_{0,\,\text{unknown}}}{I_{0,\,\text{standard}}} \tag{2.15}$$

Where the C is the mass concentrations and the I_0 is the generated intensity[3]. However, the generated intensity is not the same as the measured intensity, thus Castaing introduced a sensitivity factor applied to the measured intensity ratio:

$$\frac{C_{\text{unknown}}}{C_{\text{standard}}} = K\frac{I_{\text{unknown}}}{I_{\text{standard}}} \tag{2.16}$$

Where I is the measured intensity and K is a sensitivity factor that depends on the atomic number (Z), the absorption (A), and the fluorescence (F) in the sample [2, 3]. The implementation of satisfactory sensitivity factors is a complicated task, as the X-rays are generated in an interaction volume which depends on the specimen composition and the electron probe conditions. Castaing and Deschamps established the theory experimentally in 1955, but the method was restricted by the sensitivity calculation as an iterative process. Later Philbert derived an analytical expression for iterative routines [56]. There are two main groups for the matrix corrections: the ZAF-corrections and the $\phi(\rho z)$-corrections. ZAF-corrections treat Z, A, and F independently, and is covered in Section 2.5.2. The $\phi(\rho z)$-corrections treat the Z and A together in a more complex calculation, and is covered in Section 2.5.3, as a part

[3] It is common to note the unknown as i and the standard as (i), but the more explicit notation is used in this work for clarity.

of the PAP model. The $\phi(\rho z)$ curve is the depth distribution of radiation from a certain X-ray line as a function of mass depth (ρz), i.e. the curve describes how much of the generated X-rays that is emitted from a certain level in the sample.

One way to avoid the corrections and thus also avoid the iterative process is to use thin samples. In thin samples the absorption and fluorescence can be neglected, which is typically the case for TEM specimen. Cliff and Lorimer [10] showed in 1975 that the intensity from a specimen with two elements can give the composition ratios, without the use of standards. The commercial software AZtec [23] use the CL (CL) quantification method when the "TEM EDS" setting is used [57]. The CL method have a sensitivity factor, named the "k-factor", which is dependent on the instrument settings and the atomic number effects in the specimen. The Python package HyperSpy have the CL quantification method implemented, where the inputs are a spectrum and the relevant k-factors. Additionally, HyperSpy have implementations of the Zeta method [32] and the cross-section quantification approach [58], which are element based, not ratio based as CL. Here, only the CL approach will be reviewed. Absorption corrections for TEM specimen is also implemented as an optional part of the CL quantification routines in HyperSpy for TEM specimen. These absorption corrections are based on path length of the characteristic X-ray in the specimen and estimated composition [3].

Relative quantification can be found with the intensity ratio of two similar peaks [2]. If absolute concentrations are needed, the user should measure standards with known concentrations on the setup used for the unknown sample. Using the absolute concentrations can reveal errors in the analysis, as the sum of the concentrations should be close to 100% [2]. However, using relative concentrations requires less work, and is probably the most common method for EDS analysis [2]. Similar peaks are peaks which emit similar amounts of X-rays, for example having X-ray energy not too far apart, having similar fluorescence yield (Figure 2.3), and having similar absorption (Figure 2.2). If the emitted amount of X-rays is similar, the relative composition can be calculated with:

$$C_A = \frac{I_A}{I_A + I_B} \tag{2.17}$$

Where C_A is the concentration of element A, and I_A and I_B is the measured intensity in a peak from element A and B respectively. The concentration from such calculations are in weight percent (wt.%). If the lines used emit different amounts of X-rays, a sensitivity factor can be applied to the measured intensity ratio. The sensitivity factor can take into account the atomic number, the absorption, and the fluorescence in the sample. Depending on the specimen and acquisition parameters, it might be sufficient to use a sensitivity factor that only focus on a specific parameter. For example, if the Z of the elements are close, the sensitivity factor can be based on the absorption, if absorption is the dominating factor. Equation (2.17) is rewritten as:

$$C_A = \frac{k_A \cdot I_A}{k_A \cdot I_A + k_B \cdot I_B} \tag{2.18}$$

Where k_A and k_B is the sensitivity factors for element A and B respectively. This method is referred to as the "intensity ratio method" in this work, without and with corrections.

As explained in chapter 19.10.1 in Goldstein [2, Ch. 19.10.1], there are two definitions of the ZAF-correction method, which are inverses of each other. The first definition (ZAF_A) applies the corrections to the concentration, and the second definition (ZAF_B) applies the corrections to the intensity.

$$\frac{I_{\text{i, unknown}}}{I_{\text{i, standard}}} = \frac{C_{\text{i, unknown}}}{C_{\text{i, standard}}} \cdot ZAF_A \tag{2.19}$$

$$\frac{C_{\text{i, unknown}}}{C_{\text{i, standard}}} = \frac{I_{\text{i, unknown}}}{I_{\text{i, standard}}} \cdot ZAF_B \tag{2.20}$$

The two definitions are related by the following equation:

$$ZAF_A = \frac{1}{ZAF_B} \tag{2.21}$$

Relevant for this work is ZAF_B.

Side note: The difference between the k-factor and the k-ratio

The **k-factors** are a sensitivity factor used in the CL quantification method for thin samples [3, 10]. The value of the k-factor is dependent on the instrument setup and the acceleration voltage. The CL method relates atom A to atom B in a sample with the following equation:

$$\frac{C_A}{C_B} = k_{AB}\frac{I_A}{I_B} \tag{2.22}$$

Where k_{AB} is the k-factor for the two elements A and B. The k-factor is most accurately determined experimental, but can be calculated theoretically.

When quantification of bulk samples is needed, the **k-ratio** method can be used to get an estimate of the composition [2, Ch. 19.1]. The k-ratio is the ratio between the measured intensity of an unknown and a standard, where ideally all other parameters and factors than the composition is the same. The estimate of the composition from the k-ratio can be paired with matrix corrections to give a more accurate composition. The k-ratio of element i is defined as:

$$k_i = \frac{I_{\text{i, unknown}}}{I_{\text{i, standard}}} \tag{2.23}$$

To get the more accurate composition through the k-ratio, the ZAF-corrections can be used. The corrections must be applied to both the unknown and the standard, and the composition of the unknown can be found through the equation:

$$C_{\text{i, unknown}} = C_{\text{i, standard}} \cdot \frac{(I \cdot ZAF)_{\text{i, unknown}}}{(I \cdot ZAF)_{\text{i, standard}}} = C_{\text{i, standard}} \cdot k_i \cdot \frac{(ZAF)_{\text{i, unknown}}}{(ZAF)_{\text{i, standard}}} \tag{2.24}$$

The ZAF corrections are a function of the concentration of the element, and thus the ZAF-corrections must be applied iteratively with an initial guess of the composition of the unknown. As with the k-factor, the k-ratio is most accurately determined experimentally, but can be calculated theoretically. The AZtec software from Oxford Instruments [23] can both provide the k-factor and the k-ratio for the elements in an analyzed sample, which are theoretically calculated.

2.5.2 ZAF absorption correction

The part of the ZAF corrections tested in this work are the absorption corrections. The atomic number correction (Z) is based on the backscattering factor (R) and the stopping power (S). It is stated in Goldstein that the effect of R and S tends to go in opposite directions, and that they usually cancel each other out [2, p. 300]. Both R and S is implemented in the PAP model [9], which is claimed to be more accurate than the ZAF method [2, 9, 59] The fluorescence correction (F) is excluded, because it is stated in Goldstein that this correction is usually the least important one [2, p. 307]. The low importance of the F correction is illustrated in later work [60]. The generated intensity is reduced before detection due to absorption in the specimen. The absorption reduces the measured intensity of X-rays from a certain point by:

$$I = I_0 \cdot e^{-\mu_\rho \cdot \rho \cdot t} \tag{2.25}$$

Where I is the measured intensity, I_0 is the generated intensity, μ_ρ is the mass absorption coefficient[4], ρ is the density of the specimen, and t is the path length of the X-ray in the specimen. The unit in the exponential to cancel out, as I and I_0 in the same units, either counts or arbitrary units. The unit of μ_ρ is cm^2/g, while ρ is g/cm^3, and t in cm. μ_ρ is explained in Section 2.1.1 and plotted in Figures 2.2 and 2.7. The detector is placed at a certain angle and thus the path length becomes:

$$t = z \cdot \csc(\mathrm{TOA}) \tag{2.26}$$

Where z is the depth of origin of the X-ray, TOA is the take-off angle, and csc is the cosecant function. Tilting the specimen will change the TOA (see Figure 2.18), which change the path length of the X-ray, and thus the absorption.

The most correct use of the absorption correction is to calculate the absorption for each point (or layer) in the interaction volume, which is usually done through $\phi(\rho z)$ curves. This calculation is part of the PAP method described in Section 2.5.3. For the ZAF method used in this work, the absorption correction is calculated for an average point in the interaction volume. Three approximations for the average point are tested in this work. The point is calculated as the maximum electron range where the electron still has energy $> E_C$, and this range is divided by two,

[4] Again, mass absorption coefficient is actually defined as μ/ρ, but is written as μ_ρ in this work, because the mass absorption coefficient is treated as a single variable.

three, and four to test different approximations. The electron range is calculated with the Kanaya-Okayama parameterization [61], which is available in HyperSpy [15]. The Kanaya-Okayama parameterization is given in Goldstein as [2, 22.5]:

$$R_{K-O}[\mu m] = (0.0276A/Z^{0.92}\rho) \cdot (E_0^{1.67} - E_C^{1.67}) \tag{2.27}$$

Where A is the atomic weight in g/mol, Z is the atomic number, ρ is the density in g/cm^3, E_0 is the incident electron energy in keV, and E_C is the critical ionization energy in keV. The equation is made for pure elements, but in this work the average A, Z and, ρ of the elements in the sample is used. In Goldstein, Eq. 14.1 gives the R_{K-O} in a specimen without the correction for E_C. The range R_{K-O} calculated the equation use the critical ionization energy as a threshold, because electrons with energy lower than this is not of interest. Using for example $R_{K-O}/2$ as the average point for the generated intensity is an approximation which can give a reasonable result, at least it should be in the correct order of magnitude. This simplification is partly justified by the fact that the available measured intensity I is the sum of the intensity from all points in the interaction volume.

Testing out different methods with varying complexity for calculating the absorption correction is a step towards finding a suitable implementation for HyperSpy. If a simpler model proves to be sufficient, it will allow users to understand the correction faster and possibly altering it to the specific needs, while also being easier to implement and maintain in HyperSpy.

2.5.3 The PAP model

Pouchou and Pichoir presented their PAP model for bulk corrections on a conference in 1983 and published a detailed paper about PAP in 1991 [9][5]. The model is a mathematical heavy model which is physically based on X-ray generation and emittance, and the model should be able to correct for a wide range of compositions [9]. In the 1991 publication, a simplified model called XPP is also presented[6]. Alternative methods exist for bulk corrections which produce similar results, but are mathematically different. One example of such a model is the PROZA96 model, which calculate the $\phi(\rho z)$ curve as a double Gaussian. The PROZA96 model is published by Bastin, Dijkstra, and Heijligers in 1996, as an improvement to the same authors previous model from 1988 [59, 62]. The difference between the PAP and PROZA96 models is the calculation of the $\phi(\rho z)$ curves, where the PAP model use a linear combination of two exponential functions to calculate the $\phi(\rho z)$ curve, not a double Gaussian as the PROZA96 model. Another model from Packwood and Brown [63] is also using Gaussians to calculate the $\phi(\rho z)$ curve. According to an Oxford Instruments blog post [22], it is the XPP model which is used for SEM EDS bulk corrections in AZtec[7]. Both the PAP and the PROZA96 model use the area under the $\phi(\rho z)$ curve for parameterization, where the PROZA96 model refers to the PAP paper for the calculation of this area [59]. Table 2.9 summarize the most central variables in the XPP model, with their name, their use, and their units.

[5] "PAP" is short for "Pouchou and Pichoir".

[6] "X" in XPP is probably short for e.g. express, but it is not stated in the paper.

[7] Neither the AZtec user manual nor the software [23] are mentioning how the bulk corrections are calculated.

The PAP model is a mathematical model which is based on the physics of X-ray generation and emittance. It is a model which calculates the emergent X-rays based on the depth distribution of the generated X-rays, $\phi(\rho z)$, and the absorption of the generated X-rays in the matrix at different depths, on the path to the detector. The model gives correction for homogeneous specimens, and the paper describe how it can be applied to specimen with composition varying in depth, specimen with surface coating, and lighter elements [9]. The version which is discussed here is the model for homogeneous specimen.

The $\phi(\rho z)$ curve gives the depth distribution of the generated X-rays in a bulk specimen relative to a thin specimen. The curve is a function of mass depth (ρz), where mass depth is the product of density (ρ) and depth (z) from the surface. The unit for the mass depth is g/cm^2. The intensity from each layer is divided by the intensity from a similar, but thin, specimen. As the bulk specimen have many backscattered electrons, which also generate X-rays, the $\phi(\rho z)$ curve has a distinct and general shape: The curve starts above 1, increase to a maximum, and then decrease to 0. Three $\phi(\rho z)$ curves are illustrated in Figure 2.29. The PAP model allows calculation of the $\phi(\rho z)$ curves.

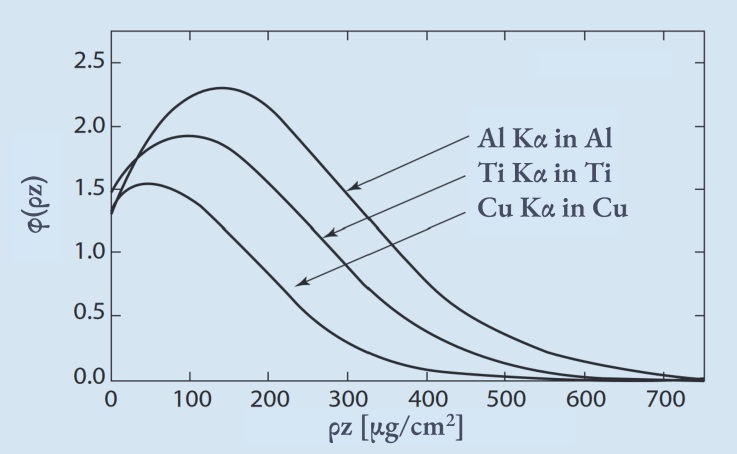

Figure 2.29: Three calculated $\phi(\rho z)$ curves. Al Kα in Al, Ti Kα in Ti, and Cu Kα in Cu, calculated at 15 kV. The curves are calculated with the PROZA model [62] Adapted from Goldstein [2, Fig. 19.9].

The following is a concise description of the PAP model. For further details, see the original paper [9], the fourth edition of Goldstein for a brief description [2], the second edition of Goldstein [64], or Reimers book on SEM [65].

General principle of the PAP model

The PAP model is in accordance with the original definitions from Castaing [55]. The calculations done in the PAP model is divided into two parts: (i) find the *generated intensity* by calculating the area F under the $\phi(\rho z)$ curve, and (ii) calculate the *emitted intensity* $F(\chi)$ based on a parameterization of $\phi(\rho z)$ with an absorption correction in each ρz layer. Both calculations are done analytically. A summary of the variables in this principle part of the PAP model is given in Table 2.9.

The generated intensity, or number of primary ionizations, of a line in element A is given as:

$$n_A = C_A \frac{N^0}{A} Q(U) F \tag{2.28}$$

Where n_A is the number of generated primary ionizations from atoms of element A, C_A is the concentration of element A in weight percent[8], N^0 is Avogadro's number, A is the atomic weight of element A[9], $Q(U)$ is the ionization cross-section of the line with the given overvoltage (U)[10], and F is the integral of $\phi(\rho z)$.

$$F = \int_0^\infty \phi(\rho z) d\rho z \tag{2.29}$$

The emitted intensity from a specimen is given as:

$$I_A \propto C_A \cdot Q(U) \cdot F(\chi) \tag{2.30}$$

Where I_A is the emitted intensity from element A, C_A is the concentration of element A in mass concentration, $Q(U)$ is the ionization cross-section, and $F(\chi)$ is the integral of $\phi(\rho z)$ with an absorption correction, where $\chi = \mu_\rho \cdot \csc(TOA)$[11]. This equation omits parameters which are equal or almost equal for the elements in the specimen, such as the solid angle of the detector, the electron flux, and the detector efficiency.

$$F(\chi) = \int_0^\infty \phi(\rho z) \cdot e^{-\chi \cdot \rho z} d\rho z \tag{2.31}$$

The relation between the emitted and generated intensity will give the absorption correction $f(\chi)$:

$$f(\chi) = \frac{F(\chi)}{F} = \frac{\text{emitted relative intensity}}{\text{generated relative intensity}} \tag{2.32}$$

PAP: Calculation of area F

The area F under the $\phi(\rho z)$ curve is proportional to the number of generated primary intensity, and does thus contain the Z dependence. F is the product of the deceleration factor ($1/S$) and the backscatter factor (R):

$$F = \frac{R}{S} \frac{1}{Q(U)} \tag{2.33}$$

The PAP paper is at times somewhat confusing, both because the lack of explanation of some symbols, and because of slightly contradicting equations. In equation (2) it is stated that $n_A = C_A(N^0/A)Q(U)F$, and in equation (3) it is stated that $n_A = C_A(N^0/A)(R/S)$. This implies that $(R/S) = Q(U)F$. However, equation (13) states that $F = (R/S) \cdot Q(U)$, which is a contradiction to equation (2) and (3). Based on a units analysis and the fact that the

[8] Note that in quantitative EDS the calculations are done in wt.%, but the results can be given in at.%.

[9] It is not stated explicit in the PAP paper, but based on [66] and an analysis of the units, A must be the atomic weight.

[10] $Q(U)$ is noted as $Q_i^A(E_0)$ in the PAP paper.

[11] χ is not explicitly defined in the PAP paper, but is taken from Love and Scott [66, Eq. (1)], which is a reference in the PAP paper.

Table 2.9: Variables from the principle of PAP. The variables are in the order of appearance.

Symbol	Name and/or definition	Units
n_A	Generated intensity. Number of generated primary ionizations from atoms of element A.	1 (a number)
C_A	Mass concentration of element A.	wt.%
N^0	Avogadro's number, i.e. $6.02E23$	1/mol
A	Atomic weight of atom A. Do not mix with the parameter A in the parameterization of $\phi(\rho z)$, further down.	Da
$Q(U)$	Ionization cross-section as a function of overvoltage U.	1 (a probability)
F	Integral or area of $\phi(\rho z)$, i.e. generated relative intensity.	Relative intensity
$\phi(\rho z)$	The depth distribution of an X-ray line.	Relative intensity
ρz	Mass density.	g/cm^2
I_A	Emitted intensity.	1 (a number)
$F(\chi)$	The integral of $\phi(\rho z) \cdot e^{-\chi \cdot \rho z}$, i.e. the depth distribution with an absorption correction.	Relative intensity
χ	$\mu_\rho / sin(TOA)$	cm^2/g

generated intensity should depend on $Q(U)$ as the probability of ionization, it is assumed that $F = (R/S)/Q(U)$ is the correct equation. Both formulations will however be tested, to verify this assumption.

The deceleration factor $1/S$ is a measure of the electrons' energy loss in the specimen, as a function of the energy that the electrons have. $1/S$ is an integral from E_0 to E_C of the product of the ionization cross-section ($Q(U)$) and the energy loss function ($dE/d\rho s$):

$$1/S = \int_{E_0}^{E_C} Q(U) \frac{dE}{d\rho s} dE \tag{2.34}$$

The ionization cross-section of a line as a function of overvoltage ($U = E_0/E_C$, see Section 2.3.2) is estimated in the PAP model for bulk specimen with the equation:

$$Q(U) \propto \frac{\ln(U)}{U^m} E_C^2 \tag{2.35}$$

Where:

$$m = \begin{cases} 0.9 & \text{for K level} \\ 0.82 & \text{for L levels} \\ 0.78 & \text{for M levels} \end{cases} \tag{2.36}$$

The K level m is taken from the PROZA96 model, which use the same function for ionization cross-section, but with an empirical improvement for the K level [59]. There are special values for m at low Z, but these are not relevant for this work. The formulation in Equation (2.35) for Q is "proportional to" and not "equal to", but when dealing with the same instrumental parameters (accelerating voltage, take-off angle, beam current, etc.), the proportionality constant is the same for all elements. In other words, for the calculations done in the PAP model, the proportionality constant is not needed, and Q can be calculated by Equation (2.35). A plot of $Q(U)$ with this equation is shown in Figure 2.30.

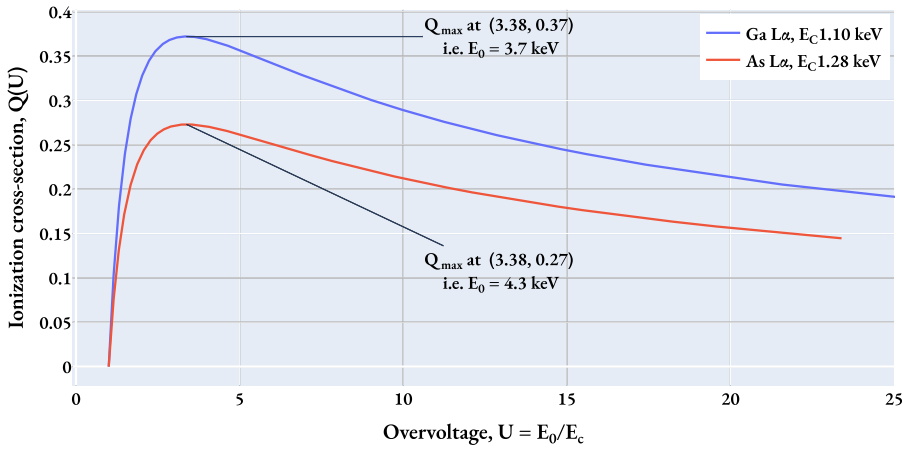

Figure 2.30: Ionization cross-section, Q as a function of overvoltage Ga Lα and As Lα. The maximum Q is annotated, which is at the same overvoltage, but different energies due to different E_C.

The average energy loss ($dE/d\rho s$) is not calculated from the law of Bethe, as that equation is not valid for low energies [9, 30]. Instead, the PAP model use a formulation for the average energy loss which is equal to the Bethe equation from around 1 keV, but is also empirically corrected for lower energies. The average energy loss is calculated as:

$$\frac{dE}{d\rho s} = -\frac{M}{J}\frac{1}{f(V)} \tag{2.37}$$

Where:

$$M = \sum_i \frac{C_i Z_i}{A_i} \tag{2.38}$$

$$J = \exp\left(\sum_i \frac{C_i Z_i}{A_i} \cdot \ln(J_i)/M\right) \tag{2.39}$$

$$J_i = 10^{-3} \cdot Z_i\left(10.04 + 8.25\exp\left(\frac{-Z_i}{11.22}\right)\right) \tag{2.40}$$

$$f(V) = \sum_{k=1}^{3} D_k \cdot V^{P_k} \tag{2.41}$$

M is the mean ionization potential of the specimen, and J is the mean ionization potential of the specimen, J_i is the mean ionization potential of element i, and $f(V)$ is a function containing the energy dependent terms which makes Equation (2.37) equal to Bethe's law for high energies and still being valid for low energies. $V = E/J$, and D_k and P_k are constants, calculated as:

$$D_k = \begin{cases} D_1 = 6.6 \cdot 10^{-6} \\ D_2 = 1.12 \cdot 10^{-5}(1.35 - 0.45J^2) \\ D_3 = \frac{2.2 \cdot 10^{-6}}{J} \end{cases} \qquad P_k = \begin{cases} P_1 = 0.78 \\ P_2 = 0.1 \\ P_3 = -(0.5 - 0.25J) \end{cases} \tag{2.42}$$

i.e.

$$f(V) = 6.6 \cdot 10^{-6} \cdot V^{0.78} + 1.12 \cdot 10^{-5} \cdot (1.35 - 0.45J^2) \cdot V^{0.1} + \frac{2.2 \cdot 10^{-6}}{J} \cdot V^{-(0.5-0.25J)} \tag{2.43}$$

The PAP paper gives an analytical solution for $1/S$ through the expression for the ionization cross-section and the deceleration of the electrons, where $T_K = 1 + P_k - m$, as:

$$1/S = \frac{U_0}{V_0 \cdot M} \sum_{k=1}^{3} D_k \cdot (V_0/U_0)^{P_k} \cdot ((T_k) U_0^{T_k} \cdot \ln(U_0) - U_0^{T_k} + 1)/T_k^2 \tag{2.44}$$

This parameterization can be used in quantification of experimental data. Figure 2.31 show the energy loss of the electrons in GaAs, GaSb, and Cu, according to the PAP model.

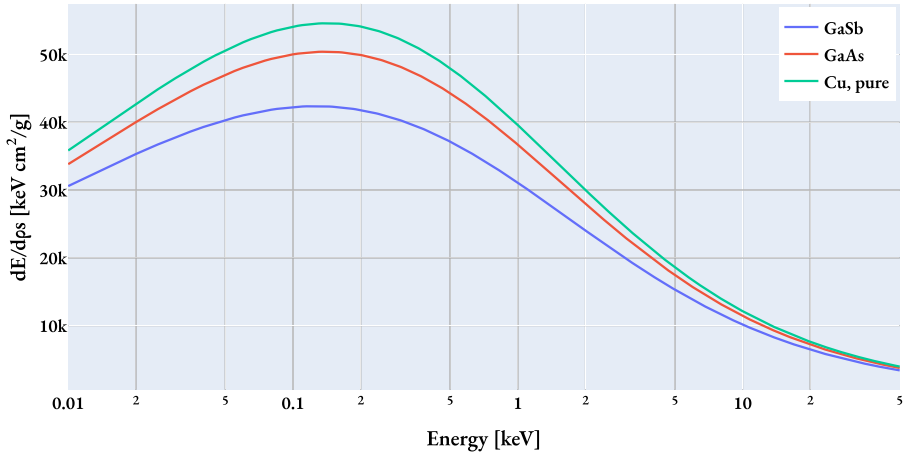

Figure 2.31: The energy loss of electrons, $dE/d\rho s$, in GaAs, GaSb, and Cu. Cu is added for comparison to the plot in the PAP paper [9, Fig. 4]. Note that the x-axis is logarithmic, i.e. going up to 50 keV.

The backscattering loss factor R is the fraction of the electrons that can generate X-rays, i.e. the electrons that are not backscattered. Higher Z material will backscatter more, and thus have a lower R. The backscattering loss factor is calculated as:

$$R = 1 - \bar{\eta} \cdot \bar{W} \cdot (1 - G(U_0)) \tag{2.45}$$

Where:

- $\bar{W} = \bar{E}_r / E_0 = 0.595 + \bar{\eta}/3.7 + \bar{\eta}^{4.55}$
- $\bar{\eta} = 1.75 \cdot 10^{-3} \cdot \bar{Z}_b + 0.37(1 - \exp(-0.015 \bar{Z}_b^{1.3}))$
- $\bar{Z}_b = (\sum C_i \cdot Z_i^{0.5})^2$
- $G(U_0) = (U_0 - 1 - (1 - \frac{1}{U_0^{1+q}})/(1+q))/((2+q) \cdot J(U_0))$
- $J_G(U_0) = 1 + U_0 \cdot (\ln(U_0) - 1)$
- $q = (2\bar{W} - 1)/(1 - \bar{W})$

$\bar{\eta}$ is the mean backscattering coefficient, $\bar{W}$ is the mean reduced energy of the backscattered electron, $\bar{Z}_b$ is the weighted mean atomic number, and U_0 is the overvoltage. $G(U_0)$ is an equation from Coulon and Zeller [9, Reference 28], calculated with $J_G(U_0)$ and q. The backscattering factor for Z=1 to Z=90 is plotted with different overvoltages in Figure 2.32. At higher Z the backscattering loss factor is lower, because a fewer of the electrons can generate X-rays.

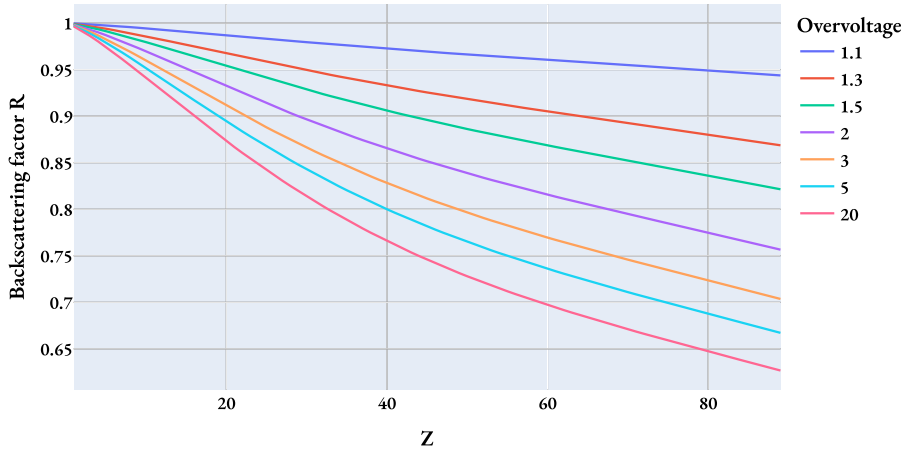

Figure 2.32: Backscattering factor for Z=1 to Z=90, with different overvoltages. The atomic number is on the x-axis, and the backscattering factor is on the y-axis. The different lines are for different overvoltages.

PAP: Emergent intensity $F(\chi)$

$F(\chi)$ is the emergent intensity from the specimen, which is calculated from a parameterization of $\phi(\rho z)$ with added absorption correction. The system of equations which lead to the parameterization of $\phi(\rho z)$ is given in the original paper [9]. The section covers the necessary calculations to find the emitted intensity, which is described as the "Simplified model: XPP". The structure of the XPP model is similar to the PAP model, and XPP is chosen in this work as it is the model which is used in AZtec [22]. Thus, the following equations are for the XPP model.

The emergent intensity of a specimen is given by Equation (2.30) and the definition of $F(\chi)$ is given by Equation (2.31). The analytical solution of $F(\chi)$ is given by:

$$F(\chi) = \frac{A}{a+\chi} + \frac{\phi(0) - A}{b+\chi} + \frac{B}{(b+\chi)^2} \tag{2.46}$$

Where A, B, a and b are the parameterization of $\phi(\rho z)$, and $\phi(0)$ is the surface ionization. The absorption correction factor can then be calculated by the emergent intensity divided by the generated intensity, as:

$$f(\chi) = \frac{F(\chi)}{F} \tag{2.47}$$

Calculating the surface ionization potential $\phi(0)$, the mean depth of ionization $\bar{R}$, and the initial slope P is the next step in the XPP model. These three parameters are used to calculate A, B, a, and b, which is used to get the parameterization $F(\chi)$ for $\phi(\rho z)$.

The surface ionization potential is the amount of ionization happening at the surface of the specimen, which is the starting point for the $\phi(\rho z)$ curve. The surface ionization potential is given by:

$$\phi(0) = 1 + 3.3(1 - 1/U_0^{2-2.3\bar{\eta}}) \cdot \bar{\eta}^{1.2} \tag{2.48}$$

The surface ionization potential, $\phi(0)$ is illustrated for Z=1 to Z=90 with differing overvoltages in Figure 2.33. $\phi(0)$ is > 1 because of backscattered electrons that generate X-rays at the surface.

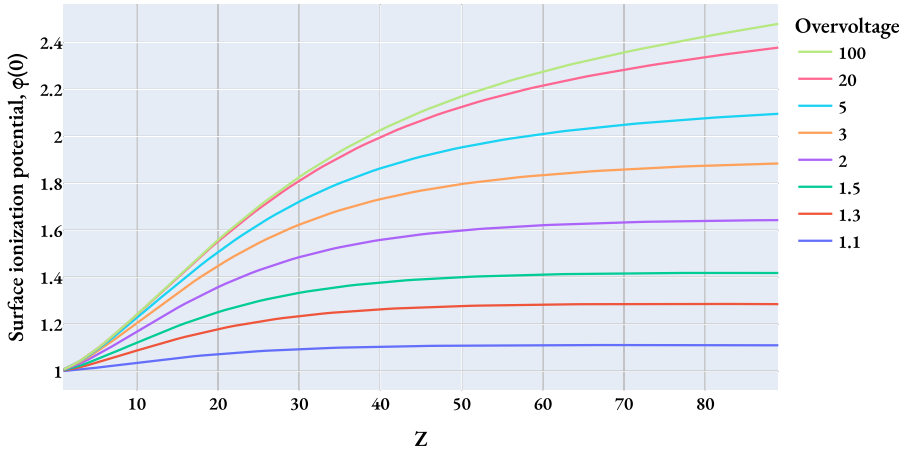

Figure 2.33: Surface ionization potential for Z=1 to Z=90, with different overvoltages. The atomic number is on the x-axis, and the surface ionization potential is on the y-axis. The different lines are for different overvoltages.

The average depth of ionization, $\bar{R}$, is given by:

$$\bar{R} = F/(1 + [X \cdot \ln(1 + Y \cdot (1 - 1/U_0^{0.42}))]/\ln(1 + Y)) \tag{2.49}$$

Where X and Y are given by:

- $X = 1 + 1.3\ln(\bar{Z}_b)$
- $Y = 0.2 + \bar{Z}_b/200$

The initial slope P is given by:

$$P = g \cdot b^4 \cdot F/\bar{R}^2 \tag{2.50}$$

Where g and b are given by:

- $g = 0.22\ln(4\bar{Z}_b) \cdot [1 - 2\exp(-\bar{Z}_b \frac{U_0 - 1}{15})]$
- $b = 1 - 10(1 - \frac{1}{1+U_0/10})/\bar{Z}_b^2$

The parameters A, B, a, and b are used to calculate the parameterization $F(\chi)$ for $\phi(\rho z)$. They can also be used to calculate $\phi(\rho z)$, which is done further down. Additionally, the parameter ε is used in the calculation of A and B. The parameters are calculated sequentially, starting with b, then a, then ε, then B, and finally A.

$$b = \sqrt{2} \cdot (1 + \sqrt{1 - \bar{R} \cdot \phi(0)/F})/\bar{R} \tag{2.51}$$

$$a = [P + b \cdot (2\phi(0) - b \cdot F)]/[b \cdot F \cdot (2 - b\bar{R}) - \phi(0)] \tag{2.52}$$

$$\varepsilon = \frac{a - b}{b} \tag{2.53}$$

The parameter A and B are then calculated by:

$$B = [b^2 \cdot F \cdot (1 + \varepsilon) - P - \phi(0) \cdot b \cdot (2 + \varepsilon)]/\varepsilon \tag{2.54}$$

$$A = [B/b + \phi(0) - b \cdot F] \cdot \frac{1 + \varepsilon}{\varepsilon} \tag{2.55}$$

With A, B, a, b and $\phi(0)$ calculated, the absorption correction $f(\chi)$ and the emergent intensity through $F(\chi)$ can be calculated with Equation (2.47) and Equation (2.46) respectively.

Plotting the $\phi(\rho z)$ curves can be done with the now calculated parameters A, B, a, b and $\phi(0)$, as:

$$\phi(\rho z) = A \cdot \exp(-a \cdot (\rho z)) + (B \cdot (\rho z) + \phi(0) - A) \cdot \exp(-b \cdot (\rho z)) \tag{2.56}$$

This should cover the necessary theory for the XPP model to be implemented in code developed in this project.

Chapter 3

Method

This chapter describes the method used in this project. The method is divided into four parts: the materials studied, the instruments used, the acquisition settings in the measurement series, and the data treatment. The data treatment is described further with the code in the Jupyter notebooks, which is documented with comments and docstrings. The notebooks and the data are available at GitHub in the repositories "eds-sem-bulk-corrections" and "sem-eds-qc".

3.1 Materials and specimen

In this study, two different test materials were studied: GaAs and GaSb wafers pieces. Both specimens are compound III-V semiconductors, assumed to be pure (99.99%) and homogeneous, as they are semiconductor application standards. SE and BSE imaging was used to locate flat areas for the acquisition of the spectra. SE images of the analyzed areas are included below. Overview images are shown in Figure 3.1, and the close up images are shown in Figure 3.2, and Figure 3.3. The images are acquired with the ET detector, which combines SE and BSE signals. The analyzed areas are annotated in the images.

The specimen were from 300 µm thick and polished wafers, which had a 1 : 1 ratio of Ga and As or Sb, respectively. These specimens of known composition are readily obtainable and could serve as test materials. These materials allow comparison of Z effects and provide X-ray lines suitable for comparison of performance and quantification. The use of wafers were chosen to have clean and flat surfaces, which would be easy to obtain. Ga has Z=31 and As has Z=33, where both have L-peaks in the low energy range, and K-peaks in the mid/high energy range. Sb has Z=51, with L-peaks in the mid-energy range, and K-peaks in the highest energy range for SEM. See Table 2.2 for the theoretical line energies. Small (ca. 10x10 mm) pieces were taken from 2″ wafers, and glued with Ag-paint to a 300 µm thick p-doped Si 2″ wafer, which was cut in half and used as a sample holder. The Si wafer was attached to an Al FIB stub, which was loaded into the SEM.

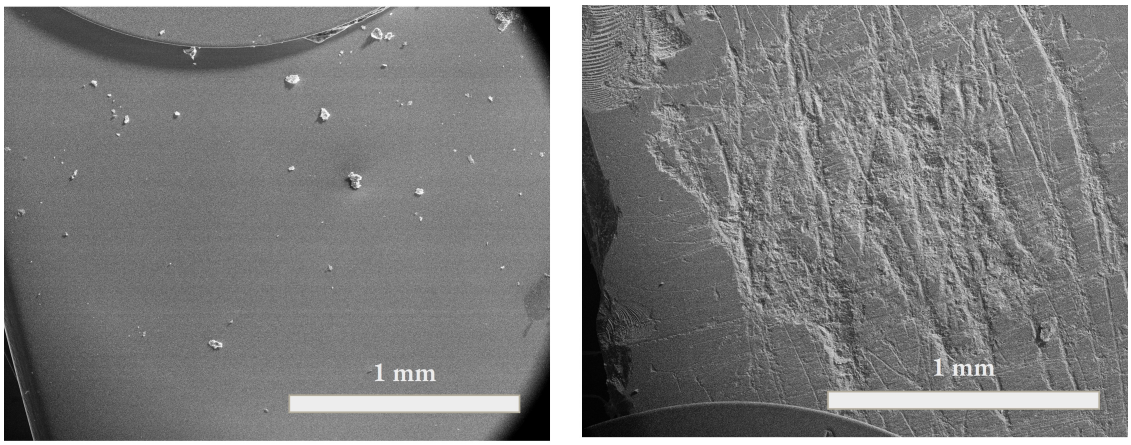

Figure 3.1: Overview of the GaAs and GaSb specimens, from the ET detector. The spectra are acquired in the middle of the images. Panel (a) is GaAs, and panel (b) is GaSb. The GaSb wafer have areas which are very scratched, but also areas which are smooth.

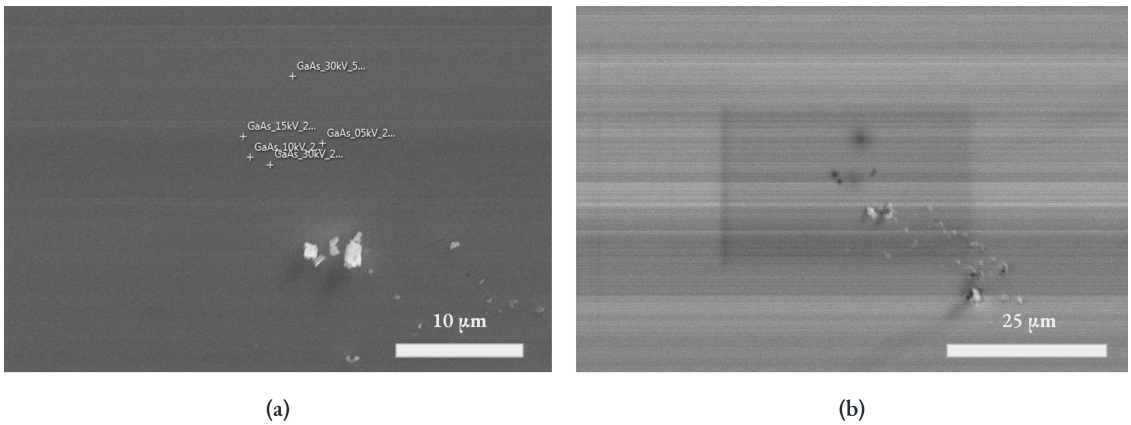

Figure 3.2: Close up of the GaAs specimen, Annotated in panel (a) are the areas which were analyzed. Panel (b) is a zoomed out view of the area in panel (a), after the spectra have been acquired. This image shows both beam damage from the focused probe beam as black dots, and the whole area from the scanning as a darker square. The darker square is Z contrast in the BSE signal.

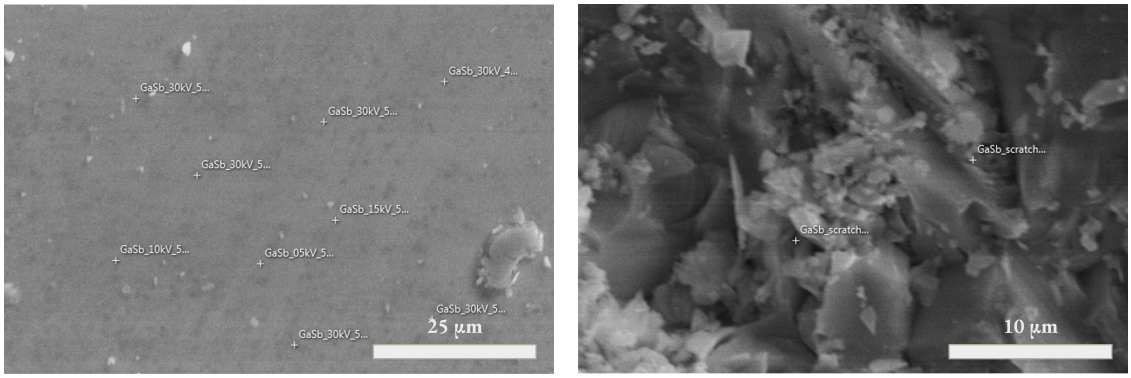

(a) (b)

Figure 3.3: Close up of the GaSb specimen, from the ET detector. Panel (a) is the polished area, and panel (b) is the scratched area. Both panels are annotated with the areas which were analyzed.

3.2 Instruments

The acquisition of the spectra was done with an Oxford Instruments Xmax^N 80 mm^2 silicon drift detector for EDS, equipped on a SEM Apreo from FEI. The Apreo is a field emission SEM, which in addition to the EDS sensor has an Everhart-Thornley detector, in-lens detectors for SE and BSE, a directional BSE detector, and a navigation camera. In this work, the ET detector was used to verify that the areas studied were clean, flat and representative. The maximum accelerating voltage is 30 kV, and the maximum beam current is 400 nA. During this work, the acceleration voltage has been in the range 5 – 30 kV, and the beam current has been in the range 25 – 400 pA. The acquisition settings used in this study are listed in Table 3.2 and Table 3.3. The instrument is located at the NTNU NanoLab, a NorFab facility.

The details about the EDS detector is from [67] and the description provided by NanoLab. The Oxford Xmax^N SDD has an 80 mm^2 active area. The specifications list the following FWHM energy resolutions at 50k cps: Mn Kα at 127 eV, F Kα at 64 eV, and C Kα at 56 eV. Giving the specifications like this is in compliance with the ISO 15632:2012 standard [43]. All elements from Be to Cf can be analyzed, as the detector has a thin polymer window. The detector is mounted at 35°. The process time settings range from 1 to 6, and they have no further explanation of what the number indicates. The detector is operated with the AZtec software, provided by Oxford Instruments NanoAnalysis [23].

3.3 Acquisition settings in the measurement series

The settings selected are based on Goldstein [2] and the goal of analyzing spectra with varying acquisition parameters. The acquisition settings for each spectrum are given in Table 3.1. The acquisition is divided into four groups, where the two first are acquisition with varying acceleration voltage and constant beam current. (A) is the voltage series on GaAs, and (B) is the voltage series on GaSb. The two other series test parameter variation on the GaSb specimen: (C) is with varying PT, (D) is with varying i_b, PT, and E_0. The voltage series is used to study the effect of

the acceleration voltage, to figure out if an optimal voltage exists. The other acquisition settings tested variations of different settings on the GaSb specimen, to see if any of these settings could improve the quality of the spectra. Table 3.2 show settings for (A) and (B), Table 3.3 covers (C) and (D). Dead time (DT) and input count rate (ICR) is a function of the other settings.

Some variables were kept constant during all the acquisition. The tilt of the specimen was kept at 0°, and thus the TOA was 35°, because of the mounted angle of the detector. The live time for each spectrum was 120 s, except for two of the spectra in the (D) series, which had a high DT. The range of the spectra was $0 - 20$ keV, with a scale of 10 eV/channel.

Table 3.1: Experimental settings of acquired and used spectra in this work. The spectra are divided into four groups: (A) voltage series GaAs, (B) voltage series GaSb, (C) different PT, and (D) different i_b, E_0, and PT. All spectra were recorded with $0 - 20$ keV energy range over 2048 channels, at working distance 10 mm (optimal for the detector), and with TOA 35°due to the detector tilt.

Group	**Sample**	E_0 *[kV]*	i_b *[pA]*	**PT**	**ICR** *[k counts]*	**DT** *[%]*	**Comment**
GaAs E_0 series, A	GaAs	5	25	6	0.9	3	
A	GaAs	10	25	6	1.8	6	
A	GaAs	15	25	6	3	12	
A	GaAs	30	25	6	8	25	
A	GaAs	30	50	6	16	44	Additional spectrum
GaSb E_0 series, B	GaSb	5	50	6	1.1	4	
B	GaSb	10	50	6	2	9	
B	GaSb	15	50	6	6	18	
B	GaSb	30	50	6	17	44	
PT change, C	GaSb	30	50	4	17	13	
C	GaSb	30	50	2	17	7	
C	GaSb	30	50	1	17	4	
i_b, E_0, and PT change, D	GaSb	15	200	6	22	53	61 s live time
D	GaSb	15	400	6	42	77	59 s live time
D	GaSb	30	400	1	160	28	Very high counts

Table 3.2: Measurement series A and B, which tested different E_0 on GaAs and GaSb.

Setting	Values	Comment
Beam energy	30, 15, 10, and 5 kV	To study the effect of different E_0.
Beam current	25 pA or 50 pA	25 pA for GaAs and 50 pA for GaSb. Set to get sufficient amount of counts and maximum DT around 30% at 30 kV. Then kept constant when E_0 was decreased in the voltage series. Different beam current for the specimen was chosen to see the effects on Ga.
Process time	6 (maximum)	Set to the highest to influence the acquisition as little as possible, i.e. giving the highest energy resolution.
DT GaAs	25%, 12%, 6%, 3%	DT is not a setting, but a result of other settings. The low DT at the lower E_0 was due to fewer counts.
DT GaSb	44%, 18%, 9%, 4%	
Data type	PointID	The voltage series was only done with PointID, while mapping was tested in the measurement series summarized in Table 3.3.
Live time	120 s	To get sufficient amount of counts.
Additional spectrum	GaAs, 30 kV, 50 pA	An additional spectrum on GaAs with the same settings at the 30 kV spectrum of GaSb. Taken to directly compare the 30 kV spectra.

Table 3.3: Measurement series B and C, which tested variation in i_b, PT, and E_0. These measurements were only done on the GaSb specimen.

Setting	Values	Comment
Beam energy	15 and 30 kV	Further inspect the effect of the Sb K-peaks just below 30 kV.
Beam current	50, 200, and 400 pA	To study ICR and DT, with values given in Table 3.1.
Process time	1, 2, 4, and 6	To study the effect of PT, e.g. on energy resolution and coincidence events.

3.4 Data treatment

The data treatment is divided into three parts: acquisition and extraction, performance parameters, and quantification. All the notebooks run on Python 3.10, with the packages listed in Table 3.4. All dependencies were installed using the package manager Mamba 1.4.0, with Conda 22.11.1. When contributing to HyperSpy, the developer version of HyperSpy was installed using pip 23.0. One notebook is attached in the appendix of this thesis, and both this and the other notebooks are available at GitHub in the repositories "sem-eds-qc"[1] and "eds-sem-bulk-corrections".

Table 3.4: Dependencies for the developed notebooks.

Package name	Description
HyperSpy 1.7.4	Multi-dimensional data analysis toolbox.
Plotly 5.13.1	Interactive, open-source, and browser-based graphing library.
NumPy 1.23.5	Scientific computing with Python.
Pandas 1.5.3	Data analysis package.
JupyterLab 3.6.2	Web-based interactive development environment.
SciPy 1.10.1	Scientific computing with Python.
Matplotlib 3.7.1	Static, animated, and interactive visualizations.

3.4.1 Acquisition and extraction - AZtec

Acquisition and extraction is done with AZtec version 5.0, provided by Oxford Instruments NanoAnalysis [23]. Steps for acquisition is described in Appendix A of Lundeby [68]. The "SEM EDS" setting was selected. Point measurements was done with "Point & ID". The point spectra was extracted as ".emsa" files.

Summarized, the acquisition and extraction in AZtec was done as follows:

1. Navigated to the area of interest with the ET detector
2. Selected the setting "SEM EDS" and acquisition type "Point & ID"
3. Selected settings for the acquisition, see Table 3.1, and started the acquisition
4. Verified the element with the spectrum and an interactive periodic table
5. Noted down the composition calculated by AZtec
6. Extracted the spectra as ".emsa" files for notebook analysis

Initial qualitative analysis was done with the AZtec software, to get an overview of the spectra. All spectra were quantitatively analyzed with the AZtec software to later compare with HyperSpy and the notebooks developed in this thesis. The "SEM EDS" quantification in AZtec give the composition and the calculated k-ratios for each

[1] "qc" = quality control

element. Additionally, quantification with the "TEM EDS" setting in AZtec was tested, where both the composition and calculated k-factors were extracted. This "TEM EDS" step was done to verify that AZtec does use matrix corrections, and to get the k-factors for CL quantification with HyperSpy.

3.4.2 Performance parameters - Jupyter notebooks

A Jupyter notebooks was developed for the calculation of SEM EDS performance parameters, i.e. the top and middle row of Figure 1.1. The notebooks for performance parameters calibrates the spectrum, and calculates: the Duane-Hunt limit, the energy resolution, the Fiori P/B, peak intensities, FWHMs, peak deviations, and specified peak ratios. The list below describes the steps in the notebooks, which are included as headers in the notebooks. See Appendix A for the notebook, or view it on GitHub. The performance parameter notebook does the following steps:

1. Import the packages
2. Select spectra, and specify settings like i_b, E_0, ICR, and PT
3. Import the data with HyperSpy, set the elements in the spectrum, and slice off the noise peak
4. Calculate the Duane-Hunt limit, and slice the spectrum to the limit
5. Make a model of the spectrum, and fit it to the data
6. Calibrate the offset and scale
7. Calibrate the energy resolution
8. Calibrate the energy and width of the peaks
9. Calculate Fiori P/B, peak intensities, FWHMs, and peak deviations
10. Calculate the relevant peak ratios
11. Save the results in a DataFrame in a ".csv" file

3.4.3 Quantification - HyperSpy and Jupyter notebooks

The different quantification routines and bulk corrections performed in the notebooks are made available at the author of this thesis' GitHub in the repository "eds-sem-bulk-corrections", under the user "brynjarmorka"[2]. The initial quantification was done with the intensity ratio method, where the intensities were extracted from a model fit of the spectrum through HyperSpy. The next paragraphs describe: the Cliff-Lorimer (CL) method in HyperSpy, the calculation of the ZAF absorption correction, and the implementation of the XPP model.

The CL quantification in HyperSpy was done according to the documentation. The Jupyter notebook with the quantification is named quant-of-SEM-EDS-with-Cliff-Lorimer.ipynb. The spectrum was loaded, and the elements were set. The data was sliced after the noise peak at 0.2 eV, and at the E_0 from the metadata. A model, with

[2] https://github.com/brynjarmorka/eds-sem-bulk-corrections/

a polynomial background and Gaussian peaks, were made and fitted. The intensities of the peaks were extracted, and given as input to the CL quantification routine. The k-factors, calculated by AZtec based on the element and E_0, were also given as input to the Cliff Lorimer routine, and are tabulated in Table B.1. The different absorption correction thicknesses were tested for a range of thicknesses between 50 nm and 10k nm. The results, as compositions, were plotted for inspection, and saved in an external file.

The ZAF absorption corrections (A) use the intensities from a model fit, and applies absorption corrections to these. A Jupyter notebook with the ZAF absorption correction is named ZAF-absorption-correction-model.ipynb. To calculate A, the code needs some factors. The average density was calculated with `density_of_mixture()` from HyperSpy. The electron range is calculated with an implementation of the Kanaya-Okayama parameterization. The average depth is calculated as the maximum electron range, divided by 2, 3, or 4. The path length is calculated with the TOA and the average depth. With these factors, the measured intensity is corrected with Equation (2.25), to get an approximation for the generated intensity. The generated intensities are used to calculate corrected compositions, which are given in atomic percent. In the end, the results are saved in an external file.

The XPP model is implemented in Python files, which are imported into Jupyter notebooks. The implementation of the equations are separated into smaller functions in the Python files, so that they are more flexible and easier to reuse. The Python files contains many functions which does small steps, and thus the code is easier to reuse and debug. Unlike the performance parameters, the XPP model is exemplified through two notebooks. One notebook in the repository is used to apply the model on the acquired spectra, and another notebook is used to plot different parts of the model. The Python files PAP-parameterization.py, PAP-helper-functions.py, and PAP-area.py are for the calculation of the XPP model. The PAP-parameterization.py file calculates $F(\chi)$ and $f(\chi)$, see Section 2.5.3 and Equation (2.32). The PAP-helper-functions.py file contains helper functions, e.g. for getting the theoretical energy of a line, and converting at.% to wt.%. The PAP-area.py file calculates F, see Section 2.5.3. The code is based on the PAP paper [9], and all the equations are described in Section 2.5.3. Additionally, all the equations are written out with LaTeXin the notebooks, and every function has a NumPy-style docstring. The files and notebooks contains many lines and are cannot be printed practically, and thus the code is not attached, but it is available under a MIT license at the author of this thesis' GitHub, in the repository "eds-sem-bulk-corrections".

Chapter 4

Results

This chapter presents the results of the thesis. The results are divided into three parts: an initial qualitative analysis of the spectra, followed by the performance parameters of the setup and acquisition parameters, and finally the quantification results. As seen in the SE images presented in Section 3.1, the areas chosen for the analysis are homogeneous and relatively clean. Scratched areas on the GaSb specimen are shown in Figure 3.3 panel (b), where some spectra were acquired, but not included in the results of this thesis.

4.1 Qualitative analysis

Here, an overview of the spectra is presented, where some characteristics and artifacts are identified. General plots of the spectra are given in Figures 4.1 to 4.3.

The lines given in Table 2.2 for Ga, As, and Sb have been identified in the spectra. All spectra also had a peak at C Kα. The GaSb spectra included a well-defined O Kα peak, while the GaAs spectra had barely any signal from the O Kα line. As annotated in Figure 4.1, the GaSb spectra also included two Sb M-signals: ζ and γ, where ζ is a clearly defined peak, while γ is a slight increase in intensity. These two M-peaks are not listed in the HyperSpy database, but were found through AZtec [23] and other literature [35].

Artifacts are present in all spectra, in varying degrees. The artifacts identified are listed and described in Table 4.1. The artifacts present in the spectra are the background, the noise peak, the carbon and oxygen stray peak, coincidence peaks, the internal Si fluorescence peak, and the Si escape peak from Sb Lα.

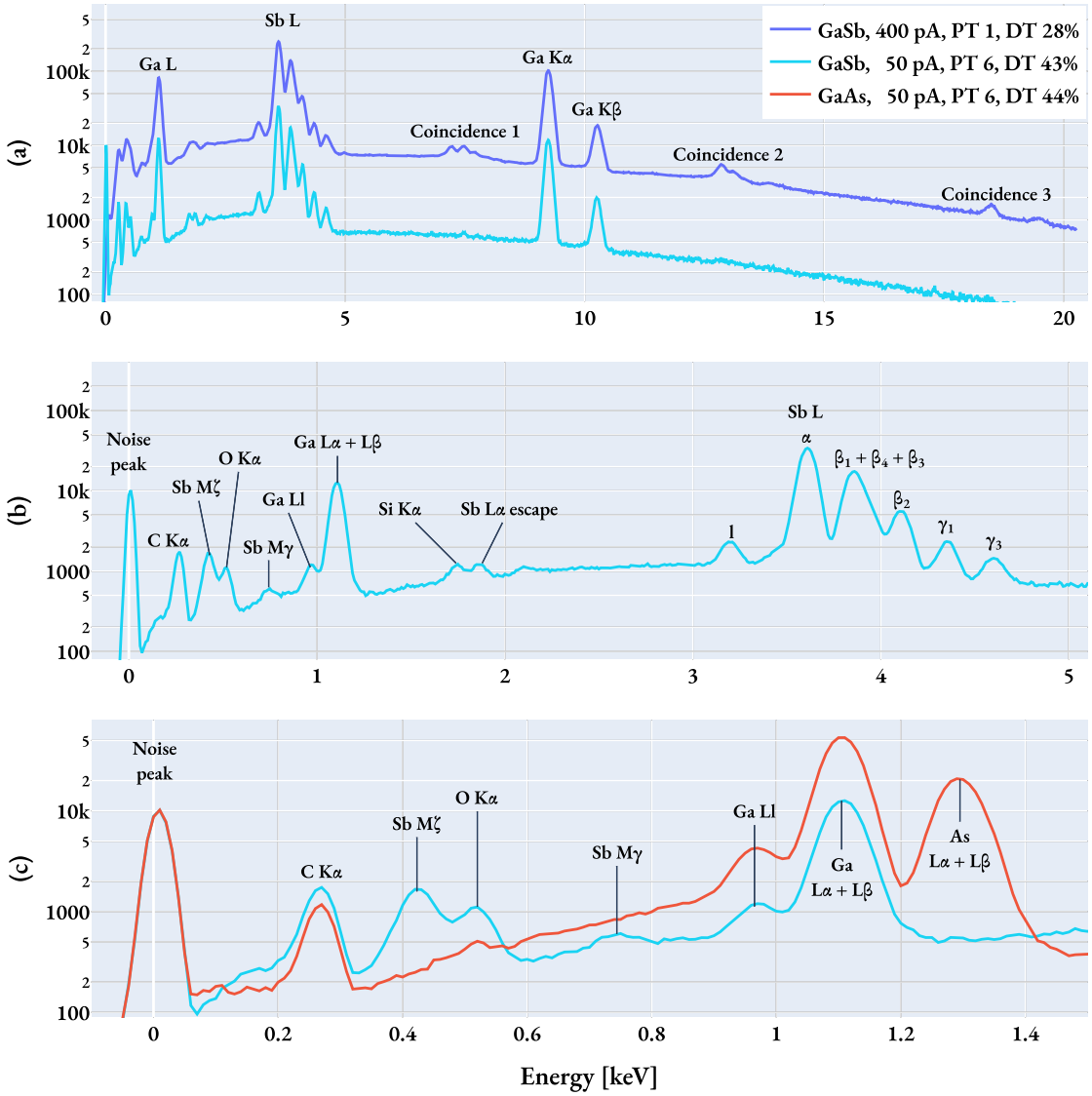

Figure 4.1: Overview of the GaSb spectra. The blue line in panel (a) have lower resolution and more artifacts than the light blue line. The light blue line is plotted in panel (b) over a shorter energy range, and with peaks annotated. Panel (c) show the light blue line on an even shorter energy range, with the GaAs spectrum in red for reference. All three spectra are acquired with 30 kV.

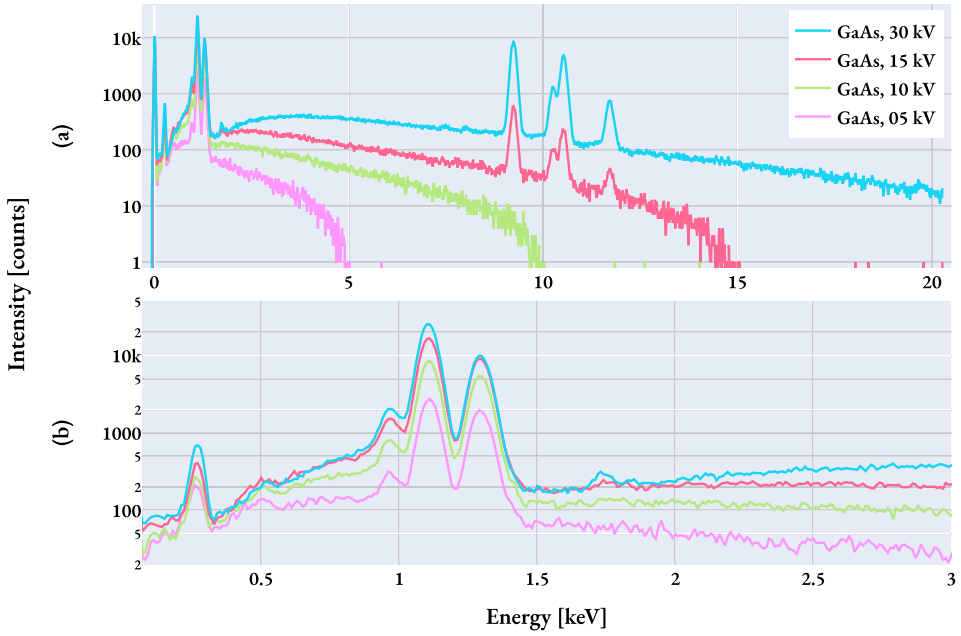

Figure 4.2: Group (A), the GaAs voltage series. The figure gives an overview of the spectra, and show the effect of overvoltage. All four spectra have $i_b = 25$ pA and PT 6.

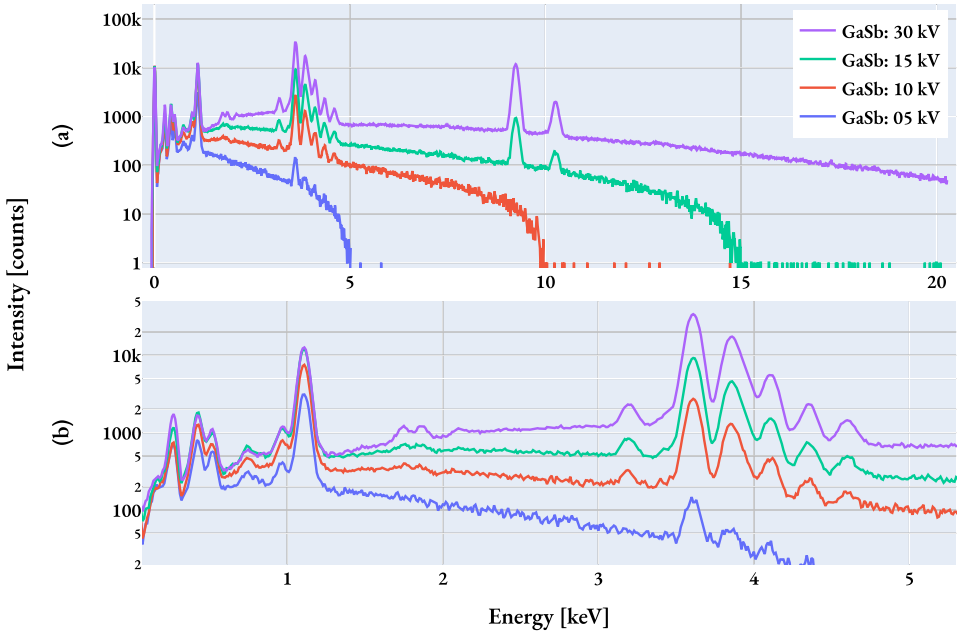

Figure 4.3: Group (B), the GaSb voltage series. The figure serves the same purpose as Figure 4.2, but for GaSb. The tailing background is the vertical lines above E_0. All four spectra have $i_b = 50$ pA and PT 6.

Table 4.1: The artifacts present in the spectra. See Figures 4.1 to 4.3.

Artifact	Where the artifact is present and a comment
Background	All spectra. Increase with higher count rate.
Absorption edge effect on background	Most prominent in GaAs. Reduces the background intensity above the Ga L absorption edge. In Figure 4.2 panel (b) the background drop from around 600 to around 170 counts.
Noise peak	All spectra. Located almost at 0 keV.
Coincidence peaks	Only the spectra with very high count rates. Figure 4.1 with GaSb taken at 30 kV, 400 pA, and PT 1 show coincidence peaks from: (Sb L + Sb L), (Sb L + Ga K), and (Ga K + Ga K).
Tailing background noise from coincidence events	Present in spectra taken at 5, 10, and 15 kV. Coincidence events from two arbitrary counts give a tailing background. Exemplified by the green 15 kV line in Figure 4.3 panel (a), where vertical lines (one count each) are present between 15 and 20 keV.
Internal fluorescence peak	Visible in some spectra. A low signal, barely a peak in some spectra, at Si Kα. Most prominent in 30 kV spectra and spectra with high count rates.
Si escape peak	Most GaSb spectra show some escape signal from Sb Lα at 1.86 keV, labeled in Figure 4.1 panel (b). The coincidence counts from (Sb L + Sb L) marked as "Coincidence 1" in Figure 4.1 panel (a) has one peak at 7.2 keV and one at 7.5 keV, where the latter could be a combination of coincidence events and escape counts from Ga Kα ($9.25 - 1.74 = 7.51$).
Stray C	All spectra show a C Kα peak, with some variation in intensity.
Stray O	All spectra of GaSb show an O Kα peak. The GaAs spectra have much lower, but still present signal at 0.52 keV.

4.2 EDS performance parameters

The performance parameters of the EDS system are directed towards the setup and the acquisition parameters. The metrics are the energy resolution, the scale and offset, the peak ratios, the deviations in peak positions, the Duane-Hunt limit, the Fiori peak-to-background ratio. Additionally, results from the user parameters process time, beam energy, and beam current are presented. To show how the info in a single spectrum varies with the selected line of reference, information from the lines are presented from two selected spectra in Table 4.2. The two selected spectra are both acquired with 30 kV, 50 pA, PT 6, DT 44%, and ICR = 17k cps for GaSb and ICR = 16.5k cps for GaAs. The table lists the theoretical energy of the line, the change in position after calibration, the FWHM of the peak, the area of the peak, the Fiori P/B of the line, and the estimated FWHM of Mn Kα using Equation (2.13).

Table 4.2: Info from the lines acquired at 30 keV, 50 pA, and PT 6. The lines are sorted by area (counts in the peak). Both the GaAs and GaSb spectra have DT 44%, with ICR = 17k cps for GaSb and ICR = 16.5k cps for GaAs.

Specimen	Line	Energy	Δ E	FWHM	Area	Fiori P/B	Estimated FWHM(Mn Kα)
		[keV]	*[eV]*	*[eV]*	*[k counts]*		*[eV]*
	Ga Lα	1.098	2	67	333	586	128
	Ga Kα	9.252	2	163	302	762	134
	As Kα	10.544	2	173	183	622	135
GaAs	As Lα	1.282	2	72	140	236	129
	Ga Lβ	1.125	0	68	56	97	129
	Ga Kβ	10.264	2	161	39	124	123
	As Kβ	11.726	2	181	27	117	135
	As Lβ	1.317	0	71	23	39	129
	Sb Lα	3.605	-0.4	102	355	385	127
	Ga Kα	9.252	-2	161	189	408	133
GaSb	Sb Lβ_1	3.844	-2	101	152	168	124
	Ga Lα	1.098	2	65	74	86	128
	Sb Lβ_2	4.101	0	108	55	63	127
	Ga Kβ	10.264	-2	160	24	59	121

4.2.1 Energy resolution

The energy resolution, as the estimated FWHM of the Mn Kα peak, is both a function of the detector and certain acquisition parameters. The energy resolution should not be a function of the specimen, but as it is calculated with Equation (2.13), the outputted number depends somewhat on the peaks in the spectrum. This is shown in Table 4.2, where the highest and lowest estimated energy resolution is 123 eV and 135 in the GaAs spectrum, and 121 eV and 133 eV in the GaSb spectrum. The energy resolutions, calculated through HyperSpy, are listed for all spectra in Table 4.3, with the relevant acquisition parameters. In the GaSb spectra the best energy resolution was 124 eV, obtained with PT 6, ICR = 22k cps, $E_0 = 15$ kV, and $i_b = 200$ pA. In the GaAs spectra the best energy resolution was 127 eV, obtained with PT 6, ICR = 880 cps, $E_0 = 5$ kV, and $i_b = 25$ pA. These numbers for the energy resolution is calculated with HyperSpy, which have an issue explained in Section 2.4.3. As Table 4.3 shows, the energy resolution is affected by the two acquisition parameters: (i) process time and (ii) input count rate. The ICR change with E_0 and i_b. Specifying a single energy resolution for the detector should be accompanied by the acquisition parameters used to obtain that energy resolution. Preferably, the value should also be an average with an uncertainty, calculated by several measurements with equal acquisition parameters. This is not done here, but the values in Table 4.3 show that PT 6 give the best energy resolution at about 127 ± 2 eV. When Table 4.2 with the variations based on the peak of reference is taken into account, the energy resolution is more like 127 ± 6 eV.

4.2.2 Scale, offset, and peak position deviations

The energy scale and offset are the parameters which are used to calibrate the spectra. Both metrics are quite consistent between the spectra. The averaged values and the standard deviations are listed in Table 4.4. The calculated scale of the detector is equal to the instrument setting at 10 eV per channel, with very low standard deviation between the spectra at 0.04 eV/channel. The zero offset was calculated to be -0.205 keV, which is a deviation of half a channel from the instrument setting of -0.2 keV. The standard deviation of the offset is 0.004 keV.

No significant deviations in peak positions were observed. The maximum deviation was 2 eV, and the minimum deviation was -2 eV, which is very low compared to the energy of the lines which are > 1 keV and the FWHM of the peaks in the 100 eV range.

4.2.3 Peak ratios

The results from the peak ratios are listed in Table 4.5. The peak ratios are useful to alert carbon contamination over time, and to identify and quantify stray radiation with certain sample geometry. As the results are neither a series over time nor taken with the required sample geometry, the results in the table are a demonstration of the metric without any further interpretation. However, the Ga Kα/Lα ratio can be used as an indicator for absorption, when comparing different specimens. Peak ratios are also used for quantification, but needs bulk corrections. The table show that some peak ratios vary greatly with the acquisition parameters, e.g. the ratio between Ga Lα and Sb Lα.

Table 4.3: The energy resolutions in eV in the different spectra. The table is sorted by increasing energy resolution. All energy resolutions are calculated with Equation (2.13) through HyperSpy.

Specimen	PT	E_0	i_b	ICR	Energy resolution
		[kV]	*[pA]*	*[k counts]*	*[eV]*
	6	15	200	22	124
	6	15	50	5.7	125
	6	15	400	42	125
	6	30	50	17	127
	6	10	50	2.3	127
GaSb	6	5	50	1.1	128
	4	30	50	17	132
	2	30	50	17	143
	1	30	400	160	158
	1	30	50	17	158
	6	5	25	0.9	127
	6	10	25	1.8	127
GaAs	6	30	25	8.0	128
	6	30	50	16.4	129
	6	15	25	3.3	129

Table 4.4: The scale and offset in the spectra.

Samples	Scale, average	Scale, std	Offset, average	Offset, std
	[keV/channel]	*[keV/channel]*	*[keV]*	*[keV]*
Instrument setting	0.010000	-	-0.2000	-
GaSb	0.010001	8.7E-06	-0.2044	4.4E-03
GaAs	0.010018	6.6E-05	-0.2075	4.9E-03
GaSb + GaAs	0.010007	3.8E-05	-0.2054	4.3E-03

Table 4.5: Peak ratios calculated. The values vary with the beam energy, and thus the beam energies are grouped, and an average is given with the corresponding standard deviation.

Peaks	E_0	Peak ratio	STD	Comment
Sb Lα / Sb Lβ_1	All	2.34	0	Equal for all 11 GaSb spectra
Ga Lα / Sb Lα	5 kV	33.31	-	1 GaSb spectrum
"	10 kV	1.73	-	1 GaSb spectra
"	15 kV	0.76	0.008	3 GaSb spectra
"	30 kV	0.21	0.004	6 GaSb spectra
Ga Kα / Ga Lα	15 kV	0.19	0.0005	3 GaSb spectra
"	15 kV	0.07	-	1 GaAs spectrum
"	30 kV	2.61	0.06	6 GaSb spectra
"	30 kV	0.90	0.005	2 GaAs spectra

4.2.4 Process time

One of the acquisition parameters which was tested was the process time. The process time is a trade-off between the energy resolution and the throughput. This effect is illustrated in Figure 4.4, which is a plot of the GaSb spectrum at minimum and maximum process time, where the PT 1 spectrum was acquired faster due to low DT. Both spectra are recorded at 30 kV with 50 pA. The figure have three panels, (a) for low, (b) for medium, and (c) for high energy X-rays. The effect of the lowered energy resolution is most prominent for the low energy X-rays. The difference between the observable center of the peaks and the theoretical line energies in panel (a) is due to the poorer calibration at sub 1 keV energies. In panel (a), the Sb Mζ and O Kα are merged together with PT 1, but are separated with PT 6. The ability to separate peaks is the definition of energy resolution, thus panel (a) is a good illustration of different energy resolutions. The Ga Ll and Ga Lα peaks are separated with PT 6, but are merged together with PT 1. With PT 4 (not shown), the Ga Ll and Ga Lα peaks still separated, but with PT 2 (not shown) they are merged together. Table 4.3 show that the energy resolution with PT 1 is 158 eV, and with PT 6 it is 127 eV. In panel (b) with the medium energies, the contrast of the peaks are lowered, i.e. the difference between the top of the peaks and the valley between the peaks are lowered. The effect of the lowered energy resolution is not as prominent panel (c) for high energy X-rays.

The effect of the process time on the FWHM of the lines is shown in Table 4.6. The table shows the measured FWHM of Ga Lα, Sb Lα, and Ga Kα for different process times. The measurement is done on the Gaussian fit of the peaks. Additionally, the FWHM of the Mn Kα is estimated for each process time. The table shows the variations on the GaSb specimen with PT 1, 2, 4, and 6. The last row shows the FWHM in the GaAs specimen at

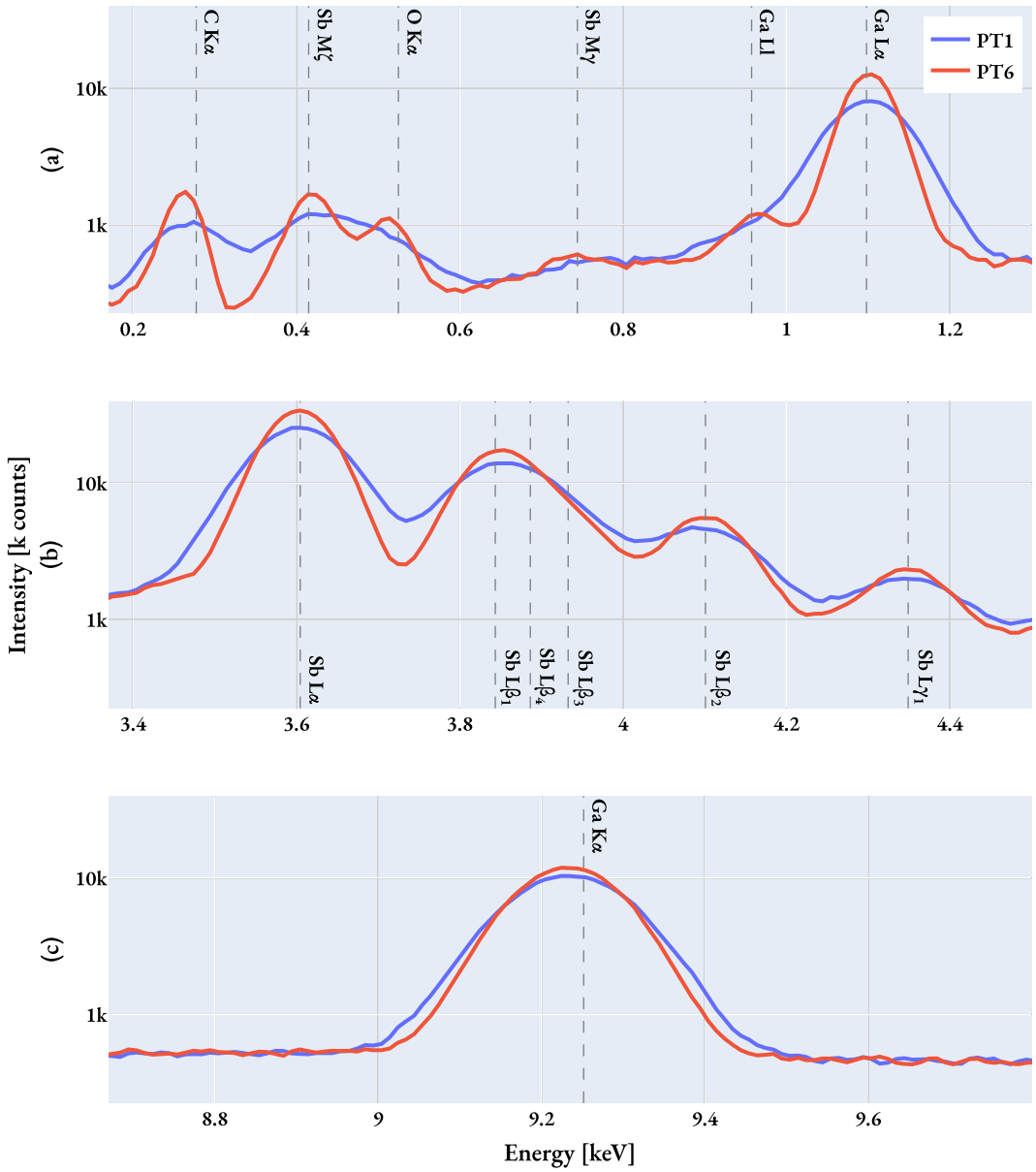

Figure 4.4: Different energy resolutions on the same specimen, because of different process times. The maximum (red) and minimum (blue) PT on the instrument is used. $E_0 = 30$ kV, $i_b = 50$ pA for both spectra. The PT 1 and PT 4 spectra are not shown, but are in between the PT 2 and PT 6 spectra. Panel (a) is the spectrum at low energy, where the effect most influential. With PT 1 the Sb Mζ and O Kα peak are merged, and the Ga Ll and Ga Lα peaks are merged. Panel (b) is the spectrum at medium energy, where the effect less influential, but the peak contrast is lowered. Panel (c) is the spectrum at high energy, where the effect is almost negligible. All three panels span 1.13 keV and have the same range of counts. The vertical dashed lines are the theoretical line energies.

PT 6 for reference. All spectra in the table were acquired at 30 kV and 50 pA. In the GaSb spectra, the PT 1 has DT 4%, PT 2 has DT 7%, PT 4 has DT 13%, and PT 6 has DT 44%. The GaAs spectrum with PT 6 has DT 44%.

Table 4.6: FWHMs of lines with different process times. All the FWHMs are in eV, calculated from the Gaussian fit. All spectra are acquired at 30 kV and 50 pA. The first four PT columns are from the GaSb specimen.

Line	PT 1	PT 2	PT 4	PT 6	PT 6, GaAs
Ga Lα	109	88	73	65	67
Sb Lα	138	122	108	102	-
Mn Kα (est.)	158	143	132	127	129
Ga Kα	182	172	165	161	163

4.2.5 Beam energy and beam current

The energy and the amount of electrons in the probe is important for the emerging X-ray spectrum. Using a low overvoltage can be problematic. The green 10 kV line in Figure 4.2 has no visible signal from the Ga Kα peak, where the overvoltage is around 1.1. The overvoltage is also an issue for the Sb L-lines in the 5 kV spectrum in Figure 4.3. The Sb L-peaks are present, but weak, and the Ll peak is not visible. This issue with the weak Sb-L peaks makes the quantification of Sb difficult at low voltages, as seen further down in Section 4.3.1. The 5 kV GaAs spectrum is quantified more accurately than the 5 kV GaSb spectrum. In the voltage series, which are group (A) and (B) in Section 3.3, the amount of counts in the lower voltages are quite low. The low amount of counts is due to keeping the beam current constant at 50 and 25 pA. Using a higher beam current on the lower energies would have made normalization more necessary, which is adding a layer of subjective decisions as the spectra must be normalized to something. Even though the 30 kV spectra in GaAs and GaSb have more counts and are smoother than the other spectra, they both have more artifacts.

As the 30 and 15 kV spectra gave better results for GaSb, they were chosen for group (C) and (D). In (C) different process times were tested, and these results are presented in Section 4.2.4. In (D) different beam currents were tested, while also changing the PT and E_0. The combination of high i_b and high PT in two of the spectra in (D) made the DT very high. Despite the high DT, the amount of artifacts in the 200 pA and 400 pA spectra were similar to the 50 pA spectra. However, with DT at 53% and 77%, the acquisition time was very long. On the quantification presented in Section 4.3.1, the beam energy appears to be more important than the beam current.

4.2.6 Duane-Hunt limit

The Duane-Hunt limits, or the effective beam energies, are presented in Table 4.7. The table shows the Duane-Hunt limit for the 5, 10, and 15 kV spectra. As the energy range recorded in the spectra were $0 - 20$ keV, the Duane-Hunt limit of the 30 kV spectra were not possible to calculate. All the calculated Duane-Hunt limits are

within 0.2 keV of the nominal beam energy, i.e. the specified beam energy in the SEM software. The average deviation is 0.06 keV, with a standard deviation of 0.04 keV. This shows that the beam energy is quite stable.

4.2.7 Fiori P/B ratio

The Fiori numbers are presented in Table 4.8, with the Fiori P/B ratio in the five rightmost columns. The ratios are for the Ga Lα, Ga Kα, As Lα, Sb Lα, and Sb Lβ. The Fiori P/B ratios have a spread between just below 100 to right under 800. The overall highest ratio is for the Ga Kα peak in the 30 kV 25 pA GaAs spectrum, with a ratio of 770. The equal settings in the GaSb spectrum have a ratio of 408 for the Ga Kα peak. For the Ga Kα peaks, the GaAs spectrum have almost twice as high Fiori P/B ratios as the GaSb spectrum. The Ga Lα peak is present in all the spectra, and it can be used for comparison. The tabulated data indicate that E_0 has the largest impact on the Fiori P/B ratio. For the Ga Lα peak, the Fiori P/B ratios is up to 6 times higher for GaAs than GaSb. This shows clearly that the Fiori P/B ratio is specimen dependent, even when using the same peak and setting.

Table 4.7: The Duane-Hunt limit in the sub 30 kV spectra. All spectra are acquired with PT 6.

Group	**Specimen**	E_0	i_b	**Duane-Hunt limit**
		[kV]	*[pA]*	*[kV]*
A	GaAs	5	25	4.92
A	GaAs	10	25	10.08
A	GaAs	15	25	14.98
B	GaSb	5	50	4.86
B	GaSb	10	50	10.05
B	GaSb	15	50	14.99
D	GaSb	15	200	15.03
D	GaSb	15	400	15.1

Table 4.8: The Fiori P/B ratios. Group A is GaAs, which is sorted by the Ga Lα ratio. Group B, C, and D is GaSb, which is sorted by the Sb Lα ratio. The "-" indicates that the line is not present in the spectrum.

Group	E_0 *[kV]*	i_b *[pA]*	**PT**	**Fiori P/B Ga Lα**	**Fiori P/B Ga Kα**	**Fiori P/B As Lα**	**Fiori P/B Sb Lα**	**Fiori P/B Sb Lβ**
A	30	50	6	586	762	236	-	-
A	30	25	6	573	770	233	-	-
A	15	25	6	414	187	250	-	-
A	10	25	6	280	-	206	-	-
A	5	25	6	155	-	140	-	-
C	30	50	4	87	407	-	386	169
C	30	50	2	84	414	-	386	169
C	30	50	1	83	414	-	386	168
B	30	50	6	86	408	-	385	168
D	30	400	1	86	320	-	360	156
B	15	50	6	110	138	-	215	97
D	15	200	6	109	131	-	214	97
D	15	400	6	107	124	-	211	95
B	10	50	6	113	9	-	140	65
B	5	50	6	91	-	-	16	5

4.2.8 Summarization of the performance parameters

This last section in the performance parameters contains a summarization of the parameters for the detector and the acquisition parameters. Table 4.9 gives the values for the parameters with a comment. The energy resolution of the detector used in this work is 127 ± 6 eV at ICR between 1 k and 42 k cps, with the highest PT available. The energy axis of the instrument is calibrated well, with low deviations between the specified scale and offset, and their calibrated values. This is strengthened by the low deviation in calibrated peak positions. The Duane-Hunt limits are all close to the nominal beam energy. The Fiori P/B ratios acquired were at the highest 770 for GaAs and 410 for GaSb.

Table 4.9: A summary of the performance parameter results.

Parameter	Value	Comment
Duane-Hunt limit	E_0 ± 0.2 keV	For the detector. Average deviation was 0.06 ± 0.04 keV, but the value specified include the maximum deviations.
Energy resolution	127 ± 6 eV	Parameter for the detector, but highly dependent on PT. Recorded at the highest PT on GaAs and GaSb. The variation is from different reference peaks in the calculation and different E_0 and i_b.
Scale	10.007 ± 0.038 eV	For the detector. The scale of the GaAs spectra varied slightly more than the GaSb spectra.
Offset	−0.205 ± 0.004 keV	For the detector.
Deviations in peak positions	0 − 2 eV	For the detector.
Fiori P/B ratio	770 for Ga Kα in GaAs	For the detector, acquisition parameters and specimen dependent. The value is the highest achieved.
Fiori P/B ratio	410 for Ga Kα in GaSb	"
Peak ratios	GaSb > GaAs and $\propto E_0$	Varying with acquisition parameters and specimen.
Beam energy	15 kV or 30 kV	Best results were acquired with higher beam energy.
Beam current	Not a specific number	Dependent on E_0, and needs to give enough counts.
Process time	Not a number	Should be high, but the highest give long acquisition time.

4.3 Quantitative analysis

This section presents the results from the quantitative analysis, using different correction methods. With 15 spectra analyzed, the tables are large and thus average values from different methods are used to give an overview of the results. The results from all 15 spectra in the initial quantification are shown in Section 4.3.1. For this and the remaining methods, a table with the average values, deviations above 10 at.%, and deviations below 5 at.% are shown. The 5 kV GaSb spectrum is excluded from these average tables, as the spectrum had several issues. The full tables with quantification using the thin film assumption, the ZAF absorption correction, and corrections with PAP are given in Appendix B.

4.3.1 Initial quantification

Initial quantification was done with the AZtec software and with the uncorrected intensity ratio method. The intensity ratio method is calculated with Equation (2.17), and it gives relative compositions as described in Section 2.5.1. AZtec too gives relative compositions, based on the elements confirmed to be present in the spectrum. Average values for the initial quantification results are shown in Table 4.10. Results from all the 15 spectra are shown in Table 4.11, and plotted in Figure 4.5. As the table and figure show, some results are close to 50 at.%. The summary table also show that on average GaSb is quantified closer to 50 at.% than GaAs. All AZtec results are with the SEM EDS setting, if not stated otherwise. In 12 of the 15 spectra, AZtec gives a result at 50 ± 2 at.%. 2 of spectra are quantified at 50 ± 4 at.%. The 5 kV GaSb spectrum is quantified at 39:61, which is the most deviating result from AZtec. The 5 intensity ratios from GaSb spectra with $E_0 = 30$ kV are at 50 ± 2 at.%. The three 15 kV results from GaSb have a deviation of ±10 at.%, which show the need for closer inspection. The remaining results are also in need of closer inspections, as the results from the uncorrected intensity ratio method give high deviations.

Table 4.10: Numbers for the at.% deviations from 50 : 50 in the initial quantification, see Table 4.11 The GaSb 5 kV spectrum is excluded from the numbers, as it is viewed as an outlier. The table gives the average deviation in at.% from 50 at.%, for GaAs and GaSb separated. The number of deviations below 5 at.% and above 10 at.% are also tabulated.

Specimen	Number	AZtec	Intensity ratio
GaAs	Average deviation, at.%	2 at.%	12 at.%
	Deviations > 10 at.%	0	4
	Deviations < 5 at.%	5	0
GaSb	Average deviation, at.%	1 at.%	6 at.%
	Deviations > 10 at.%	0	1
	Deviations < 5 at.%	9	5

Table 4.11: Initial quantification in selected spectra. Compositions from AZtec and the intensity ratio method. The table is summarized in Table 4.10. Each spectrum has two lines in the table, one for each element.

Group	Line	E_0	i_b	PT	Intensity	AZtec comp.	Intensity ratio comp.
		[kV]	*[pA]*		*[k counts]*	*at.%*	*at.%*
A	As Lα	5	25	6	13	53	43
A	Ga Lα	5	25	6	16	47	57
A	As Lα	10	25	6	37	52	40
A	Ga Lα	10	25	6	51	48	60
A	As Lα	15	25	6	62	51	36
A	Ga Lα	15	25	6	103	49	64
A	As Kα	30	25	6	84	48	36
A	Ga Kα	30	25	6	141	52	64
A	As Kα	30	50	6	180	48	36
A	Ga Kα	30	50	6	303	52	64
B	Ga Lα	5	50	6	19	39	97
B	Sb Lα	5	50	6	1	61	3
B	Ga Lα	10	50	6	46	47	75
B	Sb Lα	10	50	6	27	53	25
B	Ga Lα	15	50	6	74	49	58
B	Sb Lα	15	50	6	94	51	42
B	Ga Kα	30	50	6	191	50	48
B	Sb Lα	30	50	6	359	50	52
C	Ga Kα	30	50	4	189	50	48
C	Sb Lα	30	50	4	350	50	52
C	Ga Kα	30	50	2	184	50	49
C	Sb Lα	30	50	2	330	50	51
C	Ga Kα	30	50	1	178	50	51
C	Sb Lα	30	50	1	304	50	49
D	Ga Lα	15	200	6	155	49	57
D	Sb Lα	15	200	6	200	51	43
D	Ga Lα	15	400	6	284	49	57
D	Sb Lα	15	400	6	367	51	43
D	Ga Kα	30	400	1	1724	50	50
D	Sb Lα	30	400	1	2996	50	50

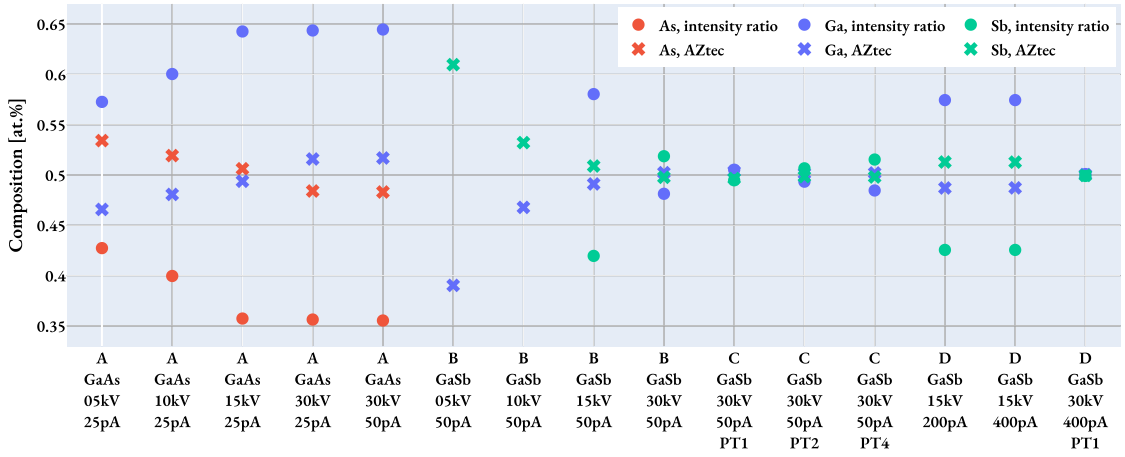

Figure 4.5: Initial quantification results in at.%. The X markers are the quantification from AZtec. The circle markers are the quantification from the intensity ratio, without corrections. The group, specimen, E_0, i_b, and PT are shown on the x-axis. The spectra without noted PT are taken with PT 6. The same data is tabulated in Table 4.11.

4.3.2 Quantification of SEM EDS data with the thin film approximation

Quantitative analysis of the SEM EDS bulk spectra was also done under the presumption that the specimen was a TEM specimen, i.e. under the thin film approximation. The thin film approximation assumes no absorption of the created X-rays in the specimen, and is a part of the Cliff-Lorimer (CL) method covered in Section 2.5.1. The presumption that the specimen is a TEM specimen was both applied in AZtec with the "TEM setting", and in HyperSpy with the CL method. TEM EDS quantification of SEM EDS data can readily be done, even though it is formally incorrect.

The results from the TEM EDS quantification routines are tabulated in Appendix B in Table B.1, and average numbers from that table is presented in Table 4.12. The calculated k-factors, which are extracted from AZtec and needed for the CL method in HyperSpy, are included in Table B.1. The CL method in HyperSpy was done with and without the TEM absorption corrections, which is a part of the implemented CL quantification function. The "CL*" column is without absorption corrections, and the other "CL" columns are with the TEM absorption corrections, where the t is the set specimen thickness. Six t values are: 50 nm, 100 nm, 200 nm, 400 nm, 1000 nm, and 10000 nm.

The GaSb spectrum at 5 kV is poorly quantified by AZtec. AZtec is quantifying the 5 kV GaSb spectrum with the Ga Lα and Sb Mζ peaks. Sb Mζ is around 0.4 keV, and at such low energy the matrix absorption is high, and the resulting composition is 91 : 9. The Sb Mζ peak is not available in HyperSpy, and no k-factor is given for the Sb Lα line in this spectrum. Thus, it is not possible to quantify the 5 kV GaSb spectrum with HyperSpy.

The TEM EDS quantification results of the SEM EDS data are in general deviating from the reference value of 50 : 50. Opposite to the SEM EDS quantification setting in AZtec, the GaAs spectra are quantified closer to

the reference value than the GaSb spectra. The "TEM EDS setting" AZtec results are deviating much more from 50 : 50 compared to the AZtec results using the "SEM EDS setting", presented in Section 4.3.1. The CL quantification without absorption corrections perform similar to AZtec, and the deviations are improved for the CL quantifications with absorption corrections, where t is set to 50, 100, 200, and 400 nm. The CL quantification with t is set to 200 nm gives better results than the uncorrected intensity ratio method, but still at an average deviation of 5 at.% from the reference value for GaAs and GaSb. When t is set to 1000 nm, the average deviations increase from 400 nm, and 4 of the GaSb spectra are quantified at > 10 at.% deviation, illustrating some issue with high t. The deviations are increased further when t is set to 10000 nm.

Table 4.12: Numbers for the at.% deviations from 50 : 50 with the thin film assumption, i.e. the TEM quantification routines. The table is a summary of Table B.1. The AZtec result is from the "TEM EDS setting", and the CL results are from the Cliff-Lorimer method in HyperSpy. CL* is without corrections, the others CL have absorption correction with input thicknesses t, in nm.

Specimen	**Number**	**AZtec** *TEM*	**CL***	**CL** *t=50*	**CL** *t=100*	**CL** *t=200*	**CL** *t=400*	**CL** *t=1k*	**CL** *t=10k*
GaAs	Average deviation, at.%	8 at.%	9 at.%	8 at.%	7 at.%	5 at.%	5 at.%	7 at.%	6 at.%
	Deviations > 10 at.%	1	1	1	0	0	0	0	2
	Deviations < 5 at.%	1	1	1	1	2	3	1	2
GaSb	Average deviation, at.%	11 at.%	9 at.%	8 at.%	7 at.%	5 at.%	7 at.%	11 at.%	21 at.%
	Deviations > 10 at.%	3	3	0	0	1	1	4	9
	Deviations < 5 at.%	0	1	0	0	3	1	5	0

4.3.3 ZAF absorption corrections

The ZAF absorption corrections were done with Equation (2.25). The calculated maximum electron range r is presented in Table B.2. To calculate the absorption correction factors, r is divided by 2, 3, and 4 to get different approximations for the average depth of origin of the X-rays. The calculated ZAF absorption correction factors are given in Table B.3, which are applied to get compositions in Table B.4, which are presented with average numbers in Table 4.13.

The ZAF absorption corrections improve the GaAs quantification, but deviations from 50 at.% in the GaSb quantification is increased. For GaAs, the best result is achieved when the maximum electron range is divided by 4, i.e. the absorption correction is applied to an average point close to the surface. When r is divided by four, the average deviation is improved from 12 at.% to 7 at.%, compared to the uncorrected intensity ratio method. With $r/4$, the number of spectra with > 10 at.% deviation is reduced from 4 to 2, and the number of spectra with < 5 at.% deviation is increased from 0 to 3. For GaSb, the average deviation decrease when r is divided by a higher number, but the deviations are > 20 at.% anyway, which is quite poor.

Table 4.13: Numbers for the at.% deviations from 50 : 50 in the ZAF absorption corrections, in Table B.4. The table gives the average and the number of deviations below 5 at.% and above 10 at.% are counted, for GaAs and GaSb separated.

Specimen	Numbers	Uncorr.	ZAF A, r/2	ZAF A, r/3	ZAF A, r/4
GaAs	Average deviation, at.%	12 at.%	11 at.%	8 at.%	7 at.%
	Deviations > 10 at.%	4	3	2	2
	Deviations < 5 at.%	0	1	2	3
GaSb	Average deviation, at.%	6 at.%	30 at.%	25 at.%	21 at.%
	Deviations > 10 at.%	1	9	9	6
	Deviations < 5 at.%	5	0	0	0

4.3.4 XPP corrections

The XPP corrections were done in two ways, where the measured intensity of a peak I_A is divided by the calculated generated intensity of the peak F, or by the calculated XPP absorption correction factor $f(\chi)$. Both ways are presented in Table B.5, where the uncorrected compositions are included for comparison. Average numbers for the XPP corrections are given in Table 4.14. F and $f(\chi)$ are calculated with the XPP notebook, and are dependent on E_0, E_C of the line, and the elements with their weight fraction of the elements. The elements and their weight fractions are used to calculate the density ρ, the mean atomic mass M, the mean ionization potential J, the mean atomic number $\bar{Z}$, the backscattering coefficient R, and μ_ρ of the line at E_0. The weight fractions used in the calculations are set to the equivalent of a 50 : 50 atomic percent composition, as this should give the best possible correction factors. A finished product for XPP bulk corrections should have iterative calculations of the weight fractions, but these results are aiming to demonstrate the possible usefulness of XPP corrections, thus the best

available input parameters are used.

The corrections with $f(\chi)$, i.e. the absorption correction, improves the GaAs quantification. Similar to the ZAF absorption corrections, the GaSb quantification is not improved when corrected with $f(\chi)$. The absorption correction with XPP reduce the average deviation in GaAs from 12 at.% to 5 at.%, which is better than the ZAF absorption correction.

When GaSb is corrected with F, the average is unchanged. However, in the uncorrected quantification, the 30 kV GaSb spectra are quantified very close to the reference value, and the F correction makes these 30 kV spectra deviate more. The quantification of the 15 kV and 10 kV GaSb spectra are improved with the F correction, which is why the average is unchanged. In the 30 kV spectra, the Ga line is given a weight which increase its composition relative to the Sb line, while the opposite is done in the 15 kV and 10 kV spectra. The XPP corrections are dependent on the beam energy, making the effect at 30 kV different from the effect at 15 kV and 10 kV.

Table 4.14: Numbers for the XPP corrected compositions listed in Table B.5. The XPP corrections are done in two ways. The uncorrected intensity ratio results are listed for reference. $f(\chi)$ the absorption correction, and F is the generated amount of X-rays, i.e. Z corrections. $f(\chi)$ is defined in Equation (2.47), and F is defined in Equation (2.29).

Specimen	**Number**	**Uncorr.**	**XPP corr.** $(I_A/f(\chi))$	**XPP corr.** (I_A/F)
GaAs	Average deviation, at.%	12 at.%	5 at.%	11 at.%
	Deviations > 10 at.%	4	0	3
	Deviations < 5 at.%	0	2	0
GaSb	Average deviation, at.%	6 at.%	38 at.%	6 at.%
	Deviations > 10 at.%	1	9	1
	Deviations < 5 at.%	5	0	3

4.3.5 Summary of the quantification results

The results presented in this section show quantification from: AZtec, uncorrected intensities, ZAF absorption corrections, and two XPP corrections. With 50 : 50 atomic weight as the reference goal, the results from AZtec are the closest. The corrections applied to the intensities push the results both towards and away from the reference value, depending on the specimen and the beam energy. The GaAs spectra are quantified closer to the reference value when corrected with absorption corrections, and correction with $f(\chi)$ from the XPP model gave an average deviation of 5 at.%. The GaSb spectra are quantified closer to the reference value when corrected with F from the XPP model, with an average deviation of 6 at.%.

Chapter 5

Discussion

The discussion chapter connects the results to the theory, with focus on the aims of this work. The overall aim is to improve the performance of SEM EDS, which is split in two parts: (1) to investigate performance parameters for the SEM EDS setup and the acquisition parameters, (2) to investigate bulk corrections for the quantification with open-source code. A good EDS analysis requires a well functioning setup, adequate acquisition parameters, and high quality data processing routines. The performance parameter part try to find possible test metrics, describe them thoroughly in the theory chapter, and implement the metrics in code. The focus for the data treatment has been to implement SEM EDS bulk corrections in open-source Python code, as this is not available in the community at the time of writing. Different approaches to the bulk corrections have been tested and are discussed in this chapter. This chapter is built up as the results chapter, i.e. first an initial qualitative analysis of the data, then the performance parameters, and finally the bulk corrections.

5.1 Qualitative analysis

The overview spectra of GaAs and GaSb in Figure 4.1 and the voltage series in Figures 4.2 and 4.3 show that the acquired data is of varying quality. Assessing the use of performance parameters on spectra of varying quality is important, as the performance parameters should be able to distinguish different quality spectra, and thus it was necessary to acquire spectra of varying quality. The spectrum quality is affected by the beam energy and the amount of counts, which is revealed by looking at group (A) and (B), being the voltage series of GaAs and GaSb. The 30 kV and 15 kV spectra are in general of good quality with high counts, low noise levels, and clear peaks. The spectra with high amount of counts have lower relative variations in the counts, seen as a more even plot of the blue 400 pA PT 1 spectrum compared to the 50 pA PT 1 spectrum in panel (a) of Figure 4.1. However, the amount of artifacts also increases with the amount of counts, exemplified by this spectrum with the highest amount of counts. An increase amount of artifacts, e.g. the internal Si fluorescence peak, is also observed in the 30 kV spectra, compared to the other voltages in (A) and (B). This increase can be due to the higher count rate in the 30 kV spectra. The 10 kV and 5 kV spectra have lower counts, as the beam current was kept constant in the voltage series. The lower counts

were expected, and as seen in the voltage series figures, the 10 kV and 5 kV plots are visually of poorer quality. With visually poorer quality, such as more noise and less clear peaks, the metrics and the quantification were expected to be worse. In general the 5 kV and 10 kV spectra performed worse than the 15 kV and 30 kV spectra, which is discussed more in Section 5.2. As the 15 kV and 30 kV spectra performed better, these voltages were chosen for group C and D, where the goal was to investigate the effect of the beam current, beam energy, and process time. These spectra all are assumed to have enough counts to be reasonably assessed with the metrics.

Qualitative analysis of EDS spectra are influenced by the choice of scale, i.e. linear or log scale. AZtec has a default setting of a linear scale, with the option of a log scale. The log scale is used in most plots in this work, as it highlights disturbances and makes the spectrum faster to assess. This is especially true when a specimen contains trace elements, as the low peaks from the trace elements are more visible in the log scale. The linear scale emphasizes the high peaks, making artifacts and disturbances less visible. The coincidence peaks from the Sb L peaks visible in panel (a) of Figure 4.1 would be invisible in a linear scale, but the presence of coincidence counts lower the Fiori P/B metrics, tabulated in Table 4.8. The lower Fiori P/B ratio implies a poorer quality, as it is fewer counts in the Sb Lα peak than it should be, and this could lead to a higher deviation in the quantification. For GaSb spectra taken at 30 kV, the Fiori P/B ratio is similar at PT 1 and PT 6 with 50 pA beam current, and both these spectra have little coincidence counts. In the 30 kV, 50 pA and PT 1 spectrum, where the coincidence rate is high, the Fiori P/B ratio is lower for Ga Kα, Sb Lα, and Sb Lβ. In the same spectrum, the amount of coincidence counts from Ga Lα does not increase, and this Fiori P/B ratio is similar to the other 30 kV spectra. The log scale reveals the coincidence peaks in the visualization, which is the source of the lower Fiori P/B ratio.

Another difference in the voltage series which would be visually hidden by a linear scale is the relative amount of counts in the background versus the peaks. Below 2 keV the difference between the 30 kV and 15 kV spectra is small, but at increasing X-ray energy the 30 kV spectra have higher relative peak-to-background counts than the 15 kV spectra. Looking at the difference between the Sb Lα peak in the 30 kV and 15 kV spectra, which does not have an overvoltage issue, the background increase with a factor of around 2.5, while the peak increase with a factor of around 4. The Fiori P/B ratios for the voltage series support this, as the general rule seems to be that a lower beam energy gives a lower Fiori P/B ratio. The trend of increasing Fiori ratio with increasing E_0 is mentioned Williams and Carter [3, p. 614] for TEM EDS, and is also observed in the SEM EDS data acquired. It is not mentioned why it increases with E_0, only that higher ratios are better. However, this E_0 trend observed is not valid for all peaks, as seen on Ga Lα in the GaSb spectra, where the value is 86, 110, 113, and 91 for 30, 15, 10, and 5 kV respectively, all with 50 pA and PT 6.

As mentioned in Table 4.1, the artifacts annotated as "Coincidence 1" in Figure 4.1 are at the same energy as possible Si escape peaks from Ga Kα. The discussion done for the coincidence peaks is equally valid if the signal has contributions from Si escape peaks. However, the absorption probability in Si is greatest at around 2 keV, which is right above the Si K absorption edge, and because of this the ASTM 1508 state that the Si escape peak is negligible from about 8 keV [42, 8.3.2]. Additionally, the coincidence peaks marked "Coincidence 1" are quite similar to "Coincidence 2" and "Coincidence 3", which support that the peaks are coincidence peaks and not Si escape peaks.

Using a linear scale would hide artifacts like these, and it would be harder to assess which acquisition parameters give satisfactory low amounts of artifacts. Another artifact that would be difficult to assess on a linear scale is the background. In general, when assessing the quality of a spectrum, the log scale is therefore preferred.

5.1.1 Artifacts

The artifacts discovered are listed in Table 4.1, and are described in Section 2.3.3. The noise peak around 0 keV is present in all spectra, and is caused by the detector. Before the model fitting the spectra were sliced after the noise peak to avoid bad fitting. The fitting in HyperSpy is done with a polynomial background and Gaussian peaks for the lines present in the selected elements. If too many elements are selected, e.g. adding Si because of a small Si peak, the fitted peak of the non-present element will usually have around zero intensity. However, getting negative intensities is mathematically possible, and can occur with the model fitting in HyperSpy, which a user should be aware of. Having peaks present in the spectrum which are not added in the model will yield a worse background fit, as the background polynomial then will compensate for the peak. One weakness of how the model fitting was done in this project, was that the spectra was sliced off around 0.2 keV, which removed the noise peak, but did not remove the low energy peaks of no interest, e.g. the C Kα peak and O Kα peak. The HyperSpy model fitting was given either Ga and As, or Ga and Sb as the elements to fit, and the C and O peaks were not included in the model fitting. Fitting with C and O was experimented with, but it did not give a significantly better fit, as the C and O peaks have low intensity. Additionally, the GaSb spectra have some low energy Sb M-lines which are not included in HyperSpy, and thus does not have a Gaussian peak fitted to them. The model fitting done in this work was inspected visually, and the fit was considered to be good enough. However, the fit might have been slightly better if the background fit was not affected by the low energy peaks of no interest. The first peak of interest in this work, regarding the quantification, is the Ga Lα peak at 1.1 keV. Thus, a better choice might have been to slice the spectra at e.g. 0.6 keV, to avoid the noise peak and the low energy peaks of no interest, and still have background to fit to before the Ga Lα peak.

All the spectra were acquired over $0 - 20$ keV, and thus the 5 kV, 10 kV, and 15 kV spectra had to be sliced at both ends. Figures 4.2 and 4.3, the voltage series, show some tailing background counts, i.e. coincidence counts above E_0. When using model fitting in HyperSpy, the background is fitted with a polynomial, and polynomials does not have an end. The fitting of the background is done from zero energy to E_0, which is available in the metadata of the spectrum. The energies above E_0 are not included in the model fitting, but the polynomial is not cut off at E_0. In other words, fitting a 15 kV spectrum recorded on a $0 - 20$ keV range gives nonphysical results above 15 keV, as the background is extrapolated without any restrictions. This is illustrated in Figure 5.1, where the data is plotted with black dots, the fit on the whole energy range is the red line, and the fit sliced at 0.2 keV to 15 keV is the green line. The red line is nonphysical, with an exponential increase of the background above E_0. Visual inspections of the model fit reveals the error easily. Slicing the spectrum correctly prevents extrapolation like this, and will even give slightly better fits. Using the Duane-Hunt limit, discussed in Section 5.2.6 as the upper limit, can be useful if the specimen is charging, as the effective beam energy then is lower than the set beam energy. Calculating the Duane-Hunt limit is also important for the fitting in HyperSpy, as the E_0 in the metadata is used to specify which lines

are present in the spectrum. For example, the 5 kV spectra models does not have the Ga K lines. If the metadata is incorrect, the model fitting will yield incorrect results. Proper input data for the fitting, i.e. the correct E_0 and the correct elements, as well as the relevant spectrum data points, is important to get the best possible model fit.

Similar absorption edge effects as observed in [36] are present in the acquired spectra, where strong absorption edges at lower to medium energy influence the background intensities strongly. This is illustrated well in Figure 2.7, where the spectrum is overlaid with the mass absorption coefficient for Si. The background intensity is reduced by the absorption edge, i.e. the intensity of the background is higher before the peak than after the peak. This makes the background modelling more difficult, as the background is modelled with a polynomial function. Lower accuracy in the background modelling could lead to worse quantification, as well as incorrect metrics discussed in this work. One possible improvement to the background modelling is to use a spline function instead of a single polynomial function.

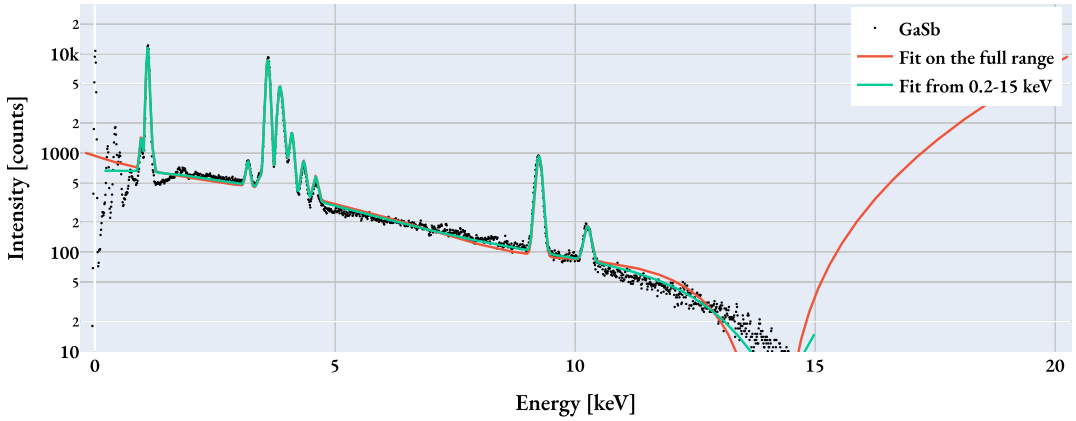

Figure 5.1: Illustration of the effect of slicing the spectra before model fitting. Correct slicing of the spectra improve the background fit, and prevents unpredictable results above the beam energy. The sliced fit is the green line, which is not perfect at the very beginning and the end, but good enough around the peaks of interest. The red line is not sliced before fitting, and it fits poorly at the beginning and very poorly at the end. Between 5 and 12.5 keV the red line is also deviating more from the data than the green line. The red line is not too bad around the peaks of interest. The black dots are the data, which are from the 15 kV 50 pA GaSb spectrum.

Some artifacts seem to be affected by the amount of counts, and other artifacts are not. As mentioned above, the coincidence events are affected by the amount of counts, giving both peaks and tailing counts. The internal fluorescence Si peak is not affected by the amount of counts as the coincidence events are, and is present at similar low relative intensities in all spectra. This Si peak is from the detector as explained in Section 2.3.1, and is expected to be present at low levels in all spectra, as SDDs have thin Si layers. The Si signal could also have some contribution from the Si wafer that the specimens are mounted on, but as the specimen wafers are 300 µm thick, the electron beam does not penetrate the wafer (in only penetrate around 5 µm at 30 kV). Additionally, any generated Si X-rays below the wafer would be absorbed by the wafer. Spectra taken on the same setup in [36] show similar relative amounts of Si on clean Al specimen stubs, illustrating that the Si signal is not from the specimen. No other peaks like Fe from the column or the detector are present in the spectra. Nor are any Ag signal present from the Ag paint

used as glue to mount the specimens. The low amount of stray signals imply that the collimator on the detector is working as intended by limiting X-rays which originate from other points than the targeted point on the specimen.

The carbon contamination gave raise to a C Kα peak, present in all spectra. The absorption is high at low X-ray energies, but the C Kα peak is present at similar relative intensities in all spectra. This C peak can both be from a contamination on the specimen, or from somewhere in the chamber, detector, or column. The most probable source is contamination on the specimen, as a post acquisition image in panel (b) of Figure 3.2, taken with the ET detector, showed darker spots on the acquired points and a darker square where the specimen was scanned. The ET detector combines SE and BSE signals, and the darker spots are therefore most likely carbon contamination on the specimen [2]. The image also have some horizontal lines, which are scanning artifacts due to improper scan settings, but these are irrelevant for the quality of the acquired spectra. The biggest dark spot, located highest, is from the 30 kV spectrum, showing that the interaction volume is larger at higher beam energies. The backscattered electrons, together with the beam electrons, are depositing C on the surface, and the backscattered electrons originates from a larger volume at higher E_0. The C signal is probably from a combination on the specimen surface, which could be plasma cleaned, and carbon present in the camber. The source of the C signal can be further investigated by looking at different specimens, and should be done when low energy lines are of interest. Additionally, at low voltages the interaction volume is smaller, and thus the surface quality is more important, i.e. being as clean as possible. As the peaks used in this work are from 1 keV and above, the signal from C is not of concern in the remainder of this work.

Another artifact observed in the spectra is the O Kα peak, which is present in the GaSb spectra, but not in the GaAs spectra. The mass absorption coefficients for GaAs is twice as high at O Kα than for GaSb, which could have been the reason for the O Kα peak not being present in the GaAs spectra, but then the same should then have been true for the C Kα peak. Thus, another explanation is needed for the absence of the O Kα peak in the GaAs spectra. It could be due to different contamination on the two specimens, where the GaSb specimen have a thicker oxide layer than the GaAs specimen. This can both be an effect of the As vs Sb, or the age of the specimens, as the GaSb specimen could have been exposed to air for a longer time than the GaAs specimen. The most probable cause is that GaSb oxidize easier that GaAs, as GaAs is quite inert and can be used as a protective layer to limit surface oxidation. As the oxygen and carbon are surface contaminants, they will not affect the generation in the bulk of Ga, As, and Sb, and the absorption from C and O can be ignored in the analysis. Another less probable explanation is that the O Kα peak is mislabeled, and is actually a Sb M-line, which is discussed in the next paragraph.

Another take-away from the qualitative analysis is that the HyperSpy database does not contain Sb M-lines. The GaSb spectra have a clear peak at what is assumed to be the Sb Mζ peak around 0.42 keV, based on the qualitative analysis AZtec, as well as the absorption edge in Sb around 0.5 keV. The energy of a line is located a few eV below the absorption edge. The online book "Practical electron microscopy" by Y. Liao [35] lists a Sb M lines at 0.733 keV, but this is only visible in the spectra as a slight increase in counts and not a real peak. The HyperSpy database and the X-ray data Booklet [28] does not list any M-lines below Z=57. A screenshot from the AZtec software, which identifies two Sb M-lines, one at 0.4 and a smaller at 0.7 keV, is shown in Figure 5.2. The screenshot is of

the spectrum with low energy resolution, and the 0.4 and 0.5 keV peak is overlapping, but the AZtec software clearly identifies the leftmost part of the merged peak as a Sb M-line. In the AZtec screenshot, the match with Te and I looks slightly better than with Sb, but the L-lines present are definitely from Sb. Using higher energy lines to confirm or reject lower energy lines are practical and safe, as an element always generate all available lines with the set beam energy. The AZtec screenshot is an indication that the peak at 0.5 keV is not a Sb M-line, but rather that the O Kα peak is labeled correctly.

The lack of the Sb M-lines in the HyperSpy database can be a source of error in the quantification, as the Sb M-lines are not included in the background modelling. A solution to this is to slice off the spectrum before fitting the background so that unavailable lines are excluded from the background modelling. This requires that the user visually inspect the lower energies thoroughly, and that the user is aware of the possibility of missing lines. Another solution is to add the Sb M-lines to the HyperSpy database, which would require more research into M-lines of elements with Z lower than 57. The use of M-lines around 0.5 keV might be limited with bulk specimen, as the absorption is high, but such lines could be useful in TEM where the absorption is lower.

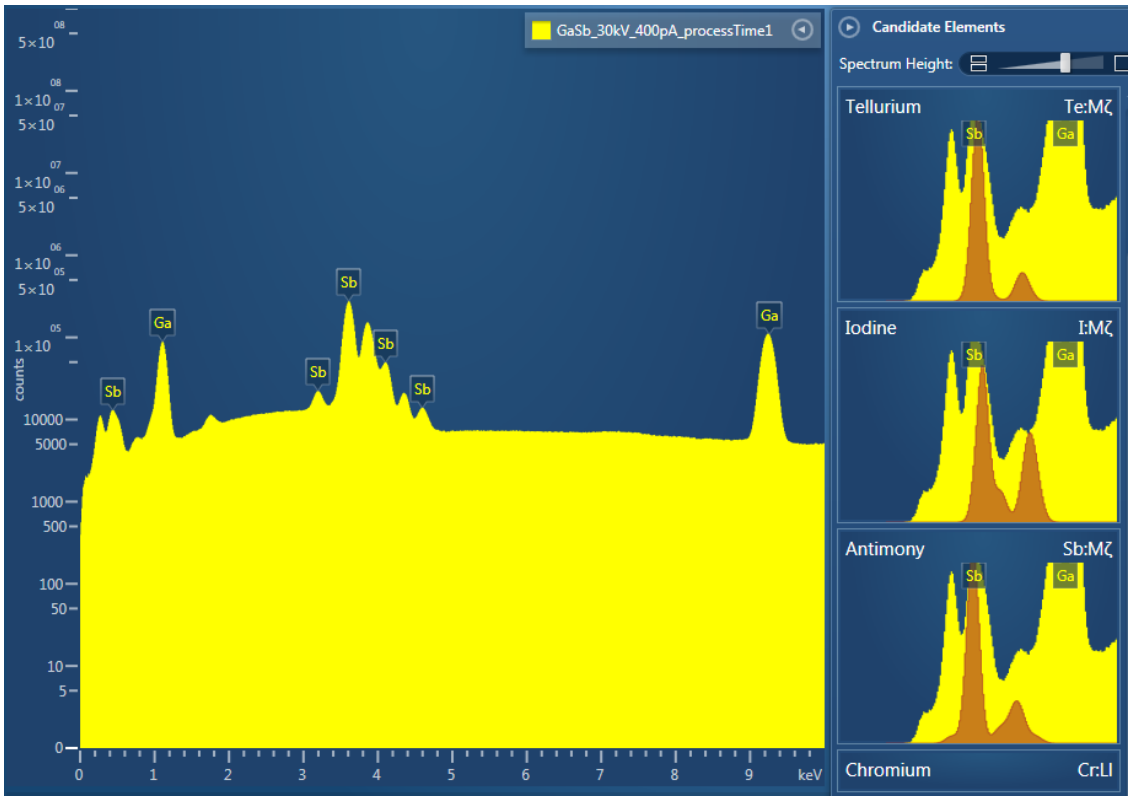

Figure 5.2: Screenshot from the AZtec software, showing the Sb M-lines identified at 0.4 and 0.7 keV. The right part of the screenshot show that Te and I match slightly better than Sb, but the L-lines present are definitely from Sb.

5.1.2 Test specimen and scratched surfaces

A complete routine for SEM EDS performance parameters should include a suggested test specimen. The test specimen must provide the relevant information in a spectrum. If a test specimen is easy to obtain and low-priced, and the corresponding test routine does not require loads of work or special software, it is plausible that more users would test their equipment regularly. Users who know their equipment well are probably capable delivering higher quality results, as they know how well their system is performing and what to do to improve it when necessary. Thus, having test routines which are both easy to perform and low-priced could improve the quality of SEM EDS results emerging from the community. Commercial test specimens and routines are available, but they are typically expensive. The aforementioned TEM EDS test specimen from Ted Pella [18], the NiO thin film, is such an example, which is based on Egerton [17]. The NiO thin film has advantages such as being a stable oxide with a single stable stoichiometry, a K-peak close to Mn Kα, and a geometry which allows extensive assessments of stray radiation. Another example, for SEM EDS, is a test specimen from the Federal Institute for Materials Research and Testing (BAM) [69], which covers the ISO 15632:2021 standard [43]. BAM are selling the test specimen for 334 EUR and a corresponding software for 335 EUR[1]. A full test in accordance with the ISO standard can be done with a cheaper sample and a Jupyter Notebook, where the user would see all the steps and the results, i.e. a transparent test routine.

A test specimen for such a routine should be a bulk specimen, as the goal is to assess a SEM setup. The specimen must provide at least one peak in the low energy (around 1 keV) region, and one peak in the medium to high energy region (around 10 keV). The spread in peaks is necessary for calibration. Testing the energy resolution at high and low energy is also recommended, at the results provided by a detector may vary. If sub 1 keV peaks are of interest, a test specimen with a peak in this region is also necessary. In the results presented in this work, the deviations in the sub 1 keV peaks are higher than for the peaks above 1 keV. The specimen should not be reactive, so that it can be used for a long time, and so that results over time can be compared. Neither should it be magnetic, as this can interfere with the electron beam and special SEM imaging modes. Using materials like a wafer is a good option, because these are reasonable priced and readily available in most laboratories. Relying on commercial vendors for test specimen can result in long waiting times, as experienced in this project. Wafers are also flat, which give the most reliable EDS results. With these requirements in mind, it is plausible to for example a GaAs or a GaSb wafer as test specimen. Pure element specimens, like Cu, could also provide as standard materials, as is suggested in Goldstein [2]. As the results show, the findings can be case specific, and thus a series of SEM EDS standard test specimens would be good, since it would allows refinements and verifications between specimen and setup. Keeping a constant standard test specimen for a setup is more important than having a unified standard between laboratories, as measurements over time on the same specimen reveals changes and thus potential errors more easily. Additionally, it would be better to run the performance parameter notebook on a spectrum from any specimen, for example the specimen of interest, than not running any quality checking routine at all. A unified agreed upon standard would be useful for comparing results between detectors and laboratories. Such comparison is very helpful when changes are done to a detector, during troubleshooting, and when different detectors are tested for purchase. Finally, the test specimen

[1] BAM web shop accessed 31.05.23 at https://webshop.bam.de/webshop_de/eds-tm002.html

should be close to what the user is normally analyzing, as the goal is to assess the performance of the setup for the user's needs.

Even though the advised test specimen above is a flat wafer, it is known that EDS analysis is done on uneven surfaces. The GaSb specimen, as shown in the overview image in Figure 3.1, has a scratched surface. According to the standards ISO 22309 [50] and ASTM E1508 [42] on SEM EDS quantification, analysis performed of non-flat surfaces gives a higher uncertainty in the quantification. The ASTM standard claims that analysis of "casual" surfaces give unpredictable variations in the quantification. SEM EDS analysis of non-flat and non-polished surfaces are of huge interest and are probably done quite frequently, thus investigating possible corrections for non-flat surfaces would be of great interest. Newbury and Ritchie [70] used Monte Carlo simulations to investigate how rough a surface can be before severely increasing the uncertainty of quantification, and they conclude that uneven surfaces with 100 nm repeated variations can increase the relative error with 5 % or more. The scratched areas analyzed in this work was only used as a reference to the flat areas, for a brief comparison of the AZtec results. The deviation from 50 : 50 was around 10 at.% for the scratched areas. Establishing corrections for non-flat surfaces would require more data. Such corrections would probably both be dependent on the surface and the material, as the issue with non-flat surfaces is that the X-rays are absorbed more or less depending on the path length through the material, which is dependent on the surface. The first step towards non-flat corrections would be to get open-source bulk corrections working properly for flat surfaces, thus the main focus in this work was on the flat areas.

5.2 EDS performance parameters

The metrics measured to evaluate the performance of the setup, the detector, and the acquisition parameters are the energy resolution, the scale, the offset, the peak deviations in calibrated positions, the peak ratios, the Duane-Hunt limit and the Fiori peak-to-background ratio. Additionally, observations for PT, E_0, and i_b are discussed.

5.2.1 Energy resolution

Section 4.2 begins with a table showing an issue with the calculated energy resolution, which is that a single spectrum gives different energy resolutions when using different reference peaks in the calculation. The energy resolutions are calculated from the FWHM of different peaks, using Equation (2.13). Calculated energy resolutions for GaAs and GaSb taken at 30 kV with 50 pA are tabulated in Table 4.2. The calculated energy resolutions for GaAs varies from 123 eV to 135 eV, and for GaSb from 121 eV to 133 eV, when using different peaks as the reference peak. The reference peak variations are between elements, K vs. L, and α vs. β, without any clear pattern. This illustrates an issue with specifying a single energy resolution for a spectrum. The energy resolution is supposed to be a property of the detector and the electronics. As explained in Section 2.4.3, the acquisition parameters like ICR and PT affect the achieved energy resolution, but the results here show that the energy resolution is also dependent on specimen and choices for calculations (i.e. reference peak and method). The ISO standard 15632 [43] on SEM EDS performance parameters is directed towards the manufacturer of the detector, where the described method for measuring the energy resolution is with an ^{55}Fe source off the microscope. However, for user laboratories the

standard specify that a polished manganese specimen can be used. This does require that the user laboratory has a polished manganese specimen.

Measuring directly on a Mn specimen is the first of three possibilities for measuring the energy resolution, introduced in Section 2.4.3. The second method is to measure the FWHM of Ni Kα, e.g. with a NiO test specimen from Ted Pella, and then multiply the FWHM by 0.926 to get the approximate FWHM of Mn Kα. This method relies on specific specimen, which can be expensive and had been ordered but not delivered during the time span of this work. Other non-standard Ni test specimen could probably be used, but the 0.926 factor is based on NiO test specimen and the results from a round-robin study in 1995 with five TEM laboratories [51]. The third method, which is given in Goldstein [2], is Equation (2.13) by Fiori and Newbury. As neither a Mn specimen nor a NiO specimen was available for this project, the third method was used. The third method is also more flexible and general, as it does not rely on specific specimen.

Claiming that the energy resolution is a property of the detector, the acquisition parameters, the specimen, and additionally the choices during calculations, raises the question of what the energy resolution of a detector actually is. The energy resolution is a much used comparison metric for EDS detectors, and is thus important. Having a single number for the energy resolution is convenient, but it is not a complete description of the energy resolution. Traditionally, the energy resolution is seen as a property of the detector, but the ISO standard 15632 [43] stress the need for specifying the ICR with the energy resolution, preferably with one number at low ICR and one at high ICR. When looking at the other acquisition parameters, the data in Table 4.3 shows a strong dependence on the PT, and a weaker trend with the ICR. These numbers are calculated with HyperSpy, which use Equation (2.13), but selects the reference peak as the alphabetically first α peak. Both the use of Equation (2.13) and the choice of reference peak was not documented properly, so the author of this work raised an issue[2] on the HyperSpy GitHub page with a suggestion for improvement with a pull request[3]. Regarding the PT, it should be selected to give the best energy resolution, as it is safe to assume that the manufacturer has done this for the specifications of the detector. The highest PT gave an energy resolution of 127 eV, while the lowest PT gave 158 eV. The ICR trend is weaker, indicating that lower ICR gives better energy resolution, but the changes are around ±2 eV. The ICR is dependent on the beam energy and the current, but also on the specimen. This specimen dependence for the ICR might be one of the factors which make the energy resolution dependent on the specimen.

Another specimen factor for the energy resolution is the available lines generated by the elements. This effect is most apparent when looking at the estimated FWHMs from multiple lines in a single spectrum, as in Table 4.2. The shared lines, i.e. Ga Lα and Ga Kβ, have similar but not identical FWHMs. Such variations of a few eV are expected with measurement noise, and is very small compared to the peak broadening from the detector, as explained in Section 2.3.1. The lowest energy resolution for both spectra is from the Ga Kβ line, implying that the Ga Kβ line is narrower compared to the other lines. For GaAs, the explanation could have been that the peak overlap some with As Kα, but that is not the case for GaSb, and another explanation is needed. The Ga Kβ peak is much less intense than the other lines used as reference, which can give slightly worse model fit. Another possibility

[2] Issue: https://github.com/hyperspy/hyperspy/issues/3098
[3] Pull request: https://github.com/hyperspy/hyperspy/pull/3099

is that the equation used to estimate the FWHM works better for α lines, but that is contradicted by the As Kβ, Sb Kβ_1, and Sb Kβ_2 lines. The most probable cause is the low intensity in the Ga Kβ peak. By cherry-picking a reference line, the reported energy resolution can be lowered, but it is not good practice, and it is not a general solution. A solution for the method using Equation (2.13) could be to average the estimated energy resolution for a fixed set of reference lines. This would then depend on a standardized test specimen. Regarding the variations of a few eV between spectra with similar or equal acquisition parameters, the cause is probably measurement noise. Such small variations when measuring the metric are expected, and would probably be solved by averaging over multiple spectra with the same acquisition parameters.

To summarize, the energy resolution of a detector should be specified with the acquisition parameters, the specimen used for the measurement, and the method used for calculating the energy resolution. Alternatively, a larger uncertainty can be used to specify a more general energy resolution. An example of the first, based on the results in Table 4.3, would be: the energy resolution of the detector is 127 eV at 30 kV and 50 pA, measured on a GaAs specimen with 16k cps, and calculated with Equation (2.13) with the Ga Kβ line as reference. The second way of specifying the energy resolution would be: the energy resolution of the detector is 127 ± 6 eV at PT 6 and ICR below 50k cps, measured on a GaAs and GaSb specimen, calculated with Equation (2.13).

5.2.2 Scale, offset, and peak position deviations

The calibration of the spectra was done with HyperSpy, and the results for the energy scale, the offset and the deviations in the peak positions are close to the expected values. The scale and offset is presented in Table 4.4, and the ΔE in Table 4.2 are representative numbers for the peak deviations. Low deviations for the scale and offset show that the detector is calibrated properly. The accuracy of the calibration is further strengthened by the low peak deviations. The GaAs spectra have one order of magnitude higher standard deviation for the scale than the GaSb spectra, which is due to more 15 kV and 30 kV spectra for GaSb. The numbers would be more similar if the same number of spectra were used for both specimens. However, the numbers are still comparable, as the scale and offset is not expected to change with the specimen nor the acquisition parameters. A peak position deviation of ±2 eV is good, because the peak widths are in the range of 100. The channel size and energy resolution limits perfect peak position.

According to the responsible engineer[4] for the SEM Apreo at NTNU NanoLab, the calibration routine for the instrument used in this thesis is just to measure specific known reference peaks, and then the software does the calibration. For peaks at energy from 1 keV, this appears to be sufficient and gives good results. However, it can be observed in panel (a) of Figure 4.1, that low energy peaks have visual peak deviations. The center of the C Kα and O Kα peaks are offset from the theoretical values, marked by vertical dashed lines. The poorer calibration at low energies can both be due to lower amount of counts here combined with high absorption, and the calibration routine. The calibration routine is probably not optimized for low energy peaks, as the routine is probably optimized for the most common use cases. If a user needs higher accuracy in the lower energy region, the spectrum should

[4] Verner Håkonsen, communication by mail and in person. Alternatively, the present responsible engineer for the SEM Apreo at NTNU NanoLab shall be able to confirm the calibration routine.

be calibrated with reference peaks in the lower energy region before the analysis. In this work, where the focus is peaks at 1 keV and above, the calibration is sufficiently accurate.

5.2.3 Peak ratios

The idea of measuring peak ratios was to get a number for the possible carbon contamination, as it is done in the work of Egerton [17]. There is some carbon present in both the GaAs and GaSb spectra, thus the peak ratios could give a number for the carbon contamination, and the change over time. However, a metric like this needs a time series of spectra, where the change in K to L peak ratio is plotted, and an increase in K over time would indicate carbon contamination. Measuring time series of spectra was not prioritized in this work, as the focus was directed elsewhere.

The peak ratios in Table 4.5 are not an example of a time series, but the ratios are still interesting. GaSb have around three times higher ratio for Ga Kα/Lα than GaAs. The higher ratio either indicates more Ga Kα or less Ga Lα signal registered. The GaAs spectra have much intensity from the As Lα peak, which can be absorbed by the Ga Lα peak, and thus giving the Ga Lα peak a higher relative intensity in the GaAs spectra. As explained in Section 2.1.1, the absorption probability is the highest right above the absorption edge. With As Lα right above the energy of Ga Lα, the As Lα X-rays are absorbed easier than the Sb Lα X-rays, and such absorption can result in more fluorescence from Ga Lα. This is an indication possible absorption issues in the GaAs bulk, which will be discussed more in Section 5.3.

One of the more interesting results which are achievable with measuring peak ratios is to get a number for the source of artifacts. This is explained in the work of Egerton [17], where the ratio between a targeted element and a grid element outside the targeted area is investigated. The grid element must contain a high and low energy line, and the element in the targeted area must contain a line in between the two lines in the grid element. In the work of Egerton, which is the routine with the NiO test specimen, the element in the targeted area is Ni and the grid element is Mo. The idea is that a high amount of Mo K signal indicate that there are electrons from the beam which are deflected and hit the grid directly. Backscattered electrons can also contribute to the Mo K signal, but increased amount of deflected beam electrons would certainly influence the ratio of K and L in Mo. If there are higher amounts of Mo L signal, the source of artifacts is more likely to be from secondary fluorescence from Ni K X-rays. Skomedal [20] investigated the use of a NiO specimen in STEM EDS in the $5-30$ kV range, and calculated these stray radiation ratios. In the present work the specimen used did not have the required geometry for such an investigation, as the specimen is a flat wafer, and flat wafers make such test for the source of artifacts impossible.

5.2.4 Process time

The optimal PT for a specimen is dependent on the aim of the analysis, as a high PT gives a better spectrum, but takes longer time. Better spectrum means higher energy resolution and fewer artifacts. Even though high PT gives a good spectrum, the amount of counts recorded per second is lowered, and thus the DT increase with increasing PT. The time aspect is especially important when measuring large EDS maps, as these can be very time-consuming

with a high PT. As seen in the results, the PT affect the energy resolution, the evenness of the spectrum through the amount of counts, the amount of artifacts with increasing ICR, and the DT.

For quantitative analysis, it is best to have a high PT, as the energy resolution is better, and the amount of artifacts is lower. This allows the user and potential automatic detection software to detect and separate peaks easier. Using automatic peak detection should be done with caution, as there are cases where peaks are labeled incorrectly. This is well reviewed and discussed in detail in a paper by D. Newbury [71]. Newbury raises concerns about the use of automatic peak detection, with examples of misidentified major constituents. Such misidentifications are a serious challenge for the credibility to EDS community, and should be avoided when possible. Acquiring spectra with a high PT limits the possibility of misidentifications, as the peaks are more visible and separable. When a specimen is labeled correctly, the peaks can be modelled as Gaussian functions. Model fitting can deal with overlapping peaks quite well, if the right lines are added to the model. A fitting algorithm can separate overlapping peaks better than the human eye.

As the process time is very influential on the energy resolution, the best PT for an analysis is dependent on the specimen. If the specimen have many close L lines which are of interest, the PT should be high. If the peaks of interest are in the higher energy range, the PT can be lower to allow higher throughput. As seen in panel (c) in Figure 4.4, the maximum and minimum PT does not make a big difference for the Ga Kα peak, but the Ga Lα peak is merged to a visible unseparable peak with Ga Ll in panel (a). However, the Gaussian modelling of the PT 1 spectra separate the low energy peaks, and the quantification is actually the one closest to the expected values. The quantification results, presented in Figure 4.5 and Table 4.11, show that higher amount of counts can give better quantitative results.

The best general PT is probably high, but not the highest possible. As mentioned in Section 2.4.3 and stated in Goldstein [2], it is often better to have slightly reduced energy resolution, as this allows a much higher throughput. For example, at 30 kV and 50 pA, PT 6 have DT 44%, while PT 4 have DT 13%. Acquiring this PT 6 spectrum then takes 2 – 3 times as long as the PT 4 spectrum, and the energy resolution difference is 127 eV vs 132 eV, given in Table 4.6. The high increase in DT and acquisition time, thus lowered throughput, is in many applications not worth the small improvement of energy resolution.

5.2.5 Beam energy and beam current

Setting the beam energy and beam current is important for the throughput and the spatial resolution of eventual EDS maps. The combination of beam energy and beam current is setting the amount of X-rays generated, and thus the amount of counts recorded. The beam energy is important for the overvoltage, which for example is an issue for the Sb L lines at 5 kV and 10 kV. Seen in the voltage series figures (Figures 4.2 and 4.3), the 15 kV and 30 kV spectra are very similar around 1 keV, but then the 15 kV spectra falls off faster than the 30 kV spectra. This can be due to the overvoltage decreasing more at 15 kV than at 30 kV, and thus the ionization cross-section is lowered.

The voltage series were acquired with constant beam current, which could have been done better with for example constant input count rate. The constant beam current was selected to make the spectra as comparable as possible,

but the low ICR at 10 kV and 5 kV made the spectra noisy, as an addition to the low overvoltages in these spectra. The combination of low beam current and low overvoltage resulted in few counts, and thus poor spectra. The idea was to acquire spectra that did not need normalization for good comparison, but other approaches could have solved this better, for example with constant ICR or lower PT. Keeping the ICR constant should result in more similar spectra which also does not need normalization, and such an approach can be tested in future works. Another solution for voltage series is to use a medium PT, e.g. PT 4, as this will give more counts in all spectra and might mitigate the issue with low ICR at low beam energies. Even though the 5 kV and 10 kV spectra had lower quality, they were still useful in this work, because the effect of performance parameters is best visualized with spectra of varying quality.

In the literature [42, 44, 50] (see Section 2.3.2), the DT is given as the parameter that determines the amount of artifacts in the spectrum, but the results in this work do not support this. These advices set 40%, 30%, and 15% as DT limits, which probably are based on the older Si(Li) detectors, while the SDDs can handle much higher count rates, and thus higher DT without the same issues with artifacts. The 2018 version of the Goldstein textbook [2] is updated with the advice saying that specifying a DT limit is not really useful for SDDs, but rather that a test spectrum should be acquired to see if the acquisition parameters are suitable for the specimen. This is in accordance with the results in this work, and the argument for this is presented below.

The two spectra with the highest DT at 53% and 77% had similar amount of artifacts as a spectrum with DT 18%, and the amount was low. The mentioned spectra are the GaSb 15 kV and PT 6 spectra, where the DT increase with i_b (50, 200, 400 pA). These three spectra were very similar, except for the amount of counts, which is proportional to i_b. The spectrum with clearly the most prominent artifacts was the one with the highest amount of counts, recorded at high i_b and low PT, which is the GaSb 30 kV, 400 pA, PT 1 spectrum. This combination gave around 6–10 times more counts in the peak of interest than the other spectra, but also clear artifacts which were not present in other spectra. The spectrum is plotted in Figure 4.1, and the artifacts are annotated. The DT of this spectrum was only 28%. The results show that artifacts are more present when the input count rate is very high. Modern SDDs are made to process counts fast, and thus the DT is not a good measurement for the amount of artifacts, because the DT is highly dependent on the PT setting. It might be that a certain PT setting have a specific DT where artifacts are getting too prominent, but as the ICR is specimen dependent, this is not very likely. It might be that the AZtec software is doing some data treatment to reduce the amount of artifacts, and thus that the outputted raw data in the `".emsa"` file is not the as "raw" as it is assumed to be. This is just speculations, as the documentation [23] does not give information about this.

In conclusion, the DT is not as useful as a parameter to determine the quality of the spectrum, and should mainly be used when considering the acquisition time. The DT advice given in Goldstein is probably the best one, which states that a test spectrum is needed to assess if the acquisition parameters are suitable for the specimen, without generating too many and intense artifacts. Other parameters like the ICR (through i_b and E_0) and PT should be used to adjust the amount of artifacts, and even though the DT is a product of these parameters.

5.2.6 Duane-Hunt limit

The calculated Duane-Hunt limits are close to the expected values, i.e. the set beam energy on the SEM. According to the ISO 22309 standard [50], it is required for quantification that the specimen is not charging and that the indicated beam energy is correct. The specimen was not expected to have charging issues, and thus the Duane-Hunt limit may look little useful in the context of this work. However, the metric is also a demonstration of the successful conductive path between the specimen, to the stage, and to ground. Calculating the metric is fast and does not need much interpretation, and thus it can be used as a quick check to see if issues with the conductive path are present. In addition, the Duane-Hunt limit was used as the upper limit for the energy range when making the models of the spectra, and thus it was useful in that context.

The apparent usefulness of this metric suffers from the same problem as the calculation of the scale and the offset: a well calibrated setup give little deviation from the expected values. The mentioned metrics does not verify that the whole setup is working correctly, but rather indicate that the parameters they test are working correctly. If the right parameters are selected, the user can be confident that the setup is working correctly and when the setup is not working correctly, the metrics can be used to find the issue. The usefulness is more apparent when there are issues with the setup or the set parameters, and having them as a part of a test routine can be useful. Conversely, having too many parameters can make a test routine overwhelming and less useful. A solution for this is to have a test routine that gives some standard output, and checks additional parameters in the background which are alerted if they are outside the expected values. Defining the expected value range for the Duane-Hunt limit needs more testing, but a starting point is $\pm 0.5 - 1$ keV [2, 47] from the set beam energy. This is much higher than the deviation seen in this work.

5.2.7 Fiori P/B ratio

The Fiori P/B ratio is a number often given by EDS manufacturers, at least for TEM EDS, where the metric is an indication of how much signal the detector can get in a peak of interest compared to the background. The background acquired in an EDS spectrum is unwanted signal, while the useful signal is the counts in the peak of interest. The numbers for TEM EDS are usually very high, for example above 3000 [18, 51]. The extremely high numbers are due to the fact that all the counts in a peak is divided by the background counts in just a single channel (or a corresponding 10 eV window) under the center of the peak. This is illustrated in Figure 2.27. The reasons for using just one channel for the background is explained in Section 2.4.5. The main reason is that the metric is not dependent on the energy resolution. This is seen in the results, where the 30 kV and 50 pA spectra at PT 1 and PT 6 have similar P/B ratios, even though the energy resolution is much better at PT 6 (158 eV vs. 127 eV). The goal of testing the Fiori P/B ratio is to figure out if the metric can be useful for characterizing and optimizing SEM EDS, either as a metric for the setup or as a metric for the quality of the spectrum through the acquisition parameters.

The data acquired gives indications of what affects the Fiori numbers. The two 30 kV GaAs spectra at 25 pA and 50 pA have the highest Fiori numbers. The number of counts is around twice as high in the 50 pA spectrum

compared to the 25 pA spectrum, but the Fiori numbers are similar. Both these 30 kV spectra have PT 6, but the 50 pA spectrum has a higher DT at 44%, while the 25 pA spectrum has a DT of 25%. This indicates that the spectra are equally good, but the acquisition time is much higher for the 50 pA spectrum. If this is the case, the Fiori ratio might be a metric which can be used to determine when a spectrum have enough counts. When acquiring EDS data, there is a threshold where more counts does not give better results, either for qualitative or quantitative analysis. This number will be heavily dependent on the specimen, as shown in different Fiori numbers from GaAs and GaSb, as well as being dependent on acquisition settings such as E_0. The targeted value is not a specific number, but rather the point where the Fiori ratio does not increase with more counts.

In general, the Fiori numbers from the GaAs spectra are higher than from the GaSb spectra. For the Ga Kα peak, which have the highest Fiori numbers, the scores from GaAs spectra are around twice as high as the GaSb spectra. For the Ga Lα peak, the difference is even bigger, with the GaAs spectra having around five times higher Fiori numbers than the GaSb spectra. This show that the metric is specimen dependent. It also shows that the metric is not necessarily a good indication for how well the quantification will be, as the GaAs spectra have bigger deviations from the expected values than the GaSb spectra.

In the GaAs spectra, the Fiori numbers for Ga Lα are higher than for As Lα, being 586 and 236 respectively. This can be explained by the higher absorption of As Lα X-rays in the material. Looking at Figure 2.2, the μ_ρ for Ga Lα in GaAs is 1387 cm^2/g, while the μ_ρ for As Lα in GaAs is 3744 cm^2/g. In other words, parts of the As Lα X-rays are absorbed, making the As peak smaller than the Ga peak.

In the GaSb spectra, the Fiori number for Ga Lα is just below 90, which is much lower than in the GaAs spectra. The absorption in the GaSb specimen is much higher, with a μ_ρ of 3981 cm^2/g for Ga Lα. The area of the Ga Lα peak is thus much lower than in the GaAs spectra, and the Fiori number is lower. At the Ga L and K peaks, the absorption is stronger in GaSb than in GaAs, and the Fiori numbers are lower.

As explained in Section 2.1.1 and stated in Goldstein [2, Ch. 4.4], an element had low self-absorption, and thus higher Fiori numbers would be expected for pure specimens. Pure specimen does not absorb as much of the background just below the line, but above the absorption edge the background intensity should be reduced. Achieving high Fiori numbers are of interest for manufacturers as a quality marker, but EDS analysis of pure specimens are seldom of high scientific interest.

Aside from the specimen, the acquisition parameters also affect the Fiori numbers. The biggest effect and trend appears to come from E_0. The E_0 trend is expected in well performing AEM setup [3], and as it is visible in the results, the trend can be assumed to be present in SEM EDS as well. However, the trend should also vary more in SEM EDS, as E_0 is in the same range as E_C, and then the overvoltages are changing more than in TEM setups. This should lead to some variation in the trend between the Fiori numbers and E_0, which is observed in the results. For the GaAs specimen, the Fiori P/B ratio of Ga Lα increase with increasing E_0. The same E_0 effect is visible for the Ga Kα, Sb Lα, and Sb Lβ peaks in the GaSb spectra. The Ga Lα peak in the GaSb spectra does not follow this trend, but this ratio is changing much less than the ratios for the three other peaks. An increase in i_b appears to have a decreasing effect on the Fiori numbers, but the effect is small. This i_b effect can be seen on the three 15 kV

GaSb spectra, with 50 pA, 200 pA, and 400 pA. The same effect is visible for the 30 kV GaSb spectra taken with 50 pA and 400 pA at PT 1, with the Ga Lα peak as an exception. The different PTs tested on GaSb in (C) and (D) does not correlate with a trend in either direction, i.e. the energy resolution does not affect the Fiori numbers.

The dependence on the beam energy can partly be explained by the overvoltage (U). The overvoltage change the ionization cross-section (Q), which can be viewed as the probability of an atom being ionized by an incoming electron. Q(U) is plotted in Figure 2.30 for Ga Lα and Ga Kα. The plot shows the general ionization trend, which is also plotted in an adapted figure from Williams and Carter in Figure 2.20 [3]. The trend is an increase with a maximum between $U = 2$ and $U = 5$, and then a decrease. From Figure 2.30, the maximum Q is achieved at 3.7 kV for Ga Lα and 4.3 kV for As Lα. As Q decrease above the maximum, the probability of exciting X-rays decrease, and from this statement alone it would be expected that the 5 kV spectra have the highest Fiori numbers, and then the number should decrease with increasing E_0. However, the opposite is observed in the data. The reason for this is that the electron beam travel deeper into the specimen with increasing E_0, illustrated by numbers for the electron range in Table B.2. At higher E_0, the probability of ionization at each level is lower, but the number of levels is higher. This explanation is not complete, as it does not explain why thin TEM specimen can achieve Fiori numbers above 3000 or 4000. When thin specimen are probed with high E_0, the probability of multiple scattering events are negligible, and thus the background level is reduced compared to thicker specimen [35].

To summarize what affects the Fiori P/B ratio, the specimen is the most important factor, followed by the beam energy. Additionally, as explained and discussed in the theory about the Fiori P/B ratio in Section 2.4.5, the calculation method is very important. Different calculation methods, such as using background windows close or far from the peak, can give different results. The window integration method appears to be the most used method, but using model fitting of the peak and the background will give results which are closer to the original definition. The use of model fitting will also reduce the user bias, which can make Fiori numbers from different detectors more comparable. This is emphasized by the ISO standard 15632 on SEM EDS performance [43], where a slightly different SNR is used, and it is calculated with integration windows. As the SNR in the ISO standard use integration windows, it is specified that "the ratio is only relevant for the comparison of spectrometers with similar resolution performance" [43, p. 4]. Using the Fiori P/B ratio as a metric for SEM EDS performance would be better, as it both can be used to compare different resolutions, and it is more robust than the SNR given in the ISO standard. However, if two different detectors have measured a Fiori number for the same peak in two different specimens, the numbers are not comparable. Thus, to get comparable numbers between detectors, the same specimen, calculation method, and acquisition parameters should be used, at least the same E_0. In other words, using the Fiori P/B for comparison of setups or detectors requires a specific and well-defined test protocol.

To finalize the discussion of the Fiori numbers, it is important to discuss if the metric is useful for SEM EDS. The Fiori P/B ratio is a robust metric for calculating the signal-to-background ratio, but it is highly dependent on the specimen and E_0. Based on the highly varying Fiori numbers between GaAs and GaSb, the metric does not seem very useful as a general metric for how well the detector performs, because the specimen appears to be an important factor. This is also an argument for why a specific range of values is not useful, unless a standard

specimen is used. However, one interesting use of the metric is to determine the difference between two spectra acquired with different beam current, or different process time. Regarding the process time, the Fiori numbers could be used to evaluate if the model fitting can separate two overlapping peaks, because the background should be the same, but if the fitting does not separate the peaks, the Fiori number will change. This could be explored further in future work. Regarding the beam current, it was observed that spectra with increased beam current, and thus increased dead time and acquisition time, had similar Fiori numbers. This is an implication that the data quality is similar, and thus that a threshold for the beam current could be found where the data quality will not improve with increased beam current. For mapping applications, this could reduce the acquisition time to allow faster or more detailed acquisition.

5.2.8 Summarization of the performance parameters

The summarization of the performance parameters in Table 4.9 gives an indication of how well the detector performs, and what acquisition parameters are important. The first paragraph is about the detector, and the second paragraph is about the acquisition parameters. The test is an easy health check of the system that can be done regularly, e.g. every session to verify the setup and test the selected acquisition settings. Satisfactory numbers, as the detector used in this work provides, indicate that the setup is working well and that quantification can be done with confidence. The parameters also indicate which acquisition setting combinations are good.

Based on the calculated metrics, the detector performs well. The energy resolution achieved at 127±6 eV is the same as the manufacturer specification. As stated in Section 3.2, Oxford Instruments claim that the energy resolution of the X-max^N detector is 127 eV [67], and this fits well with the variations observed when using different peaks as the reference peak. The energy axis through the scale and offset is calibrated well, as their deviations from the set values are small, and the deviations for the calibrated peak positions are very low. In addition to the scale and offset, the Duane-Hunt limit further indicates that there are no issues between the communication between the detector, the software and the SEM. The peak ratios can reveal contamination, and they gave indications of absorption. The Fiori P/B ratios calculated were as expected lower than in well performing TEM EDS setups. Specifying a range of values for well performing SEM EDS is not possible, as the specimen dependence is high for the Fiori P/B ratio. One useful application of the Fiori P/B ratio is to compare two spectra acquired with different beam current to optimize the acquisition time. Using the Fiori P/B ratio to compare different detectors requires the same specimen, calculation method, and acquisition parameters, at least the same E_0.

The acquisition parameters are important for acquisition of good spectra. Specific spectra acquired, such as the 5 kV spectra, had too few counts, which were reflected in low Fiori numbers and high peak ratios. The energy resolution was not affected by few counts, showing that it was high background and much noise that disturbed the poorer quality spectra, as similar energy resolution indicate that the detection worked equally well. The spectra with too few counts were due to low beam current. In addition to spectra with too few counts, the Fiori numbers and the quantification indicate that some spectra had more counts than necessary. Optimization of i_b is important for EDS analysis, because reduced acquisition time will reduce the risk of beam damage and allow faster acquisition. Faster acquisition allows more mapping, detailed mapping, and less time spent on relatively expensive and

fully booked instruments. Some spectra show issues with beam energy through overvoltage, but also through low counts, as E_0 and i_b together with specimen properties determine the number of X-rays generated in the specimen. The process time was found to be most influential on the energy resolution, as expected. Additionally, PT affected the quantification slightly, but not enough to be a concern. As the highest PT gave very high DT and thus long acquisition time, the general recommendation is to use a high PT, but probably not the highest. The energy resolution difference between PT 4 and PT 6 was low, but the acquisition time difference was large. The notebook can be used to figure out if a lower PT setting yields similar results as a higher PT setting, which can be confirmed if the Fiori ratios are similar.

5.3 Quantitative analysis

SEM EDS bulk corrections are, to the author's knowledge, not available in an open-source Python format. The DTSA-II software is open-source, but written in Java. A followup of the DTSA-II software in the newer programming language Julia is available and called "NeXL Spectrum"[5], but its documentation is still very limited. The use of Julia in scientific programming may be increasing, but the language is not as widespread as Python. Implementation of open-source SEM EDS bulk corrections in Python is a novelty, and this work is a step towards achieving this goal. This section is a discussion of the results from the quantification Section 4.3, presented in the same order as the results.

The results are compared to the theoretical reference value of a 50 : 50 composition, as this is the known composition of the two specimen tested. This way of evaluating the results is not optimal, as two errors can cancel each other out. In other words, an accurate result might just be a coincidence of multiple errors that fit with the relevant data. However, the goal of the corrections implemented is mainly to test what could be implemented in future work, and not to implement a complete and high accuracy quantification routine. Thus, comparing the results to a 50 : 50 compositions should be sufficient to evaluate the corrections implemented in this work.

5.3.1 Initial quantification

The results from the AZtec software are quite close to the expected reference values, but should not be considered as the "truth". There are variations in the results, which is expected in the order of around 2 at% in EDS analysis [2, 3], but trusting black box software can give a false sense of security. For example, the poor quality of the 5 kV GaSb spectrum was quantified without any warnings from the software, and the results were not flagged as poor. Such results can be avoided when the user takes multiple spectra, but a warning from the software would be helpful. It would be even more helpful if the user knew what the software did through the documentation, but AZtec is not documented in detail, for the public at least. Delete last sentence?

The GaSb spectrum at 5 kV is quantified far off from the expected reference values, both by AZtec and by the intensity ratio. Both methods use the Ga Lα and Sb Lα peaks, and the Sb Lα peak is at 3.6 keV, which is quite close to E_0. The overvoltage on Sb Lα in the 5 kV spectrum is below 1.4, while the overvoltage on the Ga Lα is above

[5] Available at https://pages.nist.gov/NeXLSpectrum.jl/ and https://github.com/usnistgov/NeXLSpectrum.jl

4.5, which results in a severely underestimated Sb content with the intensity ratio. As explained in Section 2.3.2, the overvoltage is important to achieve high quality spectra and quantification. The advice in Goldstein is to keep $U > 1.5$, and the 5 kV GaSb spectrum is not following this advice. As seen in Table 4.11, the intensity of the Ga Lα peak is 19 times larger than the intensity of the Sb Lα peak, thus the intensity ratio method gives a 97 : 3 composition. AZtec is doing some corrections for this, but overestimates the weight for Sb, and ends on a 39 : 61 composition. Based on the results from the 5 kV GaSb spectrum, the overvoltage should be much higher than 1.5 to avoid severe overvoltage issues. In general, it is difficult to do high accuracy quantification at low E_0 when the peaks are close to E_0, as the overvoltage between different peaks will be big, the background is changing rapidly, and the absorption can be high. To do high quality quantification at low E_0, the input parameters to the model used must be refined. The issue in the 5 kV GaSb spectrum is probably most affected by the issue with the overvoltage. This show that quantification routines needs improvement and tailoring for low beam energies.

The initial quantification also present the uncorrected intensity ratio results, and from these results it is possible to see what corrections are needed. Table 4.11 and Figure 4.5 show that the need for corrections are varying with both specimen and acquisition parameters. Different i_b is not affecting the correction needs much, but the E_0 does. All the GaAs spectra need corrections which increase the weight of the As signal to achieve a 50 : 50 composition. AZtec have applied corrections to the GaAs spectra, where the results are pushing As too high at 5 kV and 10 kV, and not high enough at 30 kV. The 15 kV GaAs corrections done by AZtec on GaAs is good, resulting at 50.6 : 49.4. The intensity ratio method show that the As content is too low. The need to increase the weight of As is due to absorption of As X-rays in the specimen, which is higher for the As line than the Ga line.

The trend in the GaSb spectra are not as clear as for GaAs. The 30 kV GaSb spectra appears to require little corrections, and have good results with the intensity ratio. The GaSb 15 kV and 10 kV spectra are quantified with Ga Lα and Sb Lα. The intensity ratio method show that the Sb content is too low in the 10 kV and 15 kV spectra, i.e. Sb needs to be increased to achieve a 50 : 50 composition. AZtec have corrected the GaSb 15 kV and 10 kV compositions to values close to 50 : 50.

Since the absorption should be stronger of the Ga Lα peak than the Sb Lα peak, the absorption should not be the reason for the low Sb content. The low Sb content in the 15 kV and 10 kV spectra can be due to the overvoltage differences. Ga Lα has overvoltage $U = 15/1.1 = 13.6$, and Sb Lα has $U = 15/3.6 = 4.2$ at 15 kV. From the estimated ionization cross-section as a function of overvoltage, seen in Figure 2.30, the maximum $Q(U)$ is at $U = 3.4$. Thus, the overvoltage at 15 kV should not be the reason for the low Sb content, as Sb Lα is close to the maximum $Q(U)$. However, as shown in Figure 2.30, higher E_C give lower $Q(U)$, and this can partly explain the difference between Ga Lα and Sb Lα. The different intensities can have other reasons too, such as different fluorescence yield, detector efficiency, or effects from atomic number. The most probable reason for the low Sb Lα intensity compared to the Ga Lα intensity is atomic number effects, as the difference between Ga and Sb is 20. Different E_C is one of the effects of different Z. The Z difference between Ga and As is just two, which may be why the GaAs spectra need different corrections than the GaSb spectra.

5.3.2 Quantification of SEM EDS data with the thin film assumption

Quantification of SEM EDS data with the thin film assumption is done to illustrate the risk of using wrong assumptions, and to test if the Cliff-Lorimer method in HyperSpy with absorption corrections can be used for quantification of SEM EDS data. In general, the TEM EDS routines gave poor quantitative results for the SEM EDS data of a bulk specimen. One interesting result is the effect of the absorption correction in the CL method, which did improve the results. The best improvement was achieved when the specimen thickness was set to 200 nm, both for GaAs and GaSb. When comparing this thickness to the electron ranges in Table B.2, there is no obvious reason why this thickness should be the best. As the table shows, the electrons accelerated by 30 kV can penetrate around 4000 nm while still have enough energy to excite the relevant X-rays. This range is decreased to around 1200 nm at 15 kV, 600 nm at 10 kV, and 200 nm at 5 kV. It might be that the thickness which gives the best corrections are varying between specimen, and using the 200 nm thickness on other specimen may not work equally well. The thickness 200 nm does not have a physical meaning, as the bulk specimens used are 300 µm.

The selection of tested thicknesses was done to cover the range of conventional TEM specimen thicknesses, and to increase the t towards bulk thicknesses. The highest thickness at 10000 nm was chosen to see the effect of the absorption correction where the thin film assumption is obviously wrong. The CL method did not raise any warnings or errors with such high numbers, and the results were not obviously wrong. This may just be a reflection of the fact that the quality of the results were compared to a reference of 50 : 50, and not an extensive analysis with multiple different compositions. This would be the next step after finding suitable quantification routine, with corresponding bulk corrections.

One strange difference between the SEM EDS and TEM EDS setting in AZtec is the default choice of Sb line for GaSb at 5 kV. The SEM EDS setting chose the Sb Lα lines, which as discussed probably has issues with overvoltage. However, the TEM EDS setting chose the Sb Mζ line at around 0.4 keV, which is does not have the same overvoltage issue, but is heavily affected by absorption in bulk specimen. The EDS detector is equipped with an ultrathin polymer window [67], which should have a low absorption of X-rays, but the matrix absorption is still high at low energies. The thin film assumption is that the matrix does not absorb the X-rays, which is probably the reason why AZtec use the Sb M-line when operated in "TEM mode". As the HyperSpy library does not include any Sb M-lines, and that AZtec did not give a k-factor for Ga Lα in the TEM quantification for this 5 kV spectrum, it was not possible to quantify the 5 kV GaSb spectrum with the CL method. It would be possible to manually measure the Sb Mζ intensity with integration windows, but this was not done as the quality of this 5 kV spectrum was poor anyway.

A major impact on the TEM EDS quantification results is the k-factors used, which is calculated theoretically by AZtec. The k-factors change with specimen, line, and beam energy, and the exact equation can be found in Williams and Carter [3]. If the k-factors could be refined, the TEM quantification results would probably improve. The results might then be more comparable to the SEM EDS results. The discussion of implementation of k-factor calculations in HyperSpy have been discussed on the HyperSpy issues page on GitHub, and on the Gitter discussion forum for HyperSpy. The conclusion so far is that the uncertainty in such calculated k-factors would

be too large, as the k-factors are a function of the detector. Achieving better k-factors can be done by measuring standard specimens on the same microscope as commonly known [2,3,38], although this process can be demanding to do consistently for a broad range of phases and compositions [3].

The use of the thin film assumption on the SEM EDS data have two implications. Firstly, it shows that the quantification routines for TEM EDS and SEM EDS is built on similar principles, but are not directly transferable. The test of the settings in AZtec confirms that the SEM EDS settings are applying some kind of matrix corrections, which are not applied in the TEM EDS settings. In the Oxford Instruments blog post [22] it is stated that the bulk corrections applied are based on the XPP model, but the documentation of AZtec does not specify this or any other information about the bulk corrections [23]. Secondly, the results presented in Section 4.3.2 show that applying absorption corrections can improve the quantification results to some degree. In general, using TEM EDS routines on bulk data is unreliable.

5.3.3 ZAF absorption correction

Absorption corrections from the ZAF model were tested to figure out if a simple and easily understandable bulk correction method could be sufficient for quantification of SEM EDS data. If it turned out to be sufficient, the implementation of such a ZAF model in HyperSpy could be done as a part of this project. As pointed out earlier in this discussion, there are multiple indications showing that the GaAs specimen needs absorption corrections, while the GaSb specimen have other issues, such as strong Z effects. It may be that the GaSb specimen also have absorption issues, but this alone cannot explain the uncorrected quantification results.

The simple model tested for absorption correction used an assumption that all the detected intensity from a line can be viewed as if it was generated at the average point in the interaction volume, and then apply ZAF absorption corrections to this point. If the point is selected properly, the model can convert the detected intensity to the generated intensity, which is then used in the quantification. The average point tested in this work was along the z-axis, at three different point in the interaction volume. The three points were the maximum generation depth, based on the Kanaya-Okayama parameterization for electron range (Equation (2.27)), divided by 2, 3 and 4. Figure 5.3 shows the three points in the interaction volume, with an illustrative $\phi(\rho z)$ curve on the left side.

The $\phi(\rho z)$ curve is the intensity from different mass depths in the specimen, which is illustrated in Figure 5.3 and plotted with calculated data in Figure 2.29. Using the parameterization of $\phi(\rho z)$ from the XPP model (Equation (2.56)), the curve for Ga Lα is plotted in Figure 5.4, at different beam energies. As this figure shows, the curves are dependent on the beam energy. The dependence on E_0 is explained in Section 2.2.2, and showed with numbers from the Kanaya-Okayama parameterization for electron range in Table B.2. The $\phi(\rho z)$ curves have a skew towards the surface where $z = \rho z = 0$. The absorption corrections done with the ZAF model show that dividing the maximum generation depth by 4 works better than by 2 or 3. This is an indication that the method might provide reasonable results, if a better average point is used. However, using a method like this with an average point might be a too simple model.

The compositional results presented in Table 4.13 show that the GaAs quantifications are improved by applying the

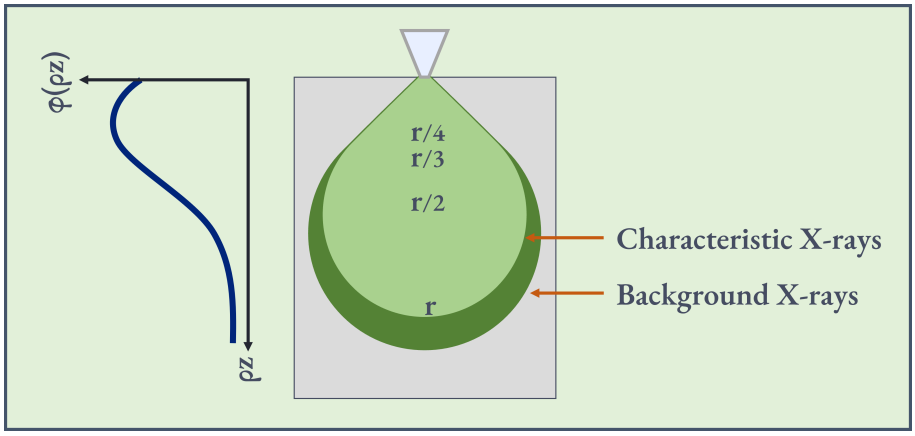

Figure 5.3: Illustration of the $\phi(\rho z)$ curve, with the interaction volume and the three selected average points for the ZAF absorption correction. The trapezoid is the incident electron beam. Adapted from [2, Fig. 19.7].

ZAF absorption corrections, but the GaSb results are not. Dividing r by a higher number made the results closer to the reference values, with an average 7 at.% deviation for GaAs, which is improved from 11 at.% deviation in the uncorrected intensity ratio results. These results show that one of the issues with the GaAs specimen is probably absorption, and that the ZAF absorption corrections can push the results in the right direction. However, the GaSb results increase from a 6 at.% deviation in the uncorrected results to a 30 at.% deviation with $r/2$, which decrease to a 21 at.% deviation with $r/4$. This is an indication that the quantification based on GaSb spectra have more important corrections than absorption.

The absorption issues in the GaAs specimen can be explained by how close the As lines are to the Ga lines. As discussed earlier, the absorption of As in GaAs is very high. The atomic number difference between Ga and As is just 2, thus giving the element similar physical properties for generation of X-rays.

The atomic number difference of 20 makes the generation properties more different for Ga and Sb compared to Ga and As. This may be part of the explanation why the absorption corrections did not improve the results for GaSb. The absorption in GaSb is high, as shown in Figure 2.2, but the results show that corrections for absorption alone is not sufficient for GaSb (see Section 2.5.2). The best correction for GaSb might include a combination of absorption and other corrections, but the assumption given in Goldstein [2, p. 300] that the two effects of Z cancel each other out is not valid for GaSb. One of the corrections applied from the XPP model is investigating the possibility for Z corrections, and the other XPP correction combines Z and A corrections.

Even though the ZAF absorption corrections improved the results for GaAs, the results are deviating too much from the reference values to be regarded as useful. Possible reasons for this is the aforementioned issues with the average point, or that the input parameters for the model is not good enough. The most important input parameter is the mass absorption coefficient, μ_ρ. In the absorption correction (Equation (2.25)), μ_ρ is used in the exponent, and small deviations in μ_ρ can give large impacts on the results. A more detailed discussion of μ_ρ is given in Section 5.3.4, as μ_ρ is also used in the XPP model.

Another reason for the deviation is the implementation of the ZAF correction, which may have bugs in the code.

To trace errors in the code, the code should be tested on a range of unknown standards with different elements and beam energies, as this will reveal how the model behaves on a broader range of data. For example, the first implementation of the range r was wrong, and when it was fixed, the quantification results for GaAs was actually worse. This show that using $50 : 50$ as the reference to evaluate the results can be misleading, and that more testing is needed to verify the usefulness of the code developed in this work. The code is implemented with both the purpose of testing different possibilities for corrections, and to be used as a starting point for future works. The implementation is done to the author's best knowledge, but the code should be tested more systematically and be reviewed by other people to ensure that it is bug free. Additionally, every model is a simplification of reality, and the models used in this work are no exception. The assumptions and simplifications made in the ZAF correction model in this work does seem to be on track for GaAs, but still having plenty of room for further improvements.

5.3.4 XPP bulk corrections

Implementation of the XPP model from the PAP paper [9] gave the possibility to plot the depth distribution $\phi(\rho z)$, and to calculate more advanced correction factors than the ZAF model, with multiple input parameters. The XPP model is using fundamental physical concepts to get an accurate description of the X-ray generation and emittance in the specimen, treating correction factors in a single framework. The corrections from the XPP model applied to the measured intensities did not give as good results as the AZtec software, which supposedly is using the same model. This difference is probably due to implementation differences, and is discussed after the plots of the $\phi(\rho z)$ curves.

While implementing physical models, it is useful to plot the results from different steps in the model to verify that the implementation is correct. Such plots can both be compared to figures in textbooks or papers, and can be used to reason about the results. Code bugs are easier to reveal and trace when parts of the code can be tested separately. Plots of the steps in the XPP model are shown in Section 2.5.3, which can be compared to the plots in the PAP paper [9]. Plotting $\phi(\rho z)$ can be done with the parameters A, B, a, b and $\phi(0)$, using Equation (2.56). Figure 5.4 is a plot of $\phi(\rho z)$ for Ga Lα in Ga, with beam energy 30 kV, 15 kV, 10 kV and 5 kV.

One of the uncertainties which was partly clarified with plotting, was how to use $Q(U)$ in the calculation of F. As mentioned in Section 2.5.3, the PAP paper is ambiguous about how to use $Q(U)$, when comparing equation (2) and (3) with (13) in the original paper [9]. With interpretations of plots, testing the implementation, a units' analysis, and additional literature [2,65], it was confirmed that equation (13) is incorrect. In the testing and plotting, the alternative uses of $Q(U)$ gave both unstable and unreasonable results.

The plot of the depth distribution $\phi(\rho z)$ in Figure 5.4 can be compared to plots in the PAP paper [9], which illustrates that the implementation of the XPP model is working mostly as intended. Other comparisons were done, for example with figure 1 and 2 in the PAP paper, where $\phi(\rho z)$ of C Kα in C and W are plotted. This plot is shown in Figure 5.5, where the general trend is equal to the plot in the PAP paper, but there are some differences, for example that the curve in C is rounder and broader in the PAP paper. The plotting of $\phi(\rho z)$ was also compared to other sources, for example figure 19.9 in Goldstein [2, Fig. 19.9], which is adapted in Figure 2.29. The plotting of $\phi(\rho z)$

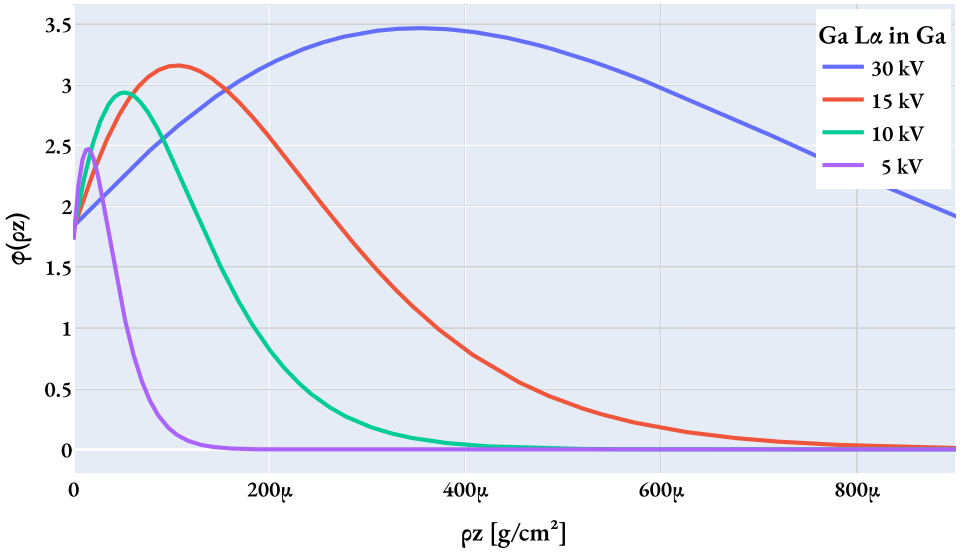

Figure 5.4: Plot of $\phi(\rho z)$ for Ga Lα in Ga. The curve is calculated with Equation (2.56). The plot shows three different beam energies, 30 kV (blue), 15 kV (red), 10 kV (green), and 5 kV (purple).

in Goldstein is done with the PROZA model [59], but the results should be similar to the XPP model. Figure 2.29 and Figure 5.6 are in general similar, but slight differences between $\phi(0)$ and the shape at the end of the curve can be seen, where the XPP model gives the curve a longer tail. These plots show that the XPP Python implementation is not perfect yet, but should be close enough to be useful. Possible sources of deviation is discussed towards the end of this section.

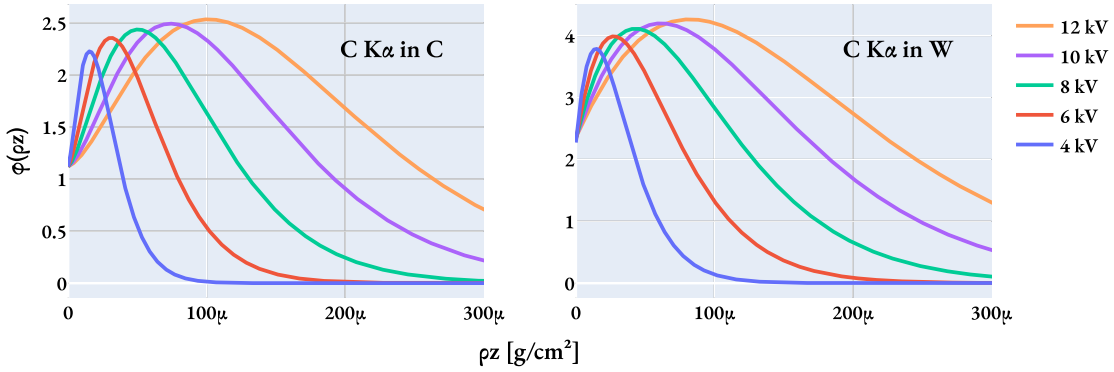

Figure 5.5: Plot of $\phi(\rho z)$ for C Kα in C and W, at different beam energies. The plot is used to compare the implementation of the XPP model to the PAP paper [9, Fig. 1 and 2].

Two type of bulk corrections from the XPP model were implemented and tested; (i) only corrected for the calculated generation of X-rays, and (ii) corrected for the ratio between the emitted and generated signal, i.e. the absorption factor. The first correction divide the measured intensity by F (see Section 2.5.3), which the area of the $\phi(\rho z)$ curve, i.e. the generated signal. This correction is supposed to correct for different Z, and should cover differences in factors like the critical ionization energy (see Section 2.1.3), and fluorescence yield (see Figure 2.3). The second correction divide the measured intensity by $f(\chi)$ (see Equation (2.47)), which is the XPP absorption factor.

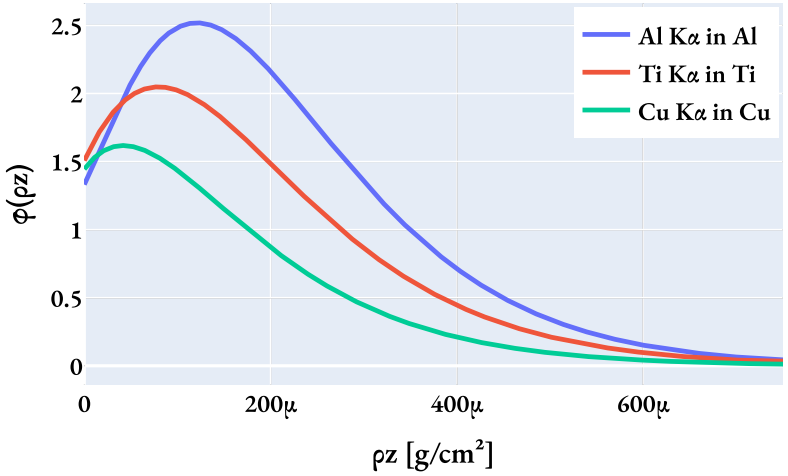

Figure 5.6: Plot of $\phi(\rho z)$ from the XPP model for Al Kα in Al, Ti Kα in Ti, and Cu Kα in Cu, with beam energy 15 kV. Comparison of the plot can be done with Figure 2.29, which is an adapted figure from Goldstein [2, Fig. 19.9].

The correction with $f(\chi)$ is supposed to correct for both atomic number Z and absorption A, as the calculated absorption factor is dependent on both F and $F(\chi)$, where $F(\chi)$ is the $\phi(\rho z)$ curve with absorption correction in each layer. F and $F(\chi)$ are illustrated in Figure 5.7. The two corrections were tested because of the implications of the previously discussed results, where GaAs need absorption corrections, while GaSb also need corrections for different Z.

The corrections with the XPP model presented in Table 4.14 show that the corrections needed differ between the two specimen. This was expected, as the materials have different properties for generation and absorption of X-rays. The GaAs specimen is corrected best with $f(\chi)$, and the results from this absorption correction is better than from the ZAF correction. The F correction on GaAs from the uncorrected results is only giving an improvement from 12 at.% to 11 at.%. This is an implication that the Z effects alone are not that strong in GaAs, but the combination of Z and A corrections gave the best results. The GaSb specimen is corrected best with F, which implies that the Z effects are most important for this specimen. As the results show, the 10 kV and 15 kV GaSb spectrum are corrected quite nicely with the F correction, but the 30 kV spectrum is pushed away from the reference value. Overall, the average quantification deviation in GaSb is both 6 at.% at the uncorrected and the F corrected results, while the $f(\chi)$ corrected results have a large deviation at 38 at.%.

The large deviation in the $f(\chi)$ corrected results for GaSb is probably caused by the μ_ρ values used in the calculation of $F(\chi)$. Section II.E in the PAP paper is discussing the absorption coefficients for the PAP model, and Appendix 5 [9, p. 63] in the paper lists some values for μ_ρ associated with the PAP procedure. These numbers are in the same range as the numbers provided by HyperSpy, but there are noticeable deviations. All the following examples for μ_ρ are in units of cm^2/g. For example, the line As Lα in GaAs bulk is given $\mu_\rho = 7000$ in the PAP paper, and the value $\mu_\rho = 3744$ by HyperSpy. Cu Lα in pure Cu is given $\mu_\rho = 1755$ in the PAP paper, and $\mu_\rho = 1515$ by HyperSpy. Cu Lβ in pure Cu is given $\mu_\rho = 6750$ in the PAP paper, while HyperSpy give $\mu_\rho = 8763$

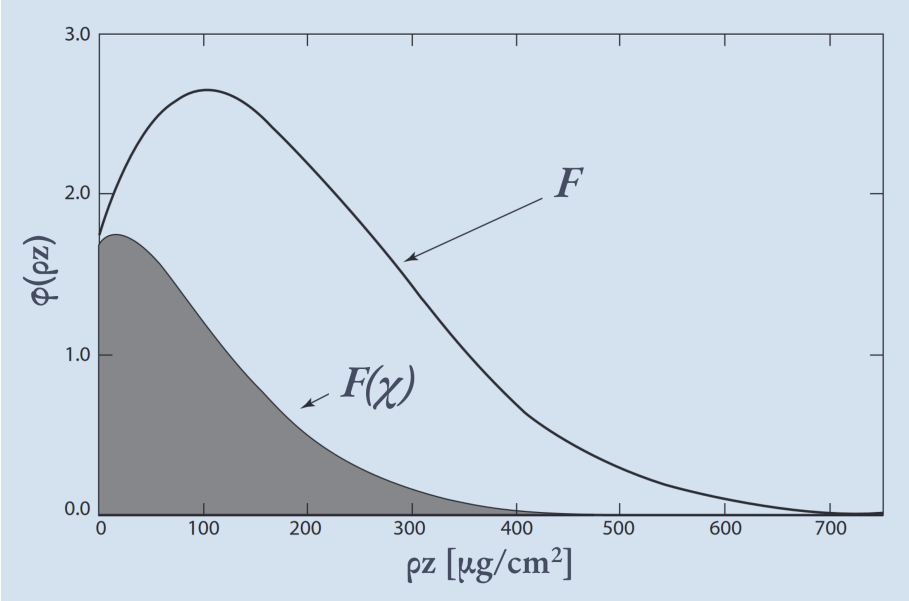

Figure 5.7: Illustration of F and $F(\chi)$. F is the area of the $\phi(\rho z)$ curve, while $F(\chi)$ is the area of the $\phi(\rho z)$ curve with absorption correction in each layer. F is the generated signal, while $F(\chi)$ is the emitted signal. $f(\chi) = F(\chi)/F$ is the absorption factor. The $\phi(\rho z)$ curve is for Al Kα in a Cu matrix at $E_0 = 20$ keV. Adapted from [2, Fig. 19.14].

for Cu Lβ_1. These deviations are almost certainly a source of error, which should lead to some adjustments of the XPP equations. Improvements to the values could be found through simulations, and should be confirmed with empirical measurements. Additionally, misidentifications of peaks are important for the value of μ_ρ, because the value is dependent on the elements present and their concentrations. It may be that the presence of C contamination on both specimen, and possible O on GaSb, are a source of error, as additional elements change the materials absorption capabilities. However, the C and O contamination are only on the surface, and their effect is limited. As explained in Section 5.3.3, the value of μ_ρ is critical because it is in the exponent of the absorption calculation. Such corrections might have been published as an update to the PAP/XPP procedure in a more recent paper. If this is a source of error, it can explain why the AZtec software is getting better results, because Oxford Instruments have gradually refined their input parameters and equations through testing.

In this work, the μ_ρ values from HyperSpy were used, and as the package is emergent from the TEM community, the values could be less accurate at low voltages. The original source is NIST standard reference database 66, mentioned in Section 2.1.1, where it is stated in the documentation of the database that the values are less accurate between 0.03 keV to 3 keV, and around absorption edges [24]. Further, the documentation to the NIST database state that revised values for μ_ρ can lead to "significant qualitative and quantitative improvement" [24][6].

The results from the two specimen show that the corrections needed are not universal. Correcting for absorption when it is not needed can lead to worse results, as seen in the GaSb specimen. The best results for the GaAs spectra is obtained with a combination of Z and A effects through the $f(\chi)$ correction, while the best results for the

[6] https://www.nist.gov/pml/nist-x-ray-form-factor-attenuation-and-scattering-tables-database-cont, accessed 26.05.23.

GaSb spectra is obtained with the Z effect through the F correction. This implies that the best results are obtained by using different corrections tailored for different specimen. It may be that such a solution is implemented in the AZtec software, for example that absorption effects are taken into account if certain conditions are met. Even though Oxford Instruments refer to the XPP model in the original PAP paper, the exact equations used in their commercial software is not published. Refining input parameters and adjusting the equations requires extensive testing and validation on different elements and specimen. Just testing different elements is not enough, as seen in the results where the Ga signal is behaving differently depending on the other element in the specimen. With the right corrections applied to the specimen of interest, the quantitative EDS results can be improved. Such corrections should be in an open-source software package, where the documentation is clear, and the code is available for inspection and modification. This would allow better EDS results and more reliable quantification, leading to higher quality research from the EDS community.

Another possible improvement to the XPP model is to use numerical solutions instead of analytical solutions. The original PAP paper is using analytical solutions to the equations, but with the computer power available in standard computers today, the equations could be solved numerically. This could lead to more accurate results, as the analytical solutions are approximations of the numerical solutions. Testing out numerical calculations of the $\phi(\rho z)$ curves can be done in future works, to see if the corrections can be improved.

Other correction models, such as the PROZA96 model [59], should also be tested in future work. The PROZA96 model can be implemented with the code developed in this work as a starting point, because there are overlapping parts between the models. The paper by Bastin et al. [59] which presents the PROZA96 model is referring to the PAP paper for calculations of the area F of the $\phi(\rho z)$ curves. This code can be copied from the XPP model. However, if the main issue is the input parameters like the μ_ρ values, the PROZA96 model might suffer from the same problems as the XPP model developed in this work. Other models which are not based on relative intensities, like the PAP and PROZA96 models, could also be tested in parallel in future works. Such models, like the Zeta method for thin specimen [3, Ch. 35.5], require the probe current as an input parameter. Measuring the probe current is not possible with the equipment available in this work, but a Faraday cup could be installed in the SEM to test out such models [2].

5.3.5 Bulk correction summary

SEM EDS analysis through AZtec can provide accurate results, which are better than the bulk corrected results from the XPP model implemented in this work. The XPP model implemented in this work is far from finished, but it is a starting point for future work. Earlier attempts[7][8] have been made to implement ZAF corrections for SEM EDS quantification in HyperSpy, but these have stagnated. The stagnation is probably in part due to the aforementioned issues with the input parameters, and that ZAF corrections may be less suited for a wide range of specimens, which $\phi(\rho z)$ corrections like the XPP model are. In other words, bulk corrections from the XPP model are probably better suited than ZAF for HyperSpy or similar software packages.

[7] Issue #800: https://github.com/hyperspy/hyperspy/issues/800
[8] Issue #2332: https://github.com/hyperspy/hyperspy/issues/2332

As discussed, the model coded in this project can be improved by refinement of the input parameters, by testing on different specimen, applying restrictions for which corrections to use in which cases, and by refining the code. There might still be errors in the implementation, and even the interpretation of the equations to use, but the general trend of the model is an improvement of the results. The corrections used suggest that the model is working, but still needs refinement. The refinement needed are probably both in the input parameters and in the implementation of the equations in the notebook. Regardless of this, the code developed and the work done is a step towards better EDS through open science.

Chapter 6

Conclusions

This chapter gives the conclusions from the work in this thesis. First all the sub-conclusions from the discussion are given, and then the main conclusion of this work is given. The aim of this work, to improve SEM EDS analysis, is put into perspective. Suggestions for future work are given in Chapter 7.

The two voltage series acquired yielded poor spectra for the 5 kV and 10 kV spectra, due to few counts, because the beam current was constant and set by a DT limit at 30 kV. The lower quality spectra were useful to see how the selected performance parameters varied with quality. Acquiring better voltage series can be done with a constant ICR, i.e. compensating for lower E_0 with higher i_b. Another possible solution is to keep i_b constant, but use a lower PT to get sufficient amount of counts at all voltages.

Achieving good spectra requires enough counts in the peaks, which is affected by E_0, i_b, and PT. Overvoltage of 1.4 gave issues, and the recommendation to use at least 1.5 might be too low. Variation in PT affect the energy resolution and the OCR, i.e. the throughput. A small reduction in energy resolution to greatly increase the throughput is in general recommended, i.e. using a medium to high PT, but not the highest.

DT is traditionally used as a practical measure to limit coincidence events, but this is outdated as it is based on Si(Li) detectors. The results and discussion show that DT as a guide is limited, as it only gives information about total acquisition time. The shift to SDDs requires that acceptable rates for coincidence events are found through testing.

Finding acquisition settings which give a suitable low level of coincidence events must be done with a test spectrum. In general, coincidence events are first present at very high ICR. Most of the spectra acquired in this work had low levels of coincidence events. This is probably due to the relatively low ICR used, compared to the capability of the detector. Additionally, the software used, AZtec, could have reduced the amount of coincidence events by automatic routines, but as the software is poorly documented, this is not confirmed.

Achieving good model fit is important in EDS analysis, and the fit is dependent on the inputs, which are the expected elements, E_0, and the data points in the spectrum. The elements must be correct and artifacts, such as

coincident events and escape peaks, must be identified, which is done by a through qualitative analysis. Mislabeling of elements in a qualitative analysis is less probable with well-spaced peaks, i.e. at higher energies and with better energy resolution. The latter is achieved with higher PT. Additionally, the wellness of the fit should always be inspected visually. When the elements are set correct, a computer can separate peaks better than the human eye, and thus in the analysis spectrum the PT can be lowered in favor of a higher throughput. The data points used in the model fit should not include the noise peak, and preferably not low energy peaks if they are not of interest. Slicing the spectrum at the effective beam energy will also improve the fit slightly, and prevents extrapolated values above E_0 if the model later is plotted.

The collimator on the here used EDS detector is working as intended, based on that the spectra have low amount of stray radiations. However, there are carbon contamination present in the chamber or on the specimen analyzed, which affects the surface of the specimen. Post acquisition BSE images show darker areas on the specimen, which are due to carbon deposition after beam exposure. In addition to the C peak, the GaSb spectra show a low peak which match with the O Kα peak. Regarding the metrics and quantification, both the peak from C and O are below the lines of interest in this work.

Another low energy line observed in the GaSb spectra is the Sb Mζ peak. No Sb M-lines are tabulated in the HyperSpy library [15] or the X-ray Data Booklet [28], but the line is clearly visible in the GaSb spectra, and not in the GaAs spectra. The line was identified as Sb Mζ through AZtec, the plot of μ_ρ, and Y. Liao [35]. A signal in the GaSb spectra was also observed from the Sb Mγ line, but this signal was weak.

The EDS detector used, an Oxford Instruments X-max^N detector, was confirmed to be well calibrated, at least for peaks above 1 keV. The spectra recorded had scale and offset which match the settings used in the acquisition, and the recorded peak deviations were deviating at most ±2 eV from the expected peak positions. The lower energy peaks of C and O from contamination and surface alteration showed a bigger deviation from the expected peak positions. If the lower energy peaks are to be analyzed, the acquisition parameters and processing routines should be optimized, and the spectra acquired should be calibrated for the lower energy peaks.

The peak ratios recorded, which show a difference between Ga Kα/Lα in GaAs and GaSb, indicate relative absorption differences between the two materials. The α/β ratios have not been systematically analyzed, but does not seem to indicate relevant information on the setup characteristic. Peak ratios can be used to assess stray radiations, but this requires special specimen geometries with for example a grid where the grid pattern is outside the targeted area, and such geometries were not used in this work.

The Duane-Hunt limit can be used to check the metadata value of E_0, specimen charging, and to verify the conductive path between the specimen and ground, which both are important for quantification. The metric does not need much interpretation, as it is a simple pass/fail test. If the deviation is too high, e.g. > 1 keV, the specimen and setup must be checked for errors. All the Duane-Hunt limits calculated in this work were well within the accepted range, with an average deviation of 0.06 keV.

The Fiori P/B ratio is useful to assess the quality of an acquired spectrum from the selected settings, but the use of

the metric to compare different detectors is limited. The Fiori metric is highly dependent on the specimen (GaAs > GaSb, and pure > mixture), and thus comparing different detectors requires that the same (standard) specimen is used. If the Fiori metric is used to compare different detectors, it is also important to calculate the metric the same way, and using model fitting is both recommended and the closest solution to the original definition of the metric. As the metric is dependent on the acquisition settings, it could be used to find the optimal settings for a given specimen. When a spectrum is recorded, and the counts in the background and peaks increase equally much, the Fiori metric will be constant. Using this fact, the metric can be used to find out where longer acquisition time or higher ICR would not increase the SNR, i.e. having a constant quality. In other words, finding the acquisition settings which give enough counts at a quality limit. This is useful to acquire higher resolution, bigger areas, or more spectra in the same time, or to reduce the acquisition time on expensive equipment.

To conclude on the first part on performance parameters: The EDS detector used is performing well, and are within the specifications. The energy resolution at 127 ± 6 eV is as the specifications, and the energy axis is calibrated well. The Duane-Hunt limits are correct. The highest Fiori P/B achieved was 770 for GaAs, and 410 for GaSb. The Python notebook for testing an EDS point spectrum is available under the MIT license at the author's GitHub page[1]. The output of the notebook can be used to compare previous and future evaluations of the setup, and an example from the 30 kV, 50 pA, PT 6 GaAs spectrum is shown in Table 6.1.

Table 6.1: Performance parameters from the 30 kV, 50 pA, PT 6 GaAs spectrum. ICR was 16.4k cps and DT was 44%.

Metric and unit	Value
Duane-Hunt limit [kV]	NaN
Scale [keV]	0.01005
Offset [keV]	0.19385
Energy resolution [eV]	129
Ratio (Ga Kα/Ga Lα)	0.91
Ratio (Ga Lα/As Lα)	2.37
Fiori P/B (Ga Lα)	586
Fiori P/B (As Lα)	236
Fiori P/B (Ga Kα)	762

Regarding the second aspect, bulk quantification routines, different approaches were tested. Assessing the quality of different quantification results based on a reference goal at 50 : 50 for Ga to As or Sb, which is known to be the composition in the analyzed specimens, is not an ideal solution. Two errors can cancel each other out. However, doing this is gives implications for how the corrections are weighed, and is regarded as sufficient for this work, when used with caution. To compare and develop quantification routines it is seen as a practical approach.

[1] https://github.com/brynjarmorka/sem-eds-qc/blob/main/SEM_EDS_performance_parameters.ipynb

The analysis and metrics recorded in this work showed that the GaAs spectrum needed absorption corrections, while the GaSb spectrum needed primarily Z corrections. In other words, the need for corrections is dependent on the specimen and the specific lines used. Achieving high quality quantification at low E_0 requires caution and tailoring, as the issues with overvoltage and absorption sensitivity are more prominent.

When quantifying SEM EDS spectra, AZtec can give accurate results, but the software is a black box and lacks proper user-end documentation. The results from the uncorrected and bulk corrected quantification routines implemented in the code in this project could not match the results from AZtec. The quantification in AZtec is using XPP bulk corrections, which can correct for both GaAs and GaSb, if implemented correctly.

The quantification of SEM EDS data with the thin film approximation based on Cliff-Lorimer is unreliable, both in AZtec and HyperSpy, and should be avoided.

The ZAF absorption correction routine implemented in this work is most useful as an indicator of possible improved results with absorption corrections. The assumption in Goldstein [2] that the Z effects in a specimen cancel out is observed to not be true for GaSb, but is to a degree true for the GaAs results, where the elements are close in atomic number. The implementation used show that the method could provide reasonable results, but that the specific implementation is too simple.

The XPP corrections implemented, for the first time in open-source Python code, could both be used for the GaAs and GaSb specimen, as the model can be used to give different corrections based on the needs of the specimen. The GaAs specimen was best corrected with $f(\chi)$, i.e. XPP absorption corrections, where the average deviation from $50:50$ was 5 at.%. The GaSb specimen was best corrected with F, i.e. XPP Z corrections, where the average deviation from $50:50$ was 6 at.%. Plots of the implemented XPP model show that there are some differences to the literature, but the model is close enough to be used. The differences are probably both due to the implementation, which is not guaranteed to be bug free, and the input parameters, which can change the output of the model drastically. One input parameter with major effects is the mass absorption coefficients (μ_ρ), which needs refinement. Values for μ_ρ were found through HyperSpy, which are less accurate at the relevant energies ($0.03 - 3$ keV) and around absorption edges, and these values are not quite equal to the values given in the paper that presents the XPP model.

A complete quantification routine for SEM EDS data must give different corrections based on the specimen. This is most likely done in AZtec, where Oxford Instruments has refined the equations and input parameters of their model. The XPP model implemented in this work is a good start, but it needs to be optimized further. It needs refinement for the input parameters and equations, squashing of bugs, and extensive testing. The results show that the model can work, but is not perfect.

The work in this thesis is split into two parts, where both are aimed at improving the performance of SEM EDS analysis. To summarize the conclusions: The first part illustrate how an analyst can assess the performance of a detector and selected acquisition settings. This is important to achieve good spectra, as it is always important to "know your equipment". The metrics tested are suited for SEM EDS analysis, obtained via an EDS point analysis

and calculated with the developed notebook. The notebook can be developed further into a more complete test routine, and the theory chapter can be used as a reference for the metrics. The second part of this work is aimed at improving the quantification of SEM EDS data, with open-source bulk corrections in Python. The results show that the XPP correction model is a good start, and a more promising path than ZAF corrections, but the XPP model needs refinement. The present study is a step towards better EDS analysis through open science.

Chapter 7

Future work

The goal of improving SEM EDS analysis had to be narrowed down in this work. This final chapter will discuss possible future work based on the results and discussion in the previous chapters. The suggestions listed in this chapter are both the previously mentioned possibilities, and other ideas that have emerged during the work. The first part are directed towards the previously mentioned possibilities, and they are:

1. Improved model fitting with spline and μ_ρ
2. M-lines for Z < 57
3. Corrections for uneven surfaces
4. Low energy calibration
5. Acquiring better voltage series
6. The usefulness of the Duane-Hunt limit
7. The usefulness of the Fiori P/B ratio
8. Testing the results with other specimens and compositions
9. Refining the input parameters for the XPP corrections, especially μ_ρ
10. Refining the equations for the XPP corrections
11. Testing numerical solutions for the XPP model
12. Testing the PROZA96 model

Modern EDS analysis is typically containing some sort of model fitting, and the work in this thesis is no exception. One possible improvement is to use a more advanced model for the background, such as a spline. It is observed in this work, and in the author's project report [36], that the background typically decrease drastically after a strong absorption edge, especially if the absorption edge is in the lower energy range. The polynomial background cannot

model abrupt changes, and will compensate with a poorer fit around the absorption edge. As the peak that gives this absorption edge is typically the peak of interest, it would be beneficial to have a better model for the background. Combination of μ_ρ can be used to estimate where the absorption edge is, and this can be used as an input to the model. Then the background can be modeled as a spline, having one node before the absorption edge and one after.

Another improvement to model fitting, especially in the lower energies, is to investigate the possibility of using M-lines for elements with Z < 57. It is observed in this work that the Sb Mζ line is visible in the spectrum, but as it is not present in the HyperSpy library, it is not used in the analysis and not in the model fitting. The interest of M-lines should be even higher for TEM EDS, as the absorption in the bulk is much lower than in bulk specimen, and thus the M-lines should be easier to detect and use.

Implementation of corrections for uneven surfaces could provide very useful. EDS analysis of uneven surfaces is readily done, even if the results are less accurate than for flat surfaces. The effect of uneven surfaces is complex, but through work with empirical data and simulations could lead to a correction method, based on the surface roughness and composition. First step towards such corrections would proper open-source bulk corrections for flat surfaces, which should be documented well so that further work is easier to do.

The peaks below 1 keV were not of interest in the metrics and compositional analysis in this work, but it was observed that the calibration in this region was poorer than above 1 keV. The calibration above 1 keV had high accuracy, but specific calibration routines for lower energy lines are probably needed to improve the calibration in this region.

When voltage series are of interest, it is important to achieve enough counts in all the spectra. The ICR decreases with lower voltage, if the i_b is kept constant, as it was in this work. Two possible suggestions to increase the amount of counts in a voltage series are to lower the PT, or to keep the ICR constant, by compensating with a higher i_b. The PT could for example be 4 instead of 6, which was shown to lower the DT much. The acquisition time could also be increased, but it is more efficient to use a slightly lower PT or compensate with a higher i_b. Both solutions could yield more comparable voltage series than the ones in this work.

The Duane-Hunt limit should be included in a test for SEM EDS performance parameters, as the metric is important to verify E_0 and the conductive path. A sophisticated and complete test routine could hide the metric when the detector is performing well, and give warnings when the deviations are too large. This is in general a good idea for metrics that test the performance, as it prevents an information overflow.

The Fiori P/B ratio should be investigated further to see if it can be used to optimize the acquisition settings for specific specimens. The metric might be used to find the ceiling where more counts does not improve the quality of the spectra, and are thus just a waste of time and resources. The Fiori metric could also be used to figure out when two peaks are overlapping too much for the computer to separate them properly. If the metric of two peaks change when the energy resolution is changed, but other acquisition parameters are kept constant, the peaks are probably overlapping too much.

The code developed for bulk corrections were not tested extensively, as it was only compared to a reference goal of 50 : 50. This was viewed as sufficient in this work to get indications for the different models, but the code should be tested more thoroughly. An extensive analysis of the code with specimen composed of multiple different elements should be done.

One of the potential main improvements to the bulk correction models are refinement of the input factors, especially μ_ρ. Deviations were observed between the listed values in the original PAP paper [9] and values used in this work from HyperSpy [15], which are from a NIST database [24]. The input parameters are important for accurate results, and should be investigated further.

The implementation and use of the XPP corrections can benefit from refinements too. The developers behind AZtec have had many years to refine their equations, and the equations used in this work are not as refined. As the XPP corrections apparently work well in AZtec, similar results should be achieved with refinements of the code in this work.

Another possible way to improve the XPP corrections is to use analytical solutions instead of numerical solutions. The original paper on XPP corrections [9] uses analytical solutions, but the equations could be solved numerically too, which may increase the accuracy.

In addition, or in comparison, to the XPP model, the other models like PROZA96 could be implemented and tested. The code in this work can be used as a starting point for the PROZA96 model, as there are overlaps between the two models. Alternatively, absolute intensity models can be tested, where the probe current is needed as an input parameter. The probe current can be measured with a Faraday cup, and would be used to calculate the absolute intensity of the X-rays, instead of the relative intensity used in the XPP model.

Other ideas for work that could be done is briefly discussed below. The test routines for the performance of a SEM EDS setup implemented in this work is not complete, and there are other tests that could be done. Useful expansion of the performance test would be on linearity, stability, shadowing, optimal WD, and detector efficiency. Additionally, a short comment is made on the use of principal component analysis (PCA) for noise reduction in EDS maps, and completing the XPP correction model, where input specimen have unknown composition.

In Goldstein [2, p. 232] it is stated that the two most important tests for an EDS detector are linearity and stability. This is stated in the section about what to look for when buying a detector. The reason for not including these two test in the work is that they depend on the measurement of the probe current. Linearity of the detector is that the number of X-rays measured is proportional to the number of X-rays generated. Stability is that the detector resolution and the peak positions does not change significantly with different probe currents. Both tests require multiple spectra of the same sample with different probe currents. The ISO 22309 standard on quantification of EDS spectra [50] also mentions these two tests.

Shadowing is another important test, as shadowing can reduce the net active sensor area of the detector, which reduce the counts registered. Shadowing can for example be caused by an erroneously mounted collimator, or by other parts in the SEM chamber. A description of how to test for shadowing is given in [72].

A test for the optimal WD could also be important, to verify if the WD that the SEM software suggest actually is the optimal one. This would be done by measuring identical spectra with different WD, plot the intensity of a major peak as a function of WD, and find the WD that gives the highest intensity. In the spectra, E_0, i_b, and live time must be kept constant. Any specimen should be suitable for this test. An EDS spectrum map, acquired at the found optimal WD, can be acquired to verify if the center of the map is the most intense area. The center of the map is the intersection of the electron beam axis and the detector axis on the specimen, and should be the most intense area if the WD is optimal.

The detector efficiency, illustrated in Figure 2.17, is more influential in SDDs than in Si(Li) detectors. Calculating the detector efficiency is not trivial [69], and is most accurately done with radiation from a synchrotron. As the illustration shows, the detector efficiency in SDDs change with energy, and thus a calculation with a normal EDS spectrum requires many peaks. The EDS-TM002 test specimen from BAM [69] can be used, and inspiration from this specimen and their routine can be a starting point.

Aside from the test routines, there are other ideas for future work. In the work of Skomedal [20], PCA is shown to be useful in noise reduction of EDS maps. PCA is a statistical method that reduces the dimensionality of a dataset [73], and is used in many fields. For EDS maps, PCA can be used to separate the signal from peaks and the noise (e.g. background), which could allow better qualitative and quantitative analysis. Maps were acquired in this work too, but there was not enough time to test out denoising routines properly.

The work done in this thesis on implementation of the XPP corrections can be viewed as the first iteration in a quantification routine. The XPP model, and other correction models, use composition as an input parameter. This is paradoxical, as the goal of the quantification is to find the composition. However, for unknown compositions, this is solved by iterating over the quantification routine multiple times, with an initial guess for the composition. As the results show, the XPP corrections are improving the results, but the results are not perfect. In other words, the first step in an eventual iterative routine is not good enough. First the accuracy of the XPP corrections should be improved, when the input composition is perfect, and later the iterative routine can be implemented. Doing the corrections in an iterative routine can be done with multiple initial guesses for the compositions, as the calculations in the model are not heavy. With multiple initial guesses, the best fitting results after iterations can be used as the final results. Implementing an iterative routine for the XPP model should not be too difficult, but it would be unnecessary in this work, as the first step is not accurate enough, yet.

Bibliography

[1] W. Callister and D. Rethwisch, *Materials Science and Engineering*. Wiley, 2014.

[2] J. I. Goldstein, D. E. Newbury, J. R. Michael, N. W. M. Ritchie, J. H. J. Scott, and D. C. Joy, *Scanning Electron Microscopy and X-Ray Microanalysis*. Springer, 4 ed., 2018.

[3] C. Carter and D. Williams, *Transmission Electron Microscopy: A Textbook for Materials Science*. Springer, 2 ed., 2009.

[4] R. Jenkins and J. L. De Vries, *Practical X-ray Spectroscopy*. Springer, 2 ed., 1982.

[5] J. M. Hollas, *Modern spectroscopy*. Wiley, 4 ed., 2004.

[6] M. Dehlinger, C. Fauquet, S. Lavandier, O. Aumporn, F. Jandard, V. Arkadiev, A. Bjeoumikhov, and D. Tonneau, "Spatial resolution of confocal XRF technique using capillary optics," *Nanoscale research letters*, vol. 8, no. 1, 2013.

[7] C. Fiori, C. Swyt, and J. Ellis, "The theoretical characteristic to continuum ratio in energy dispersive analysis in the analytical electron microscope," *Microbeam Analysis 1982*, pp. 57–71, 1982.

[8] W. Duane and F. L. Hunt, "On X-Ray Wave-Lengths," *Phys. Rev.*, vol. 6, pp. 166–172, Aug 1915.

[9] J.-L. Pouchou and F. Pichoir, "Quantitative analysis of homogeneous or stratified microvolumes applying the model "PAP"," *Electron Probe Quantitation*, pp. 31–75, 1991.

[10] G. Cliff and G. W. Lorimer, "The quantitative analysis of thin specimens," *Journal of Microscopy*, vol. 103, no. 2, pp. 203–207, 1975.

[11] J. S. Nilsen and A. T. van Helvoort, "Composition analysis by STEM-EDX of ternary semiconductors by internal references," *Microscopy and Microanalysis*, vol. 28, pp. 61–69, 2021.

[12] V. Tchantchaleishvili and M. Wilson, "The importance of free and open source software and open standards in modern scientific publishing," *Publications*, vol. 1, 06 2013.

[13] ISO 22029:2022, "Microbeam analysis — EMSA/MAS standard file format for spectral-data exchange," Standard 3, Microbeam analysis, 2022. Accessed 16.02.23 at https://www.iso.org/standard/78268.html.

[14] N. Ritchie, "Getting Started with NIST DTSA-II," *Microscopy Today*, vol. 19, 01 2011.

[15] F. de la Peña, E. Prestat, V. T. Fauske, P. Burdet, J. Lähnemann, P. Jokubauskas, T. Furnival, M. Nord, T. Ostasevicius, K. E. MacArthur, D. N. Johnstone, M. Sarahan, T. Aarholt, J. Taillon, pquinn dls, V. Migunov, A. Eljarrat, J. Caron, C. Francis, T. Nemoto, T. Poon, S. Mazzucco, actions user, N. Tappy, N. Cautaerts, S. Somnath, T. Slater, M. Walls, F. Winkler, and DENSmerijn, "Hyperspy/hyperspy: Release v1.7.4," May 2023.

[16] P. Virtanen, R. Gommers, T. E. Oliphant, M. Haberland, T. Reddy, D. Cournapeau, E. Burovski, P. Peterson, W. Weckesser, J. Bright, S. J. van der Walt, M. Brett, J. Wilson, K. J. Millman, N. Mayorov, A. R. J. Nelson, E. Jones, R. Kern, E. Larson, C. J. Carey, İ. Polat, Y. Feng, E. W. Moore, J. VanderPlas, D. Laxalde, J. Perktold, R. Cimrman, I. Henriksen, E. A. Quintero, C. R. Harris, A. M. Archibald, A. H. Ribeiro, F. Pedregosa, P. van Mulbregt, and SciPy 1.0 Contributors, "SciPy 1.0: Fundamental Algorithms for Scientific Computing in Python," *Nature Methods*, vol. 17, pp. 261–272, 2020.

[17] R. Egerton and S. Cheng, "Characterization of an analytical electron microscope with a nio test specimen," *Ultramicroscopy*, vol. 55, no. 1, pp. 43–54, 1994.

[18] Ted Pella, Inc., Redding, CA, USA, *Technical Notes: Evaluating an Analytical TEM with the NIOX Test Specimen*, 2019. Accessed 10.02.23 at https://www.tedpella.com/.

[19] I.-E. Nylund, "Evaluation of energy-dispersive spectroscopy characteristics for improved compositional analysis," Master's thesis, Norwegian University of Science and Technology, 2017.

[20] M. S. Skomedal, "Improving quantitative EDS of III-V heterostructure semiconductors in low voltage STEM," Master's thesis, Norwegian University of Science and Technology, 2022.

[21] P. Lechner, C. Fiorini, R. Hartmann, J. Kemmer, N. Krause, P. Leutenegger, A. Longoni, H. Soltau, D. Stötter, R. Stötter, L. Strüder, and U. Weber, "Silicon drift detectors for high count rate X-ray spectroscopy at room temperature," *Nuclear Instruments and Methods in Physics Research Section A: Accelerators, Spectrometers, Detectors and Associated Equipment*, vol. 458, no. 1, pp. 281–287, 2001.

[22] S. Burgess, "Oxford Instruments blog post: "How to overcome challenges in publishing EDS results"?," 2021. Accessed 10.02.23 at https://www.oxinst.com/blogs/how-to-overcome-challenges-in-publishing-eds-results.

[23] Oxford Instruments, "AZtec user manual," 2013. Accessed 20.01.23 at https://utw10193.utweb.utexas.edu/InstrumentManuals/Oxford%20EDS%20AZtec%20User%20Manual.pdf.

[24] C. Chantler, K. Olsen, R. Dragoset, J. Chang, A. Kishore, S. Kotochigova, and D. Zucker, "Detailed Tabulation of Atomic Form Factors, Photoelectric Absorption and Scattering Cross Section, and Mass Attenuation Coefficients for Z = 1-92 from E = 1-10 eV to E = 0.4-1.0 MeV." Standard Reference Database 66 from the National Institute of Standards and Technology, Gaithersburg, MD., 2005. Accessed 16.04.23 at https://

www.nist.gov/pml/x-ray-form-factor-attenuation-and-scattering-tables, also published in J. Phys. Chem. Ref. Data 29, pp. 597-1048, 2000.

[25] T. S. Curry, J. E. Dowdey, and R. C. Murry, *Christensen's Physics of Diagnostic Radiology*. Lippincott Williams and Wilkins, 4 ed., 1990.

[26] R. Jenkins, R. Manne, R. Robin, and C. Senemaud, "IUPAC - Nomenclature system for X-ray spectroscopy," *Pure and Applied Chemistry (IUPAC Publications)*, vol. 63, no. 5, pp. 735–746, 1991.

[27] M. Siegbahn, "Relations between the K and L Series of the High-Frequency Spectra," *Nature*, vol. 96, pp. 676–676, Feb. 1916.

[28] A. C. Thompson, D. T. Attwood, M. R. Howells, J. B. Kortright, A. L. Robinson, J. H. Underwood, K.-J. Kim, J. Kirz, I. Lindau, P. Pianetta, H. Winick, G. P. Williams, and J. H. Scofield, *X-Ray Data Booklet*. Lawrence Berkeley National Laboratory, University of California, 2 ed., 2004.

[29] R. D. Deslattes, E. G. Kessler, P. Indelicato, L. de Billy, E. Lindroth, J. Anton, J. S. Coursey, D. J. Schwab, C. Chang, R. Sukumar, K. Olsen, and R. A. Dragoset, "NIST Standard Reference Database 128: "X-ray Transition Energies (version 1.2)"." National Institute of Standards and Technology, Gaithersburg, MD., 2005. Accessed 16.04.23 at http://physics.nist.gov/XrayTrans.

[30] M. Inokuti, "Inelastic collisions of fast charged particles with atoms and molecules—the bethe theory revisited," *Rev. Mod. Phys.*, vol. 43, pp. 297–347, Jul 1971.

[31] E. Lifshin, M. F. Ciccarelli, and R. B. Bolon, "Proceedings of the 8th international conference on x-ray optics and microanalysis," *Pendell Midland, Michigan*, p. 141, 1980.

[32] M. Watanabe and D. Williams, "The quantitative analysis of thin specimens: A review of progress from the Cliff-Lorimer to the new zeta-factor methods," *Journal of microscopy*, vol. 221, pp. 89–109, 2006.

[33] B. M. Notaros, *Electromagnetics*. Pearson, 1 ed., 2010.

[34] EDAX, "Background Analysis and Modeling," *EDAX Insight*, vol. 17, 09 2019.

[35] Y. Liao, "Practical electron microscopy and database," *An Online Book*, 2006.

[36] B. M. Mæhlum, "Improving qualitative and quantitative SEM EDS analysis with open-source data processing." Norwegian University of Science and Technology, 2022. Project report in TFY4520.

[37] J. A. Bearden and A. F. Burr, "Reevaluation of X-Ray Atomic Energy Levels," *Rev. Mod. Phys.*, vol. 39, pp. 125–142, Jan 1967.

[38] P. J. Goodhew, J. Humphreys, and R. Beanland, *Electron Microscopy and Analysis*. Taylor and Francis, 3 ed., 2001.

[39] T. E. Everhart and R. F. M. Thornley, "Wide-band detector for micro-microampere low-energy electron currents," *Journal of Scientific Instruments*, vol. 37, no. 7, pp. 246–248, 1960.

[40] T. Koshikawa and R. Shimizu, "Secondary electron and backscattering measurements for polycrystalline copper with a retarding-field analyser," *Journal of Physics D: Applied Physics*, vol. 6, no. 11, p. 1369, 1973.

[41] Oxford Instruments, "Silicon drift detectors explained," 2012. Accessed 20.02.23 at https://engineering.temple.edu/sites/engineering/files/Oxford%20EDS-%20Silicon%20Drift%20Detectors%20Explained.pdf.

[42] ASTM E1508-12a(2019), "Standard Guide for Quantitative Analysis by Energy-Dispersive Spectroscopy," standard, ASTM Subcommittee E04.11 on X-Ray and Electron Metallography, 2019.

[43] ISO 1532:2021, "Microbeam analysis — Selected instrumental performance parameters for the specification and checking of energy-dispersive X-ray spectrometers (EDS) for use with a scanning electron microscope (SEM) or an electron probe microanalyser (EPMA)," Standard 3, Microbeam analysis, 2021.

[44] D. E. Newbury and N. W. Ritchie, "Performing elemental microanalysis with high accuracy and high precision by scanning electron microscopy/silicon drift detector energy-dispersive X-ray spectrometry (SEM/SDD-EDS)," *Journal of Materials Science*, vol. 50, no. 2, pp. 493–518, 2015.

[45] K. Thompson, "Is Energy Resolution Still an Important Specification in EDS?," *Microscopy Today*, vol. 21, pp. 30–34, 07 2013.

[46] D. B. Williams, "Standardized definitions of X-ray analysis performance criteria in the AEM," *Microbeam Analysis 1986*, pp. 443–448, 1986.

[47] N. W. M. Ritchie, "DTSA-II." National Institute of Standards and Technology, 2007. Software available at https://cstl.nist.gov/div837/837.02/epq/dtsa2/index.html.

[48] N. W. M. Ritchie, "Manipulating Spectra with DTSA-II," *Microscopy Today*, vol. 19, pp. 34–39, 04 2011.

[49] M. Postek and A. Vladár, "Does Your SEM Really Tell the Truth?-How Would You Know? Part 4: Charging and its Mitigation," *Proceedings of SPIE–the International Society for Optical Engineering*, vol. 9636, 10 2015.

[50] ISO 22309:2011, "Microbeam analysis — Quantitative analysis using energy-dispersive spectrometry (EDS) for elements with an atomic number of 11 (Na) or above," Standard 2, Microbeam analysis, 2011.

[51] J. Bennett and R. Egerton, "NiO Test Specimens for Analytical Electron Microscopy: Round-Robin Results," *Microscopy and Microanalysis*, vol. 1, no. 4, pp. 143–149, 1995.

[52] Oxford Instruments, "Ultim Max," 2022. Accessed 10.02.23 at https://nano.oxinst.com/products/ultim-max.

[53] S. M. Zemyan and D. B. Williams, "Standard performance criteria for analytical electron microscopy," *Journal of Microscopy*, vol. 174, no. 1, pp. 1–14, 1994.

[54] EDAX, "Elite T EDS System for the TEM," *EDAX Insight*, vol. 16, 09 2018.

[55] R. Castaing, "Electron probe microanalysis," in *Advances in Electronics and Electron Physics* (L. Marton and C. Marton, eds.), vol. 13, pp. 317–386, Academic Press, 1960.

[56] J. Philibert, "X-ray Optics and X-ray Microanalysis," in *Advances in Electronics and Electron Physics*, pp. 317–386, Academic Press, 1963.

[57] S. Marks, "Oxford Instruments blog post: "What makes TEM EDS different from SEM EDS"?," 2022. Accessed 10.02.23 at https://www.oxinst.com/blogs/what-makes-tem-eds-different-from-sem-eds.

[58] K. MacArthur, T. Slater, S. Haigh, D. Ozkaya, P. Nellist, and S. Lozano-Perez, "Quantitative Energy-Dispersive X-Ray Analysis of Catalyst Nanoparticles Using a Partial Cross Section Approach," *Microsc. Microanal.*, vol. 22, pp. 71–81, 2016.

[59] G. F. Bastin, J. M. Dijkstra, and H. J. M. Heijligers, "PROZA96: an Improved Matrix Correction Program for Electron Probe Microanalysis, Based on a Double Approach Gaussian phi(rho z)," *X-Ray Spectrometry*, vol. 27, no. 1, pp. 3–10, 1998.

[60] P. Burdet, S. Croxall, and P. Midgley, "Enhanced Quantification for 3D SEM-EDS: Using the full set of available X-ray lines," *Ultramicroscopy*, vol. 148, 10 2014.

[61] K. Kanaya and S. Okayama, "Penetration and energy-loss theory of electrons in solid targets," *J. Phys. D. Appl. Phys.*, vol. 5, p. 43, 1972.

[62] G. F. Bastin and H. J. M. Heijligers, "Quantitative Electron Probe Microanalysis of Ultra-Light Elements (Boron-Oxygen)," in *Electron Probe Quantitation, Workshop at the National Bureau of Standards* (K. F. J. Heinrich and D. E. Newbury, eds.), pp. 145–161, Plenum Press, New York, 1988.

[63] R. H. Packwood and J. D. Brown, "A Gaussian expression to describe phi(rho z) curves for quantitative electron probe microanalysis," *X-ray Spectrometry*, vol. 10, no. 3, pp. 138–146, 1981.

[64] J. I. Goldstein, D. E. Newbury, P. Echlin, D. C. Joy, A. D. Romig, C. E. Lyman, C. Fiori, and E. Lifshin, *Scanning Electron Microscopy and X-Ray Microanalysis*. Springer, 2 ed., 1992.

[65] L. Reimer, *Scanning Electron Microscopy: Physics of Image Formation and Microanalysis*. Springer Series in Optical Sciences, Springer, 2 ed., 1998.

[66] V. D. Scott and G. Love, "The prospects of a universal correction procedure for quantitative EPMA," *Scanning*, vol. 12, no. 4, pp. 193–202, 1990.

[67] Oxford Instruments, "X-MaxN 20/50/80/150mm2 SDD - Technical Datasheet." Accessed 25.05.23 at https://smlouvy.gov.cz/smlouva/soubor/9628379/08_XMAX%20N%20TDS.pdf, 2016.

[68] D. Lundeby, "Improving the accuracy of TEM-EDX quantification by implementing the zeta-factor method," Master's thesis, Norwegian University of Science and Technology, 2019.

[69] V. Rackwitz, M. Krumrey, C. Laubis, S. Richter, F. Scholze, P. Wobrauschek, and U. Wätjen, "New reference and test materials for the characterization of energy dispersive X-ray spectrometers at scanning electron microscopes," *Anal. Bioanal. Chem.*, vol. 407, pp. 3045–3053, 2015.

[70] D. E. Newbury and N. W. M. Ritchie, "Quantitative SEM/EDS, Step 1: What Constitutes a Sufficiently Flat Specimen?," *Microsc. Microanal.*, vol. 19, pp. S2–S3, 2013.

[71] D. E. Newbury, "Misidentification of Major Constituents by Automatic Qualitative Energy Dispersive X-ray Microanalysis: A Problem that Threatens the Credibility of the Analytical Community," *Microsc. Microanal.*, vol. 11, pp. 545–561, 2005.

[72] M. Procop, V.-D. Hodoroaba, R. Terborg, and D. Berger, "Determination of the Effective Detector Area of an Energy-Dispersive X-Ray Spectrometer at the Scanning Electron Microscope Using Experimental and Theoretical X-Ray Emission Yields," *Microsc. Microanal.*, vol. 22, no. 6, pp. 1360–1368, 2016.

[73] I. Jolliffe, *Principal Component Analysis*. Springer Series in Statistics, Springer, 2002.

Appendices

Appendix A

Notebook: Performance parameters

This is the notebook for the SEM EDS performance parameters. The notebook is available on GitHub through this link[1]. The notebooks and code for the quantification and bulk corrections are located in the GitHub repository "eds-sem-bulk-corrections", under the user "brynjarmorka". The notebook below have headers which are listed in Section 3.4.2. The example spectrum run through in the notebook is the GaSb spectrum with 30 kV, 50 pA, and PT 6.

[1] https://github.com/brynjarmorka/sem-eds-qc/blob/main/SEM_EDS_performance_parameters.ipynb

SEM EDS performance parameters

June 1, 2023

1 Import the packages

[ ]:
```
import hyperspy.api as hs
import numpy as np
import pandas as pd
from helper_functions import elementlines, nearestlines, theoretical_energy
```

2 Select spectra, an specify settings like i_b, E_0, ICR, and PT

[ ]:
```
##### SEM Apreo March 2023 #####
path = '../../Masteroppgave/2023-03-08_EDS-Apreo/exports/'
# All data files are available in the repository at:
# https://github.com/brynjarmorka/eds-sem-bulk-corrections/tree/main/data

##### GaAs #####
elements = ['Ga', 'As']
lines_of_interest = ['Ga_Ka', 'As_Ka', 'Ga_La', 'As_La', 'Ga_Kb', 'As_Kb']
fiori_peaks = ['Ga_La', 'As_La', 'Ga_Ka']
line_ratio_list = [['As_Ka', 'As_La'], ['Ga_Ka', 'Ga_La'], ['Ga_La', 'As_La']]

# setting file name, beam current, input count rate and process time
file_current_ICR_PT = [
    ['GaAs_05kV_25pA.emsa', 25, 880, 6], # 0
    ['GaAs_10kV_25pA.emsa', 25, 1750, 6], # 1
    ['GaAs_15kV_25pA.emsa', 25, 3300, 6], # 2
    ['GaAs_30kV_25pA.emsa', 25, 8000, 6], # 3
    ['GaAs_30kV_50pA.emsa', 50, 16400, 6], # 4
]

##### GaSb #####
# Sb_Ka has to high energy
# elements = ['Ga', 'Sb']
# lines_of_interest = ['Ga_Ka', 'Ga_Kb', 'Ga_La', 'Sb_La', 'Sb_Lb1']
# fiori_peaks = ['Ga_La', 'Sb_La', 'Ga_Ka', 'Sb_Lb1']
# line_ratio_list = [['Ga_Ka', 'Ga_La'], ['Sb_La', 'Sb_Lb1'], ['Ga_La',␣
 ↪'Sb_La']]
```

```
# file_current_ICR_PT = [
#     ['GaSb_05kV_50pA.emsa', 50, 1080, 6], # 0
#     ['GaSb_10kV_50pA.emsa', 50, 2300, 6], # 1
#     ['GaSb_15kV_50pA.emsa', 50, 5700, 6], # 2
#     ['GaSb_15kV_200pA.emsa', 200, 22000, 6], # 3
#     ['GaSb_15kV_400pA.emsa', 400, 42000, 6], # 4
#     ['GaSb_30kV_50pA.emsa', 50, 17000, 6], # 5
#     ['GaSb_30kV_50pA_noPPUC.emsa', 50, 17000, 6], # 6
#     ['GaSb_30kV_50pA_processTime1.emsa', 50, 17000, 1], # 7
#     ['GaSb_30kV_50pA_processTime2.emsa', 50, 17000, 2], # 8
#     ['GaSb_30kV_50pA_processTime4.emsa', 50, 17000, 4], # 9
#     ['GaSb_30kV_400pA_processTime1.emsa', 400, 160000, 1], # 10
# ]

number = 4  # change ´number´ to change file
file = file_current_ICR_PT[number][0]
beam_current = file_current_ICR_PT[number][1]
input_count_rate = file_current_ICR_PT[number][2]
process_time = file_current_ICR_PT[number][3]

# common settings
make_info_on_all_lines = True
zero_peak_end_index = 40
model_background_order = 6
```

3 Import the data with HyperSpy, set the elements in the spectrum, and slice off the noise peak

[ ]:
```
def load_data(path, file, elements, zero_peak_end_index, plot_s=False):
    """Loading data with HS and adding the elements, eventually removing the␣
 ↪zero peak"""
    s = hs.load(path + '/' + file, signal_type='EDS_SEM')
    s.add_elements(elements)
    if zero_peak_end_index is not None:
        s = s.isig[zero_peak_end_index:]

    Vacc = s.metadata.Acquisition_instrument.SEM.beam_energy
    x = s.axes_manager[0].axis  # x-axis in keV
    name = f'{file[:-5]}'
    if plot_s:
        s.plot(xray_lines=True)
    return s, Vacc, x, name
```

[ ]:
```
s, Vacc, x, name = load_data(path, file, elements, zero_peak_end_index)
```

[ ]:
```
# these are temporary arrays used to show the effect of the calibrations
scale_list = [s.axes_manager[0].scale]
offset_list = [s.axes_manager[0].offset]
energy_res_list = [s.metadata.Acquisition_instrument.SEM.Detector.EDS.
 ↪energy_resolution_MnKa]
```

4 Calculate the Duane-Hunt limit, and slice the spectrum to the limit

[ ]:
```
# # Duane-Hunt method to find the real E_0
def calculate_duane_hunt(s=s, buffer_start=2, buffer_end=0.1,␣
 ↪xaxis_plot_buffer=0.5, dh_plot=False):
    x_max = s.axes_manager[0].high_value  # highest x-axis value in keV, used␣
 ↪in Duane-Hunt
    if Vacc > x_max:
        print(f'Vacc={Vacc} > x_max={x_max}, Duane-Hunt not possible')
        return np.nan
    else:
        s_dh = s.deepcopy()
        dh_start = Vacc-buffer_start
        dh_end = Vacc-buffer_end
        s_end = s_dh.isig[dh_start:dh_end] # slice with keV
        m_end = s_end.create_model(auto_background=False)
        m_end.add_polynomial_background(order=1)
        m_end.fit()
        x_s_end = s_dh.isig[dh_start-xaxis_plot_buffer:
 ↪dh_end+xaxis_plot_buffer].axes_manager[0].axis
        dh_bg_zero_index = np.argmin(np.abs(m_end[-1].function(x_s_end) * s_dh.
 ↪axes_manager[0].scale))
        dh_limit = x_s_end[dh_bg_zero_index]
        print(f'Duane-Hunt limit: {dh_limit:.3f} keV')

        return dh_limit
```

[ ]:
```
dh_limit = calculate_duane_hunt(dh_plot=False)
```

```
Vacc=30.0 > x_max=20.27, Duane-Hunt not possible
```

[ ]:
```
# Using Duane-Hunt to slice the spectrum
def use_dh_to_slice_spectrum(dh_limit=dh_limit, s=s, plot=False):
    if np.isnan(dh_limit):
        print('No Duane-Hunt limit found, not slicing the spectrum')
    else:
        s = s.isig[:dh_limit]
        print(f'Spectrum sliced at {dh_limit:.2f} keV')
        if plot:
```

```
            s.plot(xray_lines=True)
    return s
```

[ ]:
```
s = use_dh_to_slice_spectrum(dh_limit, plot=False)
x = s.axes_manager[0].axis  # x-axis in keV, after slicing
```

```
No Duane-Hunt limit found, not slicing the spectrum
```

5 Make a model of the spectrum, and fit it to the data

[ ]:
```
# creating a model and fitting it
def make_model(s=s, model_background_order=model_background_order,␣
 ↪plot_m=False):
    m = s.create_model(auto_background=False)
    m.add_polynomial_background(order=model_background_order)
    m.fit_background()
    m.fit(bounded=True)
    if plot_m:
        m.plot(plot_components=True)
    return m
```

[ ]:
```
m = make_model(s=s, model_background_order=model_background_order, plot_m=False)
```

[ ]:
```
def remove_lines_not_in_model(m=m, lines_of_interest=lines_of_interest,␣
 ↪line_ratio_list=line_ratio_list):
    lines_in_model = [c.name for c in m][:-1] # not including the background

    lines_to_remove = []
    for line in lines_of_interest:
        if line not in lines_in_model:
            # print(f'NB!: {line} not in model')
            lines_to_remove.append(line)

    line_ratio_to_remove = []
    for linepair in line_ratio_list:
        if linepair[0] not in lines_in_model or linepair[1] not in␣
 ↪lines_in_model:
            # print(f'NB!: {linepair} not in model, ratio not possible')
            line_ratio_to_remove.append(linepair)

    # remove the lines from the lists
    for line in lines_to_remove:
        lines_of_interest.remove(line)
    for linepair in line_ratio_to_remove:
        line_ratio_list.remove(linepair)
```

[ ]:
```
remove_lines_not_in_model()
```

6 Calibrate the offset and scale

[ ]:
```
def sort_lines(lines_of_interest):
    """Sort lines_of_interest by area, taking area from m[line].A.value
    Used because the calibrate_energy_axis(calibrate='resolution') use the␣
↪first line,
    and using the strongest line gives a good reference energy for the function␣
↪by
    Newbury and Fiori (1978), documented in Goldstein (2018).
    """
    lines_of_interest = sorted(lines_of_interest, key=lambda x: m[x].A.value,␣
↪reverse=True)
    return lines_of_interest
```

[ ]:
```
lines_of_interest = sort_lines(lines_of_interest)
all_lines = [l.name for l in m if not l.isbackground]
all_lines = sort_lines(all_lines)
```

[ ]:
```
def calibrate_axis(m=m, s=s, rounds=2, xray_lines=lines_of_interest):
    """Calibrating the scale and offset of the energy axis."""
    print('Calibrating energy axis (with many elements it can take multiple␣
↪minutes)')

    for i in range(rounds):
        print(f'Calibrating offset and scale, round {i+1} of {rounds}')
        m.calibrate_energy_axis(calibrate='offset', xray_lines=xray_lines)
        offset_list.append(s.axes_manager[0].offset)
        m.calibrate_energy_axis(calibrate='scale', xray_lines=xray_lines)
        scale_list.append(s.axes_manager[0].scale)

    print(f'Scale: {scale_list[-1]:.6f} eV/px \nOffset: {offset_list[-1]:.6f}␣
↪keV')
    return scale_list[-1], offset_list[-1]
```

[ ]:
```
scale, offset = calibrate_axis(rounds=2, xray_lines=lines_of_interest)
# using all lines gives basically the same result
# scale2, offset2 = calibrate_axis(rounds=1, xray_lines=all_lines)
```

```
Calibrating energy axis (with many elements it can take multiple minutes)
Calibrating offset and scale, round 1 of 2
Calibrating offset and scale, round 2 of 2
Scale: 0.010046 eV/px
Offset: 0.193846 keV
```

7 Calibrate the energy resolution

[ ]:
```
def calibrate_resolution(m=m, s=s, rounds=2, xray_lines=lines_of_interest[:3]):
    """
    Calibrating the energy resolution, i.e. the energy resolution at the Mn Ka␣
↪line.
    NB! The reference line is the first line in xray_lines, thus the first line␣
↪should be well defined.

    Using the three strongest lines to first calibrate the width, then estimate␣
↪the energy resolution,
    which is done with only the first line in lines_of_interest
    """
    for i in range(rounds):
        print(f'Calibrating energy resolution, round {i+1} of {rounds}')
        m.calibrate_energy_axis(calibrate='resolution', xray_lines=xray_lines)
        energy_res_list.append(s.metadata.Acquisition_instrument.SEM.Detector.
↪EDS.energy_resolution_MnKa)

    print(f'Calibrated energy resolution: {energy_res_list[-1]:.3f} eV')
    return energy_res_list[-1]
```

[ ]:
```
energy_resolution = calibrate_resolution()
```

```
Calibrating energy resolution, round 1 of 2
Calibrating energy resolution, round 2 of 2
Calibrated energy resolution: 128.676 eV
```

[ ]:
```
def print_calibration_info(scls=scale_list, offs=offset_list,␣
↪eres=energy_res_list):
    # make pretty print of calibration info
    infos = [' ', 'Scale [eV/channel]', 'Offset [keV]', 'E-res [eV]']
    row1 = ['Current', f'{scls[-1]:.6f}', f'{offs[-1]:.6f}', f'{eres[-1]:.3f}']
    row2 = ['Original', f'{scls[0]:.6f}', f'{offs[0]:.6f}', f'{eres[0]:.3f}']
    row3 = ['Δ original', f'{(scls[-1] - scls[0])/scls[-2]*100:.3f} %',
    f'{(offs[-1] - offs[0])/offs[-2]*100:.3f} %', f'{(eres[-1] - eres[0])/
↪eres[0]*100:.3f} %']
    row4 = ['Δ last step', f'{(scls[-1] - scls[-2])/scls[-2]*100:.3f} %',
    f'{(offs[-1] - offs[-2])/offs[-2]*100:.3f} %', f'{(eres[-1] - eres[-2])/
↪eres[-2]*100:.3f} %']

    for i in range(len(infos)):
        print(f'{infos[i]:<20}{row1[i]:<15}{row2[i]:<15}{row3[i]:<15}{row4[i]:
↪<15}')
```

[ ]:
```
print_calibration_info()
```

```
                    Current        Original       Δ original     Δ last step
```

```
Scale [eV/channel]  0.010046        0.010000        0.461 %         0.282 %
Offset [keV]        0.193846        0.200000        -3.134 %        -1.293 %
E-res [eV]          128.676         130.000         -1.019 %        0.031 %
```

8 Calibrate the energy and width of the peaks

[ ]:
```
def calibrate_lines(m=m, rounds=2, xray_lines='all'):
    """Calibrating the energy and width of the specified lines in m."""
    for i in range(rounds):
        print(f'Calibrating peak positions, round {i+1} of {rounds}')
        m.calibrate_xray_lines(calibrate='energy', xray_lines=xray_lines,␣
↪kind='single') # use kind='multi' for better results? Dunno
        m.calibrate_xray_lines(calibrate='width', xray_lines=xray_lines,␣
↪kind='single')
```

[ ]:
```
calibrate_lines(rounds=2, xray_lines=lines_of_interest)
```

```
Calibrating peak positions, round 1 of 2
Calibrating peak positions, round 2 of 2
```

9 Calculate Fiori P/B, peak intensities, FWHMs, and peak deviations

[ ]:
```
def make_lines_info(m=m, all_lines=make_info_on_all_lines, sort_by='Area',␣
↪lines_of_interest=lines_of_interest):
    lines_info = {}
    for i in range(len(m) - 1): # last component is the background
        if (all_lines == True) or (m[i].name in lines_of_interest):
            lines_info[m[i].name] = {
                'Theoretical E [keV]': theoretical_energy(m[i].name),
                'Calibrated E [keV]': np.round(m[i].centre.value, 4),
                'Area': np.round(m[i].A.value, 1),
                'Fiori P/B': np.round(m[i].A.value / (m[-1].function(m[i].
↪centre.value) * scale), 1),
                'FWHM [eV]': np.round(m[i].fwhm * 1000, 3),
                'Sigma [keV]': np.round(m[i].sigma.value, 4),
                'Height': np.round(m[i].height * scale, 1),
                'FWHM(Mn Ka)' : np.round(np.sqrt(2.5*(5898.7 - m[i].centre.
↪value*1000) + (m[i].fwhm*1000)**2), 3),
            }
    lines_info = pd.DataFrame(lines_info).T
    lines_info['Delta E [eV]'] = np.round((lines_info['Calibrated E [keV]'] -␣
↪lines_info['Theoretical E [keV]'] ) * 1000, 2)
    lines_info = lines_info.sort_values(by=sort_by, ascending=False)
    return lines_info
```

[ ]:
```
lines_info = make_lines_info(all_lines=make_info_on_all_lines, sort_by='Area')
lines_info
```

[ ]:

	Theoretical E [keV]	Calibrated E [keV]	Area	Fiori P/B	\
Ga_La	1.0980	1.1000	332711.7	585.8	
Ga_Ka	9.2517	9.2537	301654.4	761.5	
As_Ka	10.5436	10.5456	183007.1	621.5	
As_La	1.2819	1.2839	140489.7	236.2	
Ga_Lb1	1.1249	1.1249	55576.2	97.2	
Ga_Kb	10.2642	10.2662	38822.9	123.6	
As_Kb	11.7262	11.7282	26698.9	117.4	
As_Lb1	1.3174	1.3174	23467.4	39.1	
Ga_Ll	0.9573	0.9573	18099.5	33.1	
Ga_Lb3	1.1948	1.1948	15338.0	26.4	
Ga_Ln	0.9842	0.9842	8347.7	15.2	
As_Ll	1.1196	1.1196	6924.7	12.1	
As_Lb3	1.3860	1.3860	6700.0	11.0	
As_Ln	1.1551	1.1551	2710.0	4.7	

	FWHM [eV]	Sigma [keV]	Height	FWHM(Mn Ka)	Delta E [eV]
Ga_La	66.866	0.0284	46960.0	128.327	2.0
Ga_Ka	162.634	0.0691	17505.2	134.396	2.0
As_Ka	172.548	0.0733	10009.8	134.743	2.0
As_La	72.009	0.0306	18412.9	129.315	2.0
Ga_Lb1	67.993	0.0289	7714.3	128.676	0.0
Ga_Kb	161.035	0.0684	2275.3	122.529	2.0
As_Kb	181.136	0.0769	1391.1	135.043	2.0
As_Lb1	71.444	0.0303	3100.0	128.676	0.0
Ga_Ll	64.838	0.0275	2634.5	128.676	0.0
Ga_Lb3	69.266	0.0294	2089.9	128.676	0.0
Ga_Ln	65.355	0.0278	1205.5	128.676	0.0
As_Ll	67.895	0.0288	962.6	128.676	0.0
As_Lb3	72.634	0.0308	870.6	128.676	0.0
As_Ln	68.546	0.0291	373.1	128.676	0.0

10 Calculate the relevant peak ratios

[ ]:
```
def peak_ratio(line1, line2, m=m):
    # give the K to L ratio of a line, e.g. 'Ga_Ka' to 'Ga_La'
    try:
        m[line1]
        m[line2]
    except ValueError:
        print('line not in model:', line1, line2)
        return np.nan
    return np.round(m[line1].A.value / m[line2].A.value, 3)
```

```
def calculate_all_line_ratios():
    line_ratios = {}
    for line_pair in line_ratio_list:
        pair_name = line_pair[0] + '/' + line_pair[1]
        line_ratios[pair_name] =  peak_ratio(line_pair[0], line_pair[1])
    line_ratios = pd.DataFrame(line_ratios, index=['Line ratio']).T
    return line_ratios
```

[ ]:
```
line_ratios = calculate_all_line_ratios()
print(line_ratios)
```

```
            Line ratio
As_Ka/As_La       1.303
Ga_Ka/Ga_La       0.907
Ga_La/As_La       2.368
```

11 Save the results in a DataFrame in a ".csv" file

[ ]:
```
def dead_time(s=s, m=m):
    real_time = s.metadata.Acquisition_instrument.SEM.Detector.EDS.real_time
    live_time = s.metadata.Acquisition_instrument.SEM.Detector.EDS.live_time
    dead_time_percent = (real_time - live_time)/real_time*100
    print(f'Dead time: {dead_time_percent:.1f}%')
    return round(dead_time_percent, 1)
```

[ ]:
```
dead_time_percent = dead_time(s=s, m=m)
```

```
Dead time: 43.7%
```

[ ]:
```
def make_output():
    key_output = pd.DataFrame({
        'Name': [name],
        'Nominal beam energy [kV]': [Vacc],
        'Beam current [pA]': [beam_current],
        'Process time' : [process_time],
        'ICR' : [input_count_rate],
        'Dead time [%]': [dead_time_percent],
        'Live time [s]': [round(s.metadata.Acquisition_instrument.SEM.Detector.
 ↪EDS.live_time, 1)],
        'Duane-Hunt limit [kV]': [dh_limit],
        'Scale [keV]': [scale],
        'Offset [keV]': [offset],
        'Energy resolution [eV]': [energy_resolution],
    })
    for ratio_pair in line_ratios.T.columns:
```

```
        key_output[f'Ratio ({ratio_pair})'] = line_ratios.T[ratio_pair][0]

    for line in fiori_peaks:
        try:
            key_output[f'Fiori PB ({line})'] = lines_info.loc[line, 'Fiori P/B']
        except KeyError:
            key_output[f'Fiori PB ({line})'] = np.nan

    return key_output
```

[ ]:
```
key_output = make_output()
key_output.T
```

[ ]:

	0
Name	GaAs_30kV_50pA
Nominal beam energy [kV]	30.0
Beam current [pA]	50
Process time	6
ICR	16400
Dead time [%]	43.7
Live time [s]	120.0
Duane-Hunt limit [kV]	NaN
Scale [keV]	0.010046
Offset [keV]	0.193846
Energy resolution [eV]	128.675916
Ratio (As_Ka/As_La)	1.303
Ratio (Ga_Ka/Ga_La)	0.907
Ratio (Ga_La/As_La)	2.368
Fiori PB (Ga_La)	585.8
Fiori PB (As_La)	236.2
Fiori PB (Ga_Ka)	761.5

[ ]:
```
def save_output():
    # save the output-df to a csv file
    key_output.T.to_csv(f'results/{name}_output.csv')
    # saves the line info df to another csv file
    save_lines_info = True
    if save_lines_info:
        lines_info.to_csv(f'results/lines_info/{name}_lines_info.csv')
```

[ ]:
```
save_output()
# ![Image](https://folk.ntnu.no/brynjamm/marathon_dabz.gif)
```

Appendix B

Quantification result tables

This appendix contains the following tables:

- Table B.1 - Quantification of SEM EDS data with the thin film assumption.
- Table B.2 - The calculated range of electrons, r, where the electrons still have enough energy to excite the listed X-ray line.
- Table B.3 - The absorption correction factors for the ZAF model.
- Table B.4 - Quantification of SEM EDS data with the ZAF absorption correction.
- Table B.5 - Quantification of SEM EDS data with the corrections form the XPP model.

The table with initial quantification, i.e. from AZtec and the intensity ratio method, is given in Table 4.11.

Table B.1: Quantification of SEM EDS data with the thin film assumption, i.e. TEM EDS routines. Compositions in at.% from AZtec and the CL method in HyperSpy. CL* is without corrections, the others have absorption corrections with thicknesses t, in nm. The calculated k-factors from AZtec is also tabulated. The table is summarized in Table 4.12. Each spectrum has two lines in the table.

Gr.	Line	E_0	i_b	PT	k-factor	AZtec TEM	CL*	CL	CL	CL	CL	CL	CL
		[kV]	*[pA]*			*at.%*		*t=50*	*t=100*	*t=200*	*t=400*	*t=1k*	*t=10k*
A	As Lα	5	25	6	1.21	45	45	47	48	51	54	60	63
A	Ga Lα	5	25	6	1.09	55	55	53	52	49	46	40	37
A	Ga Lα	10	25	6	1.31	42	42	43	45	47	51	57	61
A	As Lα	10	25	6	1.22	58	58	57	55	53	49	43	39
A	As Lα	15	25	6	1.33	38	37	39	40	43	47	53	58
A	Ga Lα	15	25	6	1.26	62	63	61	60	57	53	47	42
A	As Kα	30	25	6	4.19	42	42	42	42	42	42	43	50
A	Ga Kα	30	25	6	3.27	58	58	58	58	58	58	57	50
A	As Kα	30	50	6	4.19	42	41	42	42	42	42	43	50
A	Ga Kα	30	50	6	3.27	58	59	59	58	58	58	57	50
B	Ga Lα	5	50	6	1.09	91	-	-	-	-	-	-	-
B	Sb Mζ	5	50	6	0.96	9	-	-	-	-	-	-	-
B	Ga Lα	10	50	6	1.22	42	52	55	58	62	67	76	85
B	Sb Lα	10	50	6	3.30	58	48	45	42	38	33	24	15
B	Ga Lα	15	50	6	1.26	29	39	42	45	49	56	67	80
B	Sb Lα	15	50	6	2.75	71	61	58	55	51	44	33	20
B	Ga Kα	30	50	6	3.27	45	57	56	56	56	55	53	36
B	Sb Lα	30	50	6	2.32	55	43	44	44	44	45	47	64
C	Ga Kα	30	50	4	3.27	45	57	57	57	56	55	53	36
C	Sb Lα	30	50	4	2.32	55	43	43	43	44	45	47	64
C	Ga Kα	30	50	2	3.27	45	58	58	57	57	56	54	37
C	Sb Lα	30	50	2	2.32	55	42	42	43	43	44	46	63
C	Ga Kα	30	50	1	3.27	45	59	59	59	58	57	55	38
C	Sb Lα	30	50	1	2.32	55	41	41	41	42	43	45	62
D	Ga Lα	15	200	6	1.26	29	38	41	44	49	56	67	79
D	Sb Lα	15	200	6	2.75	71	62	59	56	51	44	33	21
D	Ga Lα	15	400	6	1.26	29	38	41	44	49	56	67	79
D	Sb Lα	15	400	6	2.75	71	62	59	56	51	44	33	21
D	Ga Kα	30	400	1	3.27	45	59	58	58	58	57	55	37
D	Sb Lα	30	400	1	2.32	55	41	42	42	42	43	45	63

Table B.2: Selected maximum ranges of creation for lines in different specimen, based on the Kanaya-Okayama parameterization. The path length of the X-rays are $r \cdot \csc(TOA)$. The ranges are used to calculate the ZAF absorption correction factors, listed in Table B.3.

Specimen	**Line**	r **at 30 kV** *[µm]*	r **at 15 kV** *[µm]*	r **at 10 kV** *[µm]*	r **at 5 kV** *[µm]*
GaAs	Ga Lα	4.13	1.29	0.65	0.19
	As Lα	4.12	1.28	0.64	0.19
	Ga Kα	3.56	0.72	0.08	-
GaSb	Ga Lα	4.02	1.25	0.63	0.19
	Sb Lα	3.92	1.15	0.53	0.09

Table B.3: Absorption correction factors (A) from the ZAF method used. The absorption correction factors are in the three rightmost columns, indicated by "A r/x", where x is the number that the maximum electron range is divided by. Similar specimen, line, and E_0 have the same A, thus the 15 kV and 30 kV GaSb A-factors are grouped together.

Groups	**Line**	E_0 *[kV]*	A **with r/2**	A **with r/3**	A **with r/4**
A	As Lα	5	1.41	1.26	1.19
A	Ga Lα	5	1.14	1.09	1.07
A	As Lα	10	3.27	2.20	1.81
A	Ga Lα	10	1.58	1.35	1.26
A	As Lα	15	10.67	4.85	3.27
A	Ga Lα	15	2.48	1.83	1.57
A	As Kα	30	1.23	1.15	1.11
A	Ga Kα	30	1.08	1.05	1.04
B	Ga Lα	5	1.64	1.39	1.28
B	Sb Lα	5	1.02	1.01	1.01
B	Ga Lα	10	5.24	3.02	2.29
B	Sb Lα	10	1.14	1.09	1.07
B, D	Ga Lα	15	27.19	9.04	5.21
B, D	Sb Lα	15	1.32	1.20	1.15
B, C, D	Ga Kα	30	1.27	1.17	1.13
B, C, D	Sb Lα	30	2.56	1.87	1.60

Table B.4: Compositions from the intensity ratio method with absorption corrected intensities. The uncorrected at.% value is tabulated for reference. See Table B.3 for the correction factors. Average numbers are given in Table 4.13. Each spectrum has two lines in the table.

Groups	Line	E_0 [kV]	i_b [pA]	Uncorr. at.%	at.% with r/2	at.% with r/3	at.% with r/4
A	As Lα	5	25	43	48	46	45
A	Ga Lα	5	25	57	52	54	55
A	As Lα	10	25	40	58	52	49
A	Ga Lα	10	25	60	42	48	51
A	As Lα	15	25	36	71	60	54
A	Ga Lα	15	25	64	29	40	46
A	As Kα	30	25	36	39	38	37
A	Ga Kα	30	25	64	61	62	63
A	As Kα	30	50	36	39	38	37
A	Ga Kα	30	50	64	61	62	63
B	Ga Lα	5	50	97	98	98	98
B	Sb Lα	5	50	3	2	2	2
B	Ga Lα	10	50	75	93	89	86
B	Sb Lα	10	50	25	7	11	14
B	Ga Lα	15	50	58	97	91	86
B	Sb Lα	15	50	42	3	9	14
B	Ga Kα	30	50	48	32	37	40
B	Sb Lα	30	50	52	68	63	60
C	Ga Kα	30	50	48	32	37	40
C	Sb Lα	30	50	52	68	63	60
C	Ga Kα	30	50	49	33	38	41
C	Sb Lα	30	50	51	67	62	59
C	Ga Kα	30	50	51	34	39	42
C	Sb Lα	30	50	49	66	61	58
D	Ga Lα	15	200	57	97	91	86
D	Sb Lα	15	200	43	3	9	14
D	Ga Lα	15	400	57	97	91	86
D	Sb Lα	15	400	43	3	9	14
D	Ga Kα	30	400	50	33	39	41
D	Sb Lα	30	400	50	67	61	59

Table B.5: Compositions with XPP corrections. The two type of corrections used are to divide the measured intensity I_A of each peak by: (1) the absorption correction factor $f(\chi)$ for the line, and (2) by the calculated generated intensity F. The table is summarized in Table 4.14. Each spectrum has two lines in the table.

Groups	**Line**	E_0 *[kV]*	i_b *[pA]*	**Uncorr. intensity ratio** *[at.%]*	**XPP corr.** $(I_A/f(\chi))$ *[at.%]*	**XPP corr.** (I_A/F) *[at.%]*
A	As Lα	5	25	43	43	44
A	Ga Lα	5	25	57	57	56
A	As Lα	10	25	40	42	41
A	Ga Lα	10	25	60	58	59
A	As Lα	15	25	36	39	36
A	Ga Lα	15	25	64	61	64
A	As Kα	30	25	36	36	37
A	Ga Kα	30	25	64	64	63
A	As Kα	30	50	36	36	37
A	Ga Kα	30	50	64	64	63
B	Ga Lα	5	50	97	97	91
B	Sb Lα	5	50	3	3	9
B	Ga Lα	10	50	75	79	65
B	Sb Lα	10	50	25	21	35
B	Ga Lα	15	50	58	67	50
B	Sb Lα	15	50	42	33	50
B	Ga Kα	30	50	48	48	56
B	Sb Lα	30	50	52	52	44
C	Ga Kα	30	50	48	48	56
C	Sb Lα	30	50	52	52	44
C	Ga Kα	30	50	49	49	57
C	Sb Lα	30	50	51	51	43
C	Ga Kα	30	50	51	50	58
C	Sb Lα	30	50	49	50	42
D	Ga Lα	15	200	57	66	49
D	Sb Lα	15	200	43	34	51
D	Ga Lα	15	400	57	66	49
D	Sb Lα	15	400	43	34	51
D	Ga Kα	30	400	50	50	58
D	Sb Lα	30	400	50	50	42

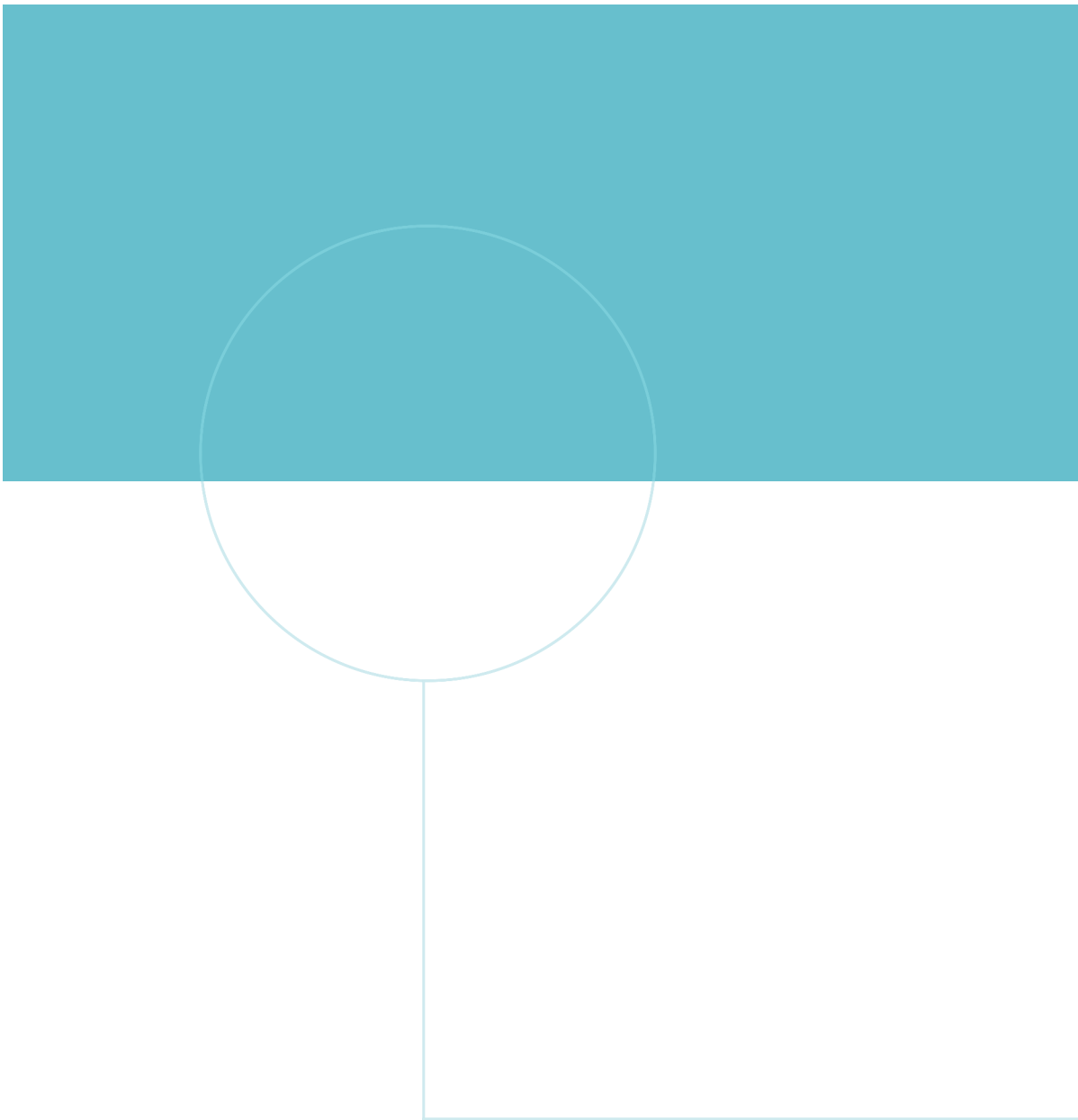

NTNU

Norwegian University of
Science and Technology